Deeply Virtual Compton Scattering at COMPASS

Dissertation zur Erlangung des Grades
"Doktor der Naturwissenschaften"

am Fachbereich 08- Physik, Mathematik, Informatik
der Johannes Gutenberg-Universität, Mainz

JG|U

vorgelegt von
Johannes Vincenzo Giarra
geboren in Steinfurt

Mainz, 20.06.2022

Hereby I, Johannes Vincenzo Giarra, declare that I have completed this thesis, entitled: *Deeply Virtual Compton Scattering at COMPASS* independently, by making use only of the specified literature. If not stated otherwise, the content is entirely the product of my own work.

Mainz, den 20.06.2022

_____
Signature

Abstract

Studying hard exclusive reactions in lepton-nulceon scattering like for e.g. hard exclusive photoproduction in *Deeply Virtual Compton Scattering* (DVCS), allows to study the 3-dimensional nucleon structure in the framework of *Generalized Parton Distribution function*s (GPDs). From the DVCS cross section, combinations of *Compton Form Factor*s (CFFs) can be extracted, which are used to further constrain the related GPDs.

In 2016 and 2017, COMPASS measured DVCS ($\mu p \rightarrow \mu' p' \gamma$) on a 2.5 m long liquid hydrogen target using high energy (160 GeV), positively and negatively charged polarized muon beams provided by the M2 beamline of the SPS at CERN. The scattered muons and the produced real photons were detected by the COMPASS spectrometer, which was supplemented by an additional electromagnetic calorimeter for the detection of large-angle photons. To perform an exclusive measurement of the full final state, the target was surrounded by a barrel-shaped time-of-flight system to detect the recoiling target protons.

The exclusive photon event sample is extracted using a dedicated event selection to identify all participating particles. This event selection includes the use of exclusivity conditions like for e.g. restricting the missing mass and is further improved by a kinematic fit under the assumption of the topology of a exclusive photon event. Its quality is used as an additonal selecting criterium. The fitalso improves the resolution of the event kinematics, in particular on the square of the four-momentum transfer to the proton $|t|$.

The selected data sample does not only include DVCS events, but also contributions by radiative photons produced in the *Bethe-Heitler* (BH) process and a background contamination by photons originating from the decay of neutral pions. These contributions are determined using dedicated Monte-Carlo samples and are subtracted from the data sample to obtain the pure DVCS contribution.

The DVCS cross section is extracted in bins of $|t|$, separately for each beam charge and polarization. These cross section values are averaged over both beam charges, which allows to extract the $|t|$-dependence of the charge spin cross section sum. Studying this dependence allows to extract the slope parameter B by a binned log-likelihood fit using an exponential ansatz of the from: $e^{-B|t|}$. The slope parameter is dominated by the contribution of the imaginary part of CFF $\mathcal{H}$. At the COMPASS kinematics, which covers the x_{Bj}-domain of sea quarks, it is related to the transverse extension of the proton due to the quark distributions.

In the present analysis about 2/3 of the available data in 2016 are used. The 2017 sample is expected to provide two to three times higher statistics, which will allow to extend the analysis and extract the dependence of the slope parameter on x_{Bj}.

Zusammenfassung

In exklusiven Streuprozessen, wie etwa der exklusiven Photoproduktion in der sogenannten tiefvirtuellen Comptonstreuung (DVCS), kann die 3-dimensionale Struktur der Nukleonen untersucht werden. Diese wird durch generalisierte Partonverteilungsfunktionen (GPDs) beschrieben. Die GPDs stehen in Beziehung zu sogenannten Compton-Formfaktoren (CFFs), die durch Messungen des DVCS-Wirkungsquerschnitts bestimmt werden können.

Eine entsprechende Messung wurde in den Jahren 2016 und 2017 mit dem COMPASS-Experiment an der M2-Strahlführung des SPS am CERN durchgeführt. Hierbei wurden hochenergetische (160 GeV), positiv und negativ geladene Myonen mit entgegengesetzter Polarisation an einem 2.5 m langen Flüssigwasserstofftarget gestreut. Die gestreuten Myonen und das reelle Photon wurden mit dem COMPASS-Spektrometer gemessen, das dazu durch ein zusätzliches elektromagnetisches Kalorimeter ergänzt wurde. Für die Rückstoßprotonen aus dem Target wurde ein das Target umgebender Detektor genutzt, der die Flugzeit und den Energieverlust der Protonen misst.

Die exklusive Messung aller am Prozess beteiligten Teilchen erlaubt es die Photonstreuereignisse mit Hilfe einer speziellen Selektion zu extrahieren. Durch die exklusive Messung lässt sich z.B. die fehlende Masse überprüfen und zur Selektion verwenden. Zusätzlich erlaubt sie auch einen kinematischen Fit aller beteiligter Teilchen, dessen Qualität einerseits dazu genutzt wird, die Selektion weiter zu verfeinern und anderseits die erzielte Auflösung bei den kinematischen Variablen zu verbessern, vorallem für das Quadrat des Viererimpulsübertrags auf das Proton $|t|$.

Neben den DVCS-Ereignissen beinhalten die selektierten Daten auch Photonen aus dem Bethe-Heitler Prozess und dem Zerfall von neutralen Pionen. Diese Beiträge werden mit Hilfe von Monte-Carlo-Simulationen bestimmt und anschließend von den Daten subtrahiert.

Mit den resultierenden DVCS-Ereignissen wird der entsprechende Wirkungsquerschnitt in verschiedenen $|t|$-Intervallen und separat für beide Strahlladungen bestimmt. Mittelt man anschliessend über beide Strahlladungen, erhält man den $|t|$-abhängigen DVCS-Wirkungsquerschnitt. Dies erlaubt es die $|t|$-Abhängigkeit durch eine Maximum-Log-Likelihood-Methode, mit dem Ansatz: $e^{-B|t|}$ anzupassen. Die Steigung B wird durch den Beitrag des imaginären Teils des CFF $\mathcal{H}$ dominiert, welcher direkt mit der transversalen Ausdehnung der Quarkverteilungen im Proton zusammenhängt. Im Bereich der COMPASS-Kinematik erfolgt die Messung im x_{Bj}-Bereich der Seequarks.

Gegenwärtig werden in der Analyse etwa 2/3 der vorhandenen 2016er Daten genutzt. Sobald die 2017 Daten hinzugenommen werden, ist es auch möglich die Abhängigkeit der Steigung von x_{Bj} und damit auch die Ausdehnung des Protons bei verschiedenen Werten von x_{Bj} zu bestimmen.

Contents

Introduction

-"What is it made of?"- (*unknown*)

This simple question comprises a fundamental desire to understand the structure of matter. This desire persists provably since the ancient times and probably also far back. A philosophic attempt of approaching this question goes back to the Greek philosopher Demokrit, who coined the term *atom*[1] in his idea that everything in existence is composed of small, indivisible 'particles'. Further he assumed that there are different kinds of atoms, which are also responsible for the different observed properties of objects. A first noteworthy scientific approach was by the English natural scientist John Dalton. In his book A NEW SYSTEM OF CHEMICAL PHILOSOPHY [49], published in 1808, he presented new ideas on chemical elements. According to this, each element consists of a specific kind of indistinguishable 'atoms'. The specific atoms of each element differ by their masses and can be combined with, or seperated from atoms of other elements. The first elementary particle was discovered in 1897 by the English physicist J. J. Thomson and named *electron* [62] after the Greek word for 'amber'. Inspired by his discovery he deduced the idea for an atomic model known as 'plum pudding model' [63]. Here, the negatively charged electrons are embedded in a positively charged cloud, like plums in a pudding. In 1911, Ernest Rutherford observed in his famous experiment, where α-particles are scattered off a thin gold foil [154], that the observed pattern of the scattered α-particles was in vast contrast to expectations based on this atomic model. Rutherford concluded that instead of a positive charge cloud, the atom must rather have a positively charged massive core. This *nucleus* is small in size and surrounded by electrons, so most of the space occupied by an atom is empty. This astonishing insight on the structure of atoms was followed by the discovery of the *proton* (1919 by E. Rutherford) as the first constituent of the atom core, giving it its appropriate name (gr. prôton="first"). The discovery of the *neutron* in 1932 by J. Chadwick [43] provided the last missing constituent of atoms as we view them today. Still, knowing all its pieces does not allow to conclude on the details of its structure. In particular how the atom can form a stable system consisting of particles with opposite electrical charge. So already in 1913, inspired by the results of Rutherford's scattering experiment and the interpretation of the black body radiation by Max Planck, Niels Bohr developed a model, in which the electrons circle the atom core in a stable orbit [177]. This model marks the starting point for the development of quantum theory, which gives the basic concept of our understanding of physics on the atomic scale and below. The quantum concept was further developed in the mid 1900s and evolved to the framework of quantum mechanics. Generalizations of this framework led to the development of quantum field theories to describe subatomic particles and their interactions on the quantum level. These developments were accompanied by experimental discoveries,

---

[1]gr. atomos="indivisible"

revealing for e.g. the non-elementary character of the nucleons (proton and neutron) and the vast spectra of particles. Detailed studies of the nucleon structure resulted in the development of the *quark-parton model* (QPM), in which the nucleon is described as a composite system of elementary constituents.

All these discoveries and developments led to the formulation of the *Standart Model* (SM) of particle physics, which was finalized in the mid 1970s (see Fig. 1.1). The elementary particles contained in the
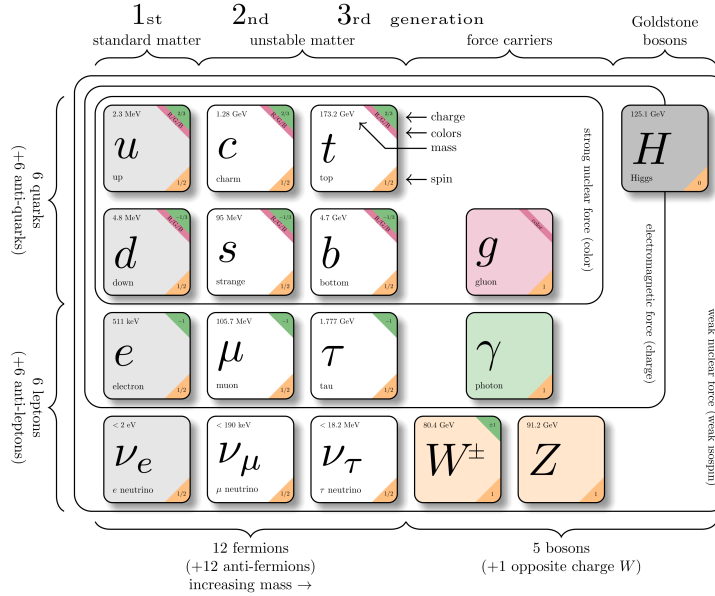
Figure 1.1: Diagram of the SM. Figure adopted from Ref. [39].

SM are the origin of the observed matter and antimatter and of the fundamental forces responsible for their interaction. Matter and antimatter are formed by half integer spin particles called *fermions*, namely *quarks* and *leptons* and their corresponding antiparticles. Quarks are the constituents of all known composite particles (hadrons) and appear in 6 different flavours. The elementary particles are characterized by a set of *quantum numbers*, corresponding for e.g. to their electric charge and spin. These quantum numbers characterize the properties of the particles, except of their masses, which emerge from the Higgs mechanism. In this mechanism the massive particles are interacting with the omnipresent Higgs field, due to the exchange of the Higgs boson. Its discovery in 2012 [1, 44] completed today's picture of the SM. The term *boson* comprises all integer spin particles, that are exchanged, when transmitting the fundamental forces. Three of the four fundamental forces are included in the framework of the SM, namely the elecromagnetic, the weak and the strong force. These forces are described by *quantum field theories*. As of today a description of the gravitational force in terms of a quantum field theory is missing. The theory of the weak and electromagnetic forces is the summarized in the *quantum flavour-dynamics* (QFD). Within its framework the corresponding bosons are either electric charged *W-bosons*, neutral *Z-bosons* or *photons*. The theory of strong force is called *quantum chromodynamics* (QCD) and the exchange bosons are so called *gluons*. The properties of quarks and their interaction through the strong force lead to the observed properties of the nucleons.

The nucleon structure can be studied in measurements of deep inelastic lepton-nucleon scattering (DIS). The complexity of these structures is contained in distribution functions, among which the GPDs provide access to unravel the complex 3-dimensional structure and the spin composition of nucleons. Experimentally, GPD related quantities are studied in hard exclusive reactions, like for e.g. exclusive

photoproduction in DVCS. In DVCS these quantities are called CFFs and can be extracted using *cross section* measurements.

Subject of this thesis is the extraction of the DVCS cross section from data on muon-proton scattering taken by the COMPASS[2] experiment in 2016/17. It is organized as follows. Chapter 2 describes the general properties of the measurement of lepton-nucleon scattering and its theoretical description. This includes summaries of the QPM and its QCD extension, the framework of GPDs, their relation to CFFs and the corresponding observables in measurements of DVCS. The COMPASS experiment, located at CERN[3] is introduced in Chapter 3. It provides the details on the requirements of the experimental setup for an exclusive measurement of DVCS in high energetic muon-proton scattering. Beside the general detector setup this Chapter also includes a summary of the Data Acquisition (DAQ) and data reconstruction, as well as of the Monte-Carlo (MC) simulation of physics processes and their detector responses. The data set used in the present analysis is discussed in Chapter 4. Here, dedicated analysis procedures to investigate the data quality and to improve its comparison to simulated data are presented. This includes improved methods for a more precise determine of detector efficiencies and calibrations, in particular efficiencies related to the muon trigger system. Also methods to extract crucial inputs to the cross section calculation, like for e.g. the effective muon flux, are discussed. The selection criteria used to extract exclusive photon events, the application of a kinematic fit and methods to identify non-DVCS events are discussed in Chapter 5. These contributions to the exclusive photon data sample are photons produced by *bremsstrahlung* in the BH process or photons originating from a decay of neutral pions. The Chapter concludes with a discussion of kinematic distributions showing the contribution of DVCS, *Bethe-Heitler* and neutral pions. The spectrometer acceptance for exclusive photon production and a review of the quality of the MC simulation of the exclusive photon event sample is given in Chapter 6. The extraction of the DVCS cross section, the results and their interpretations are discussed in Chapter 7. Chapter 8 summarizes the most crucial analysis steps, the presented results and conclusions, and gives a brief outlook on further DVCS analysis of the 2016/17 data sample.

---

[2]Common Muon Proton Apparatus for Structure and Spectroscopy (COMPASS)
[3]Conseil européen pour la recherche nucléaire (CERN)

The structure of nucleons

The following Chapter gives a summary of today's understanding of the nucleons and the methods used to investigate its structure. A way to analyse this structure is by perfomring lepton-nucleon scattering, which is introduced in Section 2.1. These measurements provide experimental observables that allow to study the nucleon properties and also give first hints on the nucleon being a composite particle of point like constituents. These insights led to the development of the *quark-parton model* (QPM). Its first implementation and its extension by *quantum chromodynamics* (QCD) are discussed in Section 2.2. The deeper understanding of the nucleon structure conducted to the concept of *Generalized Parton Distribution function*s (GPDs) (see Sec. 2.4) and their capability to study the 3-dimensional nucleon structure and disentangle the contributions to the nucleon spin. Experimental observables, which are related to GPD can be extracted from measurements of hard exclusive reactions, in particular in hard exclusive photon production, namely in the *Deeply Virtual Compton Scattering* (DVCS) process. This process and its cross section is subject of the discussion in Section 2.5. A summary of previous experimental approaches measuring DVCS and its measurement at COMPASS are specified in Section 2.6 and 2.7.

2.1 | Lepton-nucleon scattering

The measurement of lepton-nucleon scattering is a versatile tool to study the structure of nucleons. An illustration of the process in lowest order *quantum electrodynamics* (QED) is shown in Figure 2.1. Here, the process is displayed as one-photon-exchange between the lepton and the nucleon. In the process also an exchange of a Z-boson is possible, but due to its high mass this exchange is suppressed and therefore negligible at COMPASS kinematics. Higher order corrections to this process comprise additional radiation of real photons (bremsstrahlung) by the lepton or emission and re-absorption of virtual photons and lepton-antilepton fluctuations. These corrections can be calculated in a perturbative approach of QED. The order of the correction depends on the number of additional interaction vertices, each contributing an additional factor of the electromagnetic coupling α. One distinguishes between the elastic and inelastic lepton-nucleon scattering, which are discussed in further detail in Section 2.1.2 and 2.1.3.
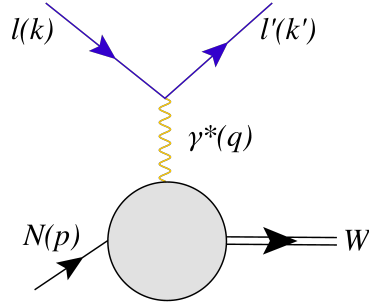
Figure 2.1: Illustration of lepton-nucleon scattering in the one-photon-exchange approximation.

2.1.1 | Kinematics of lepton-nucleon scattering

The lepton-nucleon scattering is described by two variables, which correspond to the kinematics of the virtual photon. Two commonly used variables are the Lorentz invariant quantities Q^2 and ν, which are the so called photon virtuality and its energy. These variables are calculated using the four-momenta of the participating particles in the process. These are denoted as k and k' for the incoming and scattered lepton, p for the nucleon and q for the virtual photon:

$$k = (E, \vec{k}), \quad k' = (E', \vec{k}'), \quad p = (E_N, \vec{p}) \quad \text{and} \quad q = (k - k') = (\nu, \vec{q}).$$

The photon virtuality Q^2 is calculated as:

$$Q^2 = -q^2 = -(k - k')^2 = 2(EE' - \vec{k} \cdot \vec{k}') - m_l^2 - m_{l'}^2 \approx \frac{4EE'}{c^2} \sin^2(\theta/2), \tag{2.1}$$

with θ denoting the angle between $\vec{k}$ and $\vec{k}'$ in the laboratory frame. Its approximation is valid in cases where the lepton mass m is small compared to its energy and can be neglected. The energy of the virtual photon is given as:

$$\nu = \frac{pq}{M} \overset{\text{lab}}{=} E - E'. \tag{2.2}$$

Here, M is the mass of the nucleon. In the laboratory frame, where the nucleon is at rest ($p = (Mc, \vec{0})$), ν corresponds to the difference in the energies of the incoming and scattered lepton. As ν is not dimensionless, a frequently used variable is:

$$y = \frac{qp}{pk} \overset{\text{lab}}{=} \frac{\nu}{E}. \tag{2.3}$$

In the laboratory frame y is given by the difference between the lepton energies divided by the energy of the incoming lepton.
Another commonly used quantity is the Lorentz invariant *Bjorken scaling variable*:

$$x_{Bj} = \frac{Q^2}{2pq} = \frac{Q^2}{2M\nu}. \tag{2.4}$$

In case of elastic lepton-nucleon scattering, x_{Bj} is equal to one, while in the inelastic case $x_{Bj} < 1$. As y and x_{Bj} are both dimensionless, it is convenient to use those variables instead of Q^2 and ν when

describing lepton-nucleon scattering.

The final state of the process is characterized by its invariant mass W, which is given as:

$$W^2 c^2 = (q + p)^2 = p^2 + 2pq + q^2 = M^2 c^2 + 2M\nu - Q^2. \tag{2.5}$$

For the elastic lepton-nucleon scattering W corresponds to the mass of the initial nucleon ($W = M$), while in the inelastic scattering W is larger ($W > M$).

2.1.2 | Elastic lepton-nucleon scattering

The term elastic refers to lepton-nucleon scattering processes with the same particles in its initial and final state. The topology of the reaction is summarized as:

$$l + N \rightarrow l' + N',$$

and illustrated in Figure 2.2.

Since the late 1920s, it is known that the proton is a charged, half integer spin particle. Due to the spin, the proton has a magnetic moment. The first experiments dedicated to study the magnetic moment of the proton were performed by R. Frisch and O. Stern in 1933 [69]. These experiments and subsequent high precision measurements in the late 1940s and early 1950s resulted in a larger value of the magnetic moment than what was expected for an point like particle. This anomalous magnetic moment of the proton led to the conclusion that the proton must imply a complex structure. The electromagnetic structure of the proton was further studied in elastic lepton-nucleon scattering. First measurements using a 188 MeV electron beam and a hydrogen or helium target were performed at the Stanford Linear Accelerator Center (SLAC) in the mid 1950s by a team led by R. W. McAllister and R. Hofstadter [126]. The study of the cross sections allowed a first determination of the electric form factor (FF). Its Q^2-dependence can be described by a so called dipole form factor and confirms the finite size of the proton. This study was extended to perform systematic measurements of the cross sections for leptons scattering off light and heavy nuclei targets [106].
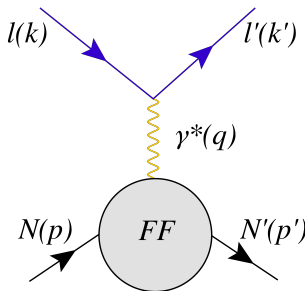

Figure 2.2: Illustration of the elastic lepton-nucleon scattering in the one-photon-exchange approximation.

2.1.2.1 | Cross sections and form factors

In today's notation the differential cross section of elastic lepton-nucleon scattering in one-photon-exchange approximation reads as [64]:

$$\frac{d\sigma}{d\Omega} = \left(\frac{d\sigma}{d\Omega}\right)_{\text{Mott}} \cdot \left[\frac{G_E^2(Q^2) + \tau G_M^2(Q^2)}{1 + \tau} + 2\tau G_M^2(Q^2)\tan^2\frac{\theta}{2}\right] \tag{2.6}$$

$$\text{with } \tau = \frac{Q^2}{4M^2c^2}.$$

Equation 2.6 is commonly known as *Rosenbluth formula*. Here, $d\Omega$ is the solid angle element the lepton is detected in and θ is the polar angle of the scattered lepton in the targets center of mass system (CMS). The so called Mott cross section is given by:

$$\left(\frac{d\sigma}{d\Omega}\right)_{\text{Mott}} = \frac{\alpha^2(\hbar c)^2}{4E^2\sin^4\frac{\theta}{2}} \cdot \frac{E'}{E} \cdot \left(1 - \beta^2\sin^2\frac{\theta}{2}\right) \tag{2.7}$$

$$= \left(\frac{d\sigma}{d\Omega}\right)_{\text{Rutherford}} \cdot \frac{E'}{E} \cdot \left(1 - \beta^2\sin^2\frac{\theta}{2}\right),$$

where $\beta = v/c$ is the lepton velocity with respect to the speed of light and $\hbar$ the Planck constant divided by 2π. The first part of this equation is also known as the Rutherford cross section. It describes the scattering between two point-like and spinless particles. The half integer spin of the lepton is responsible for the second term in Equation 2.7, while the ratio E/E' accounts for the nucleon recoil.

The functions $G_E(Q^2)$ and $G_M(Q^2)$ in Equation 2.6 are the electric and magnetic elastic form factors of the nucleon, which are at low Q^2 the Fourier transformations of the spatial distributions of its charge and magnetic moment. These factors are also known as *Sachs form factors* and are related to the historically introduced Dirac and Pauli form factors (F_1 and F_2) by [61]:

$$G_E = F_1 - \tau F_2 \text{ and } G_M = F_1 + F_2.$$

2.1.2.2 | Determination of elastic form factors

A way to disentangle $G_E^2(Q^2)$ and $G_M^2(Q^2)$ is by utilizing the so called *Rosenbluth separation*. Here, Equation 2.6 is transformed to [137]:

$$\left(\frac{d\sigma}{d\Omega}\right)_{\text{reduced}} = \frac{\epsilon(1 + \tau)}{\tau}\left(\frac{d\sigma}{d\Omega}\right)_{\text{exp}} \Big/ \left(\frac{d\sigma}{d\Omega}\right)_{\text{Mott}} \tag{2.8}$$

$$= G_M^2(Q^2) + \frac{\epsilon}{\tau}G_E^2(Q^2)$$

$$\text{with } \epsilon = \left[1 + 2(1 + \tau)\tan^2\frac{\theta}{2}\right]^{-1}.$$

Where $(d\sigma/d\Omega)_{\text{exp}}$ is the experimentally measured cross section. By exploiting its linear dependence on ϵ, Equation 2.8 allows to separate $G_E^2(Q^2)$ and $G_M^2(Q^2)$ at fixed values of Q^2. In the limit of $Q^2 \to 0$ these form factors correspond to the electric charge of the nucleon normalized to the elementary charge e and its magnetic moment normalized to the nuclear magneton μ_N:

$$G_E^2(0) = q/e, \quad G_M^2(0) = \mu/\mu_N.$$

A result of the electric and magnetic form factors of the proton [31] is shown in Figure 2.3, obtained by a high precision measurement of elastic electron-proton scattering at the Mainz Microtron (MAMI). The Q^2-dependence of the form factors is displayed with respect to the standard dipole parametrization ($G_{\text{std.dipole}}$) [103]:

$$G_E = \frac{G_M}{\mu_p} = G_{\text{std.dipole}}(Q^2) = \left(1 + \frac{Q^2}{0.71\,\text{GeV}^2}\right)^{-2}.$$

Here, μ_p is the value of anomalous magnetic moment of the proton. This parametrization corresponds to exponential decreasing distributions of the charge and the magnetic moment of the nucleon. The high precision measurement reveals deviations from the exponential behavior, which are present already at small Q^2 and increase to larger values of Q^2. The observed discrepancies are caused by the complex structure of the proton, which is not considered in the dipole ansatz.
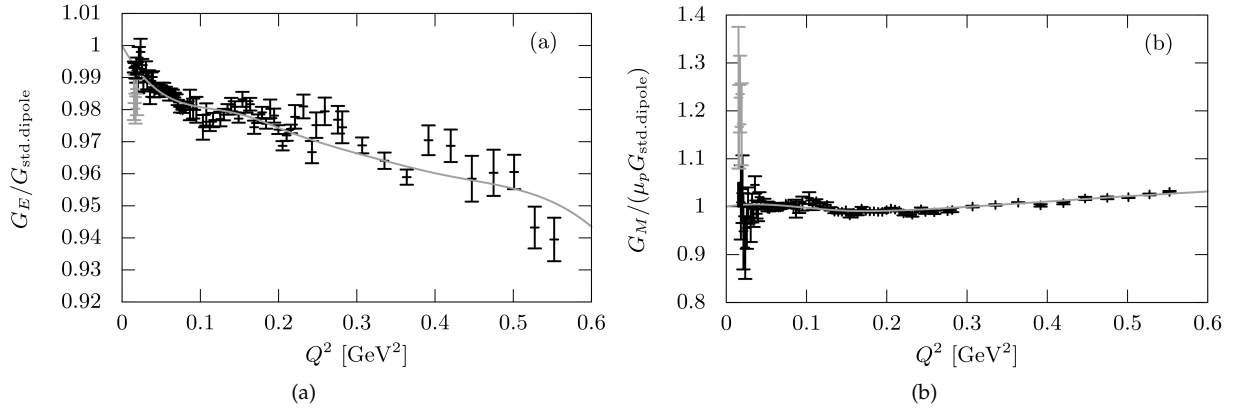
Figure 2.3: Results on G_E (a) and G_M (b) relative to the standard dipole ansatz ($G_{\text{std.dipole}}$) extracted by the Rosenbluth separation from elastic electron-proton scattering at MAMI (black points). The grey curves show a spline fit. Figures taken from Ref. [31].

2.1.3 | Inelastic lepton-nucleon scattering

When studying the nucleon structure using higher beam energies and therefore at larger Q^2, additional reaction channels open up. In this kinematic regime the scattering process is referred to as inelastic scattering. In contrast to elastic scattering the final state particles in inelastic scattering are either excited states of the initial nucleon (nucleon resonances) or particles produced due to the fragmentation of the target nucleon. The scattering process is illustrated in Figure 2.4 and its topology is summarized as:

$$l + N \rightarrow l' + X.$$

Here, X summarizes all particles in the hadronic final state. If the invariant mass of the finals state exceeds the mass of the individual nucleon resonances, one refers to the process as *deep inelastic scattering* (DIS).
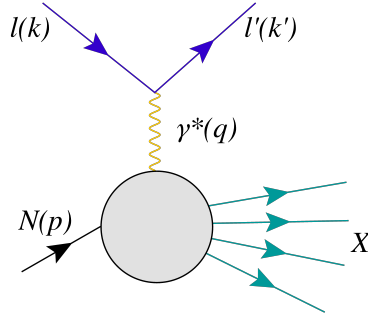
Figure 2.4: Illustration of the (deep) inelastic lepton-nucleon scattering in the one-photon-exchange approximation.

2.1.3.1 | Cross section

The inelastic double differential cross section for scattering off polarized leptons on polarized nucleons in LO QED is given by [171]:

$$\frac{d^2\sigma}{d\Omega dE'} = \frac{\alpha^2}{2MQ^4}\frac{E'}{E}L_{\mu\nu}W^{\mu\nu} \tag{2.9}$$

$$\propto [L^{(S)}_{\mu\nu}(k;k')W^{\mu\nu(S)}(q;p) - L'^{(S)}_{\mu\nu}(k,s_l;k',s_l')W^{\mu\nu(S)}(q;p)$$

$$- L^{(A)}_{\mu\nu}(k,s_l;k')W^{\mu\nu(A)}(q;p,s_N) - L'^{(A)}_{\mu\nu}(k;k',s_l)W^{\mu\nu(A)}(q;p;s_N)].$$

The emission of a virtual photon and its absorption by the nucleon are described in terms of a leptonic and hadronic tensor ($L_{\mu\nu}$ and $W^{\mu\nu}$). The tensors are associated with the coupling of the lepton or nucleon to the exchange boson (virtual photon) and this coupling is expressed by leptonic and hadronic currents. For the full representation of the tensors see Reference [171]. Those tensors can be divided into a symmetric (S), spin independent part and an asymmetric (A), spin dependent part. Here, s_l and s_l' correspond to the spin of the initial and final state lepton and s_N to the spin of the initial state nucleon. While the emission of the virtual photon by the lepton is calculable in QED, its absorption by an extended nucleon with unknown substructure is parameterized by so called *structure functions*.

2.1.3.2 | Structure functions

The structure functions are introduced as unknown quantities, which can be determined by dedicated measurements. Splitting the hadronic tensor into its symmetric and anti-symmetric part:

$$W_{\mu\nu}(q;p,s_N) = W^{\mu\nu(S)}(q;p) + iW^{\mu\nu(A)}(q;p,s_N), \tag{2.10}$$

where:

$$\frac{1}{2M}W^{\mu\nu(S)}(q;p) = \left(-g_{\mu\nu} + \frac{q_\mu q_\nu}{q^2}\right)W_1 + \left[\left(p_\mu - \frac{p \cdot q}{q^2}q_\mu\right)\left(p_\nu - \frac{p \cdot q}{q^2}q_\nu\right)\right]\frac{W_2}{M^2} \tag{2.11}$$

and

$$\frac{1}{2M}W^{\mu\nu(A)}(q;p,s_N) = \varepsilon_{\mu\nu\alpha\beta}q^\alpha\left\{Ms_N^\beta G_1 + [(p \cdot q)s_N^\beta - (s_N \cdot q)p^\beta]\frac{G_2}{M}\right\}, \tag{2.12}$$

and taking into account the time and parity invariance of QED, in total four structure functions are introduced. Two of those functions are averaged over the spin and therefore spin-independent (W_1 and W_2) [58], while the remaining two are spin-dependent functions (G_1 and G_2) [105, 123]. The symbols $g_{\mu\nu}$ and $\varepsilon_{\mu\nu\alpha\beta}$ in Equation 2.11 and 2.12 represent the metric and the antisymmetric Levi-Civita tensor. As the structure functions are not dimensionless, it is convenient to use the expressions:

$$MW_1(\nu, Q^2) = F_1(x_{Bj}, Q^2),$$

$$\nu W_2(\nu, Q^2) = F_2(x_{Bj}, Q^2) \tag{2.13}$$

and

$$M^2\nu G_1(\nu, Q^2) = g_1(x_{Bj}, Q^2),$$

$$M\nu^2 G_2(\nu, Q^2) = g_2(x_{Bj}, Q^2), \tag{2.14}$$

Using these expressions, the differential cross section for deep inelastic scattering on unpolarized nucleons reads as [25]:

$$\frac{d^2\sigma}{dx_{Bj}dy} = \frac{4\pi\alpha^2}{Q^2 x_{Bj} y}\left[\left(1 - y - \frac{\gamma^2 y^2}{4}\right)F_2 + x_{Bj} y^2 F_1\right] \text{ with } \gamma = \frac{2Mx_{Bj}}{Q}. \tag{2.15}$$

The spin-averaged structure functions can be extracted from dedicated cross section measurements in a similar way as done for the elastic form factors by the Rosenbluth separation discussed in Section 2.1.2.2. As G_1 and G_2 and therefore also g_1 and g_2 only appear in the spin dependent part of the hadronic tensor (see Eq. 2.12), those functions are only accessible using polarized leptons and nucleons. In case, the target nucleon is longitudinal polarized ($\Leftarrow$, $\Rightarrow$) with respect to the lepton polarization ($\leftarrow$, $\rightarrow$), the differential cross section difference is expressed as [25]:

$$\frac{d^3\sigma^{\leftarrow\Rightarrow}}{dx_{Bj}dyd\phi} - \frac{d^3\sigma^{\leftarrow\Leftarrow}}{dx_{Bj}dyd\phi} = \frac{4\alpha^2}{Q^2}\left[\left(2 - y - \frac{\gamma^2 y^2}{2}\right)g_1 - \gamma^2 y g_2\right]. \tag{2.16}$$

Here, ϕ is the angle between the lepton scattering plane and the plane of the nucleon spin. One should note that g_2 is suppressed by a factor of M^2/Q^2 with respect to the leading terms, thus mainly g_1 is accessible.
If the target nucleon is transversely polarized ($\Uparrow$, $\Downarrow$) the differential cross section difference becomes [25]:

$$\frac{d^3\sigma^{\leftarrow\Uparrow}}{dx_{Bj}dyd\phi} - \frac{d^3\sigma^{\leftarrow\Downarrow}}{dx_{Bj}dyd\phi} = \frac{4\alpha^2}{Q^2}\gamma\sqrt{1 - y - \gamma^2 y^2/4} \times \left[y g_1 + 2 g_2\right]\cos\phi. \tag{2.17}$$

Here, g_2 is not suppressed, so using the results on g_1 from longitudinal polarized targets, g_2 can be determined.

2.1.3.3 | Inelastic lepton-nucleon scattering as a (virtual)photon-nucleon cross section

In the one-photon-exchange approximation lepton-nucleon scattering can also be interpreted as an interaction between a *virtual photon flux*, which is produced by the lepton, and the nucleon. As the virtual photon can be longitudinally and transversely polarized, it is convenient to express the DIS cross section in terms of its transverse and longitudinal contribution (σ_T and σ_L). In this approach the structure functions read as[102]:

$$F_1 = \frac{KM}{4\pi^2\alpha}\sigma_T^{\gamma^*N}, \tag{2.18}$$

$$F_2 = \frac{K\nu}{4\pi^2\alpha}\frac{Q^2}{Q^2 + \nu^2}(\sigma_T^{\gamma^*N} + \sigma_L^{\gamma^*N}). \tag{2.19}$$

Here, K is chosen such that it satisfies the invariant mass of the final state in the form:

$$W^2 = M^2 + 2MK, \tag{2.20}$$

so

$$K = \frac{W^2 - M^2}{2M} = \nu - \frac{Q^2}{2M}. \tag{2.21}$$

This is known as the *Hand convention*. Insert Equations 2.18 and 2.19 in Equation 2.15 the DIS cross section is given as:

$$\frac{d^2\sigma^{lN}}{dx_{Bj}dy} = \frac{K\alpha}{\pi Q^2 x_{Bj}y} \left\{ \sigma_L^{\gamma*N} \nu \left(1 - y - \frac{\gamma^2 y^2}{4} \right) \left(\frac{Q^2}{Q^2 + \nu^2} \right) + \right. \tag{2.22}$$

$$\left. \sigma_T^{\gamma*N} \left[xy^2 M + \nu \left(1 - y - \frac{\gamma^2 y^2}{4} \right) \left(\frac{Q^2}{Q^2 + \nu^2} \right) \right] \right\}.$$

Equation 2.22 can be simplified to:

$$\frac{d^2\sigma^{lN}}{dx_{Bj}dy} = \Gamma \left(\sigma_T^{\gamma*N} + \epsilon \sigma_L^{\gamma*N} \right). \tag{2.23}$$

Using the Jacobian $|d(x_{Bj}, y)/d(Q^2, \nu)| = 1/(2M\nu E_\mu)$ to alter the dependence of the differential DIS cross section and by applying the transformations given in Appendix B.1, Γ reads as:

$$\Gamma = \frac{\alpha}{2\pi} \frac{(1 - x_{Bj})}{Q^2 y E_\mu} \left[y^2 + \frac{2}{1 + \frac{Q^2}{\nu^2}} \left(1 - y - \frac{Q^2}{4E_\mu} \right) \right]. \tag{2.24}$$

As for real photons Q^2 is zero, hence the terms related to σ_L are zero, Γ is called the *virtual photon flux factor*. Using the found expression for Γ, ϵ is given by:

$$\epsilon = (xy^2 M + 1)^{-1}.$$

Using Equation 2.24, a lepton-nucleon cross section for transversely polarized virtual photons can be converted into a cross section for virtual photon-nucleon scattering by:

$$\frac{d^2\sigma_T^{\gamma*N}}{dQ^2 d\nu} = \frac{1}{\Gamma(Q^2, \nu, E_\mu)} \frac{d^2\sigma^{lN}}{dQ^2 d\nu} \bigg|_T. \tag{2.25}$$

2.2 | The Quark-Parton Model

The *quark-parton model* comprises the conclusions and insights derived from two historic models, namely the *quark model* and the *parton model*.

The *quark model* has its beginning in the early 1960s and was inspired by the discoveries of many new particles. At that time it was hard to imagine that those particles are all elementary, so it was eagerly searched for underlying rules, which could bring order to this so called 'particle zoo'. This search led to the idea of representing particles by the symmetry groups SU(3) [73, 135]. Further developing this idea, Gell-Mann [74] and Zweig [170] independently postulated a triplet, which is the simplest representation of the SU(3) group, consisting of three fundamental spin-1/2 particles, called quarks. These quarks then form quark-antiquark and three quark bound states, which represent the known mesons and baryons. This break through marks the birth of the quark model. However, some questions remained, with the most important ones being the missing experimental hints for quarks or the violation of the spin-statistics, accompanied by the fermion character of the quarks. This was resolved by introducing a new concept [89], which later results in a new quantum number called color.

2.2.1 | Naive Quark-Parton Model

The first results on inelastic electron-proton scattering [36] (see Fig. 2.5), obtained by the MIT-SLAC collaboration and presented at the 14th International Conference on High Energy Physics, 1968 in Vienna, hint to the structure of the proton. Although the observed approximate independence of the reduced electron-proton scattering cross section and therefore of the spin-averaged structure functions on $q^2 = -Q^2$ was predicted by Bjorken [34] (for $Q^2 \rightarrow \infty$), it came as a surprise to observe this scale invariance at such small vales of Q^2. Despite of the fact, that the assumptions taken by Bjorken were questionable and his arguments turned out to be flawed, the idea of scaling still served well for R. Feynmans interpretation of the experimental results.
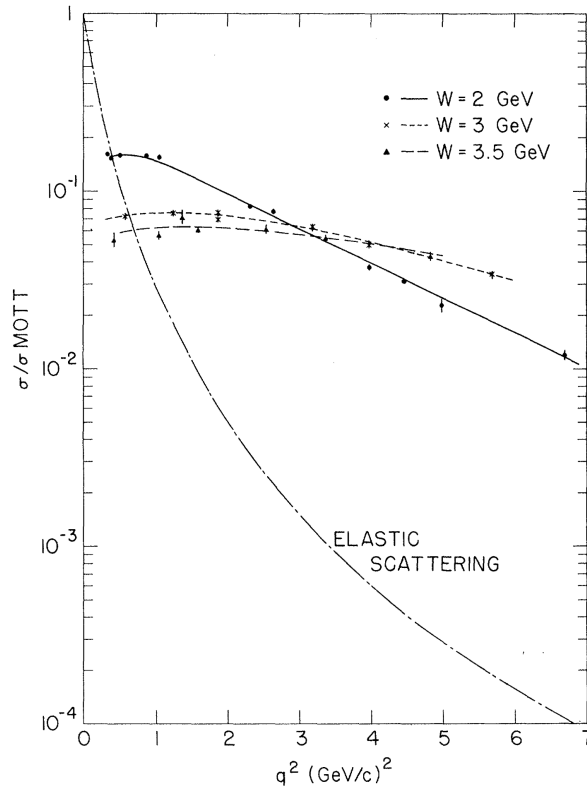
Figure 2.5: Measured differential cross section for inelastic proton-electron scattering ($d^2\sigma/d\Omega dE'$) divided by the Mott cross section as a function of q^2 for different values of W. The data was taken at SLAC with incident electron energies between $7\,\text{GeV}$ and $17\,\text{GeV}$ and scattering angles of $6°$and $10°$. As a reference, the expected behavior for elastic scattering is drawn. The observed weak dependence on q^2 is characteristic for scattering on point-like particles. Figure taken from Ref. [38].

His interpretations resulted in the development of the *parton model*, according to which the proton consist of point-like, spin-1/2 particle, called partons. Even though it was mainly developed by Feynman its first officially publication is by Bjorken and Paschos [35]. Here, the assumption is taken that the nucleon, in a lepton-nucleon scattering process, can be described as a collinear beam of free moving, mass less and point-like spin-1/2 partons in an infinite momentum reference frame. Any transverse momenta and interactions of the partons inside the nucleon are neglected. This approach is today known as the naive *quark-parton model*.

As it was later proven that quarks and partons share the same set of quantum numbers, in modern notation of the SM only the term quarks is commonly used. Hence, from now on only the term quark is used.

In the picture of the naive QPM the DIS process is not described as an interaction between the lepton and the nucleon, but as the incoherent sum of the elastic lepton scattering on all possible types of quarks (see Fig. 2.6). Under its assumptions one finds that x_{Bj}, which was introduced in Section 2.1.1, can be in-
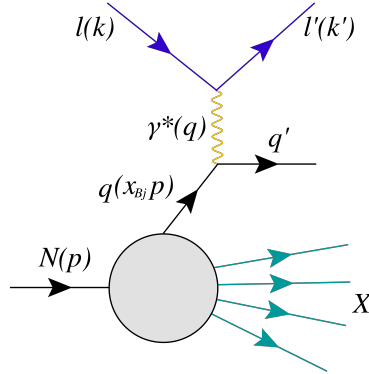
Figure 2.6: Interpretation of the deep inelastic lepton-nucleon scattering in the QPM for the one-photon-exchange approximation.

terpreted as the fraction of the nucleon four-momentum carried by a quark/antiquark. Comparing the cross section of the incoherent sum of elastic lepton-quark scattering to the cross section for unpolarized inelastic lepton-nucleon scattering (see Eq. 2.15 in Sec. 2.1.3), allows to express the structure functions in terms of so called *Parton Distribution Function*s (PDFs) as:

$$F_1(x_{Bj}) = \frac{1}{2} \sum_f e_f^2 (q_f(x_{Bj}) + \bar{q}_f(x_{Bj})), \tag{2.26}$$

$$F_2(x_{Bj}) = x_{Bj} \sum_f e_f^2 (q_f(x_{Bj}) + \bar{q}_f(x_{Bj})). \tag{2.27}$$

Here, e_f is the electric charge of a particular quark of flavour f and $q_f(x_{Bj})/\bar{q}_f(x_{Bj})$ the PDFs of the corresponding quarks/antiquarks. The PDFs, give the probability to find quarks/antiquarks of flavour f carrying a fraction x_{Bj} of the total nucleon four-momentum. They have the character of number density functions, so if integrated over the full x_{Bj}-range the result corresponds to the number of quarks/antiquarks of a certain flavour in the nucleon. In case of spin-averaged PDFs, the functions are given by the sum of the number densities of quarks/antiquarks, with spins parallel (q^+) or antiparallel (q^-) with respect to the nucleon spin:

$$q(x_{Bj}) = q^+(x_{Bj}) + q^-(x_{Bj}),$$
$$\bar{q}(x_{Bj}) = \bar{q}^+(x_{Bj}) + \bar{q}^-(x_{Bj}).$$

The assumption of the quarks/antiquarks being spin-1/2 particles is confirmed by measurements of the relation between the structure functions:

$$F_2(x_{Bj}) = 2x_{Bj} \cdot F_1(x_{Bj}). \tag{2.28}$$

Equation 2.28 is known as the Callan-Gross relation [42]. As the structure function F_1 is related to the magnetic properties of the nucleon, it is equal to zero for spin-0 and spin-1 particle. The result of the measurement, shown in Figure 2.7, is in agreement with the expectation for spin-1/2 particles.
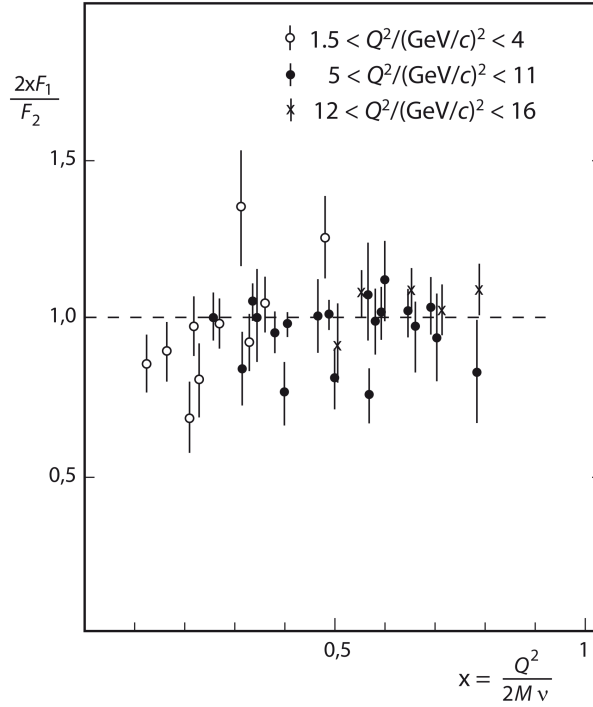
Figure 2.7: Ratio of $2x_{Bj} \cdot F_1(x_{Bj})$ to $F_2(x_{Bj})$ as function of x_{Bj} as measured by experiments at SLAC. The results confirmed that quarks are spin-1/2 particle. Figure taken from Ref. [144].

Similar to the spin-averaged structure functions, also the spin-dependent structure functions are expressed via PDFs:

$$g_1(x_{Bj}) = \frac{1}{2} \sum_f e_f^2 (\Delta q_f(x_{Bj}) + \Delta \bar{q}_f(x_{Bj})), \tag{2.29}$$

$$g_2(x_{Bj}) = 0. \tag{2.30}$$

While in the spin-averaged case $q_f(x_{Bj})$ and $\bar{q}_f(x_{Bj})$ correspond to the sum over all quark polarizations, the quark and antiquark helicity distributions $\Delta q_f(x_{Bj})$ and $\Delta \bar{q}_f(x_{Bj})$ are given by the difference between quarks/antiquarks with parallel or antiparallel spins with respect to the one of the nucleon:

$$\Delta q_f(x_{Bj}) = q_f^+(x_{Bj}) - q_f^-(x_{Bj}),$$
$$\Delta \bar{q}_f(x_{Bj}) = \bar{q}_f^+(x_{Bj}) - \bar{q}_f^-(x_{Bj}).$$

In the QPM only g_1 is related to the quark helicity distributions of the nucleon.

Despite the success of the naive QPM in interpreting experimental results of earlier DIS measurements, further measurements showed deviations from its predictions. The most important deviations are summarized in the following.
Considering the interpretation of x_{Bj} as a four-momentum fraction, the expression $x_{Bj}q_f(x_{Bj})$ gives the momentum distribution of quarks of a specific flavour. A first result, hinting to the incomplete picture of the naive QPM was by the measurements on the momentum sum rule. The sum over all types of

quarks and antiquarks in the nucleon is given as:

$$\Sigma(x_{Bj}) = \sum_f (q_f(x_{Bj}) + \bar{q}_f(x_{Bj})),$$

where the functions correspond to the PDF of a certain quark flavour (u, d, ...). In the naive QPM the prediction for the momentum sum rule is:

$$\int_0^1 x_{Bj} \Sigma(x_{Bj}) dx_{Bj} = 1. \tag{2.31}$$

Here, it is assumed that the total nucleon four-momentum is carried by the quarks and antiquarks. Considering the relation between the spin-averaged structure function F_2 and the PDFs, as introduced in Equation 2.27, $x_{Bj}\Sigma(x_{Bj})$ is equal to the structure function $F_2^N = \frac{1}{2}(F_2^p + F_2^n)$ of the nucleon. Measurements of F_2 in neutrino-nucleon (νN) and electron-nucleon (eN, electron-proton ep and electron-neutron en) scattering, resulted in:

$$\int_0^1 F_2^{\nu N}(x_{Bj}) \sim \int_0^1 \frac{18}{5} F_2^{eN}(x_{Bj}) dx_{Bj} \sim 0.5, \tag{2.32}$$

These results imply that there are constituents of the nucleon, which do not interact weak or electromagnetic [55].

The measurements of spin-averaged structure functions continued and cover today a wide kinematic range. Figure 2.8 shows a compilation of the world data on the proton structure function F_2^p measured in DIS by fixed target experiments using electron (SLAC [167], JLAB [46]), positrons (HERMES [12]) or muon (BCDMS [30], E665 [8], NMC [21]) beams and in electron/positron-proton-collider experiments (H1+ZEUS [101]). The structure function is displayed as a function of Q^2 at different values of x_{Bj}. The scale breaking shows clearly as an increase with Q^2 at low values of x_{Bj} and a decrease at high values of x_{Bj}. These observations of a clear logarithmic dependence of F_2^p on Q^2 are in contrast to the predictions of the naive QPM.
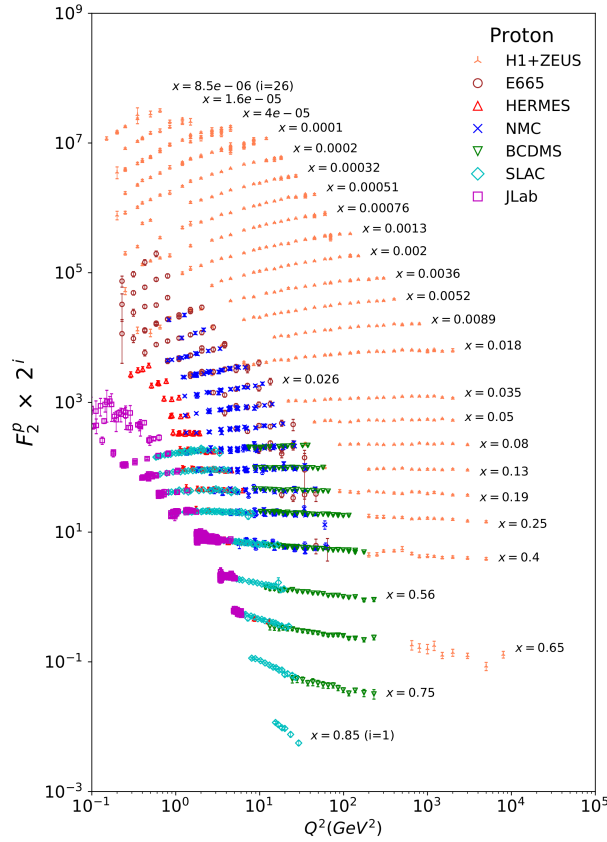
Figure 2.8: F_2^p as measured in DIS by various fixed target experiments using electron (SLAC [167], JLAB [46]), positrons (HERMES [12]) or muon (BCDMS [30] , E665 [8], NMC [21]) beam and electron/positron-proton-collider (H1+ZEUS [101]). The data is plotted as a function of Q^2 in bins of fixed x_{Bj}. For the plot the data in each x_{Bj} bin are multiplied by 2^{i_x}, where $i_x \in [1, 26]$ is the number of the corresponding bin. Figure taken from Ref. [171].

2.2.2 | QCD extended Quark-Parton Model

Further studies of the nucleon structure finally led to the modern QPM and today's understanding of the strong interactions as a quantum field theory. In the SM picture, hadrons consist of a constant number of *valence quarks* of different flavour. These quarks are constrained by the strong force and interact through the exchange of gluons. The concept of gluons was inspired by Y. Nambu [134] and later included into the QCD as the exchange vector bosons by H. Fritsch, M. Gell-Mann and H. Leutwyler [70]. Those gluons also can form quark-antiquark-pairs that again annihilate into gluons. Thus, the valence quarks are surrounded by gluons and quark-antiquark fluctuations. These fluctuations are referred to as *sea quarks*. All these particles, their interactions and fluctuations represent the complex structure of hadrons and give them their properties.

In QCD the interaction of quarks is described by a field, which is transmitted by the gluons. The gluons couple to the charge of the strong force, which is called color. Quarks always carry one of the three colors red (*r*), blue (*b*) or green (*g*), while antiquarks carry one of the corresponding anticolors $\bar{r}$, $\bar{b}$ or $\bar{g}$. The hadrons are colorless, such that in case of a baryon each quark carries a different color, while in case

of mesons the quark and antiquark carry a color and its corresponding anticolor. A major difference to electromagnetic interactions, where the photon itself does not carry an electric charge, is that the gluons carry a color and an anticolor. The possible color combinations are described by a SU(3) symmetry, which is represented by an octet and singlet [70]. The octet is given by:

$$r\bar{g},\ r\bar{b},\ b\bar{r},\ b\bar{g},\ g\bar{r},\ g\bar{b},\ \frac{1}{\sqrt{2}}(r\bar{r}-g\bar{g}),\ \frac{1}{\sqrt{6}}(r\bar{r}+g\bar{g}-2b\bar{b}),$$

while the singlet is:

$$\frac{1}{\sqrt{3}}(r\bar{r}+g\bar{g}+b\bar{b}).$$

As the singlet is colorless, only the gluons of the octet contribute to the strong interaction. Carrying color allows the gluons not only to interact with the quarks and antiquarks, but also with each other. This results in a fundamental different behaviour of the coupling in QED and QCD. While in QED the coupling constant α increases slowly with Q^2, which is explained by a (anti)*screening* of the electric charge by electron-positron fluctuations, the coupling constant of the strong interaction α_s decreases and is expected to vanish for $Q^2 \to \infty$. This dependence on the scales of Q^2 is referred to as *running coupling* and is much more pronounced in case of α_S. In leading order (LO) α_S is given by [54]:

$$\alpha_s(Q^2) = \frac{12\pi}{(33-2n_q)\cdot\ln(Q^2/\Lambda_{\mathrm{QCD}}^2)}.$$

Here, n_q is the number of active quark flavours at the Q^2-scale and Λ_{QCD} the *QCD scale parameter*. This parameter represents the scale at which the coupling diverges. Similar to the perturbative treatment of QED, introduced in Section 2.1, the radiation of additional gluons and quark-antiquark fluctuations are described via an perturbative ansatz, in which these additional processes are applied as corrections to the leading order term. The order of corrections applied in *perturbative quantum chromodynamics* (pQCD) depends on the number of additional interaction vertices, each is assigned to an additional factor of the strong coupling constant. This order is called next to leading order (NLO), next to next to leading order (NNLO) and so forth. Figure 2.9 shows a compilation of global results for α_s extracted at different scales Q^2 compared to a N^3LO pQCD calculation. For large Q^2, which corresponds to small distances, the coupling constant is small, therefore the quarks behave like free particles as it was assumed by the naive QPM. This behavior is referred to as *asymptotic freedom* and was first independently introduced by D. Gross and F. Wilczek [92] and D. Politzer [142]. At larger distances the coupling gets stronger. So the larger the distance between interacting quarks, the more they are constrained by the strong coupling. If a quark is removed from the hadron for e.g. in DIS, the strong coupling causes the quarks to hadronize. This concept is called *confinement* and describes the observation that no free quarks or gluons exist. Instead they are confined within the colorless hadron.

In the picture of DIS, the scale dependence can be interpreted as a resolution effect. As illustrated in Figure 2.10a, at a certain scale (Q_0^2), the photon resolves the valence quark structure. In this regime the observed structure functions are independent of Q^2. When increasing the resolution ($Q^2 \gg Q_0^2$, see Fig. 2.10b) the photon resolves gluon emissions and/or the sea quarks, which also carry a share of the nucleons four-momentum.

The changes of the observed quark and gluon densities at different scales is described by evolution equations. This formalism was developed over a number of years by Dokshitzer, Gribov, Lipatov, Altarelli and Parisi [18, 57, 90, 122], which are collectively referred to as DGLAP. The corresponding evolution equations are known as *DGLAP evolution equations*. These equations describe Q^2 dependent emission of gluons and quark-antiquark pairs by the quarks and gluons in different orders of α_s.
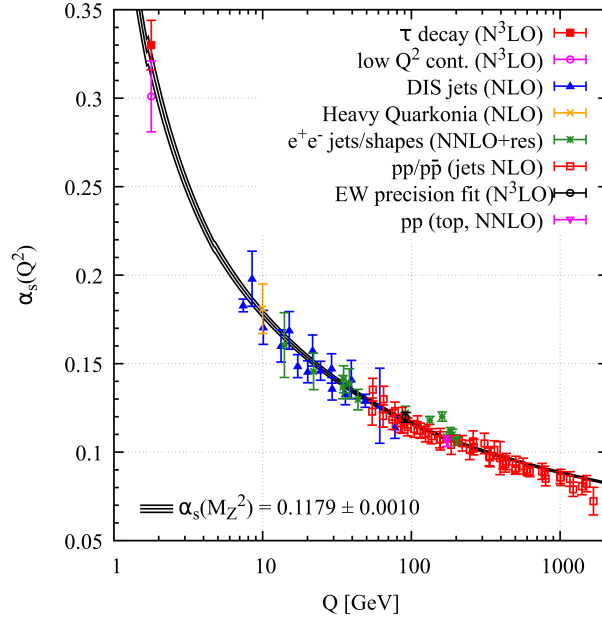
Figure 2.9: Global measurements of α_s as function of Q^2. Figure taken from Ref. [171].
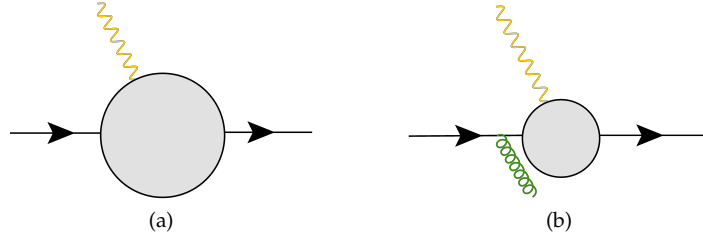
Figure 2.10: Illustration of the resolution effect at Q_0^2 (a) and at a larger scale $Q^2 \gg Q_0^2$ (b).

The evolution of a quark density q_i for a particular quark of flavour i and the gluon density g in a hadron is given by [55]:

$$
\frac{d}{d \ln Q^2}
\begin{pmatrix}
q_i(x_{Bj}, Q^2) \\
g(x_{Bj}, Q^2)
\end{pmatrix}
= \frac{\alpha_s(Q^2)}{2\pi} \sum_j \int_{x_{Bj}}^{1} \frac{d\xi}{\xi}
$$

$$
\begin{pmatrix}
P_{q_i q_j}(\frac{x_{Bj}}{\xi}, \alpha_s(Q^2)) & P_{q_i g}(\frac{x_{Bj}}{\xi}, \alpha_s(Q^2)) \\
P_{g q_j}(\frac{x_{Bj}}{\xi}, \alpha_s(Q^2)) & P_{gg}(\frac{x_{Bj}}{\xi}, \alpha_s(Q^2))
\end{pmatrix}
\begin{pmatrix}
q_j(\xi, Q^2) \\
g(\xi, Q^2)
\end{pmatrix}.
\tag{2.33}
$$

Here, j denotes a particular quark flavour and ξ the momentum fraction of the nucleon carried by a quark or gluon. The $P_{q_i q_j}(\frac{x_{Bj}}{\xi}, \alpha_s(Q^2))$, $P_{q_i g}(\frac{x_{Bj}}{\xi}, \alpha_s(Q^2))$, $P_{g q_j}(\frac{x_{Bj}}{\xi}, \alpha_s(Q^2))$ and $P_{gg}(\frac{x_{Bj}}{\xi}, \alpha_s(Q^2))$ are the

expansions in $\alpha_s(Q^2)$ of so called *splitting functions*:

$$P_{q_iq_j}(z, \alpha_s(Q^2)) = \delta_{ij}P_{qq}^{(0)}(z) + \frac{\alpha_s}{2\pi}P_{qq}^{(1)}(z) + \dots ,\tag{2.34}$$

$$P_{qg}(z, \alpha_s(Q^2)) = P_{qg}^{(0)}(z) + \frac{\alpha_s}{2\pi}P_{qg}^{(1)}(z) + \dots ,\tag{2.35}$$

$$P_{gq}(z, \alpha_s(Q^2)) = P_{gq}^{(0)}(z) + \frac{\alpha_s}{2\pi}P_{gq}^{(1)}(z) + \dots ,\tag{2.36}$$

$$P_{gg}(z, \alpha_s(Q^2)) = P_{gg}^{(0)}(z) + \frac{\alpha_s}{2\pi}P_{gg}^{(1)}(z) + \dots ,\tag{2.37}$$

with $z = x_{Bj}/\xi$. These functions describe the processes, which are shown in Figure 2.11. Here, either a gluon is emitted by a quark, resulting in a quark and gluon final state, where one is carrying the momentum fraction z and the other one the remaining momentum fraction $1 - z$ or the splitting of a gluon into a quark-antiquark pair or two gluons.
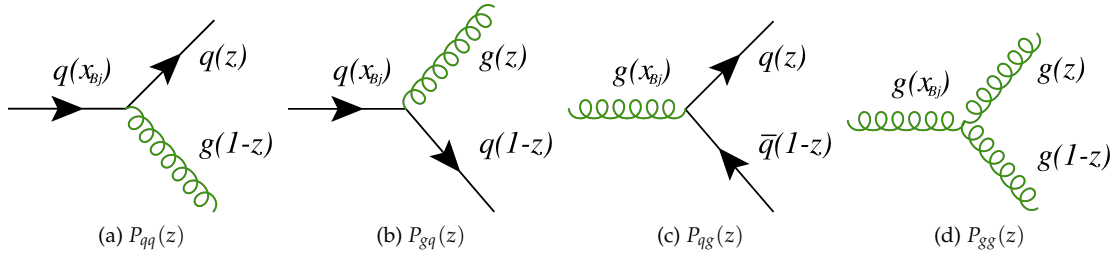
Figure 2.11: Feynman diagrams of the processes described by the splitting functions.

In leading order of α_s the splitting function are written as [55]:

$$P_{qq}^{(0)}(z) = \frac{4}{3}\left[\frac{1+z^2}{(1-z)_+} + \frac{3}{2}\delta(1-z)\right],\tag{2.38}$$

$$P_{qg}^{(0)}(z) = \frac{1}{2}[z^2 + (1-z)^2],\tag{2.39}$$

$$P_{gq}^{(0)}(z) = \frac{4}{3}\left[\frac{1+(1-z)^2}{z}\right],\tag{2.40}$$

$$P_{gg}^{(0)}(z) = 6\left[\frac{1-z}{z} + \frac{z}{(1-z)_+} + z(1-z)\right]\frac{33-2n_f}{6}\delta(1-z).\tag{2.41}$$

The $+$ in the equation for $P_{qq}(z)$ and $P_{gg}(z)$ denote that the $1/(1-z)$ singularity is regularized by:

$$\frac{1}{(1-z)} \rightarrow \frac{1}{(1-z)_+} \quad \text{where} \quad \int_0^1 dz \frac{f(z)}{(1-z)_+} = \int_0^1 dz \frac{f(z)-f(1)}{(1-z)}.\tag{2.42}$$

The limit $z \rightarrow 1$ is associated with the emission of soft gluons. This formalism can also be generalized and applied to parton helicity distributions using a modified set of splitting functions for the splitting products to have a parallel or antiparallel polarization with respect to the parent quark or gluon [19].

2.3 | Factorization and twist

The term *factorization* denotes the fact that in a perturbative field theory a cross section of a physics process can be written as a convolution of a hard and a soft part of the scattering process. As illustrated in Figure 2.12 in LO DIS the hard scattering refers to the lepton-(anti)quark interaction and can be calculated in pQCD. The non-perturbative soft part describe the (anti)quark as part of the nucleon and has to be parameterized.
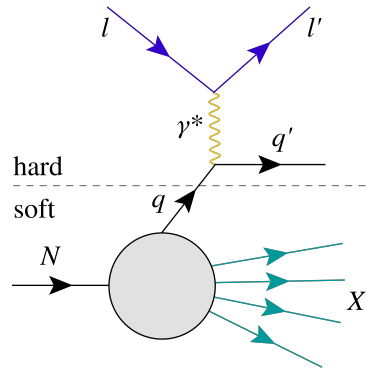

Figure 2.12: Illustration of the factorization in DIS at leading order and leading twist. The process is divided into the hard lepton-quark scattering and the soft scattering describing the quark as part of the nucleon.

In DIS this parametrization is done by introducing PDFs (see Sec. 2.2.1). The transition between the hard and the soft part of the scattering is marked by a certain scale, which is called renormalization scale. As the concept of factorization is not universal, it has to be validated for each process separately [47]. The framework to validate factorization is provided by the *operator product expansion* (OPE), which is a method to study the structure of field theories. Applying the OPE to DIS allows to expand the hadronic tensor (see Sec. 2.2.2) and therefore also the structure functions by non-singular operators and corresponding coefficient functions. The expansion is done in a power series of $(1/Q^2)$, where the exponent is given as $(\tau/2\text{-}1)$. The τ is called *twist* and is related to the dimension and the spin of an operator [109]. By performing this expansion, the non-perturbative elements are contained in the operators, while the coefficient functions include the perturbation Q^2-dependence. Due to the operators being products of currents, which are at least bilinear in the fields, the smallest possible twist is two. For more details on OPE and twist see Reference [55, 109].

2.4 | Generalized Parton Distribution functions

Although the development of QCD explained the discrepancies between experimental observations and the predictions of the naive QPM, and PDFs and form factors have been extensively measured since the late 1960s, the nucleon structure is still not fully resolved. A new approach has emerged in the 1990s in systematic theoretical studies of exclusive photon and meson production in DIS [132]. The factorization of these processes (see Sec. 2.4.1.2) derived in the framework of GPDs, which rose wide interest in 1996, when their non-forward nature was first pointed out by X. Ji [110, 111] and A. V. Radyushkin [147]. Taking into account the transverse kinematics of the processes like for e.g. the transverse momentum transfers to the partons/nucleon, GPDs allow to investigate the nucleon structure and contributions to

its spin composition, which are not accessible by the common PDFs and form factors. Further details on this are discussed in Section 2.4.3 and 2.4.4.

2.4.1 | GPDs in exclusive photon production

Before a deeper discussion on insights of the nucleon structure, which can be derived from studying GPDs, it is recommended to introduce their kinematic dependence in DVCS and provide some more details on the factorization.

2.4.1.1 | Kinematic of DVCS

A handbag diagram illustrating DVCS in lepton-nucleon scattering at leading order and leading twist is shown in Figure 2.13. Its event topology is summarized as:

$$l + N \rightarrow l' + N' + \gamma.$$
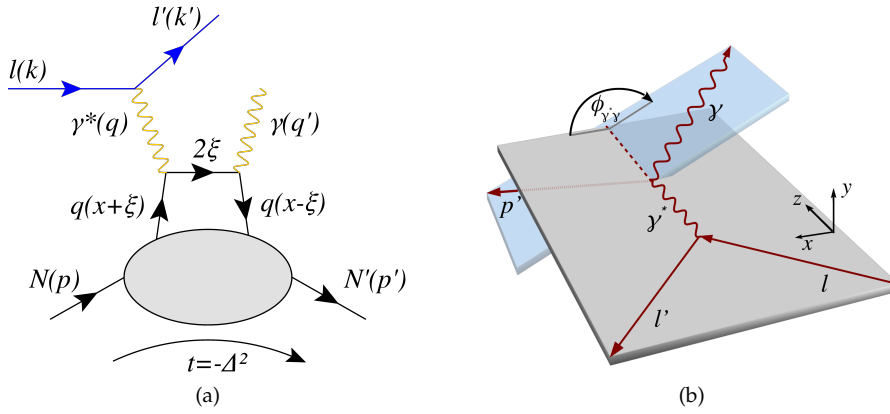
Figure 2.13: (a) Handbag diagram for DVCS in lepton-nucleon scattering in LO and leading twist. (b) Illustration of the definition of the azimuthal angle between the lepton scattering plane and the real photon production plane. Figure taken from Ref. [16].

The virtual photon is being absorbed and transfers a four-momentum q to the quark. This four-momentum transfer is partly re-emitted in form of a real photon and partly absorbed by the quark, resulting in a recoil momentum of the nucleon. The four-momentum transfer to the nucleon is denoted as $\Delta = p' - p$ and is related to the variable t by:

$$t = -\Delta^2 = (p - p')^2. \tag{2.43}$$

In literature at least two parametrization for the longitudinal momentum fraction carried by the quark are common. This fraction relates to the average nucleon momentum $\frac{1}{2}(p + p')$. In this thesis usually the symmetric parametrization is used, which was introduced by Ji [111]. In this parametrization, the difference in the momentum fraction of the quark before absorbing the virtual photon and after the emission of the real photon is denoted as 2ξ. Hence, the corresponding momentum fractions carried by the quark are $x + \xi$ and $x - \xi$. The variable x denotes the average longitudinal momentum fraction of the nucleon carried by the struck quark. When using the symmetric parametrization, the variable ξ is

related to the common Bjorken variable x_{Bj} by [27, 56]:

$$\xi = x_{Bj} \frac{1 + \frac{\Delta^2}{2Q^2}}{2 - x_{Bj} + x_{Bj}\frac{\Delta^2}{Q^2}} \overset{\text{small }\Delta}{\approx} \frac{x_{Bj}}{2 - x_{Bj}}. \tag{2.44}$$

It is therefore also called generalized Bjorken variable. For small values of Δ, ξ can be approximated by $x_{Bj}/(2 - x_{Bj})$ as given in Equation 2.44. In an alternative parametrization, introduced by Radyushkin [147], the difference in the momentum fraction is not symmetric, but only accounts for the quark after the emission of the real photon. The longitudinal momentum fractions of both parametrizations are related by [56]:

$$X = \frac{x + \xi}{1 + \xi}, \quad \zeta = \frac{2\xi}{1 + \xi}. \tag{2.45}$$

For more details on both notations see Reference [56].

Another variable, which is of particular importance for the cross section of exclusive photon production (see Sec. 2.5.1), is the angle $\phi_{\gamma*\gamma}$. As illustrated in Figure 2.13b, it denotes the azimuthal angle between the lepton scattering plane and the real photon production plane. It is calculated as [16]:

$$\phi_{\gamma*\gamma} = \frac{(\vec{q} \times \vec{k}) \cdot \vec{q}'}{|(\vec{q} \times \vec{k}) \cdot \vec{q}'|} \arccos \frac{(\vec{q} \times \vec{k}) \cdot (\vec{q} \times \vec{q}')}{|\vec{q} \times \vec{k}| \cdot |\vec{q} \times \vec{q}'|}. \tag{2.46}$$

A detailed discussion of DVCS, in particular the corresponding cross section is given in Section 2.5.

2.4.1.2 | Factorization of DVCS

In the factorization ansatz of DVCS, the GPDs occur in a convolution with a hard scattering kernel (see Fig. 2.14a). When omitting the Q^2-dependence associated to the QCD evolution, they depend on x, ξ and t. Here, x appears as a loop variable, which is integrated over. Therefore the x-dependence of GPDs is not observable and depends on model inputs. A proof for the factorization in DVCS shows that the factorization is valid for small values of t/Q^2 and can be found in Reference [48].
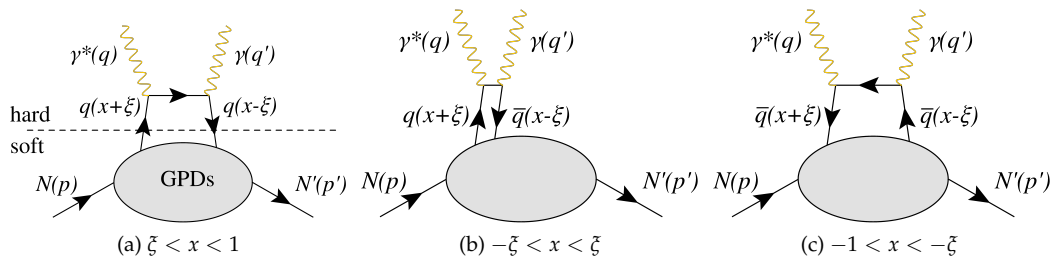
Figure 2.14: Handbag diagram for DVCS. Depending on the x-intervals The GPD is interpreted either as an emission and re-absorption of a quark (a), of a quark-antiquark pair (b) or of an antiquark (c) .

Depending on the kinematic regime the soft part can either be interpreted as an emission and re-absorption of a quark (or antiquark) by the nucleon (see Fig. 2.14a and 2.14c) or as an emission of a quark-antiquark pair or gluon (see Fig. 2.14b). The regimes, in which both momentum fractions are either positive or negative ($x \in [\xi, 1]$ or $x \in [-1, -\xi]$) and referring either to a quark or an antiquark, is called DGLAP region. For $x \in [-\xi, \xi]$, one has a positive momentum fraction $x + \xi \geq 0$ and a negative

momentum fraction $x - \xi \leq 0$. Here, the positive momentum fraction is interpreted as belonging to a quark, while the negative one is interpreted as belonging to an antiquark. This region is called ERBL region. ERBL refers to the evolution equations developed by Efremov, Radyushkin, Brodsky and Lepage [60, 139]. The two regions indicate, which evolution pattern has to be used at the factorization scale [56]. In QCD, GPDs are given by matrix elements of quark and gluon operators at light-like separation [56]. Analog to the definition of the usual parton densities. In leading twist, there are in total eight independent GPDs for each parton. Four of them are chiral-odd and four chiral-even. The chiral-even quantities are denoted as:

$$H^{f,g}(x,\xi,t), \ \tilde{H}^{f,g}(x,\xi,t), \ E^{f,g}(x,\xi,t) \text{ and } \tilde{E}^{f,g}(x,\xi,t),$$

where f indicates the corresponding flavour of the struck quark and g denotes gluons. These GPDs conserve the parton spin. The chiral-odd GPDs are denoted as:

$$H_T^{f,g}(x,\xi,t), \ \tilde{H}_T^{f,g}(x,\xi,t), \ E_T^{f,g}(x,\xi,t) \text{ and } \tilde{E}_T^{f,g}(x,\xi,t),$$

and introduce a spin flip to the parton. The GPDs H and E correspond to an average over the quark helicity and therefore referred to as spin-averaged GPDs. The GPDs $\tilde{H}$ and $\tilde{E}$ involve differences of quark helicities and are called spin-dependent GPDs. For the GPDs H and E the nucleon spin is either conserved or flipped [100].

2.4.2 | General properties of GPDs

This Section gives a brief excerpt of the general properties of GPDs and their relations to the ordinary PDFs and elastic form factors. For a more detailed discussion see for e.g. the reviews [56, 100, 112].

In the forward limit ($\xi \to 0$ and $t \to 0$) the nucleon has the same momentum and helicity configuration in its initial and final state. Here, x is equal to x_{Bj} and the GPDs reduce to the ordinary parton densities (see Sec. 2.2.1) [56]:

$$\begin{array}{llll}
H^f(x,0,0) = q(x), & \tilde{H}^f(x,0,0) = \Delta q(x) & \text{for } x > 0, & (2.47) \\
H^f(x,0,0) = -\bar{q}(-x), & \tilde{H}^f(x,0,0) = \Delta\bar{q}(-x) & \text{for } x < 0, & \\
H^g(x,0,0) = xg(x), & \tilde{H}^g(x,0,0) = x\Delta g(x) & \text{for } x > 0. &
\end{array}$$

For the remaining GPDs E and $\tilde{E}$, there exist no corresponding relations as they are multiplied by factors proportional to Δ. Therefore, they only appear at finite momentum transfers to the nucleon, where a spin flip is possible. The GPDs E^q and E^g carry information on the nucleon spin contributions by the angular momenta of quarks and gluons, which makes them of particular importance for studying the nucleon spin (see Sec. 2.4.3).

The relation between form factors and GPDs is obtained by the corresponding first moments in x [56]:

$$\int_{-1}^{1} dx H^f(x,\xi,t) = F_1^f(t), \qquad\qquad \int_{-1}^{1} dx E^f(x,\xi,t) = F_2^f(t), \qquad (2.48)$$

$$\int_{-1}^{1} dx \tilde{H}^f(x,\xi,t) = g_A^f(t), \qquad\qquad \int_{-1}^{1} dx \tilde{E}^f(x,\xi,t) = g_P^f(t).$$

Here, F_1^f and F_2^f are the Dirac and Pauli form factors for a specific quark flavour f, which were introduced in Section 2.1.2.1, and g_A^f and g_P^f are the corresponding axial-vector and pseudo-scalar form

factors. It should be pointed out that the results are ξ-independent. The integration over x removes all reference to the longitudinal direction, which defines ξ, hence the result must be independent of ξ [56]. The dependence of the form factors on t is characterized by the scale dependence of the strong coupling (see Sec. 2.2.2), which also controls the t-dependence of the GPDs [112].

Higher moments in x introduce higher order corrections to the from factors, which appear as polynomials in ξ. For the quark GPDs H^f and E^f, these higher moments are given as [100]:

$$\int_{-1}^{1} dx\, x^n H^f(x, \xi, t) = \begin{cases} a_0(t) + a_2(t)\xi^2 + a_4(t)\xi^4 + ... + a_n\xi^n & \text{even } n \\ a_0(t) + a_2(t)\xi^2 + a_4(t)\xi^4 + ... + c_{n+1}\xi^{(n+1)} & \text{odd } n \end{cases}, \qquad (2.49)$$

$$\int_{-1}^{1} dx\, x^n E^f(x, \xi, t) = \begin{cases} b_0(t) + b_2(t)\xi^2 + b_4(t)\xi^4 + ... + b_n\xi^n & \text{even } n \\ b_0(t) + b_2(t)\xi^2 + b_4(t)\xi^4 + ... - c_{n+1}\xi^{(n+1)} & \text{odd } n \end{cases}. \qquad (2.50)$$

This property of GPDs is called the *polynomiality* [56]. Similar Equations also exist for the quark GPDs $\tilde{H}$ and $\tilde{E}$, as well as for the gluons. The fact that only even powers of ξ appear, is due to the time reversal invariance: $H(x, \xi, t) = H(x, -\xi, t)$.

2.4.3 | Disentangling the nucleon spin via GPDs

First measurements of the spin-dependent structure function of the proton (g_1^p) were performed at SLAC [26] and by the European Muon collaboration (EMC) [22]. The results obtained by EMC implied that the contribution of the quark spins to the proton spin is negligible, which was in total contrast to the expectation that the nucleon spin originates exclusively from the spins of the valence quarks. These results led to the so called *spin crisis*. Although more recent measurements determined the quark spin contribution to be in the order of 30% [10] and the QCD extension of the QPM introduced the gluons, which also contribute to the nucleon spin, its composition is still not fully resolved and subject of intense investigations.

The idea of non-negligible contributions to the nucleon spin by the orbital momentum of partons was already discussed by Sehgal in the 1970s [159]. Later Ratcliffe observed that a orbital momentum is also generated by the splitting processes $q \rightarrow qg$ and $g \rightarrow q\bar{q}$ (see Sec. 2.2.2) [150]. In 1990 Jaffe and Manohar proposed a decomposition of the proton spin given as [108]:

$$\frac{1}{2} = \frac{1}{2}\Delta\Sigma + \Delta G + L_q + L_g. \qquad (2.51)$$

Here, $\Delta\Sigma$ is the sum of all helicity contributions by quarks and antiquarks, ΔG the contribution by the gluon helicity and L_q and L_g the contribution by the orbital angular momentum of (anti)quarks and gluons to the spin of the proton. It should be empathized that Equation 2.51 only represents one possible way of decomposing the proton spin. In the late 1990s Ji showed that the contributions by the total orbital momentum of (anti)quarks $\langle J_q^f \rangle$ and gluons $\langle J_g \rangle$ can be related to GPDs [110]:

$$\langle J_q^f \rangle = \frac{1}{2}\int_{-1}^{1} dx\, x[H^f(x, \xi, 0) + E^f(x, \xi, 0)], \qquad (2.52)$$

$$\langle J_g \rangle = \frac{1}{2}\int_{-1}^{1} dx[H_g(x, \xi, 0) + E_g(x, \xi, 0)].$$

These Equations are referred to as Ji's sum rules. The total orbital momentum contributions $\langle J_q^f \rangle$ and $\langle J_g \rangle$ can be explicitly decomposed into a contribution of spin and the orbital angular momentum [110]:

$$\langle J_q^f \rangle = \langle L_q^f \rangle + \langle S_q^f \rangle,$$
$$\langle J_g \rangle = \langle L_g \rangle + \langle S_g \rangle.$$

While the spin contributions can be directly measured, Ji's sum rules offer the only way to experimentally access $\langle J_q^f \rangle$ and $\langle J_g \rangle$ and therefore to determine the orbital angular momentum carried by the quarks $\langle L_q^f \rangle$ and gluons $\langle L_g \rangle$.

2.4.4 | Interpretation of GPDs in the impact parameter space

As the nucleon momentum changes in hard exclusive scattering processes, it is in general not possible to interpret GPDs in a probabilistic way as done for PDFs. Nevertheless, it is possible to find an appealing interpretation when transforming GPDs from momentum space to position space.
In the case $\xi = 0$, the longitudinal momentum fraction of the struck quark is the same in its initial and final state. Therefore, the four momentum transfer to the nucleon only has a transverse component ($\Delta = \Delta_\perp$). In this situation the requirements for a probabilistic interpretation are met. Burkardt derived that the Fourier transformation of the GPD H with respect to $\Delta_\perp$ is given by [41]:

$$q^f(x, b_\perp) = \int \frac{d^2\Delta_\perp}{(2\pi)^2} H^f(x, 0, -\Delta_\perp^2) e^{-ib_\perp \cdot \Delta_\perp} \tag{2.53}$$

Equation 2.53 gives the number density of quarks with flavour f and longitudinal four-momentum fraction x at the transverse distance $b_\perp$ (impact parameter) with respect to the transverse center of the nucleon momentum $R_\perp$. In the parton representation $R_\perp$ is given by the sum of the transverse positions $r_{\perp,i}$ of all partons i, weighted by their corresponding momentum fraction x_i:

$$R_\perp = \sum_i x_i r_{\perp,i}. \tag{2.54}$$

This representation of the center of transverse momentum localizes the nucleon in transverse direction. A similar probabilistic interpretation can be found for GPD $\tilde{H}$, which describes the polarized impact parameter dependent probability density. In a less intuitive form also an interpretation for the Fourier transformation of the GPD E exists (see Ref. [41]).

By experiments it is not possible to perform measurements at $\xi = 0$. As for $\xi \neq 0$ the longitudinal momentum of the parton/nucleon changes, the probabilistic interpretation does not hold. Nevertheless it implies a shift of the transverse center of momentum [56]. An illustration of this shift is shown in Figure 2.15. The transverse center of momenta of the nucleon before and after the scattering process, as well as the average are indicated by the horizontal solid black lines and the dashed black line, respectively. The shift in the transverse center of momenta with respect to its average are proportional to $b_\perp$. The horizontal red line illustrates the struck quark.
Although the probabilistic interpretation is lost, the measurements of exclusive reactions still allows to study the GPDs as a function of the longitudinal parton momentum at small momentum transfer to the nucleon, which provides important information on the transverse parton distribution. Commonly this is referred to as 'nucleon tomography'.
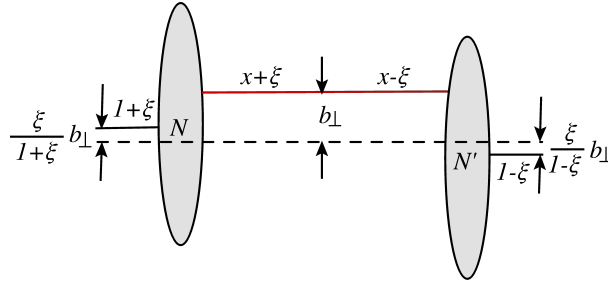
Figure 2.15: Illustration of the shift of center of transverse momentum for GPDs represented in the impact parameter space in the region $x \in [\xi, 1]$. The struck quark is indicated as a red line.

2.4.5 | Modelling of GPDs

The parametrization of GPDs by specific models, in particular their kinematic dependence, is of importance to derive information on the nucleon structure. It is distinguished between three families of models, which are either based on *double distribution*s (DDs), dual parametrization or Mellin-Barnes integrals.

The DDs, originally introduced by A. Radyushkin [148, 149] and D. Müller et al. [132] provide a guideline to parameterize the (x, ξ)-dependence and automatically satisfy the polynomiality [100]. This ansatz allows to decorrelate the longitudinal component of the transferred momentum to the nucleon (Δ) from its initial momentum by introducing two new variables. These variables are related to x and ξ, but the dependence of the GPDs on those is much easier to deduce. As the DD-ansatz only supports polynomials of ξ up to a power of n, the so called D-term was introduced by C. Weiss and M. Polyakov [143] to generate the highest power of ξ for odd n $(n + 1)$ in the moments of the GPD H and E (see Eq. 2.49 and 2.50).

Two models, that are based on DD and parameterize the (x, ξ) as well as the t-dependence of the GPDs are the so called VGG and GK model. The VGG model was developed in a series of publications, which were released between 1999 and 2005 [82, 98, 163, 164].

The parametrization for the GK model evolved in the process of fitting data from *Deeply Virtual Meson Production* (DVMP) by S.V. Goloskokov and P. Kroll [84, 85, 87]. As here the same GPDs as for DVCS are involved, DVMP data allows to derive strong constrains on the GPD model parameters. For a detailed review of both models see for e.g. Reference [100].

The study of GPDs in the impact parameter space, discussed in Section 2.4.4, implies that the GPD $H^f(x, 0, -\Delta_\perp^2)$ should become t-independent for $x \to 1$. In that case the active quark carries all the four-momentum of the nucleon, which according to Equation 2.54 brings it close to the transverse center of momentum [41]. Being close to the transverse center of momentum the impact parameter $b_\perp$ becomes small. As $b_\perp$ is the Fourier conjugated to $\Delta_\perp$, and $\Delta_\perp$ related to t, hence GPD H should not depend on t anymore. For $x \to 0$ one expects an increasing contribution by the quark-antiquark sea, resulting in a diverging behaviour of the GPD. This should translate to an increase of the nucleons transverse size, like $\alpha \ln \frac{1}{x}$ [41]. An ansatz of this kind is based on Regge theory, which arose from the study of the analytic properties of scattering amplitudes in strong interaction processes [55]. In this theory, the high energy behaviour of amplitudes is described by $(s/s_0)^{\alpha(t)}$, where s is the squared center of mass energy, $\alpha(t)$ a so called Regge trajectory and s_0 a scale factor, usually taken to be $1\,\mathrm{GeV}^2$ [55]. In the sea and gluon regime (small x_{Bj}, x) this trajectory is the Pomeron trajectory and has the quantum number of the vacuum [100].

Considering the mentioned constrains due to the expected behaviour of $b_\perp(x)$, an ansatz for e.g. of the

form:

$$H^f(x, 0, -\Delta_\perp^2) = q^f(x)e^{-a(1-x)\ln\frac{1}{x}\cdot\Delta_\perp^2} \tag{2.55}$$

can be chosen to parameterize the t-dependence of the GPD H^f [41]. Here, $q^f(x)$ denotes the corresponding quark distribution. The t-dependence of GPD H is of particular interest when investigating the correlation of the slope parameter of the DVCS cross section to the transverse extension of parton distributions in the proton. This relation is discussed in Section 2.5.3.

2.5 | Deeply Virtual Compton Scattering

Section 2.4.1 and 2.4.1.2 already introduced the kinematic of DVCS and its factorization, in which GPDs parametrize the soft part of the scattering process. In the following Sections, the general cross section for exclusive photon production and in particular the contribution by DVCS are being discussed. The DVCS contribution provides GPD related observables, named *Compton Form Factor*s (CFFs) (see Sec. 2.5.2). To disentangle the different CFFs, cross section measurements of DVCS and DVMP, using different combinations of lepton and nucleon spins in a vast kinematic range, are needed. Two examples for cross section extractions using polarized leptons, which are scattered off unpolarized nucleons are presented in Section 2.5.3 and 2.5.4.

2.5.1 | The cross section for exclusive photon production

The diagrams for processes contributing to the cross section for exclusive photon production are shown in Figure 2.16a, 2.16b and 2.16c. Besides in DVCS, a real photon can also be produced as bremsstrahlung in elastic lepton-nucleon scattering (see Sec. 2.1). This process is also referred to as *Bethe-Heitler* (BH).
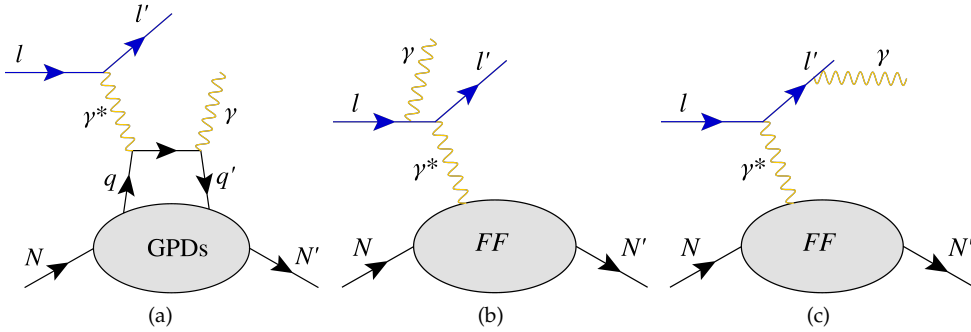

Figure 2.16: (a) Handbag diagram of the DVCS process at leading order and leading twist.
(b) and (c) Diagram of the Bethe-Heitler process at leading order. The real photon is emitted by the lepton either before or after the scattering off the nucleon.

In terms of the scattering amplitudes of DVCS and BH, the differential cross section for exclusive photon production in lepton-nucleon scattering reads as [27, 40]:

$$\frac{d^4\sigma^{lN\to l'N'\gamma}}{dx_{Bj}dQ^2d|t|d\phi_{\gamma*\gamma}} \propto |\mathcal{T}_{\text{DVCS}}|^2 + |\mathcal{T}_{\text{BH}}|^2 + \underbrace{\mathcal{T}_{\text{DVCS}}\mathcal{T}_{\text{BH}}^* + \mathcal{T}_{\text{DVCS}}^*\mathcal{T}_{\text{BH}}}_{\mathcal{I}}. \tag{2.56}$$

Here, $\mathcal{T}$ denotes the corresponding scattering amplitudes and $\mathcal{I}$ refers to the contribution by the interference of both processes to the differential cross section. Its kinematic dependence is given by the

Bjorken scaling variable x_{Bj}, the photon virtuality Q^2, the absolute value of the squared four-momentum transfer to the proton $|t|$ and the angle between the lepton scattering plane and the real photon production plane $\phi_{\gamma*\gamma}$, which have been introduced in Section 2.1.1 and 2.4.1.1.

In twist-3 approximation the contributions to the cross section are given by [27]:

$$|\mathcal{T}_{\text{BH}}|^2 = \frac{1}{x_{Bj}^2 y^2 (1 + \epsilon^2)^2 t \mathcal{P}_1(\phi_{\gamma*\gamma}) \mathcal{P}_2(\phi_{\gamma*\gamma})} \tag{2.57}$$

$$\left[c_0^{\text{BH}} + c_1^{\text{BH}} \cos(\phi_{\gamma*\gamma}) + c_2^{\text{BH}} \cos(2\phi_{\gamma*\gamma}) + s_1^{\text{BH}} \cos(\phi_{\gamma*\gamma}) \right]$$

$$\text{with } \epsilon^2 = \frac{4 x_{Bj}^2 M^2}{Q^2},$$

$$|\mathcal{T}_{\text{DVCS}}|^2 = \frac{1}{y^2 Q^2} \tag{2.58}$$

$$\left[c_0^{\text{DVCS}} + c_1^{\text{DVCS}} \cos(\phi_{\gamma*\gamma}) + s_1^{\text{DVCS}} \sin(\phi_{\gamma*\gamma}) + \right.$$

$$\left. c_2^{\text{DVCS}} \cos(2\phi_{\gamma*\gamma}) + s_2^{\text{DVCS}} \sin(2\phi_{\gamma*\gamma}) \right],$$

and

$$\mathcal{I} = \frac{\pm 1}{x_{Bj} y^3 |t| \mathcal{P}_1(\phi_{\gamma*\gamma}) \mathcal{P}_2(\phi_{\gamma*\gamma})} \tag{2.59}$$

$$\left[c_0^{\mathcal{I}} + c_1^{\mathcal{I}} \cos(\phi_{\gamma*\gamma}) + s_1^{\mathcal{I}} \sin(\phi_{\gamma*\gamma}) + \right.$$

$$\left. c_2^{\mathcal{I}} \cos(2\phi_{\gamma*\gamma}) + s_2^{\mathcal{I}} \sin(2\phi_{\gamma*\gamma}) + c_3^{\mathcal{I}} \cos(3\phi_{\gamma*\gamma}) + s_3^{\mathcal{I}} \sin(3\phi_{\gamma*\gamma}) \right].$$

The $\pm$ in Equation 2.59 denotes the lepton charge. The symbols $\mathcal{P}_1$ and $\mathcal{P}_2$ are the lepton Bethe-Heitler propagators (see Ref. [27]), while the c_0^{DVCS}, c_1^{DVCS}, and so on are Fourier coefficients, which depend on the spin configuration of the target nucleon (unpolarized U, longitudinally L and transversely polarized T with respect to the lepton polarization). The expressions for the full set of the coefficients in twist-3 approximation are given in Reference [27].

The amplitude of Bethe-Heitler and the corresponding coefficients can be calculated in QED, using the well known Dirac and Pauli form factors (F_1 and F_2, see e.g. Ref. [128, 138]) for the nucleon. The DVCS and interference contributions are given by convolutions of the hard scattering and the GPDs. These convolution integrals occur in the corresponding coefficients and are referred to as CFFs. Exemplary the Fourier coefficient c_0^{DVCS} for unpolarized nucleons is given by:

$$c_{0,U}^{\text{DVCS}} = 2(2 - 2y + y^2) \frac{1}{(2 - x_{Bj})^2} \left\{ 4(1 - x_{Bj})(\mathcal{H}\mathcal{H}^* + \tilde{\mathcal{H}}\tilde{\mathcal{H}}^*) - x_{Bj}^2 \frac{t}{4M^2} \mathcal{E}\mathcal{E}^* \right. \tag{2.60}$$

$$\left. - x_{Bj}^2 (\mathcal{H}\mathcal{E}^* + \mathcal{E}\mathcal{H}^* + \tilde{\mathcal{H}}\tilde{\mathcal{E}}^* + \tilde{\mathcal{E}}\tilde{\mathcal{H}}^*) - \left(x_{Bj}^2 + (2 - x_{Bj})^2 \frac{t}{4M^2} \mathcal{E}\mathcal{E}^* \right) \right\}$$

Here, the calligraphic letters denote to the CFFs respectively their conjugated.

2.5.2 | Compton Form Factors

In detail the CFFs read as [27]:

$$[\mathcal{H}, \mathcal{E}, \mathcal{H}^3_+, \mathcal{E}^3_+, \tilde{\mathcal{H}}^3_-, \tilde{\mathcal{E}}^3_-](\xi, t) = \sum_f e^2_f \int_{-1}^{1} dx C^-(x, \xi)[H^f, E^f, H^{f3}_+, E^{f3}_+, \tilde{H}^{f3}_-, \tilde{E}^{f3}_-](x, \xi, t), \quad (2.61)$$

$$[\tilde{\mathcal{H}}, \tilde{\mathcal{E}}, \tilde{\mathcal{H}}^3_+, \tilde{\mathcal{E}}^3_+, \mathcal{H}^3_-, \mathcal{E}^3_-](\xi, t) = \sum_f e^2_f \int_{-1}^{1} dx C^+(x, \xi)[\tilde{H}^f, \tilde{E}^f, \tilde{H}^{f3}_+, \tilde{E}^{f3}_+, H^{f3}_-, E^{f3}_-](x, \xi, t).$$

Here, $C^{\pm}$ is a coefficient function related to the hard scattering part and is convoluted with twist-2 and twist-3 GPDs. These convolution integrals arise in the vector and axial vector decomposition of the DVCS amplitude. In pQCD these coefficient function are calculated as:

$$C^{\pm} = C^{\pm}_{(0)} + \frac{\alpha_s}{2\pi} C^{\pm}_{(1)} + \mathcal{O}(\alpha_s^2),$$

$$\text{with } C^{\pm}_{(0)} = \frac{1}{\xi - x - i0} \pm \frac{1}{\xi + x - i0}.$$

Using the Sokhotski-Plemelj theorem, it is possible to decompose integrals of the form given in Equation 2.61 into a real and an imaginary part. For any arbitrary GPD F this results in:

$$\int_{-1}^{1} dx \frac{F^f(x, \xi, t)}{\xi \pm x - i\epsilon} = \mathcal{P} \int_{-1}^{1} dx \frac{F^f(x, \xi, t)}{\xi \pm x} + i\pi F^f(\pm\xi, \xi, t),$$

where $\mathcal{P}$ denotes the Cauchy principal value. In case an experimental observable is sensitive to the imaginary part of the DVCS amplitude, the maximum amount of information that can be gained at a given (ξ, t)-point is $F(\pm\xi, \xi, t)$. For an observable sensitive to the real part this corresponds to $\int_{-1}^{1} dx \frac{F^f(x, \xi, t)}{\xi \pm x}$ [94]. By reducing the range of x to $[0, 1]$ one finds eight GPD related quantities that can be experimentally extracted. For the CFFs related to GPD H, they read as [94][1]:

$$\text{Re } \mathcal{H}(\xi, t) = \sum_f e^2_f \mathcal{P} \int_0^1 dx C^-(x, \xi)[H^f(x, \xi, t) - H^f(-x, \xi, t)], \quad (2.62)$$

$$\text{Im } \mathcal{H}(\xi, t) = \sum_f e^2_f \pi[H^f(\xi, \xi, t) - H^f(-\xi, \xi, t)], \quad (2.63)$$

$$\text{with } C^{\pm}(x, \xi) = \frac{1}{\xi - x} \pm \frac{1}{\xi + x}.$$

As discussed in Section 2.4.5, the GPD H is of particular interest, when studying the transverse extension of parton distributions in the nucleons. Extracting the terms above from the DVCS cross section and therefore gain information on GPDs is challenging and requires a vast amount of experimental data. The data then serves as input to fitting procedures, in which the CFFs are constrained [99]. For detailed information on the fitting procedure used for CLAS[2] and HERMES[3] data see [94–97]. A recent approaches using neural networks on global data can be found in [130, 131].

---

[1] Notation altered to fit the one introduced in Eq. 2.61
[2] CEBAF large acceptance spectrometer (CLAS)
[3] HERA measurement of spin (HERMES)

2.5.3 | The charge spin cross section sum

Extracting the charge spin cross section sum and studying its t-dependence is the main subject of this thesis. For lepton beams with opposite charge and polarization scattering off unpolarized target nucleons it reads [16]:

$$\mathcal{S}_{\text{CS},U} = 2d\sigma \equiv d\sigma^{\overleftarrow{+}} + d\sigma^{\overrightarrow{-}} = 2(d\sigma^{\text{BH}}_{UU} + d\sigma^{\text{DVCS}}_{UU} - |P_l|d\sigma^{\text{I}}_{LU}).$$

Here, the same degree of polarization for both beams is assumed. The $\overleftarrow{+}$ and $\overrightarrow{-}$ indicate the charge ($\pm$) and helicity ($\overleftarrow{\rightarrow}$) of the lepton beam and P_l denotes its polarization. Due to the sum of both lepton charge and spin configurations, not all Fourier coefficients (see Eq. 2.57, 2.58 and 2.59 in Sec. 2.5.1) contribute to the resulting cross section sum. The bottom indices of the remaining contributions denote the combination of lepton and nucleon spin. Here, the first index indicates the polarization of the lepton and the second one the spin configuration of the target nucleon. Omitting kinematic factors, the contributions are given as [16]:

$$d\sigma^{\text{BH}}_{UU} \propto (c^{\text{BH}}_0 + c^{\text{BH}}_1 \cos(\phi_{\gamma*\gamma}) + c^{\text{BH}}_2 \cos(2\phi_{\gamma*\gamma})), \tag{2.64}$$
$$d\sigma^{\text{DVCS}}_{UU} \propto (c^{\text{DVCS}}_0 + c^{\text{DVCS}}_1 \cos(\phi_{\gamma*\gamma}) + c^{\text{DVCS}}_2 \cos(2\phi_{\gamma*\gamma})), \tag{2.65}$$
$$d\sigma^{\text{I}}_{LU} \propto (s^{\text{I}}_1 \sin\phi_{\gamma*\gamma} + s^{\text{I}}_2 \sin 2\phi_{\gamma*\gamma}). \tag{2.66}$$

As mentioned in Section 2.5.1, the Bethe-Heitler contribution can be calculated and afterwards subtracted. Doing so the the coefficients c^{DVCS}_n and s^{I}_n can be extracted by studying the $\phi_{\gamma*\gamma}$-dependence of the cross section sum.

The leading contribution (twist-2) s^{I}_1 is related to the imaginary part of the following combination of CFFs [27]:

$$s^{\text{I}}_1 \propto \text{Im}(F_1\mathcal{H} + \xi(F_1 + F_2)\tilde{\mathcal{H}} - \frac{t}{4M^2}F_2\mathcal{E}). \tag{2.67}$$

In the kinematic domain of COMPASS and for proton targets ($F_1 > F_2$), the kinematic factors multiplied with $\tilde{\mathcal{H}}$ and $\mathcal{E}$ are small. Hence, s^{I}_1 is dominated by the contribution of $\text{Im}(F_1\mathcal{H})$, which according to Equation 2.63 gives direct access to the GPD H.

By integrating the cross section over $\phi_{\gamma*\gamma}$, all azimuthal angle dependent terms are omitted and only the c^{DVCS}_0 contribution (see Eq. 2.60) remains. Neglecting all terms in c^{DVCS}_0, which are kinematically suppressed in the COMPASS domain, it reduces to:

$$c^{\text{DVCS}}_0 \propto 4(\mathcal{H}\mathcal{H}^* + \tilde{\mathcal{H}}\tilde{\mathcal{H}}^*) - \frac{t}{M^2}\mathcal{E}\mathcal{E}^*.$$

According to model predictions (GK [84, 85, 87] and KM15 [116, 118]), c^{DVCS}_0 is mainly sensitive to $(\text{Im}\,\mathcal{H})^2$. The real part $(\text{Re}\,\mathcal{H})^2$ only accounts for a small contribution ($< 10\%$ depending on the chosen model) and the contributions by $\tilde{\mathcal{H}}$, $\tilde{\mathcal{H}}^*$, $\mathcal{E}$ and $\mathcal{E}^*$ can be neglected.

As it was discussed in Section 2.4.4 for $\xi = 0$, the four momentum transfer to the nucleon Δ only has a transverse component $\Delta_\perp$, that is the Fourier conjugated to the impact parameter $b_\perp$. Using the parametrization for the longitudinal quark momentum by Radyushkin, which is introduced in Section 2.4.1.1 and closer related to the forward kinematic of DVCS, it can be shown that the impact parameter is also related to the traverse distance of the struck quark $r_\perp$ by [41]:

$$b_\perp = (1 - X)r_\perp, \tag{2.68}$$

and for $X = \zeta$ the Fourier conjugated to $\Delta_\perp$ [41]. In the ansatz for the $\Delta_\perp$-dependence of GPD H^f in Equation 2.55 (see Sec. 2.4.5), where the $\Delta_\perp$-dependence is parameterized like $e^{-B_\perp \Delta^2_\perp}$, one finds that

the slope parameter $B_\perp$ of the GPD and the impact parameter are related via[4]:

$$b_\perp^2(X = \zeta) \propto -B_\perp(X = \zeta). \tag{2.69}$$

As in experiment only $\zeta \neq 0$ can be measured, an additional factor of $\frac{1}{1-\zeta}$ has to be taken into account [41]:

$$b_\perp^2(X = \zeta) = -\frac{1}{1-\zeta} B_\perp(X = \zeta), \tag{2.70}$$

Performing a variable transformation to the symmetric parametrization using the relations given in Equation 2.45 in Section 2.4.1.1 and using the relation $t = -\Delta$ (see Eq. 2.43 in Sec. 2.4.1.1), one obtains:

$$b_\perp^2(x) = \left(\frac{1+\xi}{1-\xi}\right) B_t(x). \tag{2.71}$$

Here, B_t denotes the t-slope in the parametrization of $H^f(x, \xi \neq 0, -\Delta_\perp^2)$ ($\propto e^{B_t t}$). As the $\phi_{\gamma*\gamma}$ integrated charge spin cross section sum is proportional to c_0^{DVCS}, which is dominated by $(\text{Im }\mathcal{H})^2$, the relation between $b_\perp$ and the t-slope of the cross section B is:

$$b_\perp^2(x) = 2\left(\frac{1+\xi}{1-\xi}\right) B(x). \tag{2.72}$$

For $x = \xi$ and sufficient small values of ξ, the $b_\perp^2$ in Equation 2.72 corresponds to the transverse extension of the nucleon $r_\perp^2$ (see Eq. 2.68).

2.5.4 | The charge spin cross section difference

The charge spin cross section difference is given by [72]:

$$\mathcal{D}_{CS,U} \equiv d\sigma^{\overleftarrow{+}} - d\sigma^{\overrightarrow{-}} = 2(|P_l|d\sigma_{LU}^{\text{DVCS}} + |e_l|d\sigma_{LU}^{\text{I}}), \tag{2.73}$$

where $|e_l|$ denotes the elementary charge. When calculating the cross section difference, the Bethe-Heitler contribution cancels. The remaining cross section contributions are:

$$d\sigma_{LU}^{\text{DVCS}} \propto s_1^{\text{DVCS}} \sin(\phi_{\gamma*\gamma}), \tag{2.74}$$
$$d\sigma_{LU}^{\text{I}} \propto c_0^{\text{I}} + c_1^{\text{I}} \cos(\phi_{\gamma*\gamma}) + c_2^{\text{I}} \cos(2\phi_{\gamma*\gamma}) + c_3^{\text{I}} \cos(3\phi_{\gamma*\gamma}). \tag{2.75}$$

The analysis of the angular dependence of Equation 2.73 provides the leading twist contributions (twist-2) c_0^{I} and c_1^{I}, while the pure DVCS contribution is suppressed. Analog to s_1^{I} in Equation 2.67, c_1^{I} is related to the real part of the same combination of CFFs with the same kinematic factors. In the COMPASS kinematics, c_1^{I} is dominated by $\text{Re}(F_1 \mathcal{H})$ (see Eq. 2.62). A similar behavior is expected for c_0^{I}, although in that case more CFF combinations contribute, which makes it significantly more difficult to disentangle.

---

[4]Here, $\hbar$ is set equal to 1: $b_\perp^2 \propto \hbar^2 B_\perp$

2.6 | Experimental approaches to investigate DVCS

The disentanglement of the CFFs to constrain GPDs requires DVCS data in a wide kinematic range and different configurations of the lepton beam and target nucleon polarization. The experimental observable quantities in these measurements are cross section sums, differences and asymmetries. To provide these data samples, GPD physics was and is being addressed by several experimental programs. An overview of results obtained in DVCS measurements is shown in Figure 2.17 in terms of the kinematic coverage in x_{Bj} and Q^2 (Status in 2015). The measurements performed until 2015 mainly covered the x_{Bj}-regimes of valence quarks and gluons. They are briefly summarized in Section 2.6.1 and 2.6.2. The prospect of a measurement at COMPASS was mainly driven by the lack of data in the sea quark region, which is covered by the COMPASS kinematic acceptance. A corresponding measurement was first proposed in 2010 [72]. In 2012 a test measurement was performed using a polarized muon beam and an unpolarized proton target. The result of this measurement is discussed in Section 2.6.3. The red area in Figure 2.17 indicates the expected kinematic coverage by the future Electron-Ion Collider (EIC), which will be located at the Brookhaven National Laboratory, USA [115]. As for the status of 2022, the EIC project is approved and will start its construction presumably in 2023.
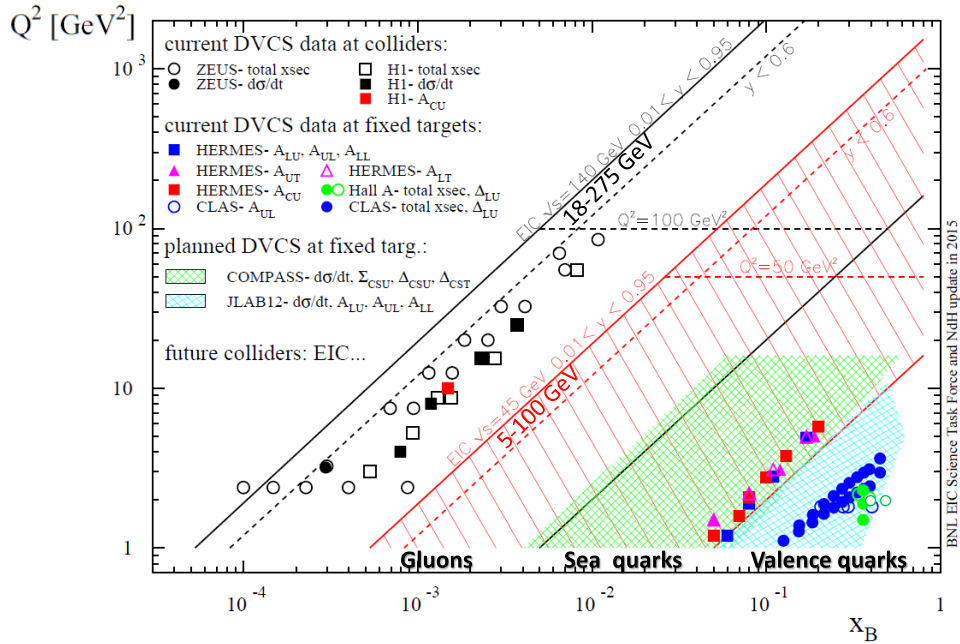
Figure 2.17: Kinematic coverage of the available and future DVCS measurements. Figure taken from Ref. [165].

2.6.1 | DVCS in the valence quark region (HERMES, CLAS and Hall A)

The results on cross section asymmetries provided by the **HERMES** collaboration cover an analysed kinematic range of Q^2 from $1\,(\mathrm{GeV/c})^2$ to $10\,(\mathrm{GeV/c})^2$, x_{Bj} between 0.03 and 0.35 and $|t|$ below $0.7\,(\mathrm{GeV/c})^2$ [13–15, 173, 174]. The data was taken between 1996 and 2005 and used the polarized 27 GeV electron and

positron beams produced by the HERA[5] facility at DESY[6] in Hamburg, Germany. These beams were scattered off a fixed gaseous hydrogen target, which was either unpolarized, longitudinal or transversal polarized. As only the final state lepton and photon were being detected by the HERMES spectrometer [7], the exclusive events were identified by requiring a missing mass, which is close to the squared mass of the proton.

Similar measurements were done at Hall A and B, located at Jefferson Lab, Virginia, USA. The measurement in 1999 provided a result on the beam-spin asymmetry (polarized beam on unpolarized target) [160]. The data was taken using the longitudinally polarized $4.25\,\mathrm{GeV}$ electron beam provided by the CEBAF[7] accelerator, which was scattered off an unpolarized liquid hydrogen target. To identify the exclusive reactions, the missing mass squared was analyzed using the measurement of the scattered electrons and photons by the CLAS spectrometer [127] that is located in Hall B. This measurement was followed up by two additional measurements in 2005 and 2009. In 2005 the electron beam energy was increased to $5.77\,\mathrm{GeV}$ and scattered off a liquid hydrogen target [81]. To measure the full three particle final state and increase the acceptance, the CLAS spectrometer was extended by a time-of-flight system for detecting the recoil proton and an additional calorimeter. In 2009 a solid ammonia target (NH_3) with a longitudinal polarization was used to measure the target-spin (unpolarized beam on polarized target) and double-spin (polarized beam on polarized target) asymmetries [141]. The **Hall A** measurements include a series of experiments (2004: E00-110 [50] and E03-106 [125], 2010: E07-007 and E08- 025 [28]), which were dedicated to measure total cross sections (sums and differences) of DVCS either using liquid hydrogen (E03-106 and E07-007) or deuterium targets (E00-110 and E08- 025) [153]. The latter allows to analyse DVCS for the neutron [28, 125]. With the experimental setup in Hall A, the full three particle final state was measured using a dedicated electromagnetic calorimeter for the photon, a plastic scintillator array for the proton and the Hall A High Resolution Spectrometer (HRS) for the scattered electrons [51]. The results from the proton scattering were used to subtract the proton contribution from the deuterium data, which allowed to access the pure neutron contribution [29]. By combining the CLAS and the Hall A results for liquid hydrogen, the $\phi_{\gamma*\gamma}$-dependence of the charge spin cross section sum and difference was analyzed in a kinematic range of Q^2 between $1.0\,(\mathrm{GeV/c})^2$ and $4.6\,(\mathrm{GeV/c})^2$, x_{Bj} between 0.10 and 0.58 and $|t|$ between $0.09\,(\mathrm{GeV/c})^2$ and $0.52\,(\mathrm{GeV/c})^2$ [113].

These combined results were also used to extract the CFFs in the valence quark region and the transverse extension of the proton [59]. The eight CFFs are treated as free parameters in a simultaneous least square fit for several leading twist observables at fixed (ξ, t)-kinematics. With each observable including contributions from several CFFs (see e.g. Sec. 2.5.3 and 2.5.4) and only a few observables available, the problem is underconstrained. Considering the dominant contributions to certain observables e.g. beam-spin observables are dominated by Im $\mathcal{H}$, they are used to formulate limits on CFFs allowing the dominant contributions to be determined by the fit with finite uncertainties. Here, the uncertainties are mostly driven by the influence of the non-dominant CFF contributions rather than the experimental data itself.

The best determined parameter by the fit is Im $\mathcal{H}$ as it is the dominant contribution. Results on its t-dependence for a total of 20 bins (x_{Bj}, Q^2) are shown in Figure 2.18. The fit to the cross section sum and differences is shown in red (open squares and solid circles: CLAS, solid triangles: Hall A). The black stars show a calculation using the VGG model. To extract the (ξ, t)-dependence of the CFFs, the t-dependence is fitted by an exponential function given as:

$$\mathrm{Im}\,\mathcal{H} = A(\xi)e^{B(\xi)t}. \tag{2.76}$$

---

[5]Hadron-Electron Ring Accelerator (HERA)
[6]Deutsches Elektron-Synchrotron (DESY)
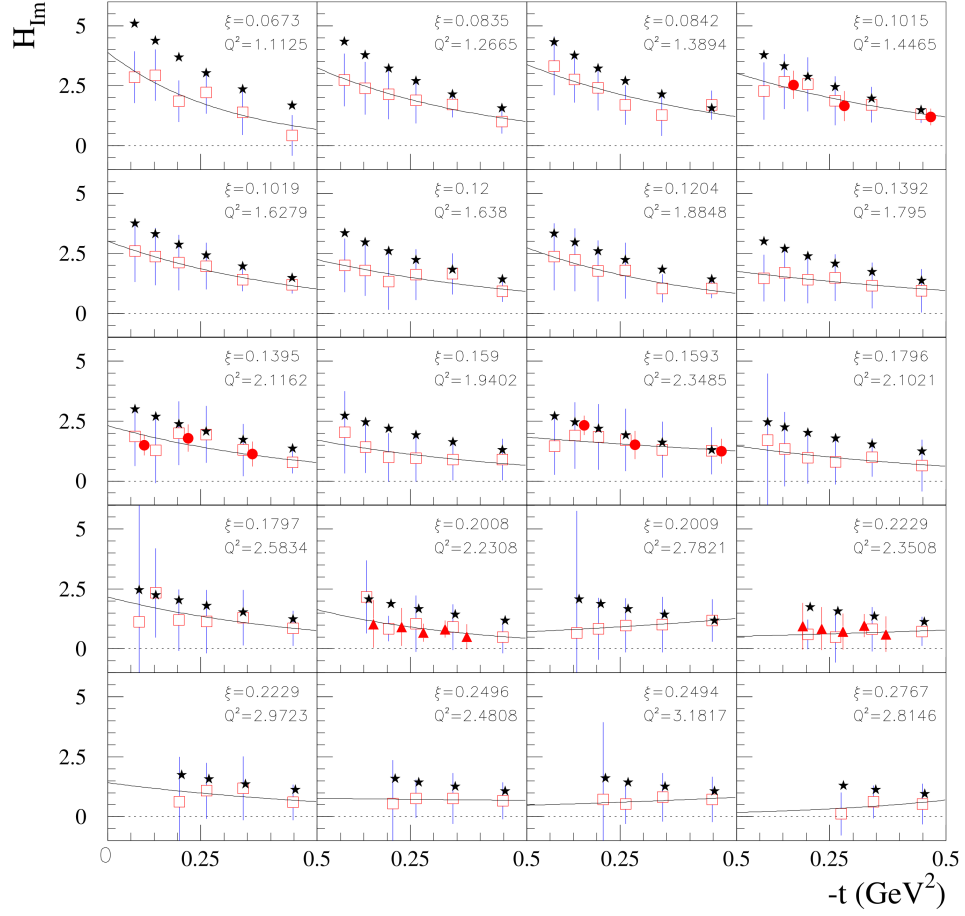[7]Continues Electron Beam Accelerator Facility (CEBAF)

Figure 2.18: The t-dependence of the CFF Im $\mathcal{H}$ is shown in 20 bins of (x_{Bj}, Q^2) based on the results of the DVCS cross section sum and difference obtained by the CLAS and Hall A experiments. The data points are shown in red (open squares and solid circles : CLAS, solid triangles: Hall A) with blue error bars and a calculation using the VGG model is shown as black stars. The black lines correspond to a fit according to Equation 2.76. Figure taken from Ref. [59].

The results of this fit are shown as the black solid lines. The amplitude A is parameterized by:

$$A(\xi) = a_A(1 - \xi)/\xi. \tag{2.77}$$

This ansatz is chosen according to the expected increase of the amplitude at small ξ, due to the sea-quark contribution and the vanishing of A in the limit $\xi \to 1$, when all longitudinal momentum is taken by a single valence quark. Similar considerations led to an ansatz for the slope parameter B:

$$B(\xi) = a_B \ln(1/\xi). \tag{2.78}$$

The fit of B is shown in Figure 2.19a as band for a 1σ variation in $a_B = (1.07 \pm 0.26) \, \text{GeV}^{-2}$. The data either correspond to the 8 CFFs extracted from the 4 observables from Hall A/CLAS measurement (solid points) or to the HERMES results (solid square). For Hall A/CLAS only the 8 lowest bins in ξ are considered as they provide the smallest uncertainties. The different curves are the result of a dual

model or the VGG model, choosing different values for the valence and sea profile parameters (b_v and b_s). The slope parameter B is related to the mean valence quark radius squared for quarks of flavour f by[8]:

$$\langle b_\perp^2 \rangle^f(x) = 4B_0(x). \tag{2.79}$$

The additional factor 2, with respect to Equation 2.72 in Section 2.5.3 arise in the fact that the latter is valid on the level of cross sections, while the former correspond to the level of amplitudes[9]. The difference between the B parameter in Equation 2.78 and B_0 in Equation 2.79 is due to B being for the singlet GPD combination related to the imaginary part of $\mathcal{H}$ at $x = \xi$, while the B_0 is for the valence GPD in the limit $\xi = 0$. This corresponds to the discussion of Equation 2.71 in Section 2.5.3 and results in a ratio of $B_0/B \simeq 0.925 \pm 0.025$. By assuming the t-dependence of the valence GPD $H^f_-(x, 0, t)$ to be exponential:

$$H^f_-(x, 0, t) = q_v(x)e^{B_0(x)t}, \tag{2.80}$$

where $q_v(x)$ is the valence quark distribution and choosing a Regge type ansatz to parameterize $B_0(x)$:

$$B_0(x) = a_{B_0} \ln(1/x), \tag{2.81}$$

a value for $a_{B_0} = (1.05 \pm 0.02)\,\text{GeV}^{-2}$ is obtained. The result on $\langle b_\perp^2 \rangle(x)$, when assuming that $B_0(x)$ is the same for u and d quarks, is shown in Figure 2.19b. The data points are the converted experimental data of $B(\xi = x)$ using Equation 2.79.

---

[8]Formula for $\hbar = 1$

[9]This originates in the relation of cross section to amplitude ($A^2 \sim \sigma$): $(e^{B_0 t})^2 = e^{2B_0 t} := e^{B_\sigma t}$.
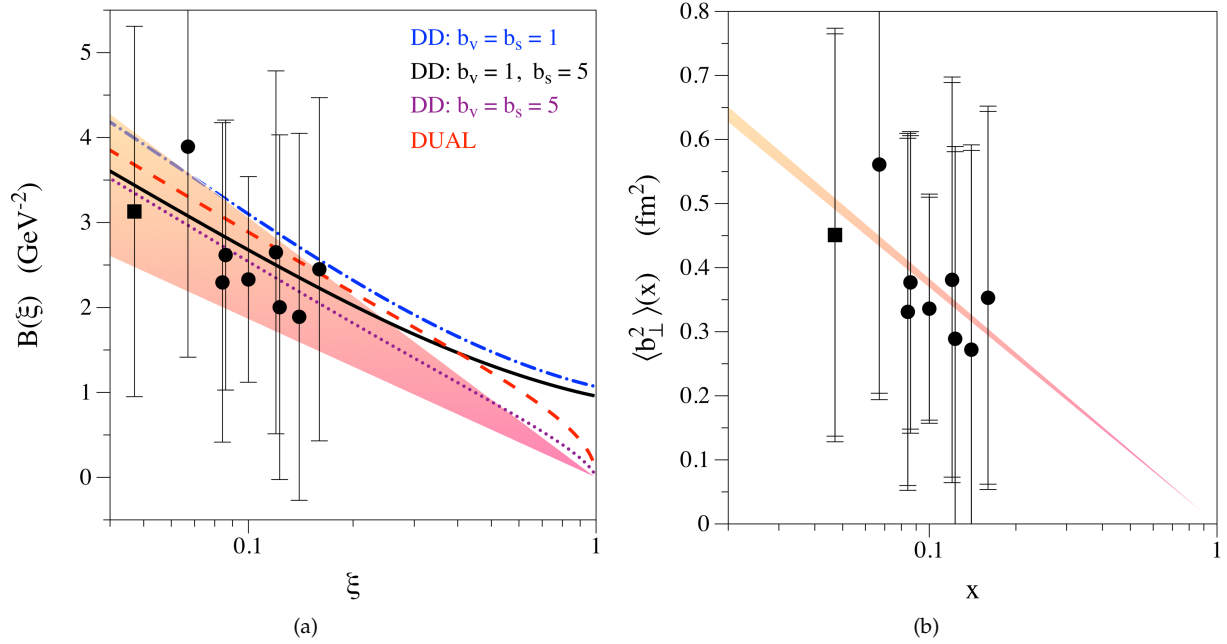
Figure 2.19: (a) Slope parameter B as a function of ξ. The black data points represent a fit of the 8 CFFs using CLAS/Hall A (solid points) or HERMES data (solid squares). The fit of $B(\xi)$ is done according to Eq. 2.78 and shown as a band with 1σ variation. For comparison, theory curves either produced by a dual model or the VGG using different values for the valence and sea profile parameters (b_v and b_s) are shown.

(b) x-dependence of $\langle b_\perp^2 \rangle$ for quarks in the proton. The data points are obtained by converting the data of $B(\xi = x)$ (see Fig. 2.19a) by using Eq. 2.79. The outer error bars represent the (small) uncertainties introduced by the model in the process of the data conversion. Figures taken from Ref. [59].

2.6.2 | DVCS in the gluon region (H1 and ZEUS)

In the gluon region, measurements of DVCS were performed by the H1 and ZEUS collaboration, aiming on extracting the t-dependence of the cross section. Both experiments were located at the HERA facility measuring all final state particles for high energy electron/positron-proton collisions. The **H1** data sample, recorded by the H1-detector [6], comprises multiple periods of data taking, which started in 1996 with a 27.6 GeV positron beam and a 820 GeV proton beam that was increased to 920 GeV in 1999. The first data set (HERA I: 1996-2000) only uses a positron beam and was used to analyse the DVCS cross section and its t-dependence in a kinematic range of Q^2 between 2 (GeV/c)^2 and 80 (GeV/c)^2, W between 30 GeV and 140 GeV and $|t|$ below 1 (GeV/c)^2. The pure DVCS contribution is obtained by subtracting the Bethe-Heitler contribution and averaging over its angular dependence. Its t-dependence is described by an exponential form: $e^{-B|t|}$.[10] The slope parameter and its statistical and systematic uncertainties are determined to be $B = (6.02 \pm 0.35 \pm 0.39)$ GeV^{-2} at a mean of $Q^2 = 8$ (GeV/c)^2 and $x_{Bj} = 1.8 \cdot 10^{-3}$ [2, 9]. For the second data set (HERA II: 2004-2007) a 27.6 GeV, longitudinal polarized electron or positron beam together with a 920 GeV proton beam were used. This configuration also al-

---

[10]In the published paper the slope parameter is denoted as b. To prevent confusion with the impact parameter and stay the introduced notation B is used instead.

lowed to measure the beam-charge asymmetry and therefore the interference between Bethe-Heitler and DVCS (see Fig. 2.20b). The slope parameter of the DVCS cross section (see Fig. 2.20a) was determined to be $B = (5.41 \pm 0.14 \pm 0.31)\,\text{GeV}^{-2}$ at a mean of $Q^2 = 10\,(\text{GeV/c})^2$ and $x_{Bj} = 1.2 \cdot 10^{-3}$ [3, 4].
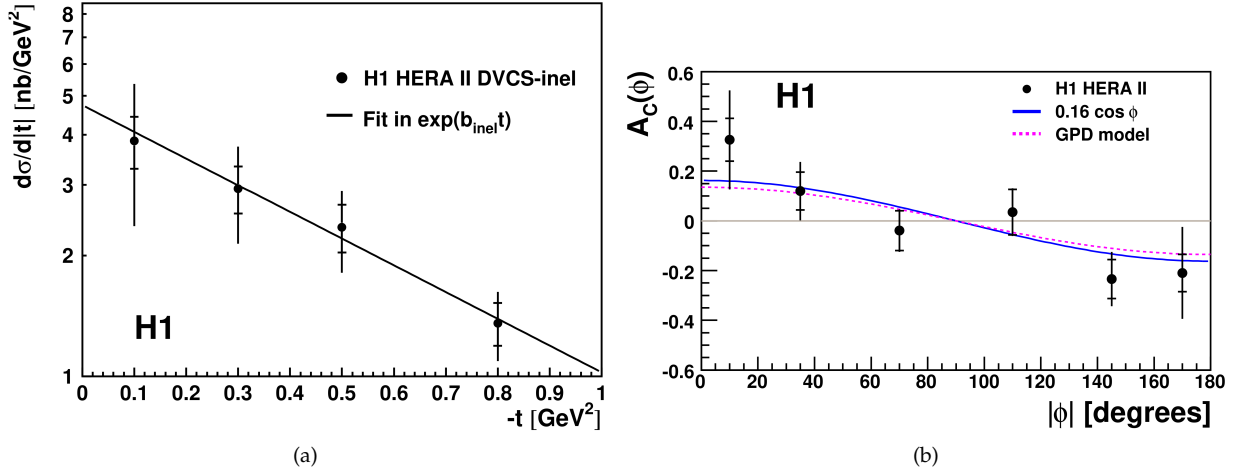

Figure 2.20: (a) The t-dependence of the DVCS cross section at a mean of $Q^2=10\,(\text{GeV/c})^2$ and $x_{Bj} = 1.2 \cdot 10^{-3}$ obtained by H1 measurement (2004-2007). The slope is fitted using an exponential ansatz of the form $d\sigma/d|t| \sim e^{Bt}$ resulting in a value of the slope parameter of $B = (5.41 \pm 0.14 \pm 0.31)\,\text{GeV}^{-2}$. (b) Beam-charge asymmetry as a function of the azimuthal angle ϕ. For comparison the function $0.16\cos\phi$ (solid blue line) together with a GPD model prediction are shown. Figures taken from Ref. [4].

A similar measurement was performed in the years 1999 and 2000, using the **ZEUS** detector [53]. As for the H1 measurement also here the full three particle final state of the (ep)-reaction was detected using the same beam energies for electrons/positrons and protons. The DVCS cross section and its t-dependence was measured in a kinematic range of Q^2 between $1.5\,(\text{GeV/c})^2$ and $100\,(\text{GeV/c})^2$ and W between $40\,\text{GeV}$ and $170\,\text{GeV}$. The slope parameter was determined to be $B = (4.5 \pm 1.3 \pm 0.4)\,\text{GeV}^{-2}$ at a mean $Q^2 = 3.2\,(\text{GeV/c})^2$ (see Fig. 2.21) [45, 175].

A compilation of the H1 and ZEUS results is shown in Figure 2.22a and 2.22b. Figure 2.22a displays the DVCS cross section ($\gamma^* p \to \gamma p$) as a function of Q^2 at a mean of $W = 82\,\text{GeV}$. The ZEUS data, taken at a mean of $W = 104\,\text{GeV}$ is extrapolated to $W = 82\,\text{GeV}$ using a W-dependence of $W^{0.52}$. For comparison, the solid line represents a prediction of the dipol model [124] and the dashed line a prediction of the GPD KM-model in Reference [117]. The data sets are comparable within their uncertainties. Figure 2.22b shows the Q^2-dependence of the determined slope parameters, using the same data sets and again in comparison with the same model predictions (dipole model: solid line and KM-model: dashed line). The GPD model and the results obtained by the first H1 data set imply a slight increase of the transverse extension of the proton with decreasing Q^2.
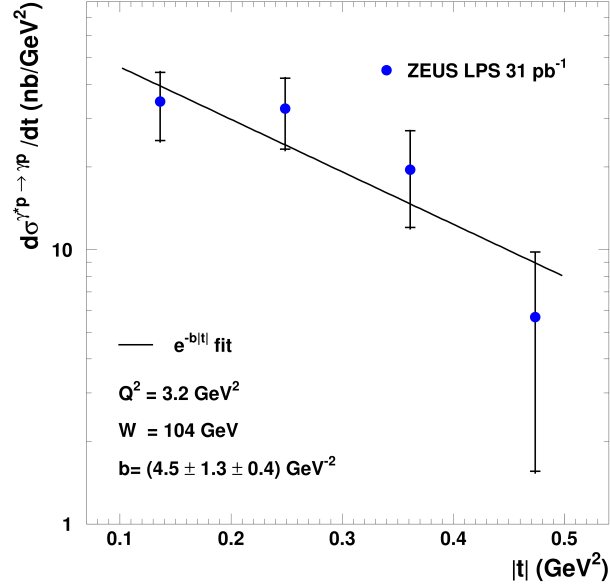
Figure 2.21: Differential DVCS cross section as a function of $|t|$. The solid line represents the result of a fit $\sim e^{-B|t|}$. Figure taken from Ref. [175].
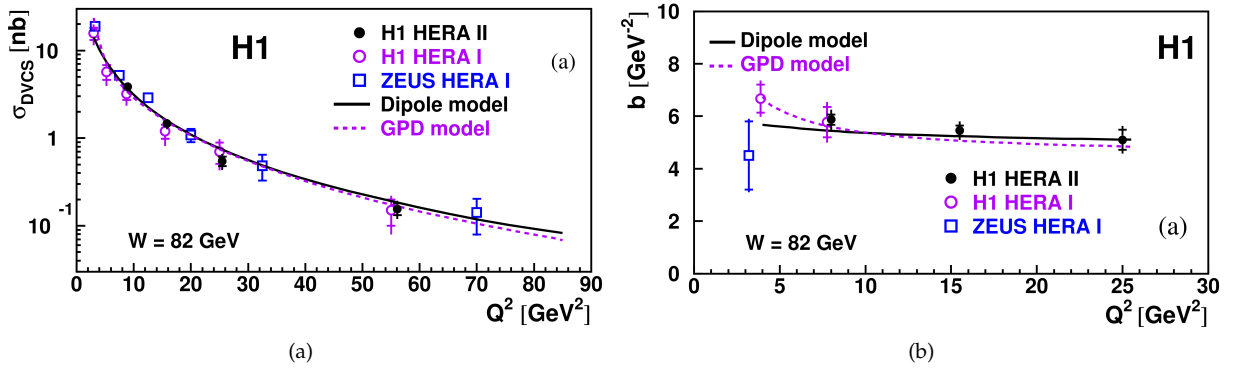

Figure 2.22: (a) Comparison of the DVCS cross section ($\gamma^* p \rightarrow \gamma p$) as a function of Q^2 at a mean of $W = 82\,\text{GeV}$ for H1 (HERA I and II) and ZEUS. The ZEUS data is extrapolated from a mean $W = 104\,\text{GeV}$ using a W-dependence of $W^{0.52}$. For comparison the solid line represents a prediction of the dipol model [124] and a dashed line a prediction of the GPD model [117].
(b) Results on the fitted t-slope parameter B as a function of Q^2 for the same data set. A weak dependence on Q^2 is observed. Figures taken from Ref. [4].

2.6.3 | DVCS in the sea quark region (COMPASS)

A first measurement of exclusive reactions in high energy muon-proton scattering was performed by the COMPASS collaboration in 2012 using a 160 GeV, polarized, positively and negatively charged muon beam and an unpolarized 2.5 m long liquid hydrogen target. The recorded data set was analysed for DVCS ($\mu p \to \mu' p' \gamma$) and hard exclusive π^0 production ($\mu p \to \mu' p' \pi^0$) to determine the corresponding cross sections [16, 17]. To detect the three particle final state the COMPASS spectrometer was supplemented by a proton recoil detector, surrounding the target and an additional electromagnetic calorimeter located directly behind the target to increase the acceptance to larger photon scattering angles. A detailed summary of the COMPASS setup for measuring exclusive reactions is given in Section 3.1.5. In the analyses the pure DVCS contribution was obtained by subtracting the Bethe-Heitler contribution and a contamination by photons produced via the decay of neutral pions. To extract the t-dependence of the binned DVCS cross section, the beam charge spin cross section sum (see Sec. 2.5.3) is calculated and integrated over its dependence on the azimuthal angle. The considered kinematic region was, Q^2 between $1\,(\text{GeV}/c)^2$ and $5\,(\text{GeV}/c)^2$, ν between 10 GeV and 32 GeV and $|t|$ between $0.08\,(\text{GeV}/c)^2$ and $0.63\,(\text{GeV}/c)^2$. The slope parameter was determined to be $B = (4.3 \pm 0.6_{\text{stat}}{}^{+0.1}_{-0.3}|_{\text{sys}})\,(\text{GeV}/c)^{-2}$ at average kinematic values of $\langle Q^2 \rangle = 1.8\,(\text{GeV}/c)^2$, $\langle W \rangle = 5.8\,\text{GeV}/c^2$ and $\langle x_{Bj} \rangle = 0.056$. Converting the slope parameter into the average squared transverse extension of the proton by [16, 130]:

$$\langle b_\perp^2 (x_{Bj}) \rangle = 2\hbar^2 \frac{B}{1 - x_{Bj}} \approx 2\hbar^2 B, \tag{2.82}$$

results in a value of $\sqrt{\langle b_\perp^2 (x_{Bj}) \rangle} = (0.58 \pm 0.04_{\text{stat}}{}^{+0.01}_{-0.02}|_{\text{sys}} \pm 0.04_{\text{model}})\,\text{fm}$. According to the discussion in Section 2.5.3, this interpretation only holds for small values of ξ at $x = \xi \approx x_{Bj}/2$.

A compilation of results on the slope parameter and the corresponding transverse extensions of the proton obtained by H1, ZEUS and COMPASS is shown in Figure 2.23a. For comparison, theory curves based on models of Kumericki-Müller (KM) [116, 117] and Goloskokov-Kroll (GK) [84, 85, 87] indicate the prediction on the Q^2 and x_{Bj} dependence (see Fig. 2.23b). The ZEUS, H1 results at an average Q^2 of $10\,(\text{GeV}/c)^2$ and the result of the 2012 COMPASS measurement hint to a smaller transverse extension of the proton than predicted by the models.
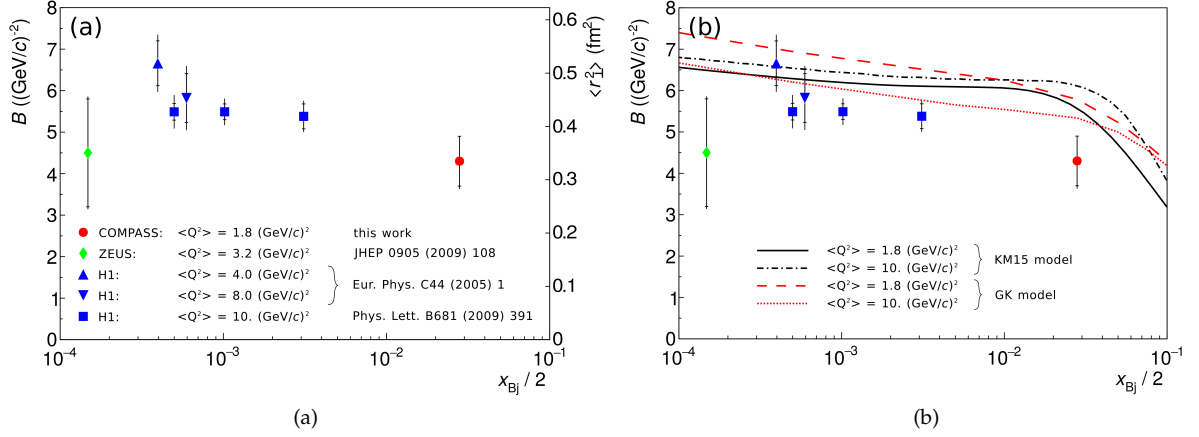
Figure 2.23: (a) Results on the *t*-slope parameter *B* and the equivalent squared average of the transverse extension of partons in the proton $\langle b_\perp^2(x_{Bj})\rangle$ from H1, ZEUS and COMPASS. The inner error bars represent the statistical, while the outer error bars represent the systematic errors.
(b) Results in comparison to theory curves extracted from the KM model [116, 117] and GK model [84, 85, 87]. Figures taken from Ref. [16].

2.7 | DVCS measurement at COMPASS in 2016/17

As it was discussed previously, COMPASS can provide measurements of DVCS in the poorly explored sea quark regime. The prospect for a high statistic data sample providing information on the x_{Bj} evolution of the slope parameter was one key argument for a DVCS dedicated data taking in 2016/17.

The COMPASS measurement does not only provide data on exclusive photon production, but in general on inelastic muon-proton scattering. This allows on one hand to extend the analysis also to other exclusive reactions like for e.g. hard exclusive π^0 or ρ^0 production and on the other hand to perform detailed studies on the background of the exclusive photon production by photons produced in DIS.

As discussed in the COMPASS II proposal [72] and later shown when analysing the 2012 data, the high muon beam energy (160 GeV) used at COMPASS, allows to study the exclusive photon production in different kinematic domains of the virtual photon energy ν. These ν-regions are chosen according to the expected contributions of physics processes to the observed cross section. In the ν-region between 80 GeV to 144 GeV Bethe-Heitler is the dominant process. This region is used to verify the simulation of the Bethe-Heitler process by comparing kinematic distribution obtained from Monte-Carlo to distributions obtained from data. It is therefore referred to as *reference region*. A substantial contribution of DVCS to the exclusive photon production cross section is expected for small values of ν. The ν-region between 10 GeV to 32 GeV is therefore used for extracting the DVCS cross section. Hence, this region is denoted as *extraction region*. The intermediate ν-region between 32 GeV to 80 GeV is referred to as *interference region*. Beside the name it should be noted that the interference between Bethe-Heitler and DVCS contributes in all ν-regions albeit with different amplitudes. The exclusive photon sample selected from the data also include a background by photons originating from a decay of neutral pions ($\pi^0 \rightarrow \gamma\gamma$). These pions are either produced in a hard exclusive process or inclusively as a product of DIS. Both contributions needed to be considered and together with the Bethe-Heitler contribution subtracted from

the data sample to determine the pure DVCS contribution to the observed cross section for exclusive photon production.

The COMPASS experiment

The COMPASS experiment [5] is located at the M2-beamline of the Super Proton Synchrotron (SPS) at CERN. The experiment emerged from two independently developed ideas for studying the structure of hadrons. In 1996 two proposals requested to use the M2-beamline. One project for DIS measurements using a muon beam and another one requesting a hadron beam for spectroscopic measurements. As the M2-beamline is capable of providing high quality muon and hadron beams, both projects were fused together to form a collaboration for QCD studies of the nucleon, later known as COMPASS. COMPASS started taking data in 2002 and ran until 2011, with a break in 2005 due to a long shutdown of the CERN accelerators. During this data taking period COMPASS performed several measurements using a muon beam (2004, 2006, 2007, 2010, 2011) and a hadron beam (2008, 2009) contributing to a deeper understanding of the gluon polarization. This data contributes to resolve the nucleon spin puzzle by studying polarized quark distributions, light meson spectroscopy and more.

After 2011 phase two of the experiment started (COMPASS-II). The performed measurements were dedicated to investigate the transverse and the three dimensional structure of nucleons. COMPASS-II was first proposed in 2010 [72] and started two years later with a measurement of the Primakoff process and a test run for the long DVCS measurement, which followed in 2016/17. In 2014, 2015 and 2018 a measurement of the *Drell-Yann* (DY) process was performed using a hadron beam on unpolarized and polarized protons. The measurement in 2015 was the first DY measurement ever using a polarized proton target and was resumed in 2018. After the long shutdown of the CERN accelerator complex in 2019/2020, COMPASS was approved for an additional data taking in 2021, performing deep inelastic scattering of muons on transversely polarized deuterons [68].

3.1 | The experimental setup of COMPASS in 2016/17

The following sections give a detailed description of the experimental setup used in 2016/17. Here, the focus is set on the detector systems crucial for the DVCS measurement. The production of the muon beam and its momentum measurement are described in Sections 3.1.1 and 3.1.2. In the Sections 3.1.3 and 3.1.4 the proton target and proton recoil detector are described. Section 3.1.5 introduces the COMPASS spectrometer, including the general identification of muon-proton scattering events by a dedicated trigger system (see Sec. 3.1.5.3), the specific identification of muons (see Sec. 3.1.5.2) and the detection of photons by electromagnetic calorimeters (see Sec. 3.1.5.4). Besides the hardware components and detector systems, also brief summaries of the Data Acquisition (DAQ) and the data reconstruction are given in Sections 3.1.7 and 3.1.8.

3.1.1 | The beam

The M2-beamline is capable to provide high energy μ^- and μ^+ beams. A schematic overview of the M2-beamline is shown in Figure 3.1. The muon beams are produced via the decay of secondary hadrons, which originate in an interaction of 400 GeV protons provided by the SPS with a berylium target (T6). By changing the length of the berylium target it is possible to adjust the amount of secondary produced hadrons, which alters the intensities of the muon beams. The secondary hadron beam decomposes mainly into charged pions and protons with a small fraction of kaons (3.6% at T6 [5]) and antiprotons. The charged pions and kaons decay, producing μ^- and μ^+ and the corresponding neutrinos. Due to the weak decay, the μ^- and μ^+ beams are naturally polarized in opposite directions (beam polarization 80±4% [5]). At the end of the 650 m long decay tunnel, the remaining hadrons are being absorbed and the muons are focused, momentum selected and deflected to reach ground level. At ground level the muon beam is deflected again to align the beam with the horizontal axis of the spectrometer. The magnet performing this deflection is part of the beam momentum station (BMS), which is a detector setup to measure the momenta of the muons and is described in Section 3.1.2. The muons are delivered as packages called spills, which are formed by the so called slow extraction of the SPS. In 2016/17 the typical extraction length was about 5 seconds.

When entering the experimental hall the muon beam is accompanied by a large halo, which includes all muons outside the nominal Gaussian profile of the beam. The so called far halo component is settled at a distance of approximately 20 cm from the beams center and corresponds to of about 7% of its total intensity. At a distance of about 15 cm from the beams center is the so called near halo component, which represents about 16% of the beam muons [5].

For the DVCS measurement the used beam energies are 160 GeV with a momentum spread of about 5%.
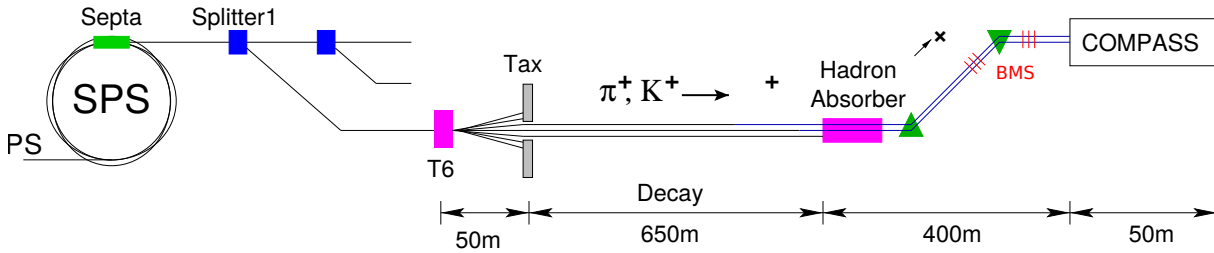
Figure 3.1: Schematic view of the M2-beamline. Figure taken from Ref. [67].

3.1.2 | The Beam Momentum Station

The beam momentum station is a setup consisting of six detector stations in total (see Fig. 3.2). These stations are either scintillator hodoscopes (BM01-BM04) or scintillating fibre detectors (BM05, BM06) and are placed around a bending magnet (B6). The actual determination of the beam momentum is performed by measuring the deflection of the muons in the magnetic field. This deflection is determined from the trajectory of the muon, measured by three detectors before and after the magnet.

This setup allows to measure the momentum of each incoming particle with a precision of about 0.5% and a reconstruction efficiency of about 93% [5].
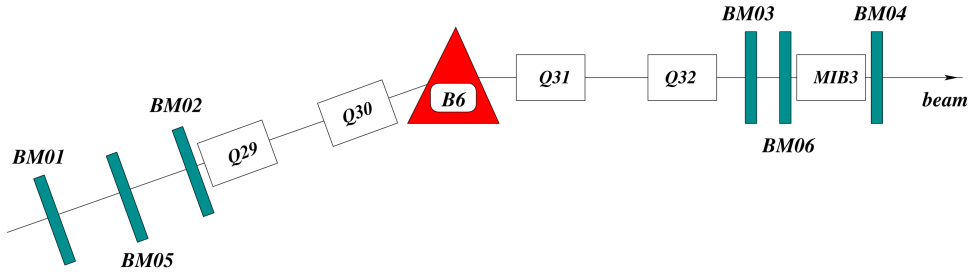
Figure 3.2: Schematic of the Beam Momentum Station (BMS). Figure taken from Ref. [5].

3.1.3 | The liquid hydrogen target

As target material liquid hydrogen is used. The hydrogen is contained in a cylindrical cell at a temperature of about 20 K and pressure of about 1.18 bar. Under these conditions the hydrogen has a density of $7.0146 \cdot 10^{-2}$ g/cm^3. A schematic illustration of the target is shown in Figure 3.3. The target cell has a diameter of 40 mm and is 2668 mm long. It is made of five layers of Kapton$^®$ foil with a total thickness of 0.125 mm. For the purpose of insulation the cell is wrapped in 30 layers of aluminized Mylar$^®$ foil, each 11 μm thick. At the upstream[1] side of the cell a stainless steel cylinder with a thicker ring part is glued to the cell. The ring connects two pipes to the target cell. The bottom pipe acts as entry for the liquid hydrogen and the pipe on top as return line for the gaseous hydrogen. The upstream side of the steel cylinder and the most downstream side of the target cell are sealed by hemispherical-shaped Mylar$^®$ (0.125 mm thick) end caps. The usable effective length of the target cell is about 2550 mm. The cell is placed inside a vacuum chamber and supported by four Rohacell$^®$ pieces to center it. The chamber is made of Carbon Fiber Reinforced Plastic (CFRP), which is formed to a pipe. It has a length of 2676 mm, an outer diameter of 80 mm and a thickness of 1 mm. The chamber is sealed on the downstream side by a 0.35 mm thick Mylar$^®$ window supported by an CFRP end cap. The total amount of material used, including the cell and the vacuum chamber, is chosen to be as small as possible to minimize the energy loss of the recoil protons leaving the target in transverse direction. More technical details on the target can be found in Reference [33]. A method to precisely determine the position of the target cell is presented in Section 4.2.

---

[1]upstream and downstream refer to the direction of the muon beam

45
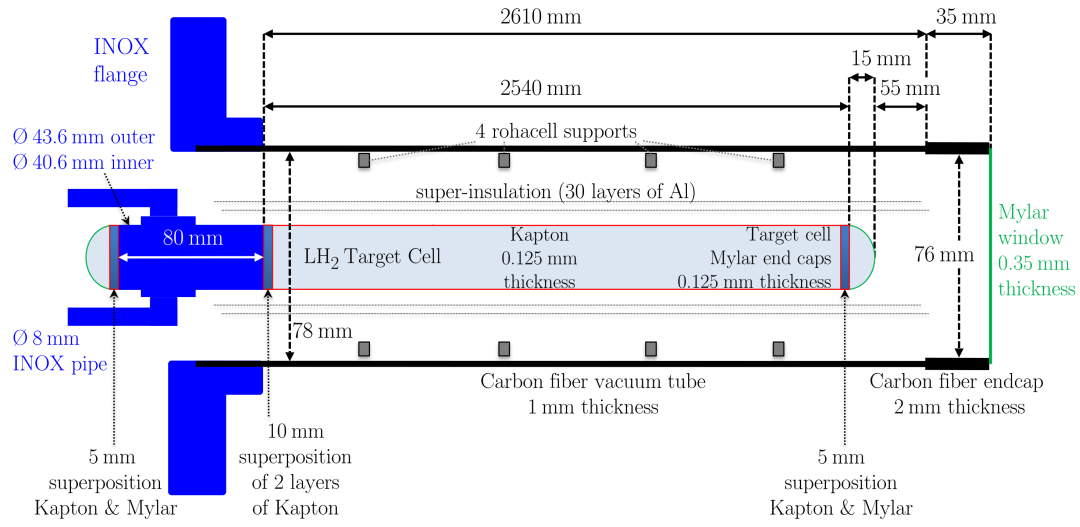
Figure 3.3: Schematic side view of the liquid hydrogen target cell and the vacuum camber. Figure taken from Ref. [161].

3.1.4 | The proton recoil detector

The proton recoil detector (CAMERA) surrounds the target to detect the recoil protons by measuring their time-of-flight (TOF) between two concentric scintillator rings. To distinguish the protons from other particles their characteristic energy loss, when traversing the scintillators, is used. A schematic view of the inner ring (ring A) and the outer ring (ring B) around the target cell is shown in Figure 3.4. Both rings are build of 24 scintillator elements each. The elements of ring A are 2750 mm long, 63 mm
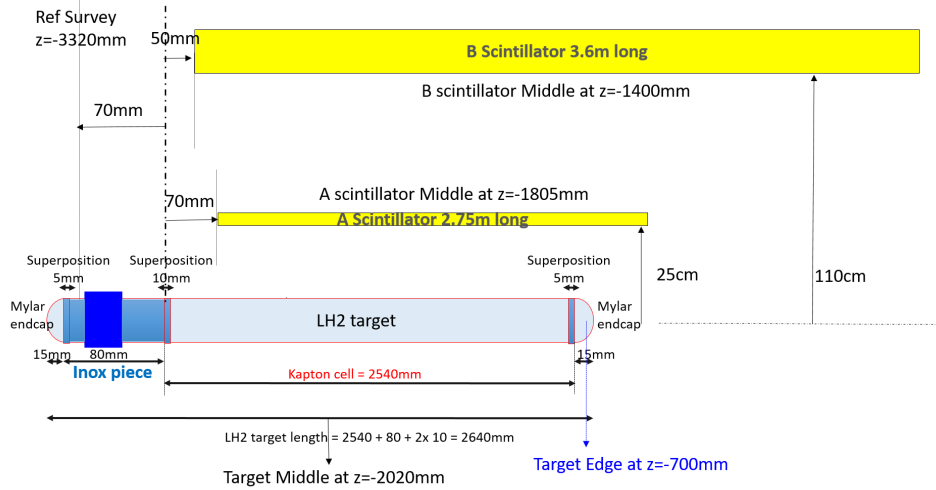
Figure 3.4: Schematic side view of the target cell and the proton recoil detector. Figure taken from Ref. [165].

wide and 4 mm thick. They are connected to a long light guide (L=1070 mm, bend by 45°) on their downstream and a shorter light guide (L=540 mm, bend by 90°) on their upstream end. Each scintillator element is read out by photomultiplier tubes (PMTs) on both sides. Ring A has a radius of 250 mm with respect to the beam axis. The outer ring (ring B) has a radius of 1100 mm. Here, both sides of the ring elements are connected to equally bent (90°) light guides of the same length (590 mm). To cover the same solid angle as ring A, its elements are 3600 mm long and 300 mm wide. Each element of ring A and B covers an azimuth angle of 15° around the target axis, but ring A is rotated by 7.5° with respect to ring B. The scintillator thickness of the ring A is chosen to allow only for a minimal energy loss of the protons, but still sufficient to produce a signal in the corresponding PMTs. A typical distribution of the signal amplitudes in ring B, as a function of the proton velocity β, is shown in Figure 3.5. The minimum velocity of protons detected in ring B is about 0.1, which corresponds to minimum four-momentum transfer to the proton of about $|t_{min.}|$=0.08 (GeV/c)^2. Until a velocity of about $\beta = 0.4$ the protons are fully absorbed by the scintillators, while for larger β the protons start to escape the ring, only depositing a fraction of their energies. For protons with velocities smaller than $\beta = 0.95$, the energy loss in the scintillator is still sufficient to produce signals in the PMTs. The signals of all the elements are sent to GANDALF[2] modules, which are multi-purpose FPGA[3] boards developed by a group at the Albert-Ludwigs-University in Freiburg, Germany [104]. The signals are digitised and sent to the DAQ (see Sec. 3.1.7), where each signal is represented by its time stamps, and the amplitude and integral of the pulse. The details of the particle reconstruction by the TOF method and calibrations of the recoil detector are discussed in Section 4.7.2.
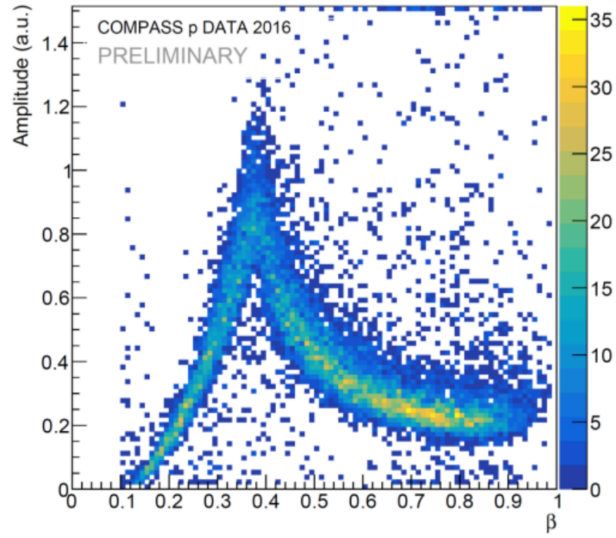
Figure 3.5: Signal amplitudes correspond to an energy deposit in the scintillator elements of ring B in dependence of the particle velocity β. Figure taken from Ref. [165].

---

[2]Generic Advanced Numerical Device for Analog and Logic Functions (GANDALF)
[3]Field-Programmable Gate Array (FPGA)

3.1.5 | The Spectrometer

An overview of the spectrometer setup COMPASS used for the DVCS measurement in 2016/17 is shown in Figure 3.6. The spectrometer, which is located behind the target area is designed to measure the final state particles produced in scattering events on a fixed target. To provide a large angle acceptance with a suitable resolution the spectrometer has two stages, namely Large Angle Spectrometer (LAS) and Small Angle Spectrometer (SAS). The LAS is the first stage of the spectrometer and covers scattering angles up to ± 180 mrad. It is directly followed by the SAS dedicated to detect particles with scattering angles below ± 30 mrad. The angular acceptance is given by the spectrometer magnets (SMs) (SM1 and SM2) in each stage, used to determine the momenta and the charge of particles. Each stage also includes different detectors for particle tracking, a muon filter system to identify muons and calorimeters (electromagnetic and hadron) for measuring particle energies. Specific for the first stage is a RICH-detector[4] for separating pions, kaons and protons. The particle identification provided by the RICH does not contribute to the DVCS measurement, but is mandatory when studying general DIS. The detector systems relevant for the DVCS measurement are presented in the next sections.

The detector positions and orientations of the detector planes are given in the main spectrometer reference system (MRS). This system is a right-handed cartesian frame where the Z-axis corresponds to the downstream facing beam axis. The X and Y directions are the horizontal and vertical directions. Before the spectrometer magnets the (0,0) in the X-Y-plane marks the center of the ideal beam axis. In earlier measurements the Z=0 position marked the center of the target, but as the target position changes depending on experimental requirements, it was kept as a historic reference point.

---

[4]Ring Imaging CHerenkov detector
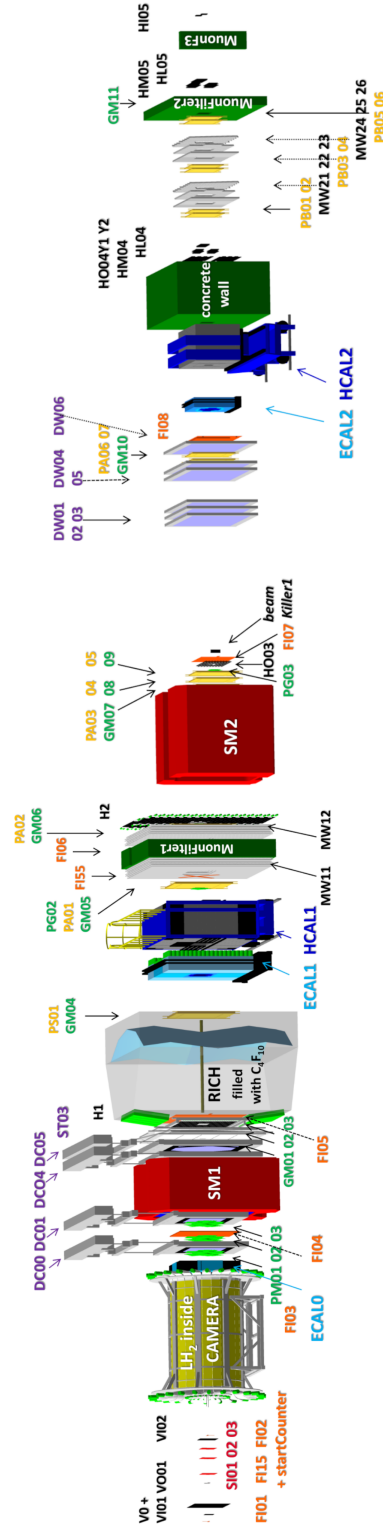
Figure 3.6: Illustration of the COMPASS experimental setup used for the DVCS measurement in 2016/17.

3.1.5.1 | Detectors for particle tracking

When performing precision measurements of scattering events it is mandatory to have high resolution detectors, which allow to track the propagation of charged particles through the spectrometer. Various types of those detectors are used in COMPASS. Their sizes and detection principles are chosen according to their area of application with respect to the beam. This distance defines the requirement on rate stability and space and time resolutions.

For reconstructing the particle trajectory one needs the two dimensional information where the particle traversed the detector planes. This information can either be obtained using segmented detectors (pixel detectors) or by using multiple consecutive detector planes each measuring one coordinate. In the latter case at least two detector planes with perpendicular orientations are needed. Here, the resolution can be increased by using additional detector planes, which are tilted with respect to the previous ones. According to the MRS detector planes with vertical or horizontal orientation are denoted by X and Y, while U and V label a clock-wise or anti-clockwise rotation.

The detectors used in COMPASS are classified according to their covered areas. In the area close to the beam or directly in the beam the so called very small area tracker (VSAT) and small area tracker (SAT) are used. Those include scintillating fibre detectors (SCIFIs), silicon strip detectors (SIs), Pixel-Gas Electron Multiplier detectors (GEMs), Pixel-Micro-Mesh Gaseous Structure detectors (MMs), GEMs and MMs. In a further distance from the beam axis the requirements on spatial and time resolutions are not so restrictive, which allows it to employ large area trackers (LATs). This class comprises Multi Wire Proportional Chambers (MWPCs), Drift Chambers (DCs), Straw[5] detectors and drift tube detectors.

An overview of the detectors, their covered areas and their spatial and time resolutions (δ_X and δ_t) is given in Table 3.1. For more details on the detectors see Reference [5].

class	detector type	covered area$/cm^2$	$\delta_X/\mu m$	δ_t/ns
VSAT	SCIFI	3.9^2 - 12.3^2	130-210	0.4
	SI	5×7	8 - 11	2.5
	Pixel-GEM	10×10	95	9.9
	Pixel-MM	5×5	90	9
SAT	GEM	31×31	70	12
	MM	40×40	90	9
LAT	MWPC	$178 \times 90\text{-}120$	1600	
	DC	$180\text{-}500 \times 127\text{-}250$	190-500	
	Straw	323×280	190	
	drift tubes	$473\text{-}447 \times 202\text{-}405$	600-3000	

Table 3.1: Overview of the detector types, covered areas, spatial and timing resolutions.

3.1.5.2 | Muon identification

The muons are identified by their relative radiation lengths (X/X_0) traversed in the materials of the spectrometer setup. Most of the radiation length is given by the absorbers (muon filter) placed in each

---

[5]due to the resemblance of the Kapton tubes to straws

spectrometer stage. These absorbers either consist of concrete or iron and are preceded and followed by tracker stations, which are called muon walls (MWs). This setup allows to identify the muons by requiring particle tracks, which traversed an absorber. Other charged particles are absorbed.

The first MW (MWA) is located at the downstream end of the LAS and consists of an iron absorber (60 cm thick) and two stations of drift tubes. Both stations comprise multiple detector layers of different orientations. The stations have an active area of about $4.8{\times}4.1\,\mathrm{m}^2$ and a central hole of $1.4{\times}0.9\,\mathrm{m}^2$. The dimensions of the central hole, which is also present in the absorber, are chosen according to the acceptance of SM2. The second MW (MWB) is located at the downstream end of the SAS and consists of a 2.4 m thick concrete wall followed by two stations of drift tubes with an active area of about $4.5{\times}2.0\,\mathrm{m}^2$ each. The tracking in front of the absorber is done by the trackers located in the SAS. For more details on the MWs see Reference [5].

3.1.5.3 | The trigger

During the data taking several different trigger systems are used. While the muon trigger has an direct impact on the physic events taken, other systems like the calorimeter trigger are used for e.g. for determining the efficiencies of the muon trigger. In principle all systems, besides the Veto system (see later in this section), provide a trigger signal, which tells the DAQ to record a certain event. The purpose of the Veto system is to suppress those trigger signals, which are produced by a halo muon.

In the following the details of the muon trigger, the Veto and the calorimeter trigger, including their working principles are discussed. Further details on the COMPASS muon trigger can be found in References [5, 32].

The muon trigger   is build of different independent subsystems, which cover distinct parts of the spectrometer acceptance (see Fig. 3.7). The systems used in 2016/17 are called Middle Trigger (MT), Ladder Trigger (LT), Outer Trigger (OT) and Large Angle Spectrometer Trigger (LAST).

Each subsystem consists of at least two hodoscopes. These perform a coincidence measurement of the
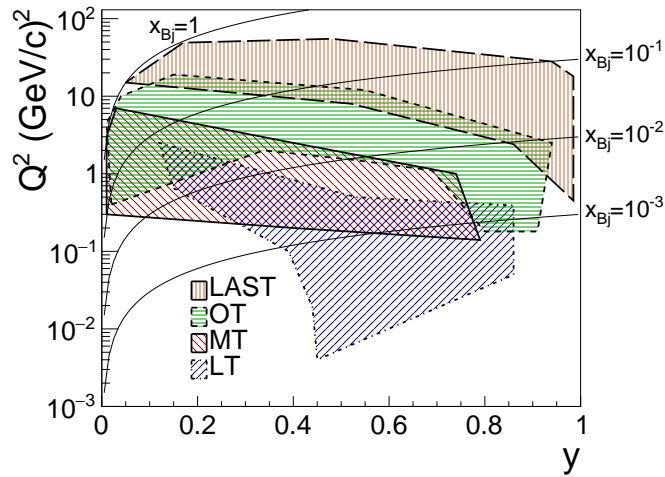
Figure 3.7: Kinematic coverage of the trigger systems as a function of Q^2 and y using a muon beam with a nominal momentum of 160 Gev/c.

scattered muons to generate a trigger signal. To exclusively trigger on the muons, the first hodoscope is

always placed upstream of an absorber and the second one downstream (see Sec. 3.1.5.2).
The hodoscopes are build of rectangular scintillator elements, that are either horizontal or vertical oriented. Each scintillator element is read out on both sides by a PMT. The orientation of the scintillator elements is chosen according to the trigger methods, shown in Figure 3.8.

(a) Target-pointing method.   (b) Energy-loss method.
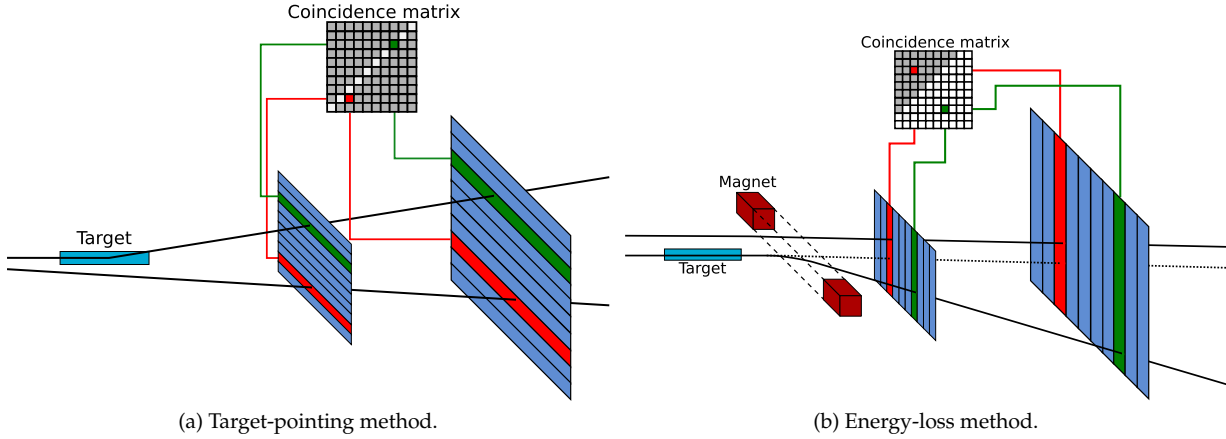
Figure 3.8: Schematics of the trigger methods. Figures taken from Ref. [168].

The first method, called Target-pointing (see Fig. 3.8a), measures the vertical angle of muons being scattered in the target region. The coincidence measurement of the two hodoscopes is represented as a diagonal matrix. For muons with very small scattering angles and therefore events with small Q^2 the Target-pointing is not feasible. In this case the deflection in horizontal direction (X-axis) of the muons, when passing the magnetic field of one of spectrometer magnets, is used. Muons interacting with the target loose a fraction of their energies, hence being more deflected than non interacting muons. This deflection is measured by hodoscopes with vertical oriented elements (see Fig. 3.8b). The corresponding coincidence measurements between elements of the hodoscope pairs, belonging to a subsystem, are represented as a triangular matrix. For some trigger systems like e.g. the outer trigger, the second hodoscope is further subdivided into two separate hodoscope planes. Each plane covers half of the acceptance of the first hodoscope. In case of the middle trigger the system is subdivided into hodoscope pairs, which are placed above or below the beam (up and down). An overview of all trigger subsystems is given in Table 3.2.

The electronics used for all trigger subsystems are similar. As a first step the signals of the two PMTs, belonging to one scintillator element, are discriminated by Constant-Fraction discriminators (CFDs). The time average of both signals is determined by a meantimer, creating a single time stamp for each element. After that, the meantimer signals of the elements, which perform a coincidence measurement are provided to the coincidence matrix. The matrix is either implemented as 6U VME[6] boards attached with a custom CMOS[7] (Matrix) chip. Or, as in case of the LAST system, the meantimer and the matrix are implemented by a GANDALF module. The signals provided by the coincidence matrices are the trigger signals sent to the DAQ.

---

[6]Versacard Multibus Eurocard (VME)
[7]Complementary Metal-Oxide-Semiconductor (CMOS)

Trigger system	Hodoscopes	Orientation	Coincidence
Middle	HM04Y1 down	horizontal	HM05Y1 down
	HM04Y1 up	horizontal	HM05Y1 up
	HM05Y1 down	horizontal	HM04Y1 down
	HM05Y1 up	horizontal	HM04Y1 up
Ladder	HL04X1	vertical	HL05X1
	HL05X1	vertical	HL04X1
Outer	HO03Y1	horizontal	HO04Y1, HO04Y2
	HO04Y1	horizontal	HO03Y1
	HO04Y2	horizontal	HO03Y1
LAS	HG01Y1	horizontal	HG02Y1, HG02Y2
	HG02Y1	horizontal	HG01Y1
	HG02Y2	horizontal	HG01Y1

Table 3.2: Overview of the Trigger subsystems.

The Veto system is used to reject trigger signals, which are caused by accidental correlations with halo muons. To detect those halo muons several hodoscopes are placed upstream of the target. These hodoscopes cover the whole region of the outer and the inner halo but leave out the central region of the beam. The veto system is divided in subsystems according to their position upstream of the target. For 2016/17 the subsystems used, starting from the most upstream one, are Veto beamline (V_{BL}), Veto Inner 1 (V_{Inner1}) and Veto Inner 2 (V_{Inner2}). A schematics of the hodoscope positions is shown in Figure 3.9 and a detailed summary of the hodoscopes geometries can be found in Reference [145]. Each hit registered by one of the hodoscopes generates a signal, which is then used to veto all trigger systems.
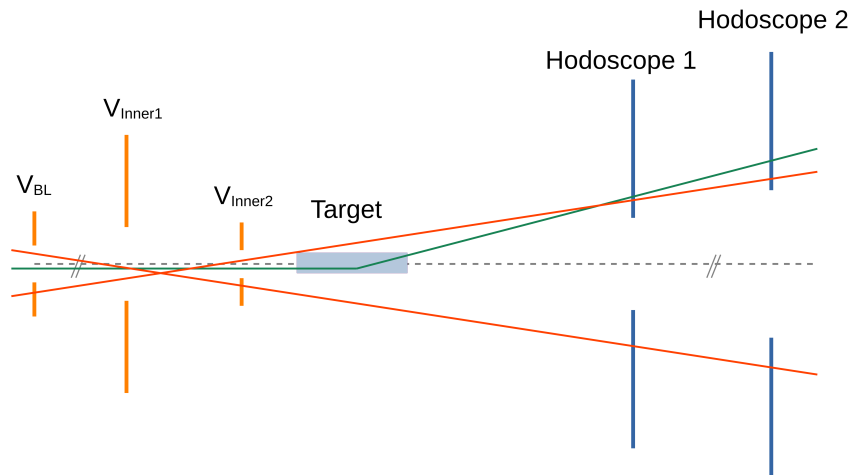
Figure 3.9: Schematic of the Veto system. The trigger signals produced by incoming muons passing one of the veto hodoscopes are rejected by the veto (red).

The calorimeter trigger provides a trigger signal, due to hadron showers produced in a muon scattering event. Hence, the signal is correlated to the scattered muons, which allows to verify signals provided by the muon trigger. As both trigger systems nearly cover the same acceptance, the calorimeter trigger provides a data sample, which can be used to determine the performance of the muon trigger system. The details on this analysis are given in Section 4.4.2.

The calorimeter trigger uses the two hadron calorimeters (HCALs), each located in one of the spectrometer stages (HCAL1 and HCAL2 in Fig. 3.6). Each HCAL is build of modules consisting of alternating layers of iron and scintillator. If a hadron hits one of the modules, it interacts with the iron producing mainly a shower of charged hadrons. Those hadrons deposit their energies into the scintillator layers, generating light, which is detected by PMTs. The combined PMT signals are correlated to the energy deposit, which produces a trigger signal as soon as a threshold is exceeded.

A detailed description of the HCALs can be found in Reference [5] and further details on the implementation of the calorimeter trigger are in Reference [172].

3.1.5.4 | The electromagnetic calorimeters

The real photons are detected by electromagnetic calorimeters (ECALs). For the 2016/17 DVCS measurement the regular COMPASS setup, which includes one ECAL in each stage (ECAL1 and ECAL2 see Fig. 3.6), was extended by an additional ECAL (ECAL0). It was located directly after the proton recoil detector. Each ECAL consists of several modules. Those are either made of lead glass or alternating layers of lead and scintillator material (Shashlyk-modules). If a photon traverses the lead glass, it produces showers of electron-positron pairs. Those pairs however produce Cherenkov light. The intensity of the Cherenkov light is measured by an PMT attached to the crystal. By combining the PMT signals of all modules exposed to the incoming photon, the corresponding integral of the combined signals is directly proportional to its energy. In the Shashlyk-modules free electrons and electron-positron showers are produced by the photon interacting with the lead. Afterwards the produced particles traverse the scintillator layer, generating light. This process repeats in each layer pair until their energy is fully absorbed. The light is guided to a PMT connected to the corresponding module, producing a signal proportional to its intensity. The combined PMT signals are again proportional to the energy of the incoming photon. As the photon gets sampled by each consecutive lead-scintillator layer, these kind of calorimeters are called sampling calorimeters.

The calorimeters used at COMPASS are either pure sampling calorimeters (ECAL0 see Fig. 3.10a) or a combination of lead glass crystals and Shashlyk-modules (ECAL1 and ECAL2, transverse size: 38.3×38.3 mm^2). As shown in Figure 3.10b and 3.10c. Due to their relative radiation hardness compared to the lead glass crystals, the Shashlyk-modules in ECAL1 and ECAL2 are used close to the muon beam in the central region of the calorimeters. The central Shashlyk-modules of ECAL1 are surrounded by lead glass modules, named 'GAMS' (transverse size: 38.3×38.3 mm^2). In the middle and outer part of ECAL1 modules called 'Mainz' respectively 'OLGA' are used. These are 4 respectively 16 times the size of a GAMS module. In ECAL2 two different kinds of GAMS are used. The inner part is made of radiation hardened modules 'RHGAMS' (by adding 0.2% cerium) and in the periphery of the ECAL the pure lead glass modules are used. The holes left in the ECALs are chosen according to the acceptance of the downstream part of the spectrometer, considering the bending by the SMs.

The dimensions and positions of the ECALs along the spectrometer are chosen to cover its total angular acceptance. Figure 3.11 shows the angular acceptance of ECAL0 and ECAL1 in the X-Z-plane of the spectrometer with respect to the position of the target cell and the proton recoil detector. The photons with the highest energies and therefore the smallest scattering angles (<0.04 rad) are covered by ECAL2. Photons with angles between 0.03 rad and 0.15 rad are detected by ECAL1 and those with higher scattering angles and therefore lowest energies by ECAL0. To guarantee a precise measurement of the photons a calibration is needed, which is discussed in Section 4.8.

(a)

(b)

(c)
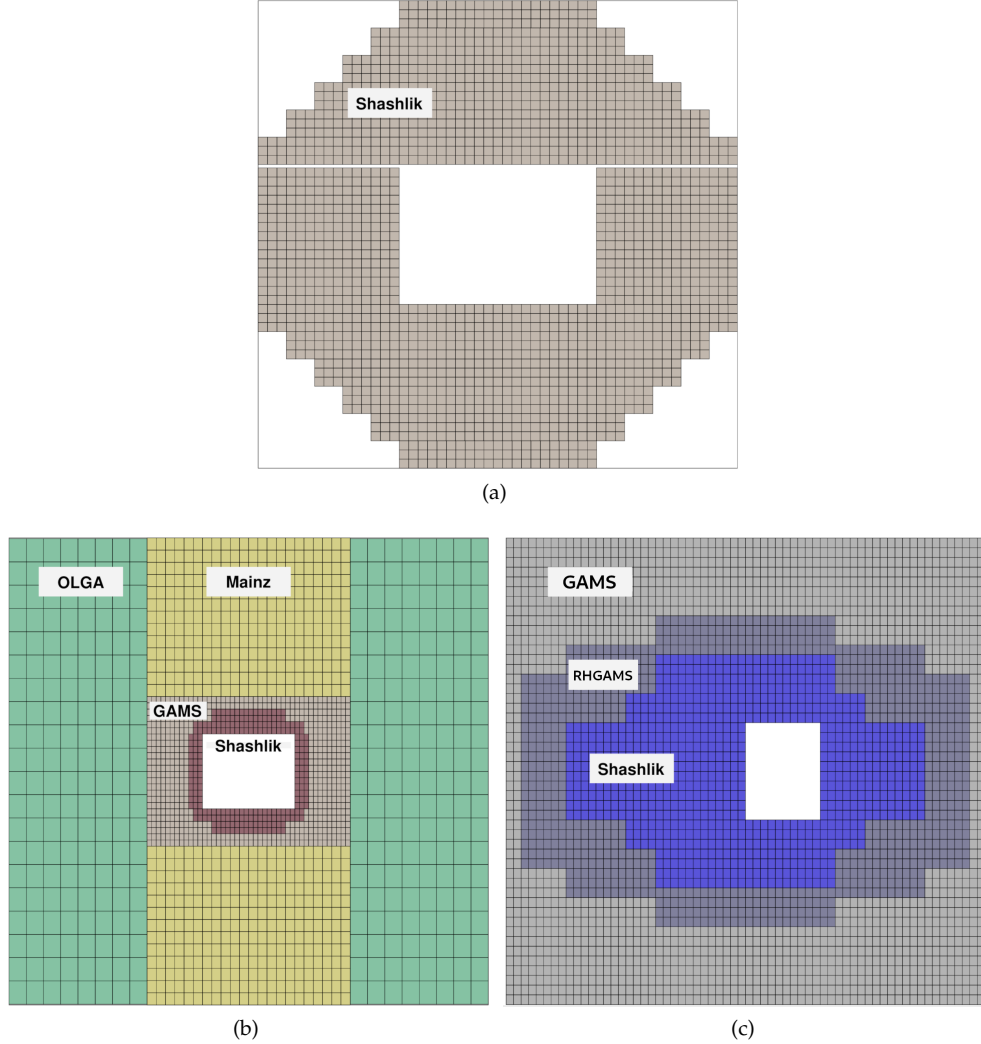
Figure 3.10: Schematic frontal view of the ECALs.
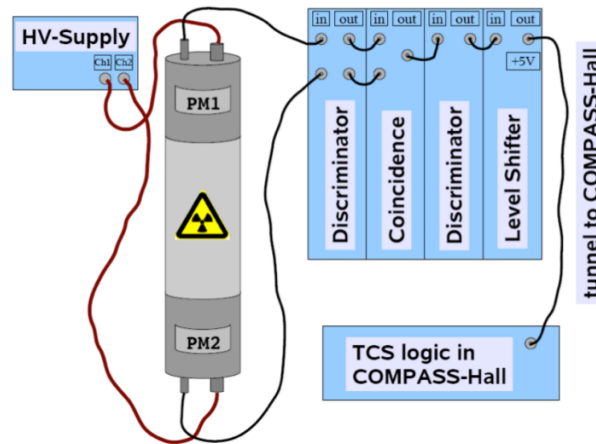(a) ECAL0 is made of Shashlyk-modules each covering an area of 38.3×38.3 mm². Its total size is 1020×1020 mm².
(b) ECAL1 has an overall size of 3970×2860 mm². The central area is build of Shashlyk-modules, surrounded by GAMS modules (38.3×38.3 mm²). In the middle and outer part the Mainz (75×75 mm²) respectively OLGA modules (143×143 mm²) are used.
(c) The cells of ECAL2 all have equal size (38.3×38.3 mm²). The used cells differ in their radiation hardness, decreasing from the center to the outer cells. The calorimeter has an overall size of 2440×1830 mm². The Figures are generated by the PHAST software [75].

Figure 3.11: Schematic view of the angular acceptance covered by ECAL0 and ECAL1 in the X-Z-plane of the spectrometer with respect to the position of the target cell and the position of ring A and ring B of the proton recoil detector. Figure taken from Ref. [165].
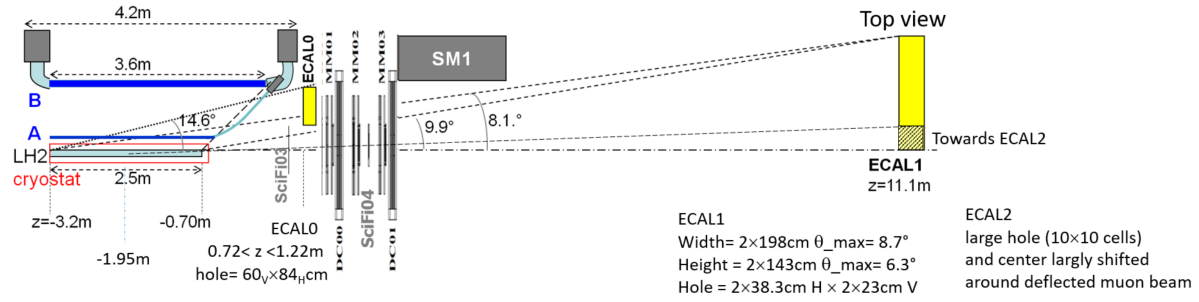
3.1.6 | The true random trigger

The true random trigger produces a randomized trigger signal, which is used to determine the incoming muon flux (see Sec. 4.3.1). Its setup is shown in Figure 3.12. To prevent the electronics having any cross talk with the electronics of the spectrometer, it is located in the basement of the COMPASS office building. The random signal is produced by measuring the β^+-decay of a ^{22}Na source. After the decay the positron annihilates with an electron, producing two photons propagating in opposite direction. Both photons are detected by two PMTs placed at opposite sides of the radioactive source. The signals from the PMTs are discriminated and provided to a coincidence unit. If both signals are measured simultaneously, a trigger signal is generated, which is then send to the DAQ located in the COMPASS experimental hall.

Figure 3.12: Schematic view of the random trigger including the radioactive source, the PMTs and the electronics to process and generate the trigger signal. Figure taken from Ref. [67].

3.1.7 | Data acquisition

The readout of all detector channels is performed by the Data Acquisition (DAQ). The modular design of the COMPASS DAQ is shown in Figure 3.13. It uses different layers, each assigned with a specific task of the signal processing. They are outlined in the following.

The first layer comprises the so called detector Front-End (FE) electronics. Here, the detector signals are pre-amplified, discriminated and finally digitised and buffered by Time-Digital-Converters (TDCs) or Analog-Digital-Converters (ADCs). To minimize the distortion of the detector signals, when propagating through the cables, the FE electronics are located in the experimental area next to the corresponding detectors.

In the next layer, digitization and detector readouts are synchronized to the trigger by the Trigger Control System (TCS). When a trigger signal arrives, the buffered data is sent via fast link to readout driver modules named CATCH[8] and GeSiCA[9]. These modules combine the data of the connected FEs and also distribute the trigger signal to initialize them. For high occupancy detectors the signal is directly transmitted to readout buffers, while for low occupancy detectors the signals are first combined by multiplexer modules (SMUX[10] and MUX-Tiger[11]) and then transmitted to the readout buffer. The link between the readout driver modules and the readout buffer is done by optical S-LINK (optical fibre).

The readout buffers are computers attached with spill buffer cards. From those spill buffer computers the data is distributed via Gigabit LAN[12] to event building computers. Here, one of the event builders receives the complete detector data belonging to an event and sorts it into one data package. The package is transferred to the CERN Tape Archive (CTA) and stored on tape. These can be accessed for further processing.

For more details on the detector readout electronics and the DAQ see Reference [5].

---

[8]COMPASS Accumulate, Transfer and Control Hardware (CATCH)

[9]GEM and Silicon Control and Acquisition (GeSiCA)

[10]S-Link Multiplexer (SMUX)

[11]Trigger Implementation for GANDALF Electronic Readout (MUX-Tiger)

[12]Local Area Network (LAN)
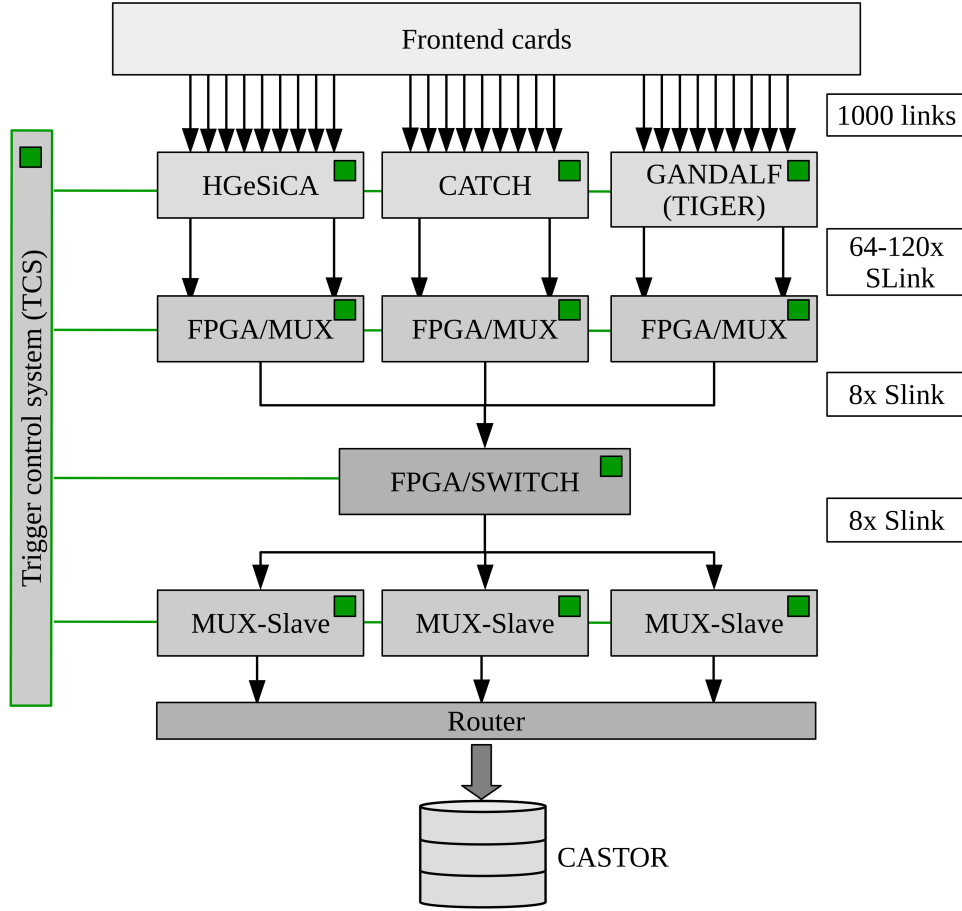
Figure 3.13: Simplified scheme of the different layers in the COMPASS data acquisition. Figure taken from Ref. [151].

3.1.8 | Data reconstruction and selection

The stored raw data contains the information of all the detector hits, their timings and ADC information of a certain event. When analysing those events, this information has to be processed to reconstruct the particle tracks and link them with parameters like e.g. momentum, charge and energy. At COMPASS this process is performed by the COMPASS Reconstruction Algorithm (CORAL).

The first step is called decoding. Here, the information of detector channels, which registered a hit, is extracted. In the next step, called clustering, the close by hits of all detector channels are grouped together forming clusters. After that the track building starts by identifying track segments in different zones of the spectrometer. The tracks are expected to follow a straight line. In COMPASS, the first zone comprises everything located upstream of the target. The next zones cover the regions from the target to SM1, from SM1 to SM2, from SM2 to the second MW and from there to the end of the spectrometer setup. In this zones all possible track segments are formed by first reconstructing the tracks in a one-dimensional projections (X or Y) along the Z-axis and combining those projections to space track segments. To connect the track segments of neighbouring zones a fit is performed, called bridging. The combined track segments are ordered using a quality function, which is based on the χ^2 and the number

of associated hits to the track. The most probable track is chosen by the combinations of the best quality function, making sure that track segments can only be assigned to a single track. To finalize the track fitting, a method based on the *Kalman fit* [71, 169] is used to give the best estimation of track parameters, like its positions, slopes and momentum. The method also considers the impact of the magnetic fields and the materials traversed by the tracks. The information on the materials, detector position and magnetic fields is collected in separate files used during reconstruction. To identify vertices, first all tracks are scanned to identify those of the muons, using the requirements on the muon identification as described in Section 3.1.5.2. By the identified muon tracks, the vertex of the primary interaction is given. To identify all tracks linked to the vertex, the point of closest approach is calculated and tracks, which are to far away, are being rejected. This only accounts for tracks, that are not identified as muon tracks. The vertex position is determined by performing an inverse Kalman filter algorithm. Within this method the relative χ^2 contribution of the track to the vertex fit is determined and if it exceeds a threshold, the track is removed from the vertex. If multiple primary vertices within an event are identified, the vertex with the best χ^2 is marked as *best primary vertex*. The result of the reconstruction is stored as ROOT[13] [146] trees in so called mDST[14]-files. A more detailed summary of the reconstruction procedure can be found in Reference [5].

After the reconstruction the desired physics events can be selected. For this a COMPASS specific, C++ based software called PHAST[15] is used. This software offers a large amount of classes and functions to identify the physics events and calculate the reconstructed kinematics. The selected information can be saved as ROOT trees or histograms for further analysis.

3.2 | Monte-Carlo Simulation

Monte-Carlo (MC) simulations are an indispensable tool to physics analysis. In the presented analysis of the DVCS, MC samples are used for calculating the acceptance of the COMPASS spectrometer (see Ch. 6) and determining the Bethe-Heitler contribution and the π^0-contamination, when calculating the cross section.
The simulation procedure can be split into two parts. The first part is the simulation of the physics process. For this specific event generators are used. The required MC data samples and the used event generators are described in Sections 3.2.1 and 3.2.2. In the second step the final state particles of the generated events are propagated through a simulation of the spectrometer setup. In this step all interactions with the sensitive detector materials and other materials are considered. Hence, the energy loss of the particles and thereby the associated detector responses are simulated. A summary of this procedure and the used software is given in Section 3.2.3.
A detailed summary of the Monte-Carlo chain and the COMPASS specific changes are given in Reference [151, 161].

3.2.1 | Monte-Carlo data samples

In total, three different Monte-Carlo samples are used to address and estimate all the contributions and corrections necessary for extracting the DVCS cross section.
The sample used for calculation the acceptance and estimating the Bethe-Heitler contribution includes exclusive photon events, generated by the HEPGEN[16] event generator. A brief summary is given in Section 3.2.2.1.

---

[13]ROOT refers to the "roots" for end-users applications
[14]mini Data Summary Tape
[15]Physics Analysis Software Tools (PHAST)
[16]Hard Exclusive Production Generator (HEPGEN)

For estimating the π^0-background, two distinct Monte-Carlo samples are used. One sample for the hard exclusive produced π^0 and the second sample for inclusive produced π^0 in DIS. Further details on the π^0-background contamination and the method used for estimating its contribution to the exclusive photon sample are given in Section 5.3.2. The exclusive π^0 production is again generated by HEPGEN. For simulating π^0 produced in DIS the LEPTO 6.1 generator (see Sec. 3.2.2.2) is used. Note that the LEPTO sample also includes events with an exclusive π^0 topology. These are removed by using the provided JETSET information, which is a MC generator for simulating the final state hadronization and is included in LEPTO. A summary of the Monte-Carlo samples, the used generators and their applications are given in Table 3.3.

Sample	Generator	Application
Exclusive photon production	HEPGEN	Calculation of the spectrometer acceptance and estimation of the Bethe-Heitler contribution.
Hard exclusive π^0 production	HEPGEN	Estimation of the background contamination by hard exclusive π^0.
π^0 production in DIS	LEPTO	Estimation of the background contamination by π^0 produced in DIS.

Table 3.3: Summary of the Monte-Carlo sample used for the DVCS cross section calculation.

3.2.2 | Monte-Carlo event generators

The generators simulate the final states of a defined scattering process. The kinematics of the beam particle are not simulated but determined by an analysis using reconstructed beam particles recorded by the true random trigger. This analysis also considers the different halo components to ensure that the beam particles used in the simulation reproduce the exact beam conditions during the measurement.

3.2.2.1 | HEPGEN

HEPGEN is dedicated to simulate hard exclusive lepton scattering processes in the kinematic domain of COMPASS. The current implementation includes processes of exclusive single photon production (DVCS and BH) as well as multiple channels for *Hard Exclusive Meson Production* (HEMP). For the DVCS analysis only the exclusive photon and the exclusive π^0 production are relevant, only those are discussed in the following. For further details see Reference [156].

The DVCS event generation is based on scattering amplitudes following the model of Frankfurt, Freund and Strikman (FFS) [65, 66]. This model only considers the contribution by the GPD *H*, which is dominant in the spin-independent DVCS process at COMPASS kinematics. More details on extensions and modifications of the generator, making it suitable for the COMPASS kinematic domain, are given in Reference [155, 156].

The description of the Bethe-Heitler process uses the proton elastic form factors. A calculation considering the exact lepton mass in the lepton propagators was derived by P. A. M. Guichon [93]. The integration of the interference between the DVCS and Bethe-Heitler amplitudes is done using the same formalism.

The generator produces events with flat kinematic distributions but assigns a set of weights to each event, which result from the predictions of the corresponding models. By weighting each event, the

model predictions are taken into account and the resulting kinematic distributions correspond to the ones expected for the physic process or processes in case a sum of weights is used. The weights for the pure DVCS (ω_{DVCS}), the pure Bethe-Heitler (ω_{BH}) and the interference (ω_{INT}) contributions are stored with the general event information. The Bethe-Heitler weights, according to the calculation of P. A. M. Guichon (ω_{PAM}), are determined during the event selection using an external function.

For simulating the hard exclusive π^0 production a model of Goloskokov and Kroll is used. A detailed description of the model and its parameters is given in Reference [86]. The corresponding event weights (ω_{π^0}) are also stored with the general event information.

3.2.2.2 | LEPTO

The LEPTO 6.1 generator provides a simulation of deep inelastic lepton-nucleon scattering. In contrast to the HEPGEN generator, the number of generated events is directly given by the corresponding DIS cross sections on parton level. Here, the PDFs and the electroweak contributions are taken into account. The hadronization to final state particles is done by JETSET, which is based on the Lund string model [20]. A detailed description of the generator and its parameters is given in Reference [107].

3.2.3 | Simulation of the spectrometer

After generating the final state particles, the next step is to simulate their propagation through the spectrometer setup. This simulation is done by the COMPASS specific TGEANT[17] software, which is based on the GEANT4[18] software package [11].

Within the simulation each particle passing the spectrometer and the magnetic fields is tracked. Thereby all relevant interactions with the sensitive detector materials and detector frame materials are considered. The result is a detailed simulation of the particles energy loss and energy deposits in the materials in each step of the propagation. Here, also multiple scattering and other particle interactions are taken into account. The information on the energy deposits into the sensitive volume of the detectors is used to simulate the corresponding detector responses (hits) and time stamps according to the detector resolutions and the particle trajectories. This digitization phase replaces the decoding phase as done for real data (see Sec. 3.1.8). After this phase the reconstruction for real data and simulated data follows the same pattern.

To obtain the reconstructed Monte-Carlo samples, the same selection as for data is applied. In case of simulated data it is also possible to access the numbers and kinematics of generated events, which are used for the determination of the spectrometer acceptance.

A detailed description of the TGEANT software and some of the improvements and adjustments for simulating the 2016/17 setup are summarized in Reference [151, 161].

---

[17]Total Geometry and Tracking (TGEANT)
[18]Geometry and Tracking (GEANT)

4

The 2016 data

The 2016 data taking was set between June 15th and November 13th. It is divided into 11 periods, which are further split into several sub-periods. Within the periods the detectors were not modified to ensure an equal performance of the spectrometer. In each period approximately the same amount of data for both beam charges was taken (μ^- and μ^+). The beam charges were switched multiple times in each period, which marks the corresponding sub-periods. Every time the beam charge was changed, the magnetic fields of the spectrometer magnets were changed accordingly, thus deflecting the beams always in the same direction. In contrast to the DVCS pilot run in 2012, the μ^- and μ^+ data was taken with comparable beam intensities. As remarked in Section 3.1.1, the beam intensity can be adjusted by altering the length of the beryllium target (T6). For the μ^- beam the target length was 500 mm, while for the μ^+ beam it was reduced to 100 mm.

For the analysis presented in this thesis the data taken from P04 until P09 are used. In these periods the beam conditions were mostly stable and the spectrometer had comparable performances. The previous periods (P00-P03) are not used for the time being due to frequently appearing beam and spectrometer instabilities. For the future a detailed review of these periods is planned to identify those parts, which can be added to the used data sample. In P10 the beam conditions changed, as it was decided to increase the intensity of the μ^+ beam to its full potential, which is about twice the intensity of the μ^- beam. This was done to obtain a small data sample with similar beam conditions as used in 2012. In the last period the vast amount of data was taken using an electron beam. It was later used to perform the calibration of the ECALs (see Sec. 4.8). A summary of the 2016 data taking is given in Table 4.1. The periods used in the present analysis are marked in green.

The following Sections summarize the studies and analysis performed to review the data quality and to extract inputs to the calculation of the DVCS cross section and the Monte-Carlo simulations. A study of the beam quality and its stability is presented in Section 4.1. Together with the information on the target position (see Sec. 4.2), its results are used to determine the effective muon flux and hence to calculate the luminosity. Both are discussed in Section 4.3. Studies on the hodoscope and trigger performances are presented in Section 4.4. The extracted efficiencies are used as inputs to the Monte-Carlo simulations. To verify the quality of data, taken with the μ^- and μ^+ beams, a detailed comparison is shown in Section 4.5. Comparisons of data distributions to distributions obtained from simulations are shown in Section 4.6. These comparisons are used to improve the data reconstruction and the Monte-Carlo simulations. The Sections 4.7 and 4.8 summarize the work, which was done on calibrating the ECALs and the proton recoil detector and extracting its efficiencies.

Period	date	Sub-periods
P00	June 15th - June 22th	$1 \times \mu^+$ and $3 \times \mu^-$
P01	June 22th - July 6th	$3 \times \mu^+$ and $3 \times \mu^-$
P02	July 6th - July 18th	$3 \times \mu^+$ and $3 \times \mu^-$
P03	July 21th - August 3rd	$2 \times \mu^+$ and $2 \times \mu^-$
P04	August 3rd - August 19th	$4 \times \mu^+$ and $3 \times \mu^-$
P05	August 19th - August 31st	$2 \times \mu^+$ and $3 \times \mu^-$
P06	August 31st - November 12th	$2 \times \mu^+$ and $2 \times \mu^-$
P07	November 17th - November 28th	$2 \times \mu^+$ and $3 \times \mu^-$
P08	November 28th - October 11th	$3 \times \mu^+$ and $3 \times \mu^-$
P09	October 13th - October 26th	$3 \times \mu^+$ and $3 \times \mu^-$
P10	October 26th - November 8th	$2 \times \mu^+$ and $4 \times \mu^-$
P11	November 9th - November 13th	$1 \times \mu^+$ and e^- for ECAL calibration

Table 4.1: Overview of the data taking in 2016. The sub-periods are given by the number of changes of the beam charge within each period.

4.1 | Analysis of the beam stability

As specified in Section 3.1.1 the beam arrives in packages called spills. Those spills follow an intensity profile, which is shown in Figure 4.1 as function of the time in spill (TiS). The beam intensity rapidly rises until it reaches its maximum. From then the intensity remains constant for about 5 seconds before it rapidly drops to zero. The phase of constant intensity is called *flat top*. For a precise determination of the muon flux only the flat top of the spills or at least the regions with rather comparable intensities should be used. A summary of an analysis to identify those regions is presented in the following. For further details see Reference [78].

4.1.1 | Obtaining the spill intensity profiles and identifying the intensity range

The beam intensity profile for each spill can be reconstructed from the recorded data. This is done using the output of a scaler, which is connected to one plane of the SCIFI02 detector. This detector is located upstream next to the target and covers the whole diameter of the beam. The connected scaler therefore counts each muon traversing the detector during a spill. By dividing the spills into multiple consecutive intervals and calculating the corresponding scaler rates within, a beam intensity profile is obtained. The spill duration is given by the slow extraction of the SPS, which was 5.5 seconds in 2016. To identify the flat top region of each spill individually, a first step is to identify an intensity range for each period and each beam charge. An example for the integrated beam intensity profiles for period 09 separately for μ^- and μ^+ is shown in Figure 4.2a and 4.2b. In both distributions a clear intensity band can be seen, which indicates the range of approximately constant intensities. The limits on this range (I_{min} and I_{max}) are chosen to be about $\pm 15\%$ of the average intensities and are indicated by the horizontal lines.
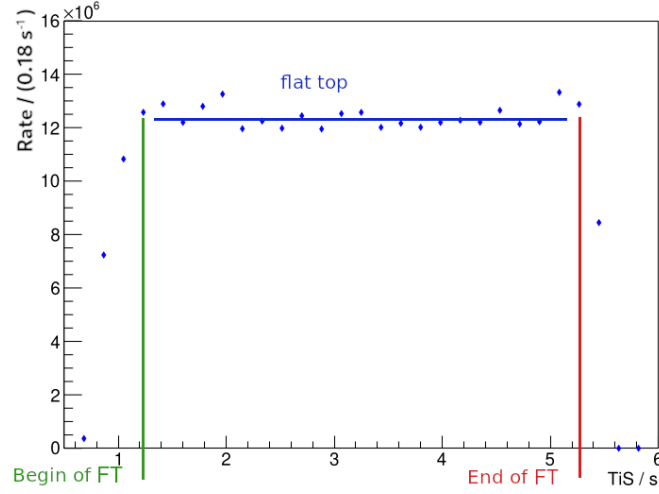
Figure 4.1: Example of a spill profile showing the flat top region. The green and blue vertical line is marking the begin and end of the flat top (FT).
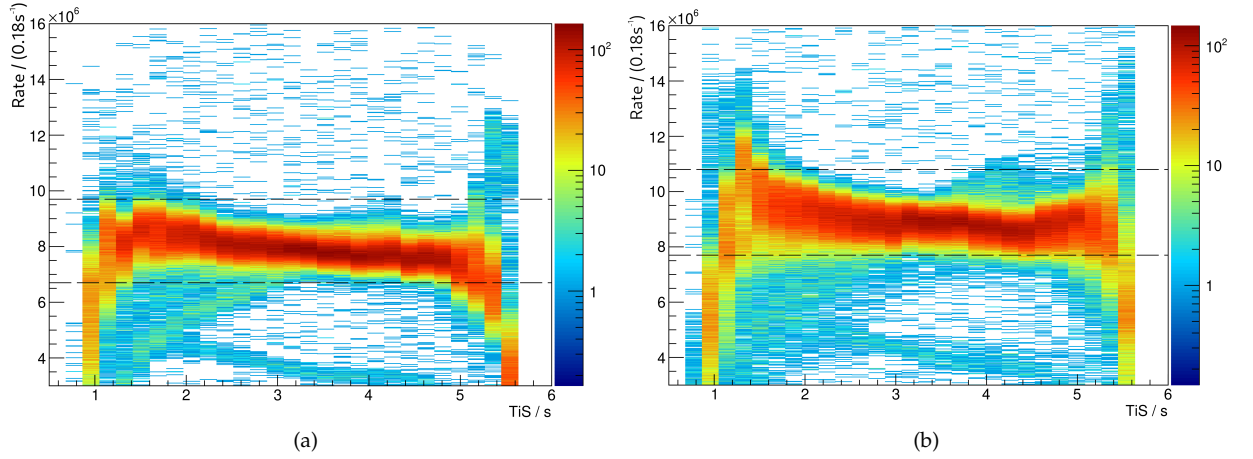
Figure 4.2: Distribution of the sum of all spill profile for the μ^- (a) and μ^+ (b) part of P09. The horizontal lines are indicating the lower and the upper limits of the intensity (I_{min} and I_{max}), which are used when identifying the flat top regions.

4.1.2 | Detailed analysis of each spill

The previously introduced limits are used to identify the flat top region for each spill individually. It is to mention that the intensity profiles within each spill can show some large variations (see Fig. 4.3a and 4.3b). These have to be taken into account when analysing the flat top regions, as they cause a shift of their begin and/or end points.

(a)

(b)
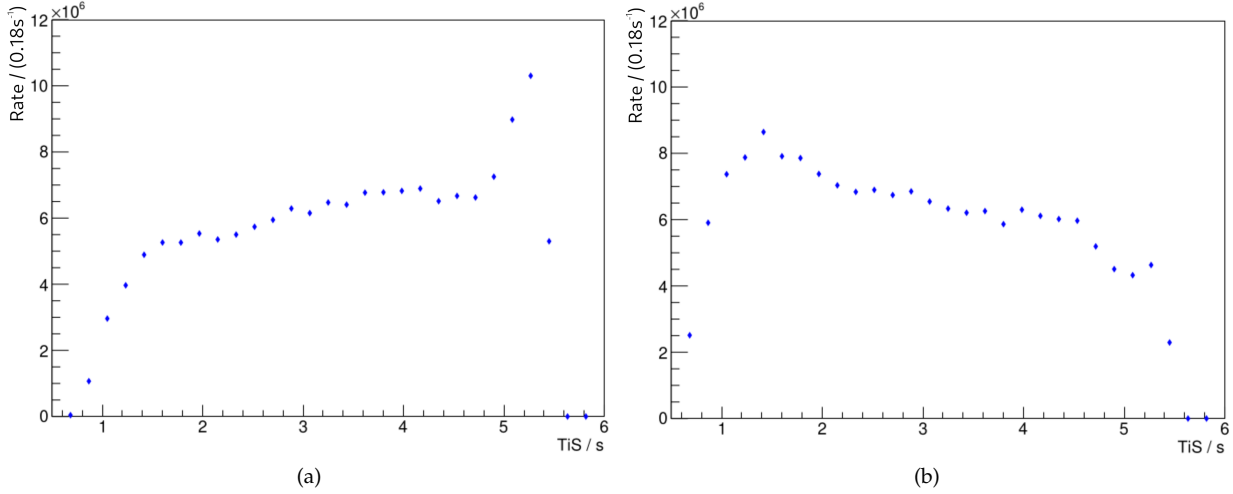
Figure 4.3: Spill with an intensity spike at the end (a) and spill with continuously decreasing intensity (b).

These conditions lead to a set of requirements for searching the begin and the end of the flat top, that are more sophisticated than just requiring an intensity, which is inside the limits. Rather it must be reviewed that in every time interval the corresponding intensity is comparable to an average intensity, within a certain range. This is done by an iterative procedure. The start of the flat top is first set to the time in spill when the intensity first exceeds I_{min}. From this point the average intensity is recalculated for each consecutive time interval. If at one point the intensity exceeds its current average by more than 20% or is outside the defined limits, the start of the flat top is delayed until an intensity is reached, which is again within the limits. From this point the calculation of the intensity average starts again. If the intensity has dropped below I_{min} and does not recover, only the part of the spill is used, where the requirement on the limits are full filled. With the start of the spill set, the stop of the flat top is set as soon as the intensity drops below I_{min}. In rare cases the scaler count in two consecutive intervals is not correctly determined, which leads to a strong fluctuations of the rate. An example is shown in Figure 4.4. The vertical and horizontal lines indicate the start, stop and length of the identified flat top. This behavior is not related to any fluctuations of the intensity but is caused by a short time issue in the read out of the scaler. As those fluctuations would cause the previously discussed iterative process to reset, they need to be identified. Therefore as soon as a large deviation of the beam intensity from the consecutive calculated average is spotted, the mean of the intensity in this time interval and its following interval is calculated. If this mean intensity fulfills the requirement above, the two time intervals are skipped and the iterative procedure continues afterwards. A typical result of this analysis for period 08 is shown in Table 4.2.
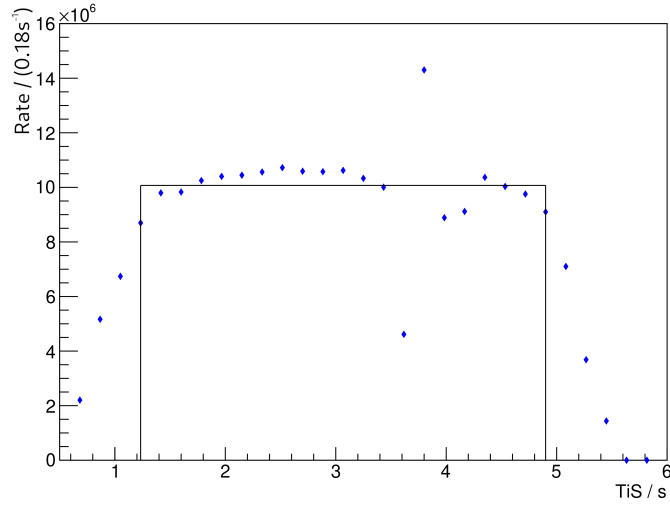
Figure 4.4: Example of a fluctuation in the rate due to an issue in the readout of the scaler count. The vertical and horizontal lines indicate the start, stop and length of the identified float top region.

The listed expressions correspond to the following conditions:

- Good spills: Start in T_{start} and stop in T_{stop},

- Bad start: Start after T_{start} but stop in T_{stop},

- Bad stop: Start in T_{start} but stop at beginning of T_{stop},

- Bad middle: Start in T_{start} but stop in T_{middle},

- Bad start and stop: Start after T_{start} and stop before T_{stop} ,

- Bad intensity: Intensity never exceeds I_{min},

- Empty spills: No spill profile.

Here T_{start} denotes the first quarter of the spill, T_{stop} the last quarter and T_{middle} the time in between, with respect to the duration of the slow extraction of the SPS (5.5 sec.).

	Num. spills	fraction / %
Good spill	37342	91.0
Bad start	550	1.34
Bad stop	881	2.14
Bad middle	221	0.54
Bad start and stop	44	0.11
Bad Int.	192	0.47
Empty spill	1869	4.55
Total	41099	-

Table 4.2: Summary of spill statistics of P08.

4.2 | Determination of the target position

A precise knowledge of the target position is essential when using an extended beam for e.g. a muon beam, because it has a direct impact on several occasions of the analysis. In the determination of the muon flux only those muons, which traversed the full length of the target, should contribute. Also the target volume specifies the location of the muon-proton scattering. Lastly, a precise description of the target in the Monte-Carlo is also mandatory for a proper simulation.

A method to identify the region of the liquid hydrogen contained inside the target cell was developed while analysing the 2012 data. The basic principle of this method are maintained but some modifications are applied to improve the identification of the target cell borders. The following Sections present the details of this method and conclude with the results on the target position and its implementation used in the data selections.

4.2.1 | Principle of the method

To identify the liquid hydrogen contained inside the cell, it is exploited that the Kapton® has a much higher density than the liquid hydrogen. Hence, a higher number of interactions with the muon beam in the Kapton® is expected. As can be seen in Figure 4.5, which shows a vertex distribution in the X-Y-plane[1] along the length of the target cell (Z-axis). These interaction vertices are selected by requiring an incoming and scattered muon and at least one additional outgoing charged track. Also only events with an sufficient four-momentum transfer are requested ($Q^2 \geq 0.2\,(\mathrm{GeV/c})^2$). These conditions ensure a good reconstruction of the vertex position (see Sec. 3.1.8) and therefore a good transversal resolution is obtained.

The target cell is clearly visible as rings in the periphery of the distribution. These multiple rings indicate that, especially in the vertical coordinate, the target cell is not perfectly straight aligned with the beam axis. In the liquid hydrogen and outside the cell the vertex distribution follows the Gaussian intensity profile of the muon beam convoluted with the corresponding interaction materials. Objective of the analysis is now to isolate the excess of vertices in the Kapton® from the intensity profile of the beam to obtain the positions of the target cell.

As a first step the target cell is subdivided into several slices along its length. The corresponding vertex distribution is shown in Figure 4.6 (down). The vertical lines indicate the limits of the consecutive Z-slices in a distance of $\Delta Z = 50\,\mathrm{mm}$. An example for a transversal vertex distribution in one of the slices

---

[1]In the MRS see Sec. 3.1.5
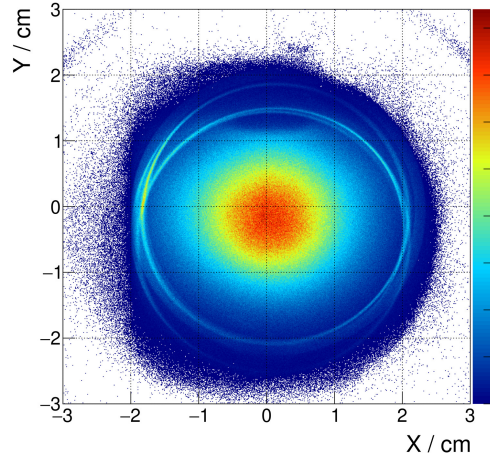
Figure 4.5: Vertex distribution in the X-Y-plane for the full target length ($Z_{tgt.,min}$=-3185 mm and $Z_{tgt.,max}$=-785 mm) without any restrictions on the target volume. The wall of the Kapton® cell is clearly visible.

is shown in Figure 4.6 (top). The center of the target cell is slightly shifted with respect to the origin (0,0)
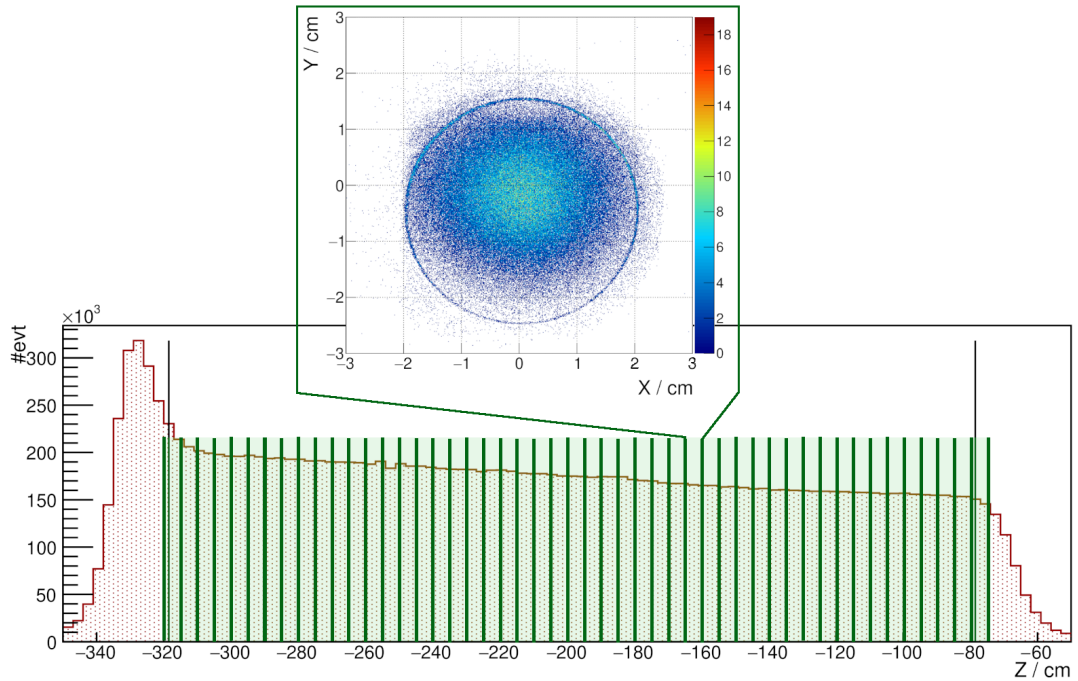
Figure 4.6: Distribution of the Z-positions of the vertices. The black vertical lines indicate the final limits of the target volume ($Z_{tgt.,min}$=-3185 mm and $Z_{tgt.,max}$=-785 mm), while the green lines mark the limits of each Z-slice (ΔZ=50 mm). The upper plot is showing the vertex distribution in the X-Y-plane for a single Z-slice.

of the MRS. To identify the radius of the cell in each Z-slice, its dependence on the azimuthal angle ϕ has to be determined, as illustrated in Figure 4.7.
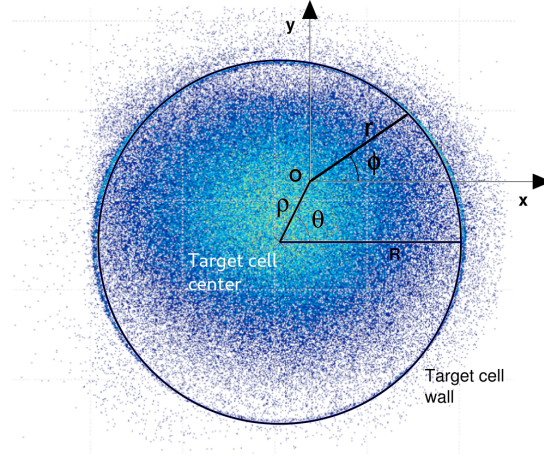
Figure 4.7: Illustration of the variables used to determine ϕ-dependence of the radius according to Equation 4.1. The shown vertex distribution in the X-Y-plane is for a single Z-slice.

Assuming a circular shaped cell the modulation of the radius in cylindrical coordinates can be expressed as:

$$r(\phi) = -|\vec{\rho}| \cdot cos(\phi - \theta) \sqrt{|\vec{\rho}| \cdot cos(\phi - \theta)^2 + R^2 - |\vec{\rho}|^2}. \tag{4.1}$$

Here $\vec{\rho}$ denotes the vector between the center of the target cell and (0,0) of the MRS, θ is the corresponding azimuthal angle with respect to the horizontal axis and R the radius of the target cell. The ϕ-modulation of the radius is determined by performing a fit according to Equation 4.1 of data points, which represent this modulation.

4.2.2 │ Determination and analyzing of the ϕ-modulation

To obtain the ϕ-dependence of the radial cell positions in each Z-slice, the corresponding vertex distributions are further subdivided into ϕ-sections. This allows to extract one-dimensional projections of the vertex distribution along r in each of those sections. An illustration of a projection, obtained for a ϕ-section with a width of $\Delta\phi$=5°, is shown as the solid black points in Figure 4.8.

The vertex distribution decreases exponentially following the intensity profile of the beam in the liquid hydrogen. In the Kapton® material an excess of vertices is obtained. To locate this region, the distribution is fitted using an exponential function to describe the background and a Gaussian to identify the peak. With the peak region localized it can be enhanced (see Fig. 4.9a) for allowing a more elaborated study of the peak. The obtained distribution cannot resolve the thickness of the Kapton® cell (about 0.01 cm), due to the finite width of the ϕ-sections the vertex distribution appears to be smeared. To finally localize the cell position, the peak profiles are fitted using a modified step function with exponential like edges. The background by the beam profile is described by a linear function. The results of the peak fit and the linear background are indicated by the red and blue dashed lines.

70
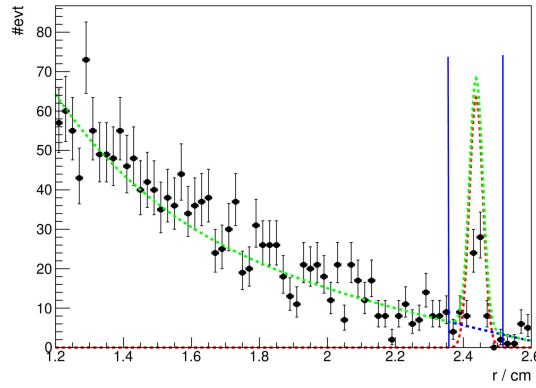
Figure 4.8: Example of an one-dimensional vertex distribution (solid points) for a ϕ-section ($\Delta\phi$=5°) in a single Z-slice (ΔZ=50 mm). The peak is localized (vertical blue lines) by fitting the distribution by a composite model (green) using an exponential background (blue) and a Gaussian for the peak (red).

Performing this procedure for all ϕ-sections belonging to a Z-slice the ϕ-dependence of r is obtained like illustrated by the points in Figure 4.9b. The horizontal error bars are given by the corresponding width of the ϕ-sections, while the vertical ones are determined according to the resulting FWHM[2] of the peak fit. The ϕ-modulation of r is fitted according to Equation 4.1 and is indicated by a solid red line.

(a)

(b)
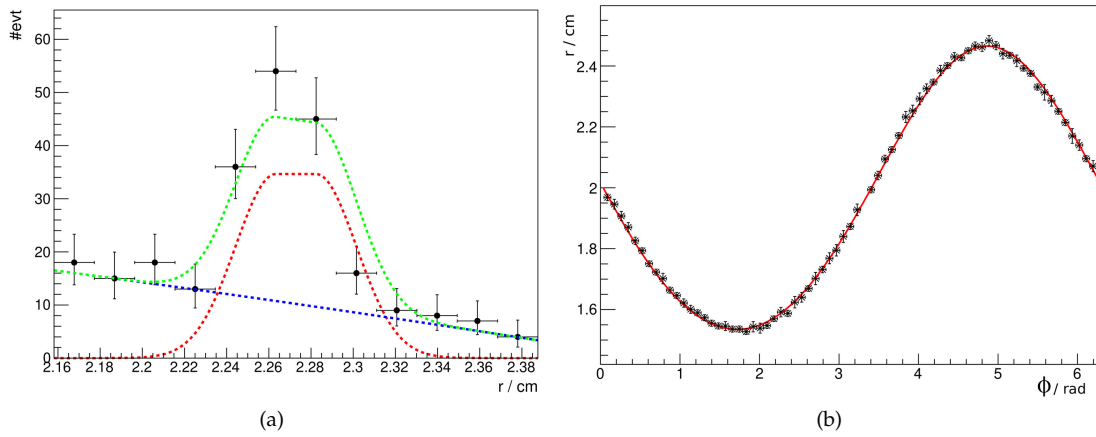
Figure 4.9: (a) Enhancement of the one-dimensional vertex distribution in the range of the target cell for a single ϕ-section in a Z-slice (ΔZ=50 mm and $\Delta\phi$=5°). The peak is fitted using a linear polynomial as background (blue) and a modified step function with exponential edges for the peak (red). (b) r as a function of ϕ for a single Z-slice. The modulation is fitted according to Equation 4.1 (red).

---

[2]full width half maximum (FWHM)

71

4.2.3 | Target position in 2016

The X, Y positions of the target center and the radius of the target cell as a function of Z are shown in Figures 4.10a, 4.10b and 4.10c. For the X-positions only a minor oscillation of about 0.5 mm is observed,

(a)

(b)

(c)
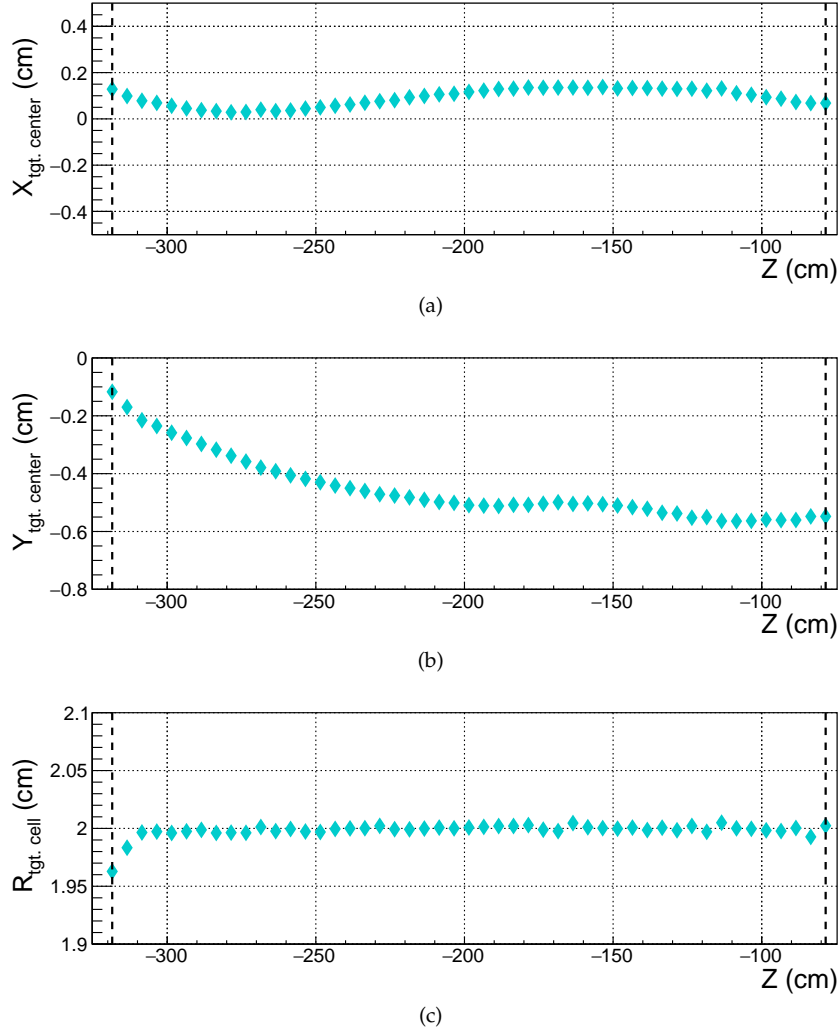
Figure 4.10: (a) X position of target center. Target is well aligned, only showing a minor oscillation (about 0.5 mm) around its average. (b) Y position of target center. In the vertical direction the target position decreases with Z by about 4.5 mm. (c) Radius of the Kapton® cell as a function of Z. The radius is constant over the full Z-range (R=20±0.05 mm), which indicates that the cell has its designated circular shaped over its full length.

which illustrates that the target is well centered in horizontal direction. In the vertical direction the target position decreases with Z by about 4.5 mm. This slight bent of the target is applied to allow for the gaseous hydrogen to gather at one end of the target. This can also be seen in Figure 4.11 as a depletion of interaction vertices at the top of the distribution. It allows to restrict the target volume in the physics analysis to a maximum of Y=12 mm, which removes the regime of the gaseous hydrogen. In

Figure 4.10c one can see that the radius is nearly constant over the full Z-range (R=20±0.05 mm), which indicates that the cell has its designated circular shaped over its full length. Along the Z-axis the target volume was chosen to be between -3185 mm and -785 mm, which is well inside the region of the liquid hydrogen and illustrated by the horizontal lines.
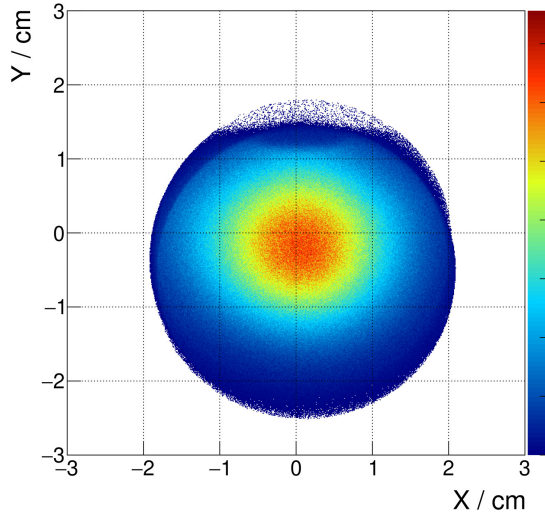
Figure 4.11: Transversal vertex distribution after applying the restrictions on the target volume. The interactions in the Kapton® cell are no longer visible.

To apply the restrictions on the target volume for physics event selections, the results are implemented in PHAST. The corresponding Z-dependence of the center positions and radii of the target cell are stored in the function PaAlgo::GetDVCSTargetLocationCenter(). Due to the complicated shape of the cell, the corresponding target description implemented in the Monte-Carlo simulation does not perfectly match the real target shape. The solution for the simulation was to integrate the target as a tilted cylinder and requiring the same volume as for the data. This is done by applying a reduced radius of the target cell, which only keeps the overlap between both descriptions [140]. The requirements for the physics analysis are implemented by two distinct functions. The function PaAlgo::CrossCells() extrapolates a beam track along the target length and reviews that it always is contained inside the volume. A second function, called PaAlgo::InTarget(), requires the vertices belonging to a beam particle to be reconstructed inside the target volume. The implementation of the PHAST functions were done by Antoine Vidon, Nicolas Pierre, Karolina Lavickova and Jan Matousek. The final cuts on the target volume used in 2016, which are given as input parameters to the functions introduced above, are:

- -318.5 cm< Z_{vtx} <-78.5 cm,

- R_{vtx} <1.9 cm and

- Y_{vtx} <1.2 cm.

4.3 | Determination of the luminosity

The method to determine the effective muon flux using a true random trigger (see Sec. 3.1.6) was first developed by EMC [129]. It allows a precise extraction of the muon flux traversing the target, which is not biased by the performance of the spectrometer. The following Section summarizes the flux analysis performed in 2016, which is in further detail described in Reference [78]. Its results are used for calculating the luminosity, which is presented in Section 4.3.2.

4.3.1 | Determination of the muon flux

The basic idea of having a true random trigger is to use its generated signals to randomly open time gates, in which the reconstructed muon tracks are counted. This information allows calculating the muon flux in each spill i by:

$$\Phi_{RT}(i) = \frac{N_{RT,tracks}(i)}{RT_{att}(i) \cdot \Delta t} \cdot TiS(i).$$

Here, $N_{RT,tracks}$ is the number of reconstructed incoming muon tracks in spill i, recorded due the random trigger. It is divided by the total time window, given by the number of random trigger attempts RT_{att} and the corresponding length Δt of the opened time gates. This fraction results in the muon flux per second, hence multiplied by the time in spill window (see Sec. 4.1) it results in the flux per spill. For determining $N_{RT,tracks}$ a dedicated selection is used, which has the following requirements:

- random trigger is set,

- at least 3 hits in beam momentum station (BMS),

- first measurement point of the track is before the target ($Z_{tgt,min.}$=-318.5 cm),

- track traversed the target cell inside its volume (PaAlgo::CrossCells()),

- momentum of particle (p) is between 140 GeV/c and 180 GeV/c,

- uncertainty of the momentum measurement is better than 0.025·p,

- track has at least 2 hits in SCIFI detectors

- and at least 3 hits in SI detectors,

- mean time of the track is within random trigger time gate (Δt=±2 ns) and

- time in spill is within the time in spill window.

Most of the those requirements ensure for e.g. that the beam momentum was correctly measured and the track was detected by a minimum number of detector planes. All selection criteria besides the requirement of a true random trigger signal are also applied when selecting physics events.

The time gate of the true random trigger, is determined from the mean time distribution of recorded track. The mean time is the difference between the track time and the trigger time. For physics trigger and for those outgoing muon tracks, which fired the corresponding trigger, this difference is zero. In case of tracks recorded by the true random trigger a flat distribution is expected. The width the time gate for those tracks is a parameter set in the data reconstruction by CORAL. It is approximately ±6ns. The number of the tracks as a function of the mean time is shown in Figure 4.12. The different colors indicate the corresponding mean time distributions, after successively adding the selection criteria listed above. Having all criteria applied, a flat distribution is obtained for meantime values between -3 ns to
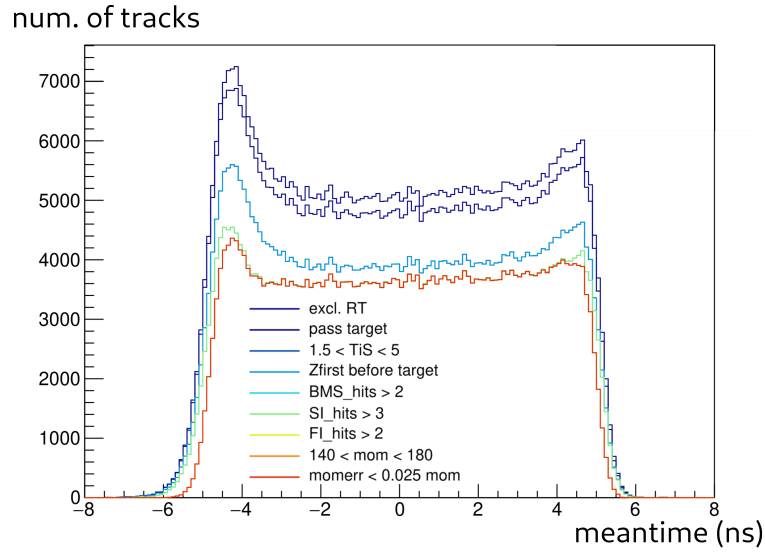
Figure 4.12: Evolution of the number of true random trigger beam tracks as function of the track mean time when successively applying the selection criteria. From the mean time distribution with all selection criterta applied the mean time gate is chosen to be ±2 ns.

3.5 ns. For a precise determination of the muon flux a constant rate of reconstructed tracks is needed. Therefore the mean time window is reduced to be in the 'safe' region between -2 ns to +2 ns. As the true random trigger, in contrast to the physics trigger is not affected by the veto, the flux has to be corrected by the veto dead-time. This dead-time can be determined for each trigger system by dividing the corresponding number of trigger signals, which are in coincidence with a delayed veto signal (delay: 23 ns), by the total number of trigger signals:

$$DT_{\text{trigger}} = \frac{\text{Trigger signals in coincidence with delayed veto}}{\text{Trigger signals}}.$$

The counting of the total and delayed trigger signals is implemented by using a scaler. In 2016/17 only the signals by the middle trigger are recorded for each spill, therefore only the veto dead-time of the middle trigger system can be calculated. Control measurements of the veto dead-time for all the physics trigger, performed from time to time during the data taking, show that the veto dead-time is similar for all trigger subsystems. Hence, the correction can be applied independently of the trigger subsystem. In general it is in the order of 8%.

4.3.2 | Results of the luminosity

The luminosity $\mathcal{L}$ is calculated for each spill i according to:

$$\mathcal{L}_i = \frac{\rho_{\text{liq. } H^2} \cdot N_A \cdot l \cdot \Phi_i}{M_p}. \tag{4.2}$$

Here, $\rho_{\text{liq. } H^2}$ is the proton density of the liquid hydrogen (0.070146 g/cm^3 at 20 °C), N_A is the Avogadro constant, M_p is the molar mass of the proton, Φ is the muon flux and l the effective target length (240 cm). The integrated luminosities for each period seperated for μ^+ and μ^- are summarized in Table 4.3.

period	$\mathcal{L}_{\mu^+}$ / 10^{36} cm^{-2}	$\mathcal{L}_{\mu^-}$ / 10^{36} cm^{-2}
P04	9.73	7.64
P05	8.09	7.14
P06	7.87	6.40
P07	9.51	8.49
P08	9.59	8.47
P09	7.48	7.07
Σ	52.27	45.21

Table 4.3: Integrated luminosity for each period separately for μ^+ and μ^- beam.

4.4 | Performance of the hodoscopes and the trigger system

The performances of the trigger system and its detectors have a large impact on the data quality and its kinematic distributions. To obtain a satisfying agreement between the data and simulated data, it is therefore of significant importance to have a precise knowledge of its performance. This includes studies on the hodoscope positions and their efficiencies, as well as on the efficiencies of the trigger subsystems. The work related to these studies is summarized in the following Sections. Further details can be found in Reference [79] and [80].

4.4.1 | Determination and adjustment of the hodoscope positions

To illustrate the objective of the analysis presented in this Section, Figure 4.13 shows the two-dimensional efficiency distribution of a LT hodoscope (HL05). The details on the extraction of the hodoscope efficiencies are described in Section 4.4.2. The drawn hodoscope boundaries and elements correspond to the geometry assumed by the reconstruction software (CORAL). The blue colored regions indicate a depletion of the efficiencies, which is due to the absence of scintillator material. This hints to the fact that there is a slight discrepancy in the description of the hodoscope positions, considered in the reconstruction and its real positions. To correct these discrepancies, a method was developed to extract the positions of each element from the reconstructed data.

The information on detector geometries and positions are stored in a so called *detector.dat* file. Its descriptions are optimized for wire detectors. This file summarizes for e.g. the X,Y and Z position of the detector centers in the MRS (see Sec. 3.1.5), the number of wires, the pitch, which is the distance between one wire to the next, and the position of the first wire in the detector reference frame (DRF). The DRF corresponds to a frame, where the reference point is the center position of the detector. For describing detectors, which have for e.g. multiple parts with different sized pitches, the detector can be divided in sub-detectors, which are each described by its own set of parameters.
For describing hodoscopes in the framework of the *detector.dat*, some technical difficulties and limitations have to be overcome. Most of the hodoscopes have an overlap between their elements. Such a feature is not implemented in CORAL. Therefore a hodoscope is described by elements without an overlap. It starts from the first wire position. This corresponds to the central position of the element located at the smallest X or Y, depending if the elements are vertically or horizontally oriented. Their widths are described by the pitch, which is in this case the distance of one element edge to the point where the overlap with the next element starts. In the description of the LT and MT hodoscopes, it has to be considered that these hodoscopes are build of different sections with different element widths.
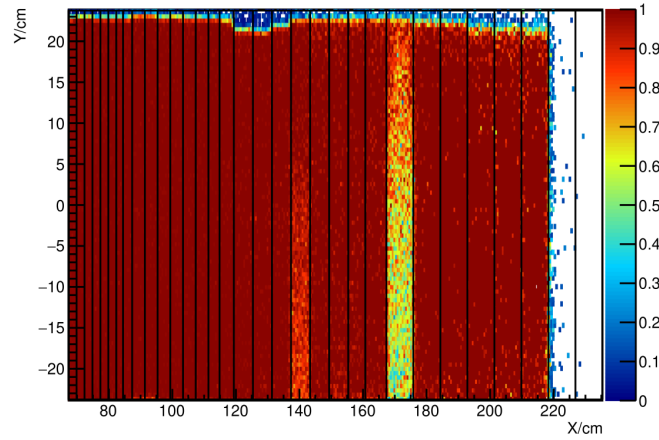
Figure 4.13: Example for a misalignment of the HL05. The borders of the histogram are indicating the hodoscope position as it is considered by the reconstruction software.

Therefore their descriptions are divided into sub-detectors.

Some hodoscopes contain holes to allow the muon beam to pass the detector and to open up acceptance regions covered by other hodoscopes. These holes are called deadzones. They can have different shapes, which are simple rectangular or more complex. Their positions and sizes are described in the DRF. For each hodoscope, it is only possible to define a single deadzone. An example for a more complex deadzone is shown in Figure 4.14, which illustrates the most upstream positioned hodoscope of the OT (HO03). Here, the description only covers the largest possible deadzone (large rectangle) without cutting in the sensitive detector area.

To extract the precise positions of each hodoscope element, the information on reconstructed muon
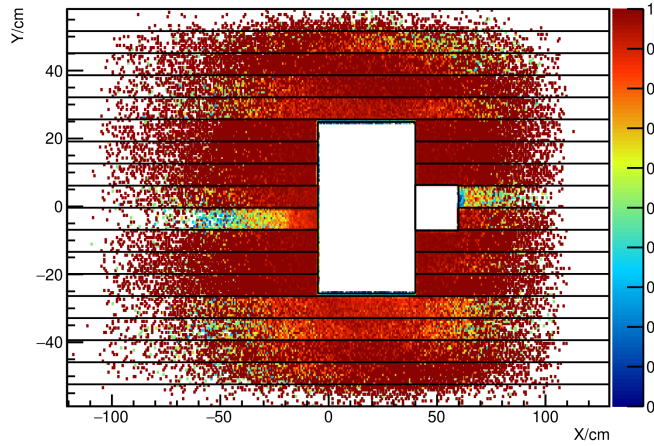
Figure 4.14: Hodoscope geometry of HO03.

tracks and their detector hits are used. Those tracks are extrapolated to the Z-position of the hodoscopes. The muon tracks are selected using a dedicated event selection, which is described in detail in Reference [79]. Here, it is important that the extrapolated tracks are not directly associated with a detector hit. This ensures that CORAL does not require the tracks to traverse the sensitive hodoscope areas. Else the

tracks are being rejected, which would prevent to gain any information on tracks, which are outside the detector geometries assumed by CORAL.

From the selected events one can extract one-dimensional track distributions separately for the X and Y-coordinate of each scintillator element. By comparing the distributions of the extrapolated tracks to those distributions requiring a hit in the elements, one obtains one-dimensional profiles of the element positions. An example of an one-dimensional X projection of extrapolated tracks along the width of an vertical oriented element of the LT hodoscope (HL05) is shown in Figure 4.15a. The corresponding distribution, when also requiring a hit in this element, can be seen in Figure 4.15b. The ratio between this distribution and the first one results in the profile, shown in Figure 4.15c. This indicates the width of the element and its corresponding positions in X. Following the same procedure but for the Y-projection the
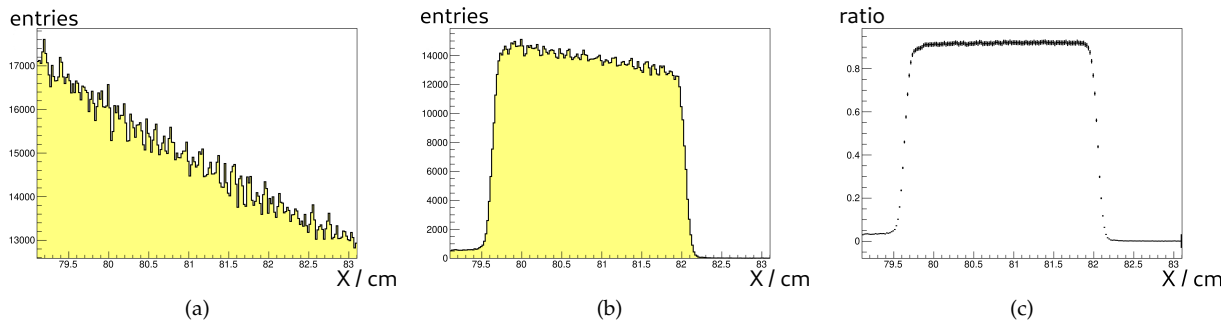
Figure 4.15: X-projection of the distribution of extrapolated tracks (a), extrapolated tracks and a hit in element element 6 of Ladder HL05 (b) and the ratio of both distributions (c).

distributions and profiles, shown in Figure 4.16a, 4.16b and 4.16c, are obtained. Here the profile indicates the Y-positions and the length of the element. The edges of the profiles are not perfectly sharp but
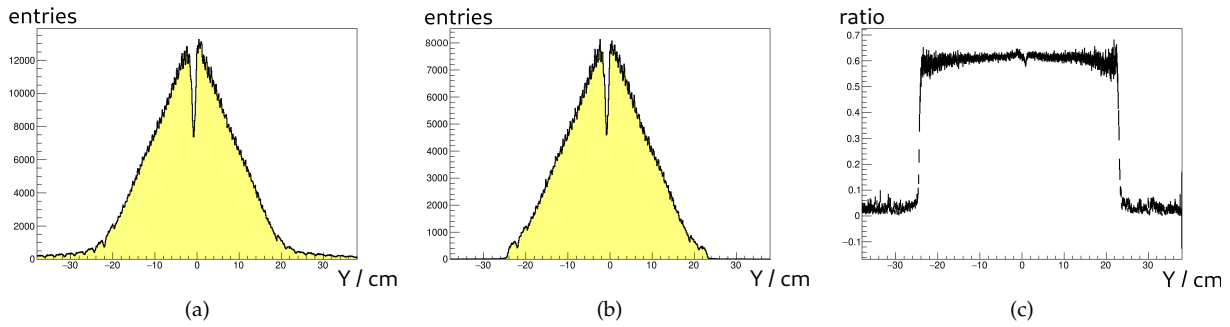
Figure 4.16: Y-projection of the distribution of extrapolated tracks (a), extrapolated tracks with and a hit in element element 6 of Ladder HL05 (b) and the ratio of both distributions (c).

smeared out. This smearing is caused for e.g. by the resolutions of the tracking detectors and additional uncertainties due to the track extrapolation.

To identify the positions of the scintillator elements, an edge search algorithm is performed, which uses the known element dimensions (widths and lengths) as a constrain. In a first step the central

positions of the leading and falling edge are independently identified. These positions are set to be half the altitude of the distribution. Next, both positions are adjusted along the two slopes, in which the distance between both is constrained by the elements width or length. In this iterative procedure it is ensured that the altitude of both positions on the slopes are always leveled.

Performing this algorithm for each element and projection, their positions are obtained. From these element positions the full hodoscope can be constructed. An example of the result for the LT hodoscope (HL05) is shown in Figure 4.17. The color profile represents the two-dimensional distribution of the ratio between the extrapolated tracks and the hits in the elements. The drawing of the hodoscope elements is done by using the results on their positions. The structures and background, which is visible outside the sensitive hodoscope area, are caused by the properties of the data selection. As the extrapolated tracks and hits are not directly associated to each other, some hits are wrongly addressed to tracks outside the sensitive hodoscope area, causing a visible background. The red color indicates elements, where the algorithm could not locate the positions due to too few tracks in this region. Here, the elements are drawn using the default information from the *detectors.dat*. Overall the drawings of the elements represent the yellow colored sensitive area of the hodoscope. The results for the other hodoscopes are illustrated in Appendix A.1.
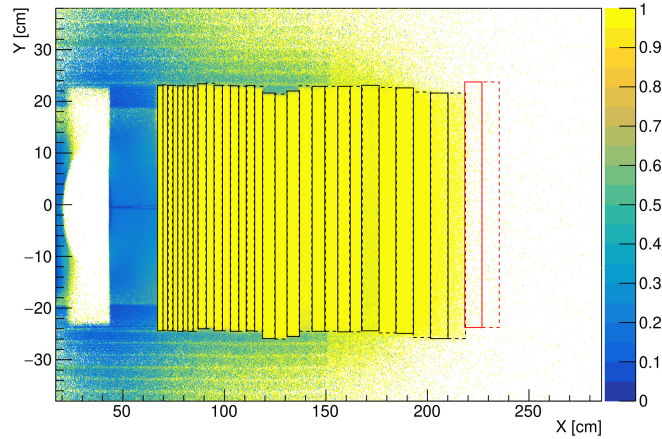
Figure 4.17: 2-dimensional distribution of the ratio of extrapolated tracks and those with hits. The results of the positions of each elements are drawn on top of the distribution. The red color indicates that it was not possible to determine the X and Y positions and dimensions of the corresponding element. In this case the drawing is done by using the information from the *detectors.dat*.

The results of this analysis are used to adjust the corresponding parameters in the *detectors.dat*. It was not possible to perform this analysis for all hodoscopes, as not all of them are being sufficiently illuminated. The method worked well for the MT and LT hodoscopes, achieving resolutions of about 0.2 mm for the widths of the elements and 1-3 mm for their lengths. As the LT and MT hodoscope are described in terms of sub-detectors and not for each single element separately, the extracted positions of the elements are used to adjust the description of each sub-detector. These adjustments are implemented in a way to cover their maximal sensitive areas. For the MT hodoscopes also a slight tilt was observed. To compensate for this, a small clock-wise rotation was introduced, which is 0.105° for the up and 0.256° for the down hodoscopes.

For the OT hodoscopes only the locations of the deadzones could be extracted. With the known dimensions of the scintillator elements their descriptions in the *detectors.dat* were reviewed and it was decided that the default ones are accurate. For the LAST hodoscopes the provided statistic was to low to draw conclusions on their positions. As no discrepancies in the description of the hodoscope positions where

spotted during the efficiency studies, it was also decided to keep the default descriptions. The only exception is in the positions of the H1 hodoscope of the LAST system. Here a known discrepancy in the horizontal position between 2016 and 2017 is taken into account. Additionally a similar analysis using the hadron data recorded in 2018 was performed by Moritz Veit to extract the vertical position of its scintillator elements. As the hodoscope was not modified between 2016/2017 and 2018, it was decided to use the extracted positions also for the reconstruction of 2016/17 data.

4.4.2 | Determination of the hodoscope and trigger efficiencies

In the following the method used to extract the hodoscope and trigger efficiencies is discussed. For further details see Reference [80].

To study the performance of the trigger systems and the hodoscopes, a sample of scattered muons is needed, which was not recorded by the trigger system itself. This sample is provided by the calorimeter trigger and by applying the selection criteria, summarized in Table 4.4. The scattered muon identification is done by using the PHAST function PaVertex::iMuPrim(), which comprises the requirements discussed in Section 3.1.5.2. Additionally these criteria are supplemented by conditions for hits in the muon walls and/or MWPCs. As the extracted efficiencies should comply for scattering events inside the liquid hydrogen target, the vertex requirements presented in Section 4.2.3 are applied.

4.4.2.1 | Hodoscope efficiencies

Based on the data sample discussed above the hodoscope efficiencies are calculated as:

$$\varepsilon = \frac{N_{\text{tracks, hit}}}{N_{\text{tracks}}}. \tag{4.3}$$

Here, N_{tracks} denotes the number of reconstructed muon tracks extrapolated to the Z-position of a hodoscope plane and $N_{\text{tracks,hit}}$ are those tracks additionally associated with a hit in this plane.

To obtain a full two-dimensional efficiency map for each hodoscope, the idea is to use the one-dimensional efficiency distribution along each element, which are integrated over the element width. Exemplary, these are shown for different elements of different hodoscopes in Figures 4.18a to 4.18e. The efficiencies extracted from the data sample are displayed as black points. Their vertical bars indicate the resolution used along the elements and the horizontal bars the uncertainty of the efficiencies. For some elements these uncertainties are considerably large at the edges, which is due to an insufficient illumination of the corresponding hodoscopes. In Figure 4.18c and 4.18d the elements are divided by the deadzone of the hodoscope.

To derive two-dimensional efficiency maps, a polynomial fit of the one-dimensional efficiency distributions for each element is performed. Hereby, only the regions with a relative statistical uncertainty, typically better then 5%, are being considered. The polynomial fits give a description of the efficiency evolution in each element, which can be extrapolated to regions with large uncertainties. The degree of the applied polynomial fits is chosen according to the complexity of the distribution they have to describe. Its results and the corresponding extrapolated efficiencies are displayed as solid red lines and blue points respectively. The two-dimensional efficiency maps, extracted by the introduced method, using the data available in period 09, are shown in Figure 4.19. For the MT and LT hodoscopes the statistic obtained, considering one period of data taking, is sufficient to determine the efficiencies with an accuracy of about 1%. In general the MT hodoscopes show a good and stable performance over all the data taking periods with efficiencies close to 100% (see Fig. 4.19a). The same applies for the LT hodoscopes. They are stable with only a few elements showing a decreasing efficiencies along their lengths. In case of HL05 (see Fig. 4.19b), this is due to an irregular setup of the meantimer. The last two

Event	■ Recorded by calorimeter trigger

Incoming muon and vertex	■ Best primary vertex (BPV)
	
	 ■ BPV in target
	    – -318.5 cm$< Z_{\text{vtx.}} <$-78.5 cm
	    – $R_{\text{vtx}} <$1.9 cm
	    – $Y_{\text{vtx}} <$1.2 cm
	
	 ■ Beam muon has track

Scattered muon	■ Found a scattered muon candidate PaVertex::iMuPrim(true,true,true,false)
	
	 ■ Has an associated track
	
	 ■ ZFirst$<$350 cm (before SM1)
	
	 ■ ZLast$>$1500 cm for LAS and ZLast$>$4000 cm for SAS hodoscopes
	
	 ■ X/X0$>$15
	
	 ■ $Q^2 >$0.1 (GeV/c)^2
	
	 ■ Momentum > 0.1 GeV/c
	
	 ■ For LAS hodoscopes: check MWA hits (before and after absorber):
	    – MWA01 hits ≥ 4
	    – MWA02 hits ≥ 4
	
	 ■ All other hodoscopes check MWB or MWPC (PB01-06) hits:
	    – MWB hits ≥ 4
	    – PB01 and PB02 hits ≥ 1 and PB03 and PB04 hits ≥ 1 and PB05 and PB06 hits ≥ 1

Table 4.4: Summary of the event selection used for determining the hodoscope and trigger efficiencies.
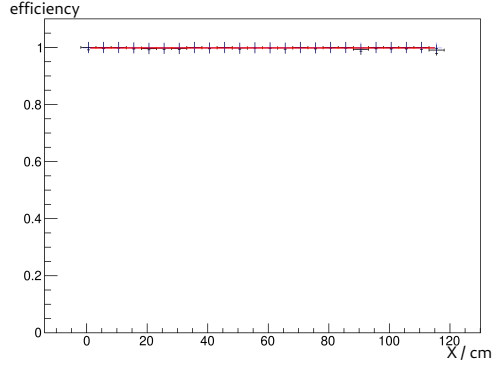
(a) Efficiency distribution for element 7
of HM04Y1.
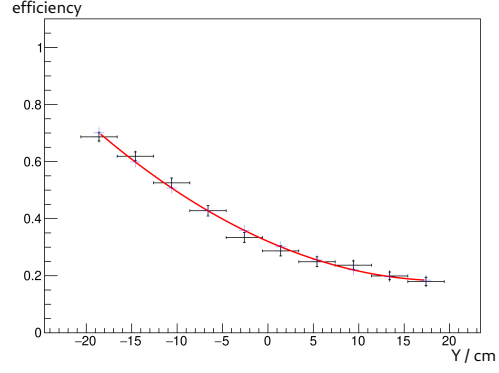
(b) Efficiency distribution for element 29
of HL04X1.
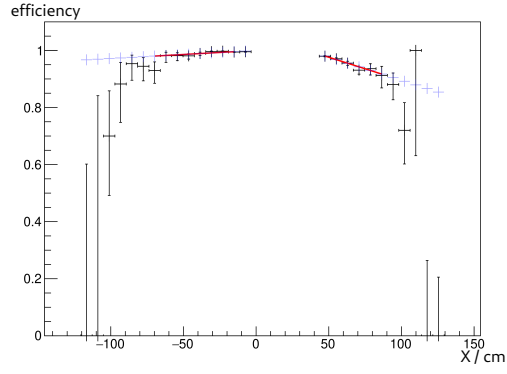
(c) Efficiency distribution for element 7
of HO03Y1.
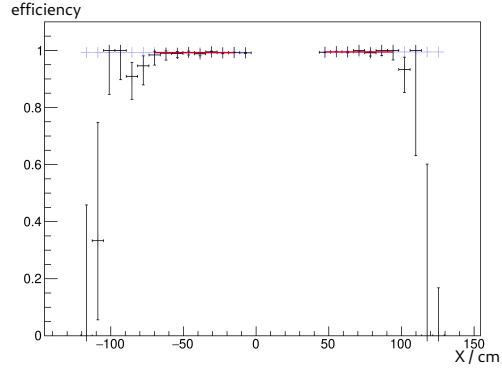
(d) Efficiency distribution for element 12
of HO03Y1.
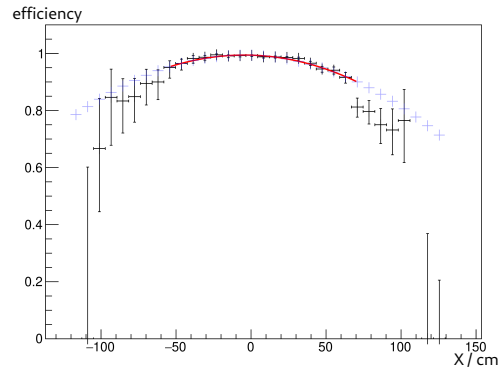
(e) Efficiency distribution for element 16
of HO03Y1.

Figure 4.18: 1-dimensional efficiency distributions for various hodoscope elements. The red lines are indicating the results of the fit and the fit ranges for the corresponding elements, while the corresponding extrapolated efficiencies are indicated by the blue points.

(a) Efficiency map for HM04Y1 down.

(b) Efficiency map for HL05X1.

(c) Efficiency map for HO03Y1.

(d) Efficiency map for HO04Y1.

(e) Efficiency map for HG01Y1.

(f) Efficiency map for HG02Y2.
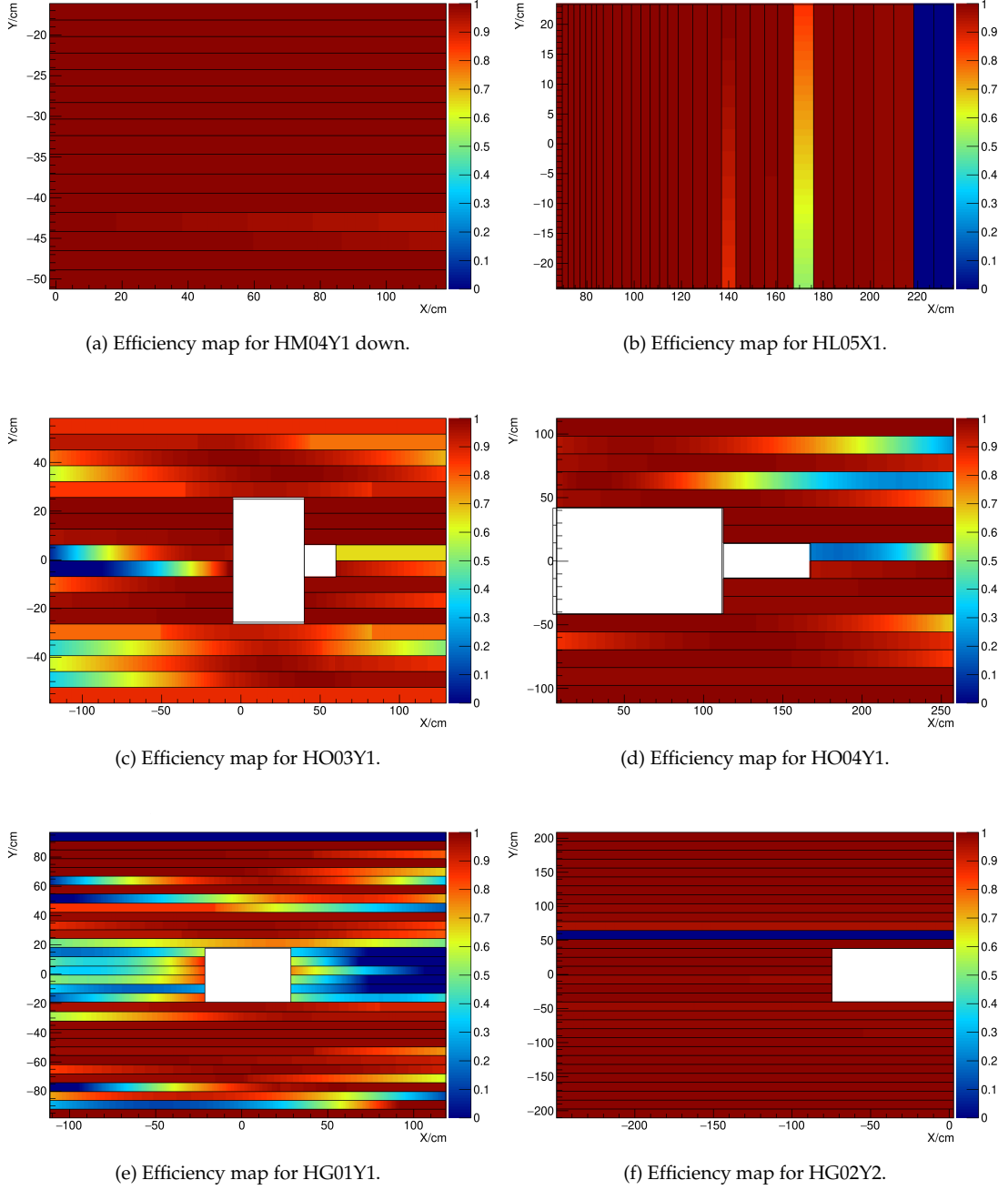
Figure 4.19: 2-dimensional efficiency maps according to the statistics of the P09 data sample for (a)-(d) and the cumulated statistics of P04-P09 for (e) and (f).

83

elements were not available in the whole 2016 data taking period, due to broken PMTs and discriminator channels, which could not be repaired before 2017. In contrast to the MT and LT hodoscopes, in the OT hodoscopes, shown in Figure 4.19c and 4.19d, efficiency variations along most of the elements are visible. Here, the high voltage settings for these hodoscopes were chosen to be optimized for the trigger efficiencies, which are dominated by the high statistics regions close to the deadzones. The drawback was that this biased the high voltage settings. Therefore the gains of the PMTs were set to be too low. Hence, for muons traversing a hodoscope element close to one side, the signal was lost for the PMT on the other side. These high voltage settings are only used starting from period 08. To increase the statistics and therefore the accuracy of the efficiency determination for the OT hodoscopes the used data for extracting those is integrated over two consecutive periods. Here, it was ensured that the observed one-dimensional efficiency distributions for each element show the same behaviour within their statistical uncertainties in both periods. If this was not the case, only the statistic of a single period was used for this particular element. For the LAST hodoscopes the cumulated statistic of all periods was used, as for the single periods it was not sufficient to draw conclusions. The HG02 hodoscopes (see Fig. 4.19f) are showing high efficiencies close to 100%, while Figure 4.19e shows considerable drops of the efficiencies for HG01, especially in its central part. These are caused by an design flaw of the hodoscopes structural integrity itself. As it is located directly before the RICH-detector, it was decided to use a minimal amount of material to minimize the hadron interactions. Hence, the dimensions of the scintillator elements were designed to have a small as possible thickness (10 mm) over a length of 2300 mm. The elements are grouped in sections, which are supported by Rohacell® boards. Over time the high weights caused the sections to bend, affecting especially the central region, which was the most fragile one due to the deadzone. In the hodoscope design the deadzone is implemented by air light guides, which are hollow and covered in highly reflective foil on their insides. The bent of this section considerably disturbed the light propagation, causing a signal loss of the PMTs on either side of the elements.

4.4.2.2 | Efficiency of the trigger electronics

As discussed in Section 3.1.5.3, a trigger signal is generated by a coincide measurement of the muons traversing two elements of two distinct hodoscopes. These coincidences are implemented by a coincidence matrix. The efficiency of the trigger electronics, are therefore also represented as a matrix where each pixel describes the efficiency of the coincidence between two hodoscope elements. These matrix pixel efficiencies are determined as:

$$\varepsilon_{trig}(i,j) = \frac{N_{\text{tracks,hit,trig}}(i,j)}{N_{\text{tracks,hit}}(i,j)}. \tag{4.4}$$

Here, $N_{\text{tracks,hit,trig}}(i,j)$ denotes the number of tracks requiring hits in the elements of two hodoscopes, that also generated a trigger signal and $N_{\text{tracks,hit}}(i,j)$ is the number of tracks with only requiring the hit information. These efficiencies only depend on the performance of the trigger electronics, responsible for processing the hodoscope signals.

Analog to the determination of the hodoscope efficiencies, also here the efficiencies are usually done for each period separately. Only for the LAST the statistics were integrated over all periods. A few examples for the trigger matrix efficiencies for period 09 are shown in Figure 4.20.

The trigger matrix efficiencies for the MT are in general very high (>98%). In the coincidence of the MT up hodoscopes only two pixels show an irregularity, caused by the trigger timing calibration (see Fig. 4.20a). The same applies to the LT as shown in Figure 4.22b. For one column the trigger electronics were not properly timed in. The matrix efficiencies describing the coincidence, between the first hodoscope of the OT (HO03) and one half of the corresponding second hodoscopes (HO04) (see Fig. 4.20c and 4.20d), are very high with only a minor issue in the trigger timing. The trigger matrix efficiencies for the two

corresponding coincidences between the first LAST hodoscope (HG01) and the two halfs of the second one, shown in Figure 4.20e and 4.20f, show clearly that the efficiencies are lower and also not that stable as for the other systems. The reason here is that due to the very low number of events a proper timing calibration is more difficult. Also the statistic available is still low, which causes large uncertainties when determining the efficiencies.

For the matrices in general it can be seen that not for all possible pixels an efficiency is obtained, as not all of the pixels provide sufficient statistics. For the trigger matrix efficiencies included into the Monte-Carlo simulation these pixels are either set to 100% efficiency or 0% efficiency.
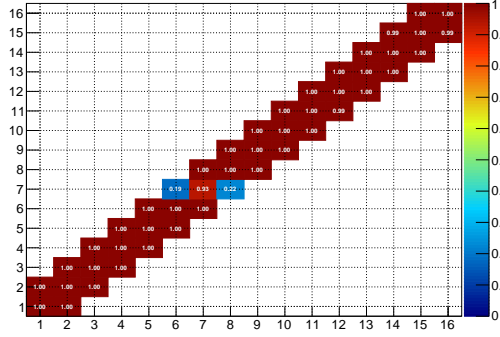
(a) Xoincidence between HM04Y1 up and HM05Y1 up.
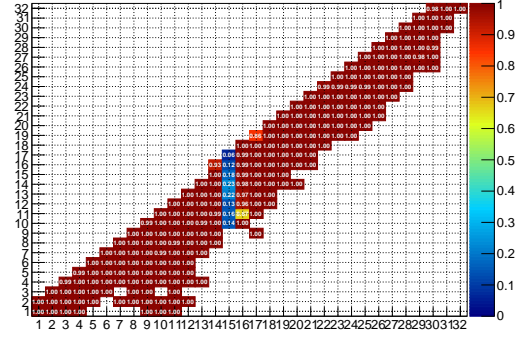
(b) Coincidence between HL04X1 and HL05X1.
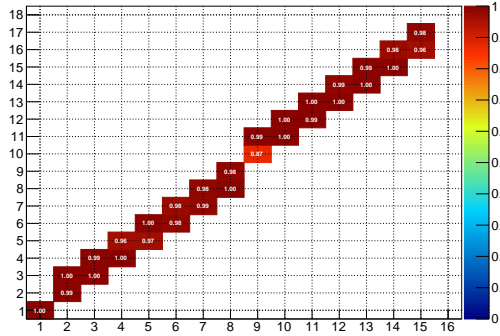
(c) Coincidence between HO03Y1 and HO04Y1.
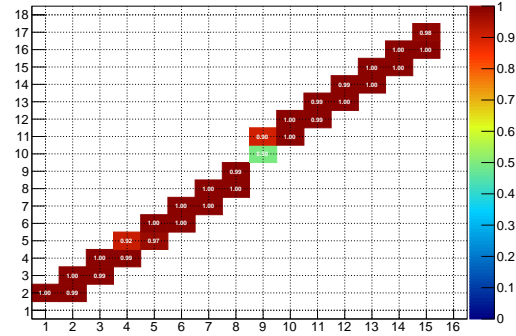
(d) Coincidence between HO03Y1 and HO04Y2.
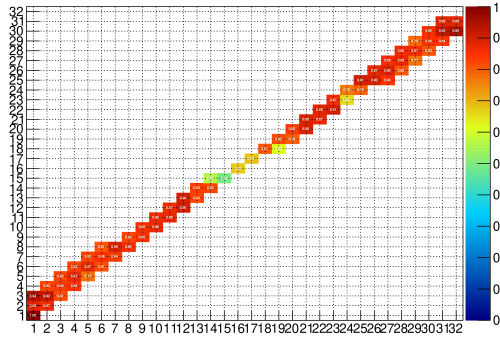
(e) Coincidence between HG01Y1 and HG02Y1.
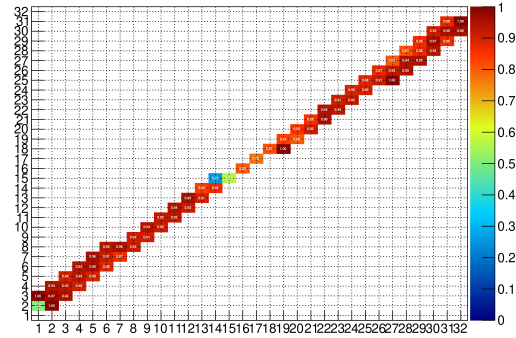
(f) Coincidence between HG01Y1 and HG02Y2.

Figure 4.20: Examples for the trigger matrix efficiencies of different trigger systems using the statistics of P09 (a)-(d) and the cumulated data statistics over all periods (e) and (f).

4.5 | Data quality

This Section comprises studies and comparisons performed to evaluate and improve the quality of the data. These include comparisons of real data distributions separated for μ^+ and μ^-, using a DIS event selection and general investigations of the detector performances. The DIS event data sample provides a high amount of statistics, which allows to detect irregularities in the reconstruction of the scattered muons.

4.5.1 | Comparison of μ^+ and μ^- data

A good agreement between the two data sets, taken either with μ^+ and μ^- beams is mandatory for a precise determination of the charge spin sum and difference of the DVCS cross section. It can be verified by comparing kinematic distributions extracted from those samples, which are obtained by a DIS event selection. The selection criteria are summarized in Table 4.5.
The incoming muons are identified by applying the same criteria as used to determine the muon flux (see Sec. 4.3.1). For identifying the track of the scattered muon, a newly developed PHAST function called PaHodoHelper::iMuPrim() is used. Additionally to the features provided by the PaVertex::iMuPrim() function, which was used in the selection presented in Section 4.4.2, this function allows to verify a trigger signal by extrapolating the tracks to the Z-positions of the corresponding hodoscopes. If the X-Y-positions of the extrapolations are not traversing the sensitive hodoscope areas, the tracks are being rejected. As described in Section 4.4.1 the sensitive areas are given by the corresponding hodoscope descriptions in the *detectors.dat*. In addition the PaHodoHelper::iMuPrim() function allows also to incorporate hodoscope areas and elements, defined in external files. This feature allows for e.g. to remove parts and elements of the hodoscopes, which had poor performances during the data taking or deviations in the description of the geometries compared to the actual ones. These parts are either identified when studying the performances and positions of the hodoscopes or by studying comparisons of kinematic distributions. Those can be either derived from data or from simulated data (see Sec. 4.6.1). The requirement on having a track measured before and after SM1 verifies a proper momentum measurement. Restrictions on the event kinematics are either due to physics or technical reasons. Having removed events with Q^2 smaller $1\,(\mathrm{GeV/c})^2$, limits the kinematic to a regime where the factorization for DIS is valid. For small values of y, it is not accurately determined, due to the momentum resolutions (of about $0.5\,\mathrm{GeV}$) of the scattered and incoming muons. The restriction to $y < 0.95$ avoids a region, which is sensitive to uncertainties in the reconstruction due to large radiative corrections with respect to the small momenta of the scattered muons.

The Figures presented in the following are obtained using the statistics of period 09. In the top Figure the distributions are shown seperated for μ^+ and μ^- and normalized according to the corresponding luminosity. The bottom Figure shows the ratios μ^+/μ^- fitted by a constant, which is indicated by a solid red line.
The X, Y and Z-distribution of the best primary vertices are shown in Figure 4.21a, 4.21b and 4.21c. The deviations visible for X_{vtx} are due to differences in the relative beam alignment between the two charges. The beams are shifted by about 1-1.5 mm. As this shift is comparable to the observed modulation of the horizontal position of the target cell (see Sec. 4.2.3), both beams are still well aligned with the target center. In the vertical direction the alignments of both beams are comparable but slightly shifted to negative Y to be well centered with the upstream end of the target cell. Along the Z-axis the alignment of the μ^- and μ^+ beams (see Fig. 4.21c) shows no hints to any deviations. In the distributions of the momenta of incoming muons, shown in Figure 4.21d, a slightly broader momenta profile for the μ^+ in comparison to the μ^- beam can be seen, shifting its average momenta to slightly higher values.

The offset of about 1.5% in the ratios of distributions, which are in good agreement, are caused by the precision of the flux determination.
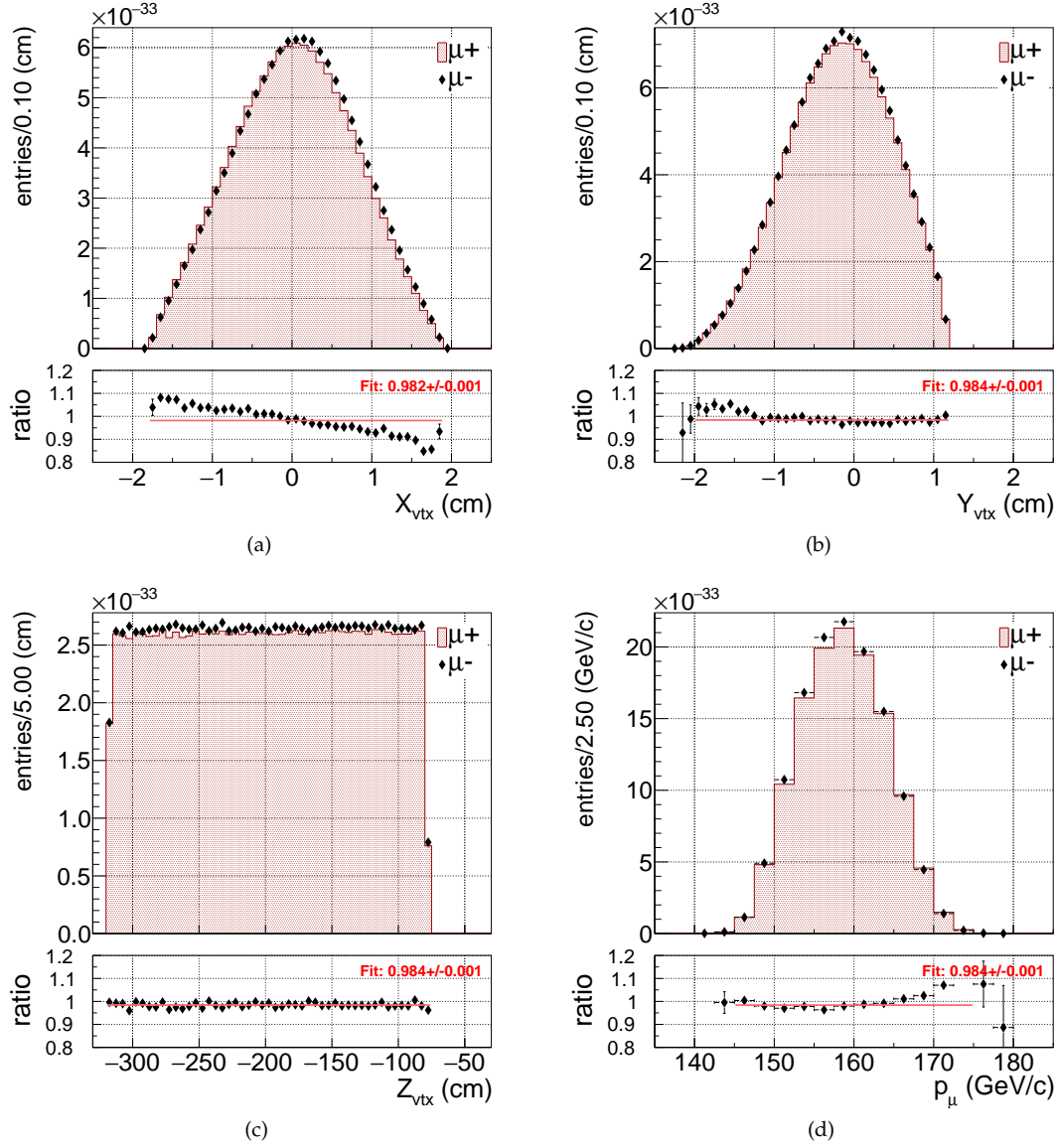
Figure 4.21: Comparisons of distributions related to the beam parameters for μ^+ and μ^-.

The momentum distribution of the scattered muon, displayed in Figure 4.22a, show a good agreement between both beam charges. A discrepancy at higher momenta of the scattered muons is due to the above mentioned higher average momenta of the μ^+ beam. The quantities related to the kinematics of the virtual photon, Figure 4.22b, 4.22c and 4.22d, show an overall good agreement between both beam charges.
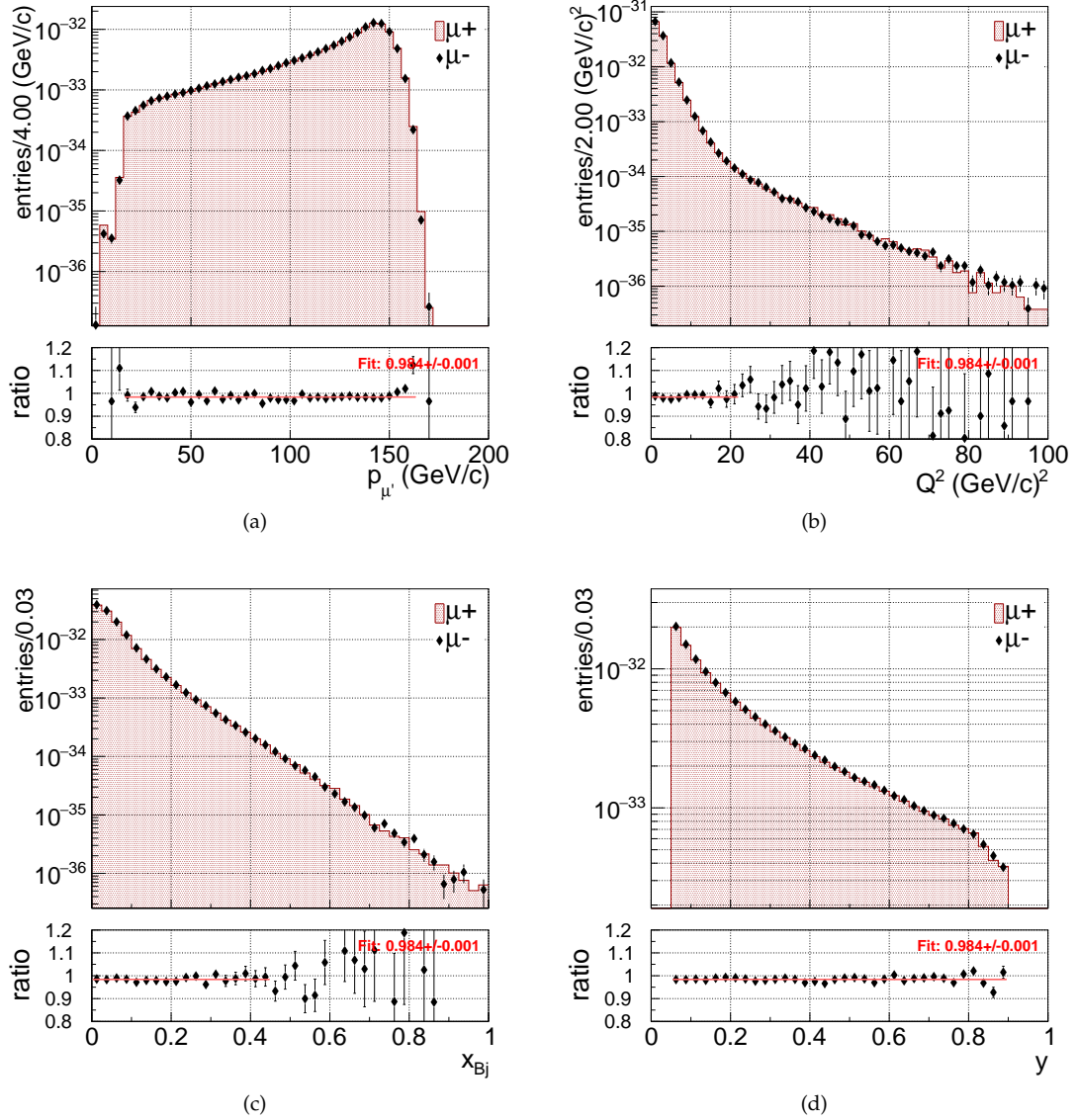
Figure 4.22: Comparisons of distributions related to the scattered muon and virtual photon for μ^+ and μ^-.

Event	■ event within the time in spill window ■ trigger: MT, LT, OT and/or LAST

Muon and vertex selection	**Vertex requirements:**
	
	■ best primary vertex
	■ in target
	   – -318.5 cm< Z_{vtx} <-78.5 cm
	   – R_{vtx} <1.9 cm
	   – Y_{vtx} <1.2 cm
	
	Incoming muon track (μ):
	
	■ first measured before the target
	  ($Z_{\text{tgt.,min.}}$=-318.5 cm)
	■ track crosses the full target length
	■ momentum: 140 GeV/c $< p_\mu <$ 180 GeV/c
	■ momentum error: $\Delta p_\mu \leq 0.025 \cdot p_\mu$
	■ meantime: -2 ns $< t_{\text{track}} <$ 2 ns
	■ hits in Beam Momentum Station (BMS): ≥ 3
	■ hits in Scintillation Fibre detectors (SCIFI): ≥ 2
	■ hits in Silicon strip detectors (SI): ≥ 3
	
	Outgoing muon track (μ'):
	
	■ scattered muon candidate
	   – PaHodoHelper::iMuPrim() (all flags set to true)
	   – additional requirements that track extrapolations are in the active hodoscope areas
	■ same charge as incoming muon
	■ rel. radiation length: X/X_0 >15
	■ first measured before and last after SM1:
	  $Z_{\text{first}} <$ 350 cm and $Z_{\text{last}} >$ 350 cm

Kinematic	■ Q^2 >1 (GeV/c)^2 ■ 0.05< y <0.9

Table 4.5: Overview of the criteria related to the general, muon and vertex requirements for the selection of DIS events.

4.5.2 | Identification of bad spills

The objective of this analysis is to identify spills, which show a deviation with respect to the majority of the spills taken under the same conditions. The properties of the spills are evaluated by parameters directly related to detector performances. These detectors are crucial for identifying certain types of physics events and therefore have an direct impact on the quality of those events. In the physics analysis these spills should be removed from the data sample. The analysis is performed using an already existing framework developed by Heiner Wollny, which was adjust and extended to match the requirements of the 2016/17 analysis.

In general the bad spills are being identified as follows. For each spill a set of reconstructed variables and parameters, representing the stability of the detector systems or analysis inputs, is chosen. Those crucial for the exclusive photon analysis are the muon flux, the ECALs and the muon trigger. In addition also the RICH-detector is part of the analysis, but as it is not of interest for exclusive photon production, it is not discussed in the following. The above mentioned set of parameters are summarized in Table 4.6. For each spill the value of each parameter is determined, which results in a distribution of

Detector system/ analysis input	Parameters
Muon flux	■ intensity of the true random trigger flux
Trigger systems	■ primary vertices per event and trigger ■ tracks per primary vertex and trigger ■ number of triggers normalized to the true random trigger flux
ECALs	■ number of neutral cluster (ECAL0/1/2) ■ energy of neutral cluster (ECAL0/1/2) ■ number of charged cluster (ECAL1/2) ■ energy of charged cluster (ECAL1/2)

Table 4.6: Overview of the corresponding parameters used to identify bad spills. The Table only includes those systems and inputs, which are of importance for the DVCS analysis.

this parameter in dependence of the corresponding spill number, as shown in Figure 4.23a. Here, the full period 09 statistics is used. To identify the bad spills, the value of each the parameter in each spill is compared to the values of a certain number of previous and following spills. Here, the root mean square (RMS) value for this parameter, evaluated in the range of the neighbouring spills, is used. The RMS is considered to be a fair estimator of the statistical fluctuations, assuming that most of the data is of a good quality. Based on this, the number of neighbouring spills, which are in a certain σ around the RMS, are determined. For all spills this results in a distribution of the numbers of similar neighbours as shown in Figure 4.24. A spill is considered as bad, if the number of similar neighbours is below a defined threshold. An example is shown in Figure 4.23b, where the bad spills are indicated in red.

(a)

(b)
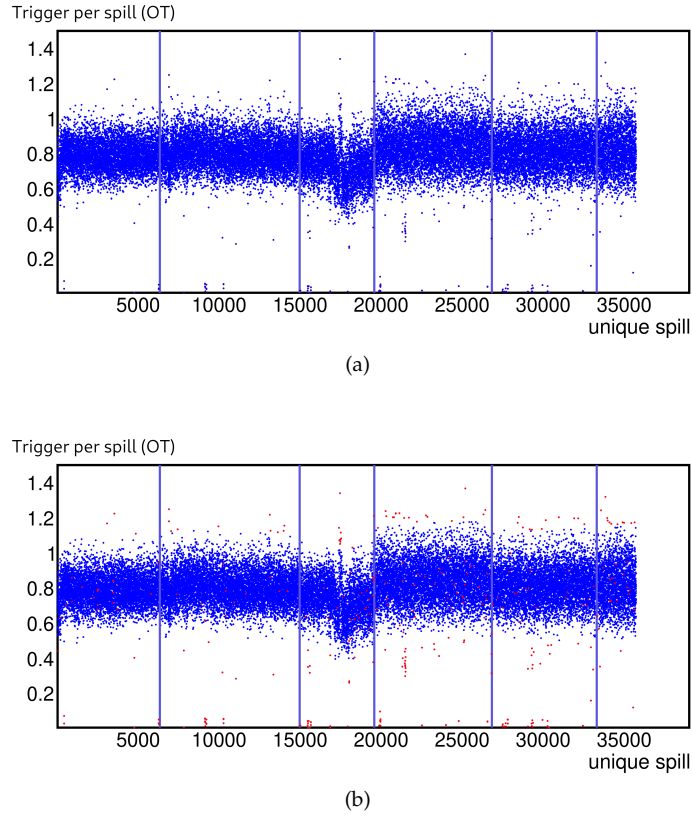
Figure 4.23: (a) Example of a distribution of the number of Outer Trigger per spill normalized to the Random Trigger flux for P09. The vertical lines are marking the different sub-periods in P09, which for most times are correlated to a switch of the beam polarization.
(b) The same distribution but the red points are indicating those spills which are considered to be bad based on the corresponding parameter.
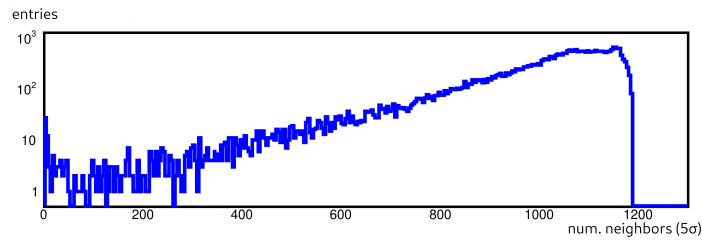
Figure 4.24: Example of a distribution for the number of neighbours in the 5σ range of the RMS value.

Studies showed that a number of ± 600 considered neighbouring spills and a width of 5σ around the RMS are a good estimate for all parameters. The thresholds for the number of requested spills are separately tuned for each parameter and period. In cases where a large number of consecutive spills differ with respect to the global distribution of all spills, it is also possible to directly set a minimal and a max-

92

imal threshold based on the parameter distributions. For specific detector systems and analysis inputs, the distributions showed high fluctuations within a period, which are not compatible with statistical fluctuations. This can be observed especially for the flux when switching the beam charges. Here the analysis in not performed for a full period but separately for each sub-period.

The results of this analysis are provided as a list for all the spills marked as bad. This list contains the run number, the unique spill number in this run and a bit flag indicating the parameter set leading to the rejection of the spill. Using these flags, the bad spill rejection can be adjusted for each physics analysis, only rejecting those spills based on parameters, which are important for a certain physics channel.

4.6 | Quality of the Monte-Carlo simulation

These Sections summarize the work done on reviewing the quality of the Monte-Carlo simulation for DIS events. In Section 4.6.1 the distributions of variables obtained from Monte-Carlo data are compared to the same distributions derived from data. The accuracy of the acceptance is reviewed in Section 4.6.2 by comparing the structure function F_2^p, extracted from the data to a well constrained parametrization.

4.6.1 | Comparison of distributions in data and Monte-Carlo data

This section is a summary of the work done by Marlene Gerstner during her Bachelors thesis (see Ref. [77]).

It comprises a comparison of for e.g. vertex distributions, momentum distributions of the incoming and the scattered muon, and other kinematic distributions between data and Monte-Carlo data. These comparisons were also performed separately for each trigger sub-system in order to identify discrepancies between the trigger and hodoscope performances and their implementation in the siumlation. This allows also to correlate those discrepancies to specific areas of the hodoscopes and investigate their impact on kinematic distributions. These information was used as an input to the PHAST function used to identify the scattered muons (PaHodoHelper::iMuPrim()). The impact of some preliminary restrictions on the hodoscope geometries is illustrated in Figure 4.25. Here, the comparisons between the ϕ-distribution of the scattered muons in data and a Monte-Carlo sample (LEPTO) (both only P09) using only the OT, once without (see Fig. 4.25a) and with geometric restrictions (see Fig. 4.25b), are shown. By applying those restrictions, an improvement in the comparision of the data and Monte-Carlo distributions is obtained, especially for small scattering angles located around the hodoscope deadzones. The restrictions on the hodoscope geometries were further improved in subsequent studies.
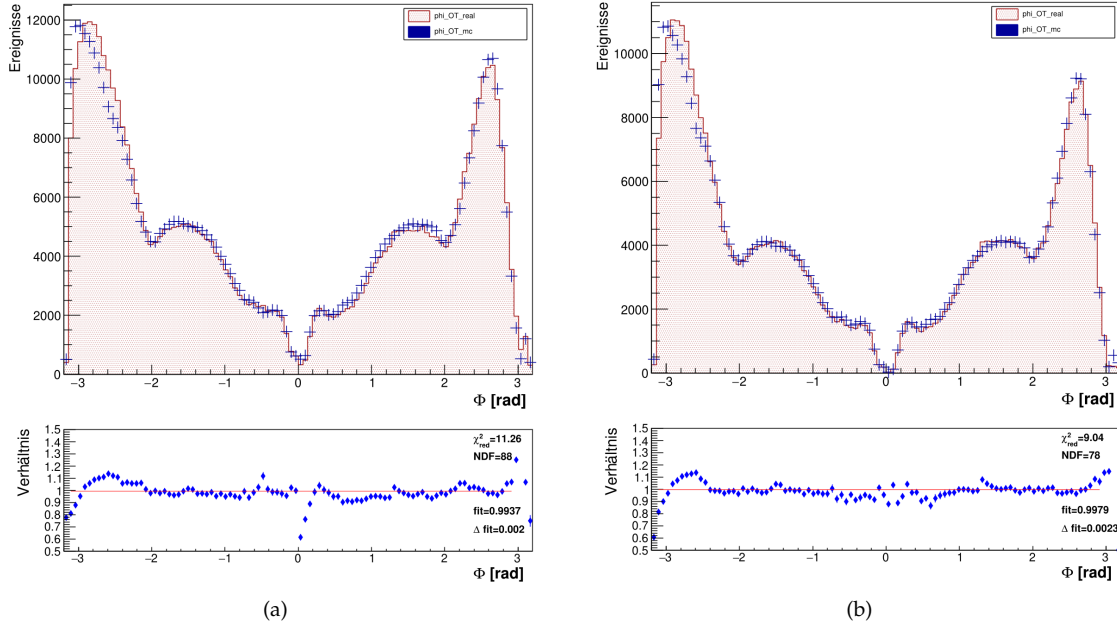
Figure 4.25: Comparison of the ϕ-distribution of the scattered muon in data and Monte-Carlo data when requesting an outer trigger. The distribution is shown before (a) and after (b) removing defined hodoscopes areas. After removing these areas, a slight improvement in the comparison is obtained. Figures taken from Ref. [77].

4.6.2 | Determination of F_2^p

The accuracy of the acceptance determination can be verified by extracting the structure function of the proton F_2^p using identified and acceptance corrected DIS events. By comparing the extracted Q^2 and x_{Bj} dependence to a well known parametrization of F_2^p, any observed discrepancies hint to irregularities in the reconstruction of Monte-Carlo data. This analysis was first performed by Karolina Lavickova and later taken over by Marlene Gerstner.

The DIS cross section in terms of F_2^p can be expressed as:

$$\frac{d\sigma_{\text{DIS}}}{dx_{Bj}dQ^2} = \frac{4\pi\alpha^2}{Q^2 x_{Bj}} F_2^p(x_{Bj}, Q^2) \tag{4.5}$$

$$\left[1 - y - \frac{Q^2}{4E_\mu^2} + \left(1 - \frac{2M_\mu^2}{Q^2}\right)\frac{y^2 + Q^2/E_\mu^2}{2(1 + R(x_{Bj}, Q^2))}\right],$$

$$\text{with } R(x_{Bj}, Q^2) \equiv \frac{\sigma_L}{\sigma_T} = F_2^p(x_{Bj}, Q^2)\frac{1 + 4M_p^2 x_{Bj}^2/Q^2}{2x_{Bj}F_1^p(x_{Bj}, Q^2)} - 1.$$

Using Equation 4.6, F_2^p in bins of x_{Bj} and Q^2 is calculated as:

$$F_2^p(\Delta x_{Bj}, \Delta Q^2) = \sigma_{1\gamma,\text{U}}(\Delta x_{Bj}, \Delta Q^2) \frac{\kappa(x_{Bj}, Q^2)}{A(\Delta x_{Bj}, \Delta Q^2)} \tag{4.6}$$

$$\frac{Q^4 x_{Bj}}{4\pi\alpha^2} \left[1 - y - \frac{Q^2}{4E_\mu^2} + \left(1 - \frac{2M_\mu^2}{Q^2} \right) \frac{y^2 + Q^2/E_\mu^2}{2(1 + R(x_{Bj}, Q^2))} \right]^{-1}$$

$$\text{with} \;\; \sigma_{1\gamma,\text{U}}(\Delta x_{Bj}, \Delta Q^2) = \frac{N_{\text{DIS}}(\Delta x_{Bj}, \Delta Q^2)}{\Delta x_{Bj} \Delta Q^2 \mathcal{L}}.$$

Here, $\sigma_{1\gamma,\text{U}}(\Delta x_{Bj}, \Delta Q^2)$ is the spin-averaged DIS cross section in one-photon-exchange approximation in bins of Δx_{Bj} and ΔQ^2. The expression:

$$\kappa(x_{Bj}, Q^2) = \frac{\sigma_{1\gamma}(x_{Bj}, Q^2)}{\sigma_{\text{meas}}(x_{Bj}, Q^2)}$$

are the radiative corrections, which are calculated as the ratio of the one-photon-exchange approximation and the measured cross section [23]. The ratio $R(x_{Bj}, Q^2)$ is chosen according to the parametrization used for the F_2 extraction by NMC[3] [133] and $A(\Delta x_{Bj}, \Delta Q^2)$ denotes the acceptance.

This calculation was performed separately for each trigger system. An example for the results of F_2^p (solid points), considering only the OT for a specific bin of x_{Bj} and seperated for μ^+ (red) and μ^- (blue) is shown in Figure 4.26. Taking the acceptance into account (open point), which is determined from a DIS Monte-Carlo sample, the F_2^p results show a good agreement with the parametrization (grey solid points). These results led to the conclusion that a decent agreement between the data and Monte-Carlo description for the scattered muon is reached, which is an important input to the DVCS analysis.

---

[3]New Muon collaboration (NMC)
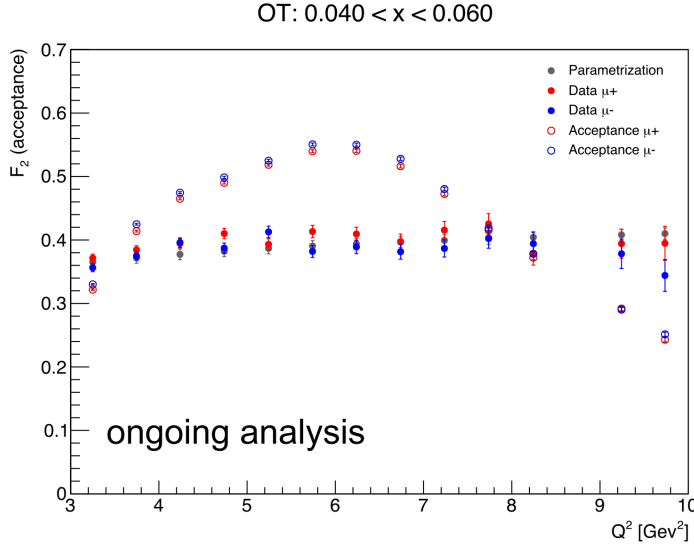
Figure 4.26: Q^2 dependence of the F_2^p (full points) and the acceptance (open points) for the Outer trigger between $0.04< x_{Bj} <0.06$. The results show a good agreement with the parametrization (grey solid points) obtained by NMC. Figure taken from Ref. [136].

4.7 | Calibration and efficiencies of the proton recoil detector

This Section summarizes the work done on the calibrations and the determination of the efficiencies of the proton recoil detector. The calibrations were done by Antoine Vidon and Brian Ventura [165, 166]. The method was already developed and used during the analysis of the 2012 data [88, 114] and then extended and adjusted for 2016/17.

To illustrate the necessity of a calibration, Section 4.7.1 covers the details on the particle reconstruction and the TOF measurement performed by the proton recoil detector. The calibrations are done based on a data set of exclusive produced ρ^0. The corresponding data selection and the different calibration steps are discussed in Section 4.7.2.

Additonal efforts on improving the simulation of the proton recoil detector were done by Brian Ventura. This includes the propagation and clustering of the Monte-Carlo hits, the momentum reconstruction and a smearing of the time stamps to mimic the time and spatial resolution of the detector. This work is not covered within this thesis, but a detailed summary can be found in Reference [165].

The efficiency of the proton recoil detector was determined by Sandro Scherrers [158] and is summarized in Section 4.7.3.

4.7.1 | Reconstruction of particles

As presented in Section 3.1.4 the TOF measurement of the proton recoil detector is performed between its inner (ring A) and outer ring (ring B). To reconstruct a particle it has to be detected by two scintillator elements, one in ring A and the other one in ring B, which are being traversed, assuming the particles to follow a straight line starting from the target cell. As each scintillator element produces a signal in two PMTs, one on the downstream end and one on the upstream end of the corresponding element, the particle is represented by four time-stamps in total. Hence, the Z-positions of the corresponding hits in

the scintillators can be expressed as:

$$Z_{A_i} = \frac{1}{2} v_{A_i} (t_{A_i}^{\text{up}} - t_{A_i}^{\text{down}}) + C_{A_i},$$
(4.7)

$$Z_{B_j} = \frac{1}{2} v_{B_j} (t_{B_j}^{\text{up}} - t_{B_j}^{\text{down}}) + C_{B_j}.$$
(4.8)

Here, A_i and B_j denote the scintillator couple in ring A and B, with i and j corresponding to the index of the 24 elements in each ring ($(i, j) \in [\![1, 24]\!]$). Following this notation the four timestamps are $t_{A_i}^{\text{up}}$, $t_{A_i}^{\text{down}}$, $t_{B_j}^{\text{up}}$ and $t_{B_j}^{\text{down}}$. The expressions v_{A_i}, v_{B_j} refer to the effective speed of light in the scintillator material and C_{A_i}, C_{B_j} to calibration constants.

Using the reconstructed hit positions in the rings, the distance of flight D can be calculated as:

$$D = \sqrt{(R_{B_j} - R_{A_i})^2 + (Z_{B_j} - Z_{A_i})^2}.$$
(4.9)

Here, R_{A_i} and R_{B_j} are the radial distances of the corresponding scintillators to the centers of ring A and ring B. In principle this distance can be different for each scintillator element, which is indicated by the indices. The determination of these distances is described in Section 4.7.2.3.

The time of flight T is determined by using the meantime of the time-stamps in ring A and B according to:

$$T = \frac{(t_{B_j}^{\text{up}} + t_{B_j}^{\text{down}})}{2} - \frac{(t_{A_i}^{\text{up}} + t_{A_i}^{\text{down}})}{2} + C_{A_i, B_j},$$
(4.10)

with C_{A_i, B_j} being additional calibration constants.

Using Equation 4.9 and 4.10 the velocity (β) and the momentum (p) of a reconstructed particle are given as:

$$\beta = D/T \quad \text{and}$$
(4.11)

$$p = m_p \beta \gamma = m_p \frac{\beta}{\sqrt{1 - \beta^2}}.$$
(4.12)

Equation 4.12 does not take the energy loss in the target or other materials into account. To obtain the momentum at the interaction vertex a correction according to the Bethe-Bloch formula is used. More details on this correction can be found in Reference [157].

4.7.2 | Calibration of the proton recoil detector

To determine the calibration constants introduced in Section 4.7.1 a data sample is needed, from which it is possible to extract the information on the recoil proton, like for e.g. its momentum, without actually using the measurement of the proton recoil detector. In principle this is satisfied for any scattering process of a muon and a target proton, where all particles in the final state, except of the recoil proton, are measured by the spectrometer. In these cases the information on those particles can be used to predict the proton kinematics.

The process of choice is the exclusive ρ^0 production ($\mu p \to \mu' p' \rho^0 \to \mu' p' \pi^+ \pi^-$). This process offers a reasonable large cross section to allow for a data sample with enough statistics for the calibration.

4.7.2.1 | Event selection for exclusive ρ^0 sample

The selection of exclusive ρ^0 events is summarized in Table 4.7 and is similar to the one used to select exclusive photons, which is discussed in detail in Section 5.1. The ρ^0 is selected by searching for two oppositely charged hadrons in a mass range of $0.5\,\mathrm{GeV/c^2} < M_{h^+h^-} < 1.1\,\mathrm{GeV/c^2}$. As the recoil proton is not measured, the exclusivity is compelled by applying a restriction on the missing Energy (E_{miss}):

$$E_{miss} = \frac{(p + q - p_{\rho^0})^2 - M_p^2}{2M_p}.$$

(4.13)

Here p, q and p_{ρ^0}, denote the four-momentum vectors of the target-proton, the virtual photon and the ρ^0 candidate.

For a reasonable calibration it is necessary to have a precise prediction of the particle momenta and the interaction vertices. On the example of the polar scattering angle of the recoil proton ($\theta_{p'}$), it can be shown that the spectrometer prediction is not able to perform a decent reconstruction, especially of the longitudinal parameters of the recoil proton. Using the spectrometer measurement $\theta_{p'}$, is expressed as:

$$\tan\theta_{p'} = \frac{(\vec{p}_{p'})_T}{(\vec{p}_{p'})_L} = \frac{(\vec{p}_\mu - \vec{p}_{\mu'} - \vec{p}_{\rho^0})_T}{(\vec{p}_\mu - \vec{p}_{\mu'} - \vec{p}_{\rho^0})_L}.$$

(4.14)

Here, the index T refers to the transverse and L to the longitudinal component of the vectors. In the COMPASS kinematics, using a 160 GeV muon beam to study exclusive reactions at small $|t|$, the denominator would be smaller than 1 GeV but with an uncertainty that is larger 1 GeV. This means that $\theta_{p'}$ cannot be precisely determined, resulting in values between 0 and π. This can be illustrated by using a toy Monte-Carlo and studying the generated and the reconstructed $\theta_{p'}$, as seen in Figure 4.27. Here,
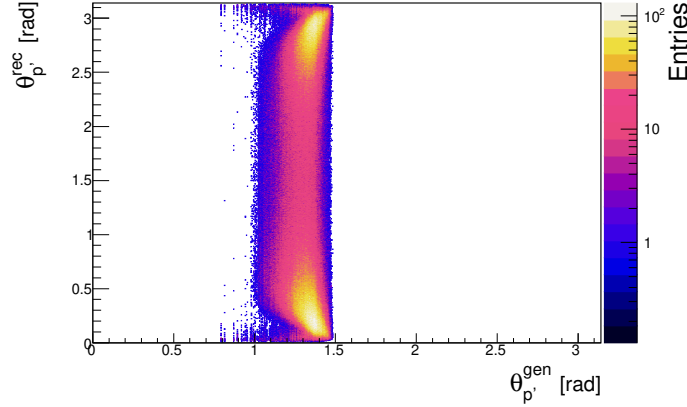
Figure 4.27: Correlation of generated and reconstructed $\theta_{p'}$ using a toy Monte-Carlo. Figure taken from Ref. [165].

one can see that there is no correlation between the both. The reconstruction is not able to provide any information on this angle. However, a kinematic fit can be used to constrain the proton kinematics. Further details on the kinematic fit and its setup for exclusive single photon events are in Section 5.2. In the following only the adjustments necessary to match the topology of exclusive ρ^0 events are discussed.

Following the same nomenclature as in Section 5.2, where $\vec{a}$ and $\vec{p}$ corresponds to a position and momentum vector, the 23 measured ($\vec{k}$) and 6 unmeasured ($\vec{h}$) parameters are:

$$\vec{k} = (\vec{a}_\mu, \vec{p}_\mu, \vec{a}_{\mu'}, \vec{p}_{\mu'}, \vec{a}_{\pi^+}, \vec{p}_{\pi^+}, \vec{a}_{\pi^-}, \vec{p}_{\pi^-}, \vec{p}_p)$$

and

$$\vec{h} = (\vec{p}_{p'}, \vec{a}_{\text{vtx}}).$$

Note that the recoil proton enters as an unmeasured quantity.
In total 12 constrains are applied. Four of those constrains are the result of the energy and momentum conversation and another 8 follow from the requirement that the four measured charged particle tracks (μ, μ', π^+ and π^-) all do originate from a common vertex. By applying 12 constrains and having 6 free parameters, which are estimated by the fit, the number of degrees of freedom is 6 (ndf=12-6=6). The impact of the kinematic fit on $\theta_{p'}$ is demonstrated in Figure 4.28a and 4.28b, where after applying a kinematic fit a reasonable distribution for $\theta_{p'}$ is obtained.

(a)   (b)
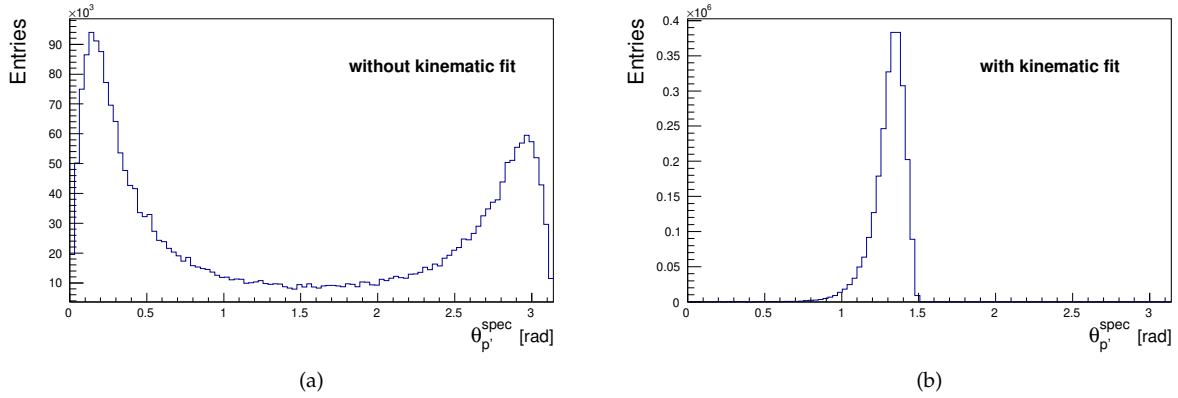
Figure 4.28: Using a toy Monte-Carlo, it can be shown that the $\theta_{p'}$-distribution calculated according to Equation 4.14 is not well reconstructed (a). After applying the kinematic fit a reasonable $\theta_{p'}$-distribution is obtained (b). Figures taken from Ref. [165].

Using the kinematic fit, it is also possible to add selection criteria, based on its results, to the exclusive ρ^0 event selection, like for e.g. requesting the fit to converge with a $\chi^2 < 10$.

Vertex selection	▪ best primary vertex
	
	▪ vertex is in target volume
	
	   – -318.5 cm$< Z_{vtx} <$-78.5 cm
	   – $R_{vtx} <$1.9 cm
	   – $Y_{vtx} <$1.2 cm

Beam muon	▪ track crosses the full target length ▪ momentum: $140\,\mathrm{GeV/c} < p_\mu < 180\,\mathrm{GeV/c}$ ▪ momentum error: $\Delta p_\mu \leq 0.025 \cdot p_\mu$ ▪ meantime: -2 ns $< t_{track} <$ 2 ns ▪ hits in Beam Momentum Station (BMS) ≥ 3 ▪ hits in Scintillation Fibre detectors (SCIFI) ≥ 2 ▪ hits in Silicon strip detectors (SI) ≥ 3
Scattered muon	▪ same charge as incoming muon ▪ rel. radiation length: $X/X_0 >$15 ▪ first measured before and last after SM1: $Z_{first} < 350$ cm and $Z_{last} > 350$ cm ▪ track extrapolations are in the active hodoscope areas (new PointHodoscope function)
ρ^0 selection	two outgoing, opposite charged tracks (h^+, h^-), which traverse less than 10 rel. radiation length ($X/X_0 <$10)
Exclusivity conditions	mass constrain assuming (h^+, h^-)=(π^+, π^-): $$0.5\,\mathrm{GeV/c^2} < M_{h^+h^-} <1.1\,\mathrm{GeV/c^2}$$ missing energy: $$-4\,\mathrm{GeV}< E_{miss} <4\,\mathrm{GeV}$$
Kinematic fit and kinematics	kinematic fit must have converged with a quality of: $$\chi^2_{red} <10$$ kinematic: ▪ $Q^2_{fit} >1\,(\mathrm{GeV/c})^2$ ▪ $0.05< y_{fit} <0.95$

Table 4.7: Summary of the event selection for exclusive ρ^0 production.

4.7.2.2 | Calibration of the azimuthal angle of the scintillator elements

This calibration is done to estimate the ϕ-position of each of the 24 elements of each ring (see Fig. 4.29). The nominal azimuthal angles of the centers of each element in the transverse plane of the detector are:

$$\forall i \in [\![0, 23]\!] \begin{cases} \varphi_{A_i}^{\text{nom}} = 120 - \frac{360}{24}i \\ \varphi_{B_i}^{\text{nom}} = 120 - \frac{360}{24}i + 7.5. \end{cases} \tag{4.15}$$

Here, the additive for $\varphi_{B_i}^{\text{nom}}$ accounts for the fact that the scintillators in ring B are rotated by 7.5° with respect to the ones in ring A.
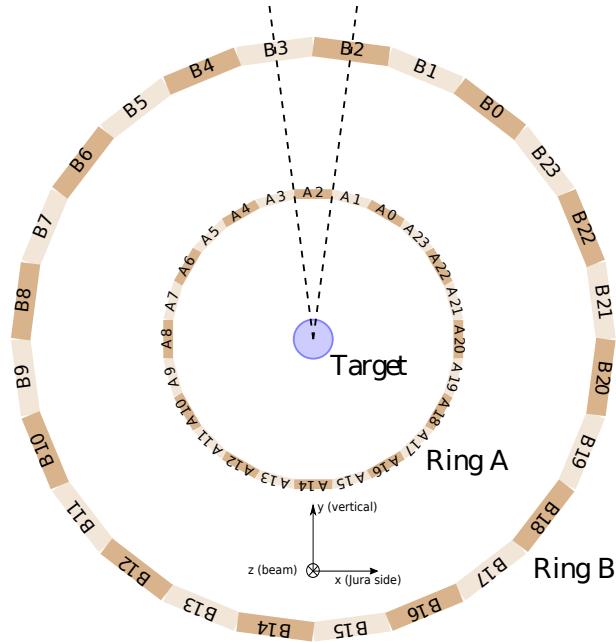
Figure 4.29: Schematic view of the proton recoil detector in the transverse plane. The different sectors are given by the 24 scintillator elements of each ring, which are numbered according to the scheme used during the calibration procedure. The elements of ring B are rotated by 7.5° with respect to the ones in ring A to improve the angular resolution of the detector. Figure taken from Ref. [165].

To estimate the azimuthal positions, one uses the distribution of the relative differences between the φ-distribution of the predicted protons in an element and its corresponding nominal position ($\Delta\varphi_{[A,B]_i} = \varphi_{[A,B]_i}^{\text{spec}} - \varphi_{[A,B]_i}^{\text{nom}}$). The φ-distributions are obtained by correlating a signal in each element to the expected φ-distribution of the spectrometer prediction ($\varphi_{[A,B]_i}^{\text{spec}}$). As this prediction is relative to the interaction vertex, a correction has to be applied to obtain its values relative to the zero axis in the laboratory frame (X=Y=0) [165]. An example for the distributions $\Delta\varphi_{[A,B]_i}$ is shown in Figure 4.30. These distributions are fitted using a symmetric sigmoid function to extract the calibration parameter used for the translation

between the exact and the nominal φ-positions:

$$\forall i \in [\![0,23]\!] \begin{cases} \varphi_{A_i} = \varphi_{A_i}^{\mathrm{nom}} + \varphi_{A_i}^{\mathrm{calib}} \\ \varphi_{B_i} = \varphi_{B_i}^{\mathrm{nom}} + \varphi_{B_i}^{\mathrm{calib}}. \end{cases} \tag{4.16}$$

(a)   (b)
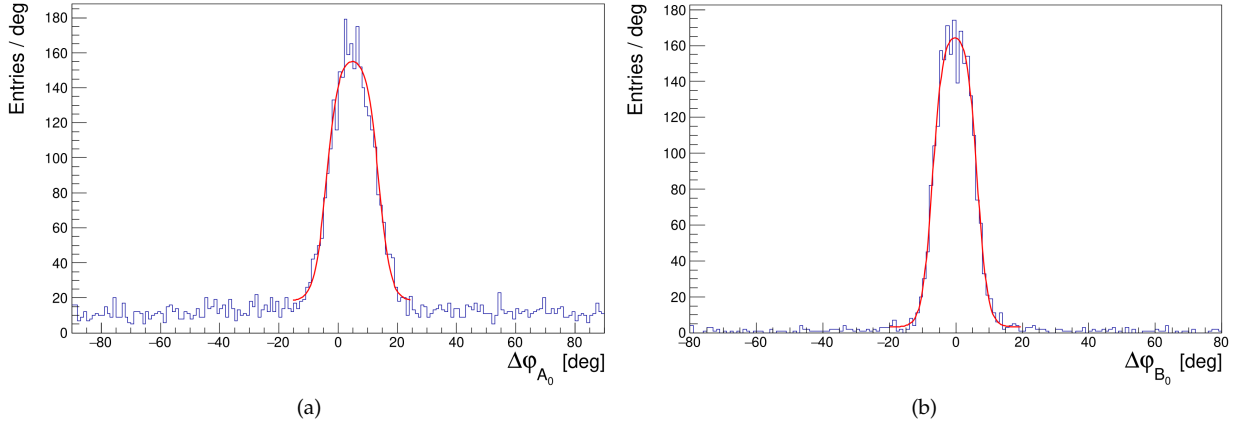
Figure 4.30: $\Delta\varphi_{[A,B]_i} = \varphi_{[A,B]_i}^{\mathrm{spec}} - \varphi_{[A,B]_i}^{\mathrm{nom}}$ distributions for element $i=0$ of ring A and B. The calibration parameters $\varphi_{[A,B]_i}^{\mathrm{calib}}$ are determined by fitting the distributions using a symmetric sigmoid function (red). Figures taken from Ref. [165].

4.7.2.3 | Study of the radial positions of the scintillator elements

According to the layout of the proton recoil detector the rings should be aligned around a common center with an radius of 250 mm for ring A and 1100 mm for ring B. Investigations on the alignment and the geometry, after the detector was assembled, showed that the two rings are cylindrical shaped but having slightly larger radii then intended:

$$R_{A,\mathrm{nom}} = 257\,\mathrm{mm},$$
$$R_{B,\mathrm{nom}} = 1116\,\mathrm{mm}.$$

Also the rings are not perfectly centered around the Z-axis ($X=Y=0$) and not aligned around the same axis either.

For an estimate of the corresponding deviations and the actual radial distances of the elements with respect to the Z-axis, one can study their deviations of the actual φ-positions from their nominal positions. The deviations for each element in ring A and B as a function of the corresponding φ-positions are shown in Figure 4.31a and 4.31b.

The oscillation obtained for ring A are a clear hint that the elements are not concentrically centered around the Z-axis, while for ring B the deviations are much smaller.

To extract the effective centers of the rings ($\vec{C}$) the corresponding distributions are fitted by:

$$F(\varphi) := p_0 + p_1 \sin(p_2 \cdot \varphi + p_3), \tag{4.17}$$

(a)   (b)
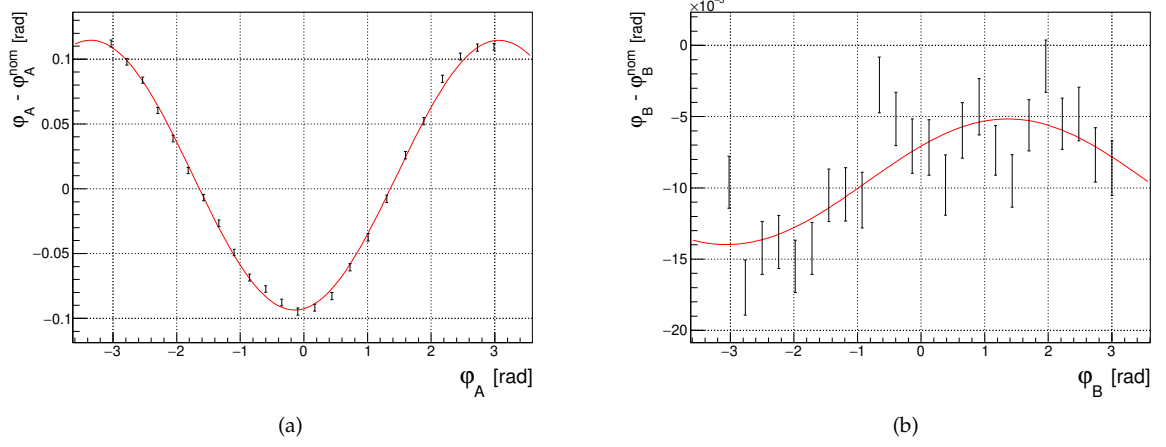
Figure 4.31: Azimuthal deviations from its nominal positions (see Eq. 4.15) as function of the azimuthal positions of the elements for ring A (a) and ring B (b). The fit according to Equation 4.17 is shown in red. Figures taken from Ref. [165].

where p_i denote a free parameter. The centers of the rings are given by:

$$\vec{C} = \begin{pmatrix} r_C \\ \varphi_C \end{pmatrix} = \begin{pmatrix} R_{\text{nom}} \cdot \tan|p_1| \\ -p_3 \end{pmatrix}. \tag{4.18}$$

The radius R as function of φ ($\forall \varphi \in \{\varphi_{[A,B]_i}, i [\![0,23]\!]\}$) with respect to the central axis (X=Y=0) is then calculated as:

$$R(\varphi) = -p/2 + \sqrt{p^2/4 - q} \quad \text{with} \tag{4.19}$$

$$p := -2\vec{\varphi} \cdot \vec{C},$$

$$\vec{\varphi} := \begin{pmatrix} 1 \\ \varphi \end{pmatrix},$$

$$q := |\vec{C}|^2 - R_{\text{nom}}^2.$$

The results are displayed in Figure 4.32. The center position of ring A is determined to be $X =$-3.73 mm and $Y =$-26.6 mm, which confirms that this ring is slightly out of focus. For ring B the resulting center position is $X =$-4.05 mm and $Y =$2.79 mm. Considering the large uncertainty of the fit and the relative large radial dimensions of the outer ring this rather small deviation is being neglected.

(a)

(b)
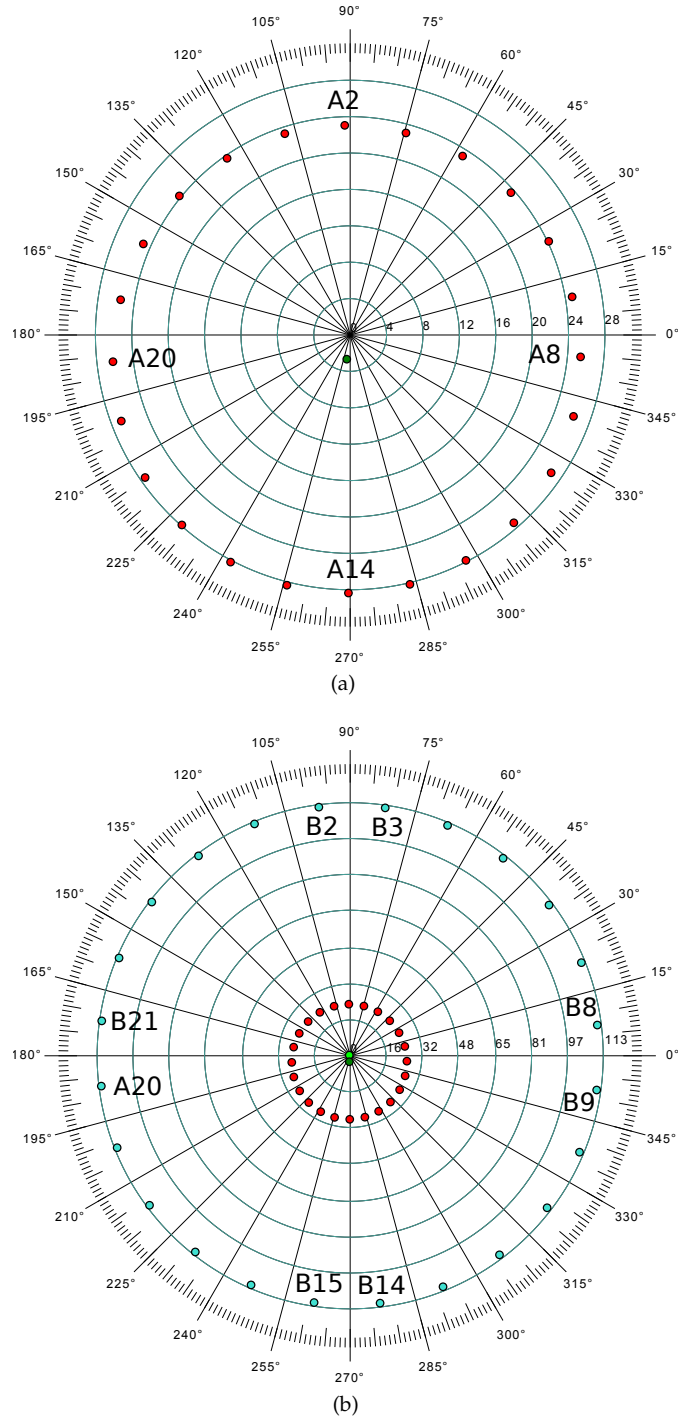
Figure 4.32: (a) Azimuthal positions of the centers of each element in ring A (red). The effective center of ring A is marked in dark green, while the nominal positions of each element are indicated by the black lines. The center of ring A is determined to be $X =$-3.73 mm and $Y =$-26.6 mm.
(b) The same with the azimuthal center positions of the ring B elements added (cyan). The effective center (marked in light green) only shows a small deviation ($X =$-4.05 mm and $Y =$2.79 mm), which is neglected considering the large radial dimension of ring B. Figures taken from Ref. [165].

4.7.2.4 | Calibration of the longitudinal position (Z-position)

As previously discussed in Section 4.7.1 also the longitudinal positions of the hits, reconstructed in the scintillator elements (see Eq. 4.8), have to be calibrated. To determine the corresponding calibration constants for each scintillator element, one uses an estimate of the actual Z-positions correlated to a hit in the elements. These estimations are extracted from the prediction of the recoil proton in the identified exclusive ρ^0 events. As an example for a hit in ring B and following the schematics in Figure 4.33 an estimate for the longitudinal hit position (Z^{spec}) is given by:

$$Z_{B_i}^{\text{spec}} = \frac{R_{B_i} - D_V}{\tan(\theta_{p'}^{\text{spec}})} + V_Z \text{ with} \tag{4.20}$$

$$D_V = \sqrt{V_X^2 + V_Y^2} \cdot \cos(\varphi^{\text{spec}} - V_\varphi). \tag{4.21}$$

Here V_X, V_Y and V_Z refers to the components of the vector pointing to the interaction vertex $\vec{V} = (V_X, V_Y, V_Z)$ and V_φ to the corresponding azimuthal angle ($V_\varphi = \arctan(V_Y/V_X)$).
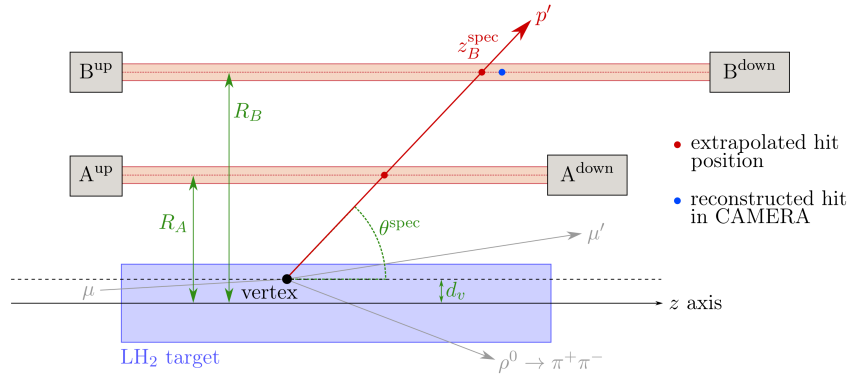
Figure 4.33: Schematic view of the detection principle of the proton recoil detector. Figure taken from Ref. [165].

With Equation 4.21 and 4.8, the calibration constants can be extracted by a straight line fit of the correlation between the corresponding Z^{spec} and the time stamps. Examples of these correlations for an scintillator element in ring A and B, as well as the fit, are shown in Figure 4.34a and 4.34b.

This procedure is performed for all scintillator elements in ring A and B. The calibration constants are in the order of approximately -1500 mm for ring A and -1400 mm for ring B. The exact values can be found in the Appendix of Reference [165].
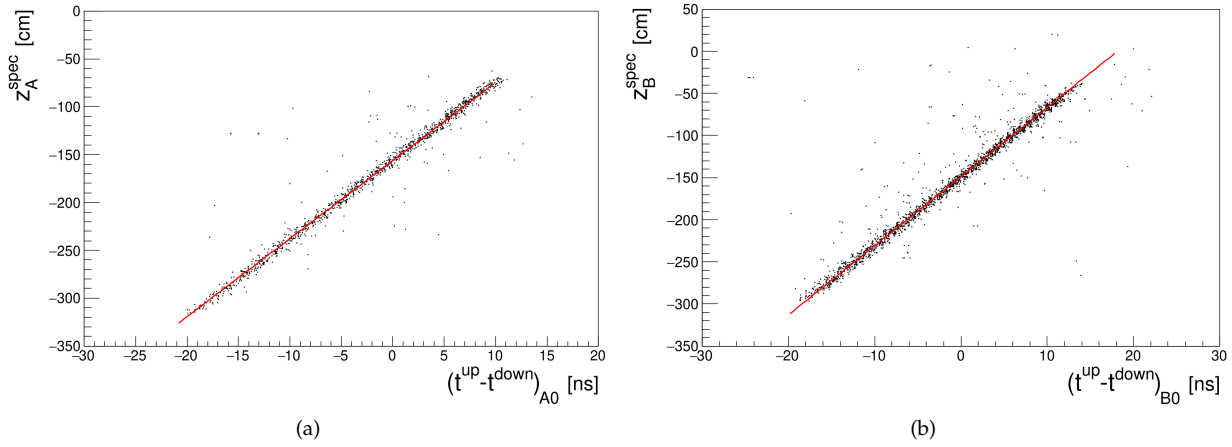
Figure 4.34: Reconstructed longitudinal hit positions in element 0 of ring A (a) and ring B (b) as function of the time difference between the measurement of the corresponding upstream and downstream PMTs. The distributions are fitted (red) according to Equation 4.8 (see Sec. 4.7.1) to determine the corresponding calibration constants for the longitudinal hit position (C_{A_i} and C_{B_j}). Figures taken from Ref. [165].

4.7.2.5 | Time of flight calibration

The final step in the calibration is the determination of the calibration constants for the time of flight (see Eq. 4.10 in Sec. 4.7.1). Using Equation 4.10 and considering the relation between the particle velocity to the distance and time of flight (see Eq. 4.12), the calibration constants are expressed as:

$$C_{A_i,B_j} = \frac{D_{A_i,B_j}}{\beta} - T_{A_i,B_j}^{\text{raw}} \quad \text{with} \tag{4.22}$$

$$T_{A_i,B_j}^{\text{raw}} = \frac{(t_{B_j}^{\text{up}} + t_{B_j}^{\text{down}})}{2} - \frac{(t_{A_i}^{\text{up}} + t_{A_i}^{\text{down}})}{2}. \tag{4.23}$$

To determine them an estimation of β is needed, which is in case of the recoil proton an unknown parameter. To perform this calibration one can use particles with a known velocity close to the speed of light ($\beta = 1$).

This condition is used in two different kinds of studies. One is using the signals produced by cosmic muons. This study was performed by Antoine Vidon and is described in detail in Reference [166].

The other one is based on the observed strong correlation between the uncorrected time of flight (T_{A_i,B_j}^{raw}) and the distance of flight (D_{A_i,B_j}). This correlation is shown in Figure 4.35 and is mainly caused by δ-rays passing the inner and outer ring at the speed of light. This study was performed by Brian Ventura and more details on this are in Reference [165]. It resulted in values for the calibration constants between 20 ns and 25 ns extracted from straight line fits of distributions like the one shown in Figure 4.35. The exact values are in the Appendix of Reference [165].
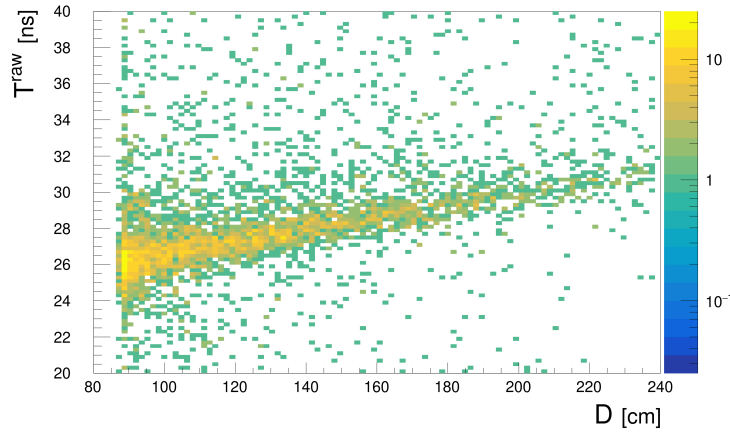
Figure 4.35: T^{raw} as function of the flight distance D for the element pair (A_0,B_0). The mean velocity β is extracted according to Equation 4.22, by a straight line fit of this distribution. The calibration constant C_{A_i,B_j} is given by the interception point of the fit and the Y-axis. Figure taken from Ref. [165].

4.7.3 | Efficiencies of the proton recoil detector

As for the calibration also the determination of the efficiency requires a data sample of predicted recoil protons, which are compared to actually measurements of the detector. Here, also the exclusive ρ^0 data sample is used. As mentioned in Section 4.7.1 a proton is detected by the four PMT signals belonging to two scintillator elements. Therefore, the total efficiency of the proton detection in a scintillator pair depends on the efficiency of each of the corresponding PMTs. The efficiency of a PMT is determined by comparing the number of detected recoil protons, which are associated to hits in the three remaining PMTs, to the number of hits in the corresponding fourth PMT. This principle is illustrated in Figure 4.36.
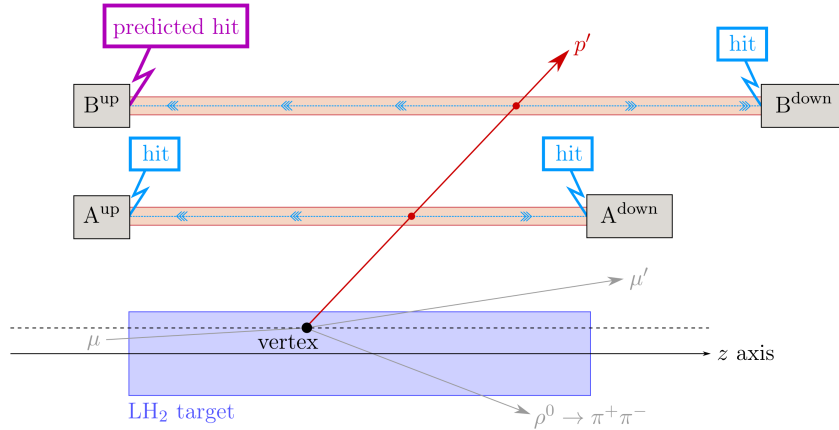
Figure 4.36: Schematic of the method to determine the proton recoil detector efficiency. Figure taken from Ref. [165].

With these predicted hits (N_{pred}) and the actually measured hits (N_{meas}), the efficiency for each PMT

107

and the corresponding binomial error are expressed as:

$$\epsilon = \frac{N_{\text{meas}}}{N_{\text{pred}}} \quad \text{and} \quad \sigma_\epsilon = \frac{1}{N_{\text{pred}}} \sqrt{1 - \frac{N_{\text{meas}}}{N_{\text{pred}}}}. \tag{4.24}$$

Examples of the Z-dependence of the efficiencies for a scintillator element in ring A and B are shown in Figure 4.37, separately for the upstream (blue) and downstream (red) PMT. In general the efficiencies in ring B are high and independent on the Z-position where the proton crosses the scintillator element. For ring A a decrease in the efficiencies is visible. This decrease is due to the much smaller thickness of the elements of ring A compared to those of ring B. For the latter, the amount of produced scintillation light is increased and it propagates better to the ends of the scintillator. In ring A the impact of the attenuation length causes a decrease of the efficiency of the PMT, which is further away from the location the light is produced. The difference between the upstream and the downstream PMT is due to the much longer light guides used to attach the downstream PMTs to the scintillator elements.

(a)   (b)
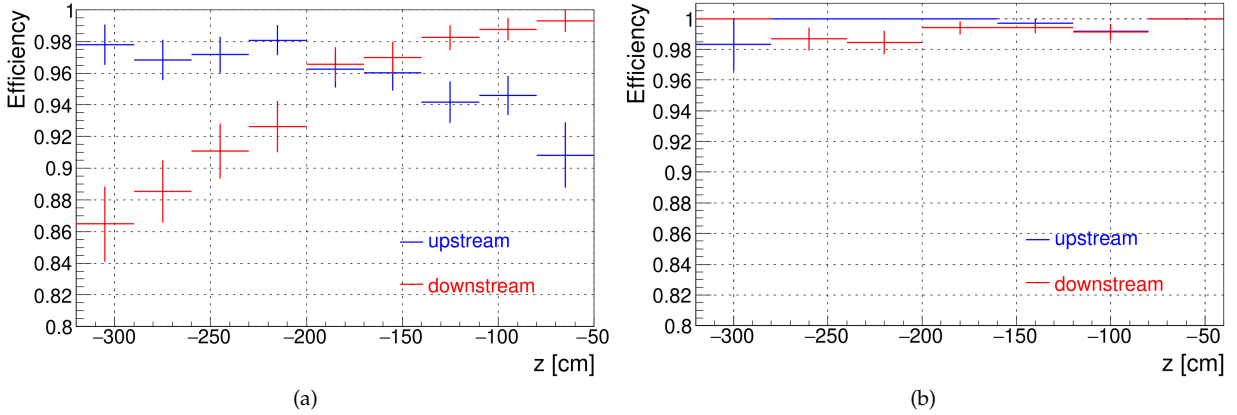
Figure 4.37: Efficiencies for the upstream (blue) and the downstream (red) PMT of element A0 (a) and B0 (b) as function of the longitudinal hit position. The decrease of the efficiencies for A0 are caused by the attenuation length of the thin light guides. The difference between the upstream and downstream PMT are due to the much longer light guides attached on the downstream side. Figures taken from Ref. [158].

4.8 | Calibration of the electro-magnetic calorimeters

For a precise measurement of the real photons by the ECALs, calibrations of the cluster time and energies have to be performed. The calibration methods and the identification of calorimeter cells, which showed a bad performance during the data taking are summarized in the Sections 4.8.1 and 4.8.2. The quality of the photon measurement can be further improved by formulating requirements on the cluster timing, which are applied in the event selection. These studies are discussed in Section 4.8.3. Most of the calibration are only needed for reconstructing data. A calibration of the cluster energy is also needed as an input to the Monte-Carlo simulation. The simulation of the clusters and the corresponding energy calibration is described in the Sections 4.8.4 and 4.8.5.

The studies summarized in the following Sections were performed by Brian Ventura, Sergei Gerassimov and Po-Ju Lin. Further details can be found in Reference [165].

4.8.1 | Timing calibration and bad cell identification

In this analysis a study of the time response of each of the cells of the three ECALS (6424 cells in total) is performed. The term time response refers to the study of the difference of the cluster time with respect to the trigger time. The cluster time is given by the time stamps the signals of each cell are assigned to, when the analog PMT signal is converted by an Sampling Analog-Digital-Converters (SADCs) . Ideally the readout of the SADCs is synchronized to an incoming trigger signal. Hence, in the differences of cluster and trigger time a peak around zero is observed, like shown in Figure 4.38a. If this is not the case, the time is corrected by a calibration constant, which simply is given by the difference between the position of the observed peak and zero. The calibration constants can be extracted by a peak finding algorithm using a fitting procedure.

Some examples of observed time distributions are shown in Figure 4.38a, 4.38b and 4.38c. An almost perfectly timed in cell can be seen in Figure 4.38a. The mean of the applied fit, which is indicated in red, is used as the corresponding calibration constant. In the case displayed in Figure 4.38b no peak at all is observed. These kind of cells are counted as bad cells and are not considered in the reconstruction to prevent any possible noise pollution of neighbouring cells. Another example for an observation is shown in Figure 4.38c. The double peak is caused by jumps in the cluster timing, which appeared during the data taking. In this case the simple peak find algorithm can not distinguish between those peaks, but as those cells are showing a clear signal, they should not be considered as bad. In order to identify such cells and also find the cells, which should be excluded, the algorithm is extended by a more sensitive bad cell detection method. In general this method is investigating the time distribution on a smaller time scale like run or spill vise and uses limits for e.g. the signal to noise ratio and the amount of spills with a successfully performed fit to conclude on the cell performances. More details on this investigations are in Reference [165].

(a)

(b)

(c)
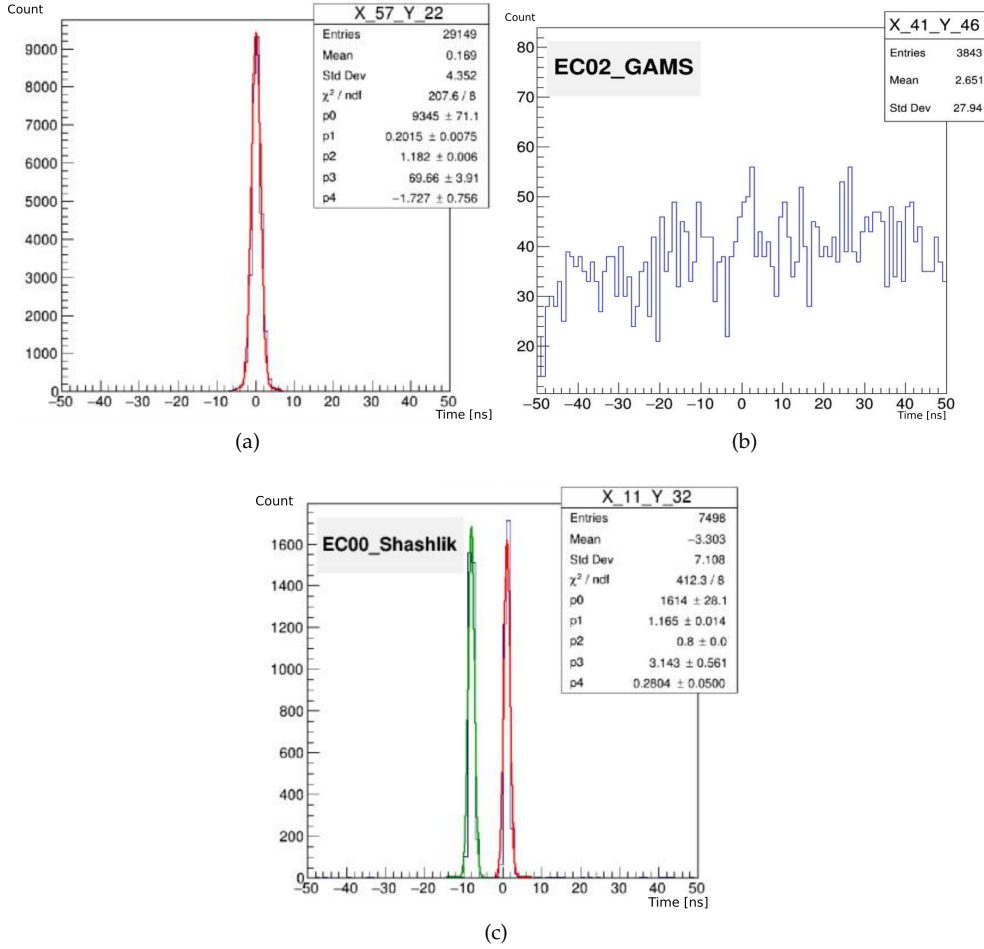
Figure 4.38: Example of various timing distributions of ECAL cells. (a) Common timing distribution for an ECAL2 cell. The mean of the signal fit (red) determines the calibration, which is applied for the corresponding cell. (b) Noisy cell with no timing information. (c) Double peak in a ECAL0 cell. The fits of both peaks are shown in red and green. Figures taken from Ref. [165].

4.8.2 | Energy calibration

The energy calibration of the calorimeters is done in multiple steps and was mainly performed by Sergei Gerassimov. These calibration steps also differ for each ECALs. In detail the calibration is expressed as:

$$A^{i,j}_{[GeV]} = A^{i,j}_{[ADC]} \times C^{i,j_0} \times \frac{L^{i,j_0}}{L^{i,j}} \times \frac{\sum_{i=1}^{N} \frac{L^{i,j_0}}{L^{i,j}}}{N} \times S^{i,p} \times S^{j}. \tag{4.25}$$

Here, the indices refer to a specific calorimeter cell i, and a run j belonging to a period p.

The first part of Equation 4.25 corresponds to the translation of the signal amplitude in the ADC channels $A_{[ADC]}$ to the energy deposit in the corresponding calorimeter cell $A_{[GeV]}$. This translation is done by a calibration coefficient C. The procedure to determine these coefficients includes also a tuning of the high-voltage settings of the PMTs connected to the corresponding cell.

110

For ECAL1 and ECAL2 this is done using a 40 GeV electron beam, which has a small diameter and a narrow energy distribution. This makes it possible to only expose a distinct section of the calorimeters to the beam. The total charge deposit in each cell is measured and compared to the energy of the electron beam. This comparison is used for a tuning of the high-voltage settings and the determination of the calibration coefficients. In this procedure the beam is deflected in vertical direction, while simultaneously moving the calorimeters in horizontal direction. This allows to take one spill of data separately for each calorimeter cell.

For ECAL0 it is not possible to use the electron beam as it cannot be moved with respect to the beam axis. Instead the calibration is done using the halo component of the muon beam. The energy deposit in the calorimeter modules give a first reference for the high-voltage settings. The properties of the muon beam are not the same as used during physics data taking, instead it is aimed for a highly defocused beam.

This kind of calibrations are usually done once per data taking in specific runs, which are indicated by j_0.

In addition the gains of the PMTs are also monitored by an Light-Emitting-Diode (LED) monitoring system. The signal amplitudes L of the LED system are recorded for each run. This allows to extract a correction to the calibration coefficients given by the ratio of the LED signal amplitude during the calibration L^{j_0} to the LED signal amplitude in a specific run L^j. Studies of the stability of the LED system, showed that for ECAL2 an instability of the power supply led to a jump in the LED signals. To correct this an additional factor only valid for ECAL2 and for spills taken in a distinct period of time was introduced:

$$N_j = \frac{\sum_{i=1}^{N} \frac{L^{i,j_0}}{L^{i,j}}}{N},$$

where N denotes to the number of cells in ECAL2.

To further improve the calibration, a data sample of reconstructed π^0 is used. Here, the measured energies of the two photons originating from the π^0 decay are used to correlate the signals in the cells corresponding to the detection of either one of the photons. The additional contributions to the energy distribution $S^{i,p}$ and S^j are chosen to provide the best reproduction of the π^0-mass peak. The data samples used for the extraction of those corrections, where either taken by using a charged pion beam scattered off the liquid hydrogen or by using the physics data taken with the muon beams. This is done because detailed studies showed that the correction extracted from the pion beam S^j is not sufficient over the full period of 2016 data taking. To compensate for this, the additional correction factor $S^{i,p}$ is extracted from identified π^0 events in the muon data integrated over a full period.

These corrections to the calibration are applied on level of the event selection by calling UserEvent16 in preparation of any UserEvent including the selection of calorimeter cluster.

For a more detailed description on the impact of the different corrections to the calibration see Reference [165].

4.8.3 | Cluster timing requirements

A study of the correlation between the cluster energies and their timing done by Brian Ventura showed, that in the exclusive photon events an energy dependent selection on the cluster time can be applied to remove noise contributions. An example for the observed correlations and the resulting restrictions to a $3\sigma_t$ distance from the mean of the signal (μ_t) is shown in Figure 4.39. Here, the data available for period 09 is used. The resulting timing restrictions are indicated as a purple dashed line and are extracted separately for each ECAL and cell type. To define them a polynomial parametrization is used to adjust to the various shapes observed when investigating different types of cells. For more details see Reference [165].

(a) ECAL0 Shashlik modules.

(b) ECAL1 Shashlik modules.

(c) ECAL1 GAMS modules.

(d) ECAL1 Mainz modules.

(e) ECAL1 OLGA modules.

(f) ECAL2 Shashlik modules.

(g) ECAL2 RGAMS modules.

(h) ECAL2 GAMS modules.
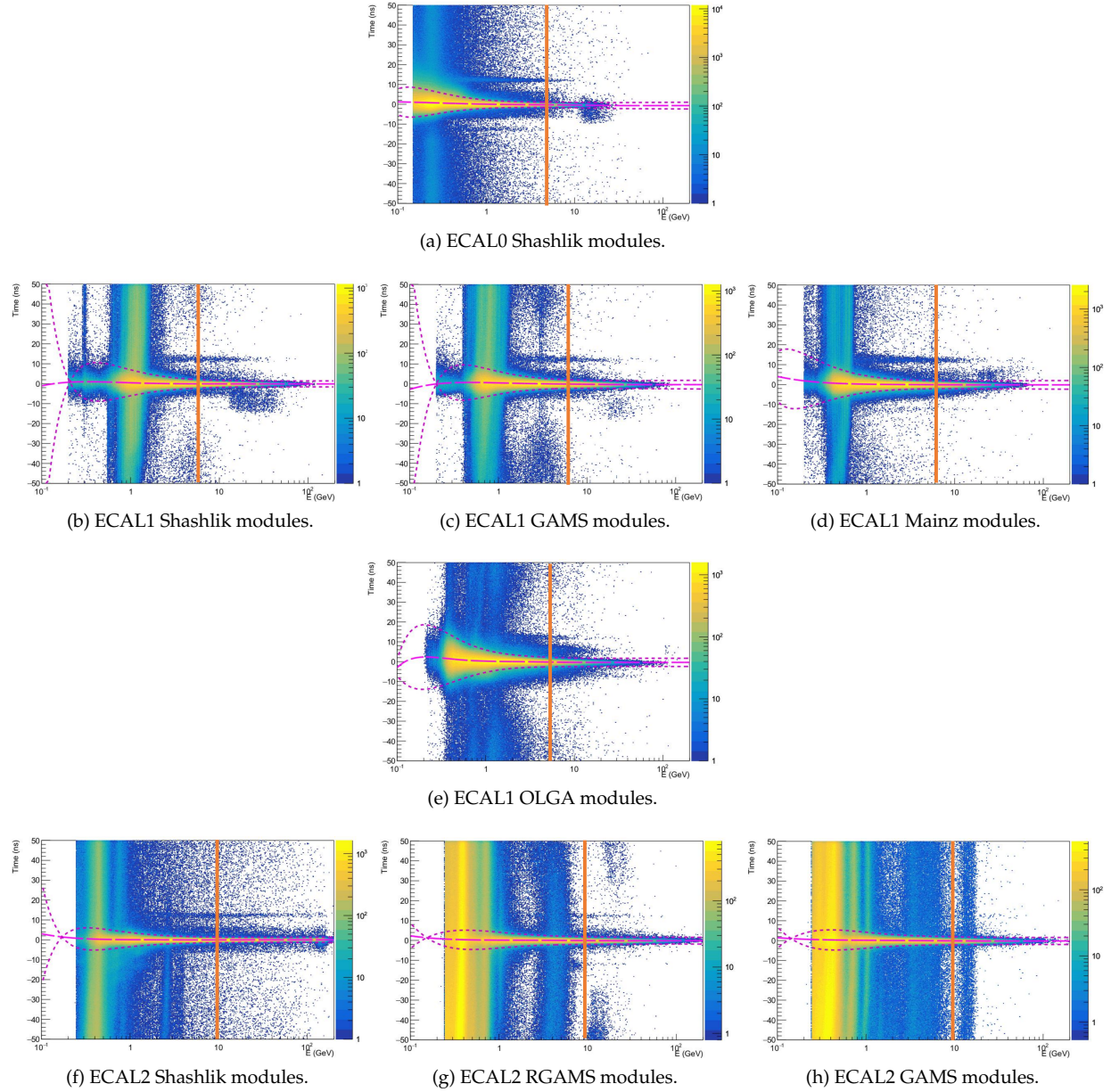
Figure 4.39: Correlation of the cluster timing and cluster energy for the different kinds of ECAL cells. The corresponding timing cuts at a distance of $3\sigma_t$ from the mean signal μ_t are indicated by the purple dashed lines. Figures taken from Ref. [165].

112

4.8.4 | Cluster simulation

The previous Sections summarized all the steps of calibration procedure, which are needed for reconstructing data. In the case of simulated data some additional calibration and optimizations are needed for simulating the electromagnetic showers produced in the ECALS and the corresponding detector responses.

The simulation of those showers is quite complex due to the production of a high amount of secondary particles, which all have to be tracked and propagated. Here, the computing time increases approximately linear with the energy of the incoming particle (see Ref. [161]). This results in extended computing times in case of the high energy COMPASS kinematics. Although the GEANT4 software offers the possibility to speed up the simulation by reducing its precision, it was found that the settings could not provide a sufficient precision within a reasonable processing time. To approach this problem, it was decided to use a tool called GFlash (see Ref. [91]). Instead of simulating each secondary particle of the shower individually, this tool offers a parametrization of longitudinal and radial shower profiles and their corresponding energy deposits. The tool was directly included in the TGEANT software (see Ref. [161]) to offer the possibility to easily adjust the parameters for the conditions of the COMPASS ECALs. The details of this procedure and a validation of the parameter set are given in Reference [161] and [152].

4.8.5 | Energy calibration for simulated data

The simulated energy deposit has to also be tuned to match it with the energy of the incident particle after the cluster reconstruction. For the 2012 setup this calibration was performed, but several changes in the simulation and the description of ECAL1 and ECAL2 were done to correct for former inaccuracies in the description of the material budget.

The necessary re-calibration was done by Po-Ju Lin. The calibration is performed assuming a linear correlation between the incident particle energy E_{gen} and the reconstructed cluster energy E_{rec}:

$$E_{\text{rec}} = E_{\text{gen}} \cdot b. \tag{4.26}$$

As the typical energies and angles of the incident particle are different for each cell type the calibration is also performed separately for each of them. The b parameter itself can be determined by a study of the correlation of the energy residuals ($\Delta E = E_{\text{gen}} - E_{\text{rec}}$) to the energy of the incident particle. An example for these correlations is shown in Figure 4.40.

The parameter b is given by the difference between the mean of the distributions to $\Delta E \equiv 0$. A summary of the resulting values of b is in Table 4.8. As a final step the relative residual distributions as

Cell type	b^{-1}
ECAL0 Shashlik	0.8409
ECAL1 Shashlik	0.8440
ECAL1 GAMS	0.8980
ECAL1 Mainz	0.9762
ECAL1 OLGA	0.9598
ECAL2 Shashlik	0.8304
ECAL2 RHGAMS	0.8735
ECAL2 GAMS	0.8706

Table 4.8: Summary of the extracted values for b^{-1}. Provided by [120].

(a) ECAL1 Shashlik modules.

(b) ECAL1 GAMS modules.

(c) ECAL2 Shashlik modules.

(d) ECAL2 RGAMS modules.
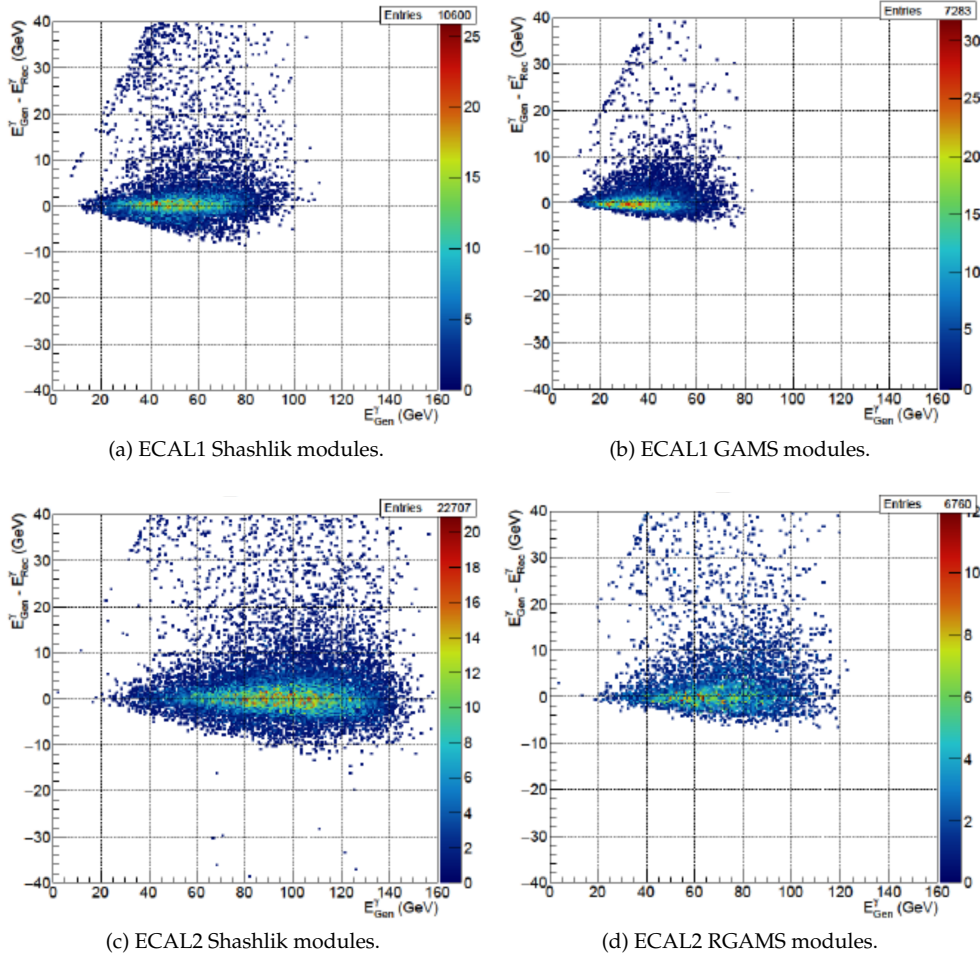
Figure 4.40: Correlation between $\Delta E = E_{\text{gen}} - E_{\text{rec}}$ and E_{gen} of the photon. The parameter b is given by the difference between the mean of the distributions to $\Delta E \equiv 0$. Figures provided by [120].

a function of reconstructed cluster energy, as shown in Figure 4.41, are fitted according to:

$$\frac{\Delta E}{E} = a + \frac{b}{E} + \frac{c}{E^2}. \tag{4.27}$$

Here, the previously determined values of b are used. The results of these fits provide the final energy calibration applied to the simulated data.

As for the energy calibration for data (see Sec. 4.8.2) this calibration is also applied on PHAST level by calling UserEvent15 before the event selection.
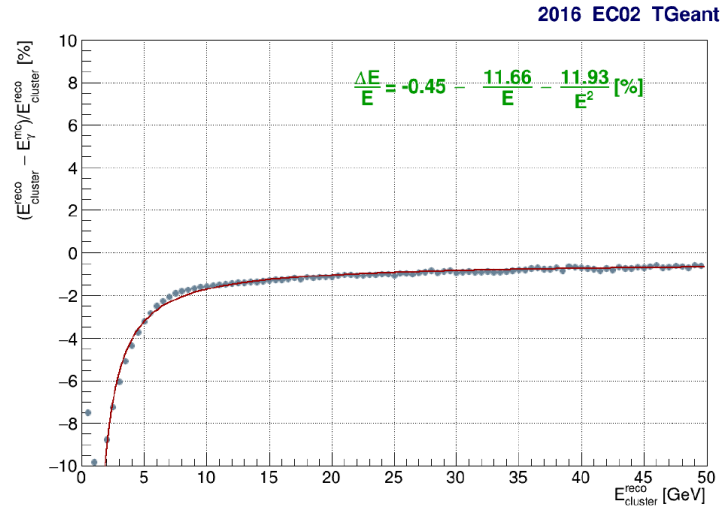
Figure 4.41: Relative residual distributions between the reconstructed and generated cluster energies as a function of reconstructed cluster energy for ECAL2. The fit according to the parametrization given in Eq. 4.27 is indicated as a red line. The result of the fit is given in green. Figure provided by [76].

The exclusive photon event data sample

This Chapter is dedicated to the identification of the exclusive photon events, which are contained in the muon-proton scattering data sample recorded by COMPASS. Section 5.1 presents an overview of the applied selection criteria. Within the selection also a kinematic fit is applied, which is discussed in further detail Section 5.2. The determination of the Bethe-Heitler contribution and the π^0-background contamination are addressed in Section 5.3.1 and 5.3.2. The Chapter concludes with a discussion of the kinematics of the selected photon events. It includes the kinematics of all previously mentioned contributions, especially that of the identified DVCS events.

5.1 | Exclusive photon event selection

The objective of the event selection is to identify those events only containing an incoming and outgoing muon, which define an interaction vertex, a real photon and a recoil proton. The full event selection is summarized in the Tables 5.1 and 5.2.

   The events have to be recorded by at least one of the physics trigger systems (MT, LT or OT) and within the time window of the spill (see Section 4.1). The spill has to pass the stability conditions according to the bad spill analysis presented in Section 4.5.2.
As a first step the vertex candidates are selected by identifying the muons. Here, only vertices are used, which have a single charged outgoing track that is assigned to the scattered muon. More details are discussed in Section 5.1.1. For identifying the real photon the ECAL cluster information is used. The details on the corresponding selection criteria are discussed in Section 5.1.2. Events that have more then a single photon candidate fulfilling these criteria are rejected. The proton candidates are identified by the measurement of the proton recoil detector using the requirements, which are discussed in Section 5.1.3. As all particles are measured the event selection is further improved by applying exclusivity conditions and a kinematic fit. These are discussed in detail in the Sections 5.1.4 and 5.2.
The exclusive photon events are build by combining the vertex candidates to the proton candidates and the real photon and rejecting all events, which have multiple valid candidates left after applying the full selection.

Event	■ apply energy calibration for ECALs:
	
	   – for real data call UserEvent16 (see Sec. 4.8.2)
	   – for simulated data call UserEvent15 (see Sec. 4.8.5)
	
	■ reject bad spills
	
	■ event within the time in spill window
	
	■ trigger: MT, LT and/or OT

Muon and vertex selection	**Vertex requirements:**
	
	■ in target
	
	   – -318.5 cm$< Z_{\text{vtx}} <$-78.5 cm
	   – $R_{\text{vtx}} <$1.9 cm
	   – $Y_{\text{vtx}} <$1.2 cm
	
	■ exactly one outgoing charged track
	
	Incoming muon track (μ):
	
	■ first measured before the target
	($Z_{\text{tgt,min.}}$=-318.5 cm)
	
	■ track crosses the full target length
	
	■ momentum: 140 GeV/c $< p_\mu <$ 180 GeV/c
	
	■ momentum error: $\Delta p_\mu \leq 0.025 \cdot p_\mu$
	
	■ meantime: -2 ns $< t_{\text{track}} <$ 2 ns
	
	■ hits in Beam Momentum Station (BMS): ≥ 3
	
	■ hits in Scintillation Fibre detectors (SCIFI): ≥ 2
	
	■ hits in Silicon strip detectors (SI): ≥ 3
	
	Outgoing charged track (μ'):
	
	■ same charge as incoming muon
	
	■ rel. radiation length: $X/X_0 >$15
	
	■ first measured before and last after SM1:
	$Z_{\text{first}} < 350$ cm and $Z_{\text{last}} > 350$ cm
	
	■ track extrapolations are in the active hodoscope areas (PaHodoHelper::iMuPrim())

Table 5.1: List of the criteria for the selection of the muons and vertices for exclusive photon events.

Photon selection	exactly one neutral cluster with: ■ valid cluster timing: $\|t_{\text{cluster}} - t_\mu - \mu_t\| < 3\sigma_t$ ■ energy above DVCS threshold: $E_{\gamma,\text{DVCS thr.}} > 4, 5 \text{ or } 10 \text{ GeV in ECAL0, ECAL1 or ECAL2}$
Proton selection	velocity of recoiled particle: $$0.1 < \beta \, (v/c) < 0.95$$
Exclusivity conditions	**all combinations of muons, photons and protons which satisfy:** ■ coplanarity: $\|\Delta\varphi\| < 0.4 \text{ rad}$ ■ vertex pointing: $\|\Delta Z\| < 16 \text{ cm}$ ■ transverse momentum balance: $\|\Delta(p_{p'})_T\| < 0.3 \text{ GeV/c}$ ■ four-momentum balance: $\|\Delta M_x^2\| < 0.3 \text{ GeV/c}$
Kinematic fit quality	kinematic fit must have converged with a quality of: $$\chi^2_{\text{red}} < 10$$ kinematic restrictions: ■ $1\,(\text{GeV/c})^2 < Q^2_{\text{fit}} < 10\,(\text{GeV/c})^2$ ■ $0.05 < y_{\text{fit}} < 0.95$ ■ $0.08\,(\text{GeV/c})^2 < t_{\text{fit}} < 0.64\,(\text{GeV/c})^2$ ■ $10\,\text{GeV} < \nu_{\text{fit}} < 144\,\text{GeV}$
Combinatorics	only one combination left
Visible π^0	combine photon to all other photons below DVCS threshold with: $$E_{\gamma,\text{low thr.}} > 0.5 \text{ or } 0.63 \text{ GeV in ECAL0 or ECAL1}$$ remove events in visible π^0 mass range: $$\|M_{\gamma\gamma} - M_{\pi^0}^{\text{PDG}^a}\| < 20 \text{ MeV/c}^2$$

Table 5.2: List of the criteria for the photon and proton selection for exclusive single photon events, including the exclusivity conditions, the requirements on the kinematic fit and kinematic range, and the rejection of visible π^0 events. [a] Particle Data Group: 134.97 MeV/c^2

5.1.1 | Muon and vertex selection

The incoming muon has to fulfill the same criteria as used for determining the muon flux (see Sec. 4.3.1). To identify the scattered muon track, the requirements for the muon identification and the standard DIS event selection, as discussed in Sections 3.1.5.2 and 4.5.1, are applied. The corresponding vertex has to be inside the target and has to have only a single outgoing charged track, which corresponds to the scattered muon.

5.1.2 | Photon selection

All neutral clusters detected by either one of the three ECALs are considered as photons. The cluster time has to be within a $3\sigma_t$ range with respect to the mean time of the beam and the mean of the ECAL signal μ_t. The parameters μ_t and σ_t are determined in Section 4.8.3.

Additionally the cluster energy has to exceed a predefined energy threshold. Those threshold depend on the corresponding ECAL and are set according to a DVCS Monte-Carlo sample. It is obtained by using the DVCS weights in the kinematic range of Q^2 between $1\,(\text{GeV/c})^2$ and $20\,(\text{GeV/c})^2$, y between 0.05 and 0.9, $|t|$ between $0.08\,(\text{GeV/c})^2$ and $0.64\,(\text{GeV/c})^2$ and ν larger than $8\,\text{GeV}$. By applying the exclusive photon selection without the requirements on the energy threshold the distributions of the reconstructed photon energies in the ECALs are obtained, as shown in Figure 5.1. The thresholds are given by the lower limits of these distributions.

(a)

(b)

(c)
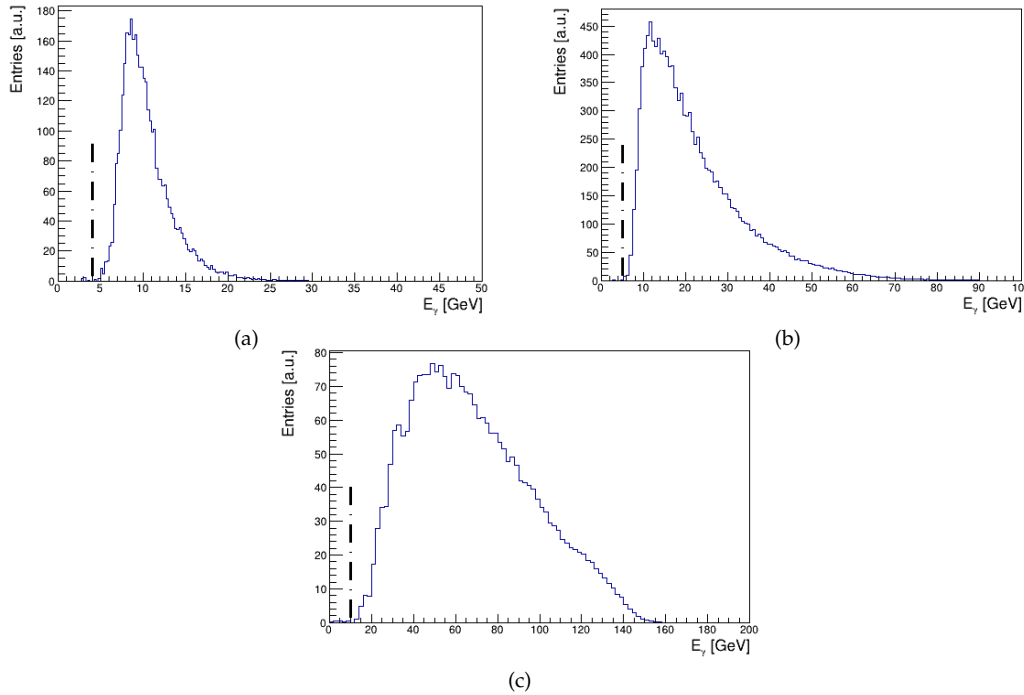
Figure 5.1: Reconstructed photon energy in ECAL0 (a), ECAL1 (b) and ECAL2 (c) obtained by applying the exclusive photon event criteria without using the energy thresholds, on an DVCS Monte-Carlo data sample. The vertical lines indicate the threshold. Figures taken from Ref. [165].

5.1.3 | Proton selection

The proton candidates are identified according to the reconstruction of particles from a measurement of the proton recoil detector as described in Section 4.7.1. The minimal and maximal velocities β for protons still producing a signal in the scintillator elements of ring B is about 0.1 to 0.95 (see Sec. 3.1.4).

5.1.4 | Exclusivity conditions

The exclusive measurement of the events allows to calculate the predicted proton kinematic using the reconstructed four-momenta of the incoming and scattered muon and the real photon as:

$$p_{p',\mathrm{pred}} = k + p_p - k' - q. \tag{5.1}$$

For an initial proton at rest the prediction for the momentum vector of the recoil proton is:

$$\vec{p}_{p',\mathrm{pred}} = \vec{k} - \vec{k}' - \vec{p}_\gamma. \tag{5.2}$$

The predicted proton kinematic can be compared to the reconstructed kinematic from the measurement of the proton recoil detector. This allows to formulate exclusivity conditions, which can be used to further constrain the event selection. As exclusivity conditions the differences between the predicted and reconstructed proton kinematic are calculated and required to be in agreement within certain limits. These limits are chosen according to a DVCS Monte-Carlo simulation.

To confirm the **coplanarity** of the predicted and reconstructed proton kinematic, the difference of the azimuthal angles is calculated as:

$$\Delta\varphi = \varphi_{p',\mathrm{pred}} - \varphi_{p',\mathrm{reco}}. \tag{5.3}$$

Figure 5.2 shows the distribution of $\Delta\varphi$ separately for μ^+ and μ^- obtained using a DVCS Monte-Carlo (a) or the data sample (b). For these distributions, all the selection criteria used to identify the particles are applied, but leaving out the presented variable. In case of the DVCS Monte-Carlo sample, the μ^- sample is scaled to the μ^+ sample. For data the integrated luminosity over all periods is used as a normalization. From the distributions seen Figure 5.2a the acceptable limit for the difference is chosen to be:

$$|\Delta\varphi| < 0.4\,\mathrm{rad}. \tag{5.4}$$

These limits are at the edges of the distributions but without removing any DVCS events.

(a)   (b)
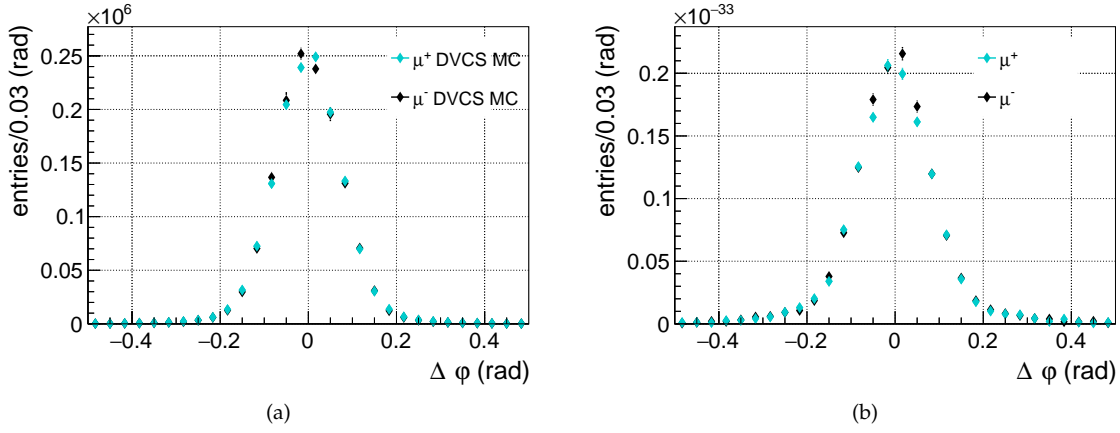
Figure 5.2: Distribution of the exclusivity variable $\Delta\varphi$ seperated for μ^+ and μ^- for a DVCS Monte-Carlo sample (a) and data (b).

The **transverse momentum balance** is verified by calculating the differences of the transverse proton momenta as:

$$\Delta(p_{p'})_T = (\vec{p}_{p',\text{pred}})_T - (\vec{p}_{p',\text{reco}})_T. \tag{5.5}$$

Its distributions for the DVCS Monte-Carlo and the data are shown in Figures 5.3a and 5.3b. The corresponding limit is chosen to be

$$|\Delta(p_{p'})_T| < 0.3\,\text{GeV/c}. \tag{5.6}$$

(a)   (b)
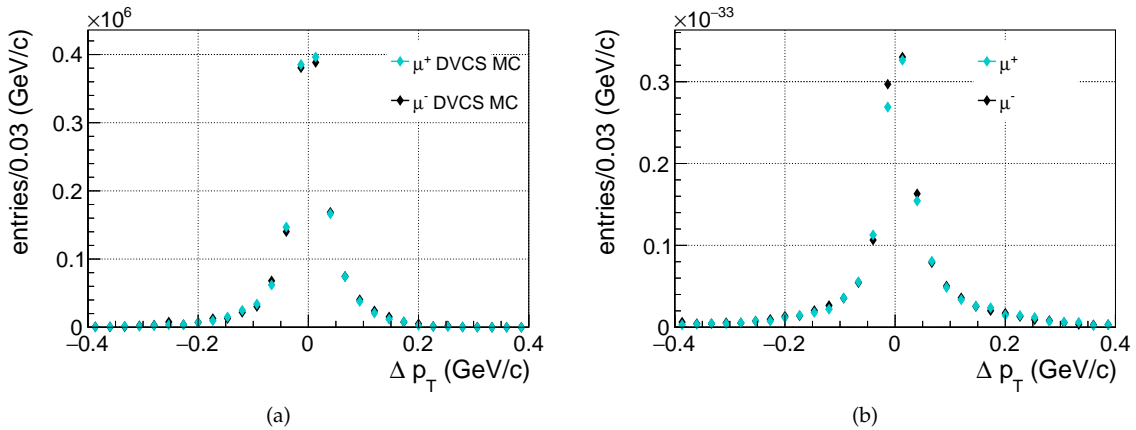
Figure 5.3: Distribution of the exclusivity variable $\Delta(p_{p'})_T$ seperated for μ^+ and μ^- for a DVCS Monte-Carlo sample (a) and data (b).

The **vertex pointing** verifies the Z-position of the primary vertex using the Z-position of reconstructed hits in ring A and B. From the positions of the hit in ring B and the vertex, the predicted Z-position, where the track crossed ring A, is determined. Comparing it to the reconstructed Z-position of the hit in the recoil detector, allows to formulate the exclusivity variable as:

$$\Delta Z = Z_{A,\mathrm{pred}} - Z_{A,\mathrm{reco}}. \tag{5.7}$$

The corresponding distributions for the DVCS Monte-Carlo and the data sample are shown in Figure 5.4a and 5.4b. The agreement is requested to be better than:

$$|\Delta Z| < 16\,\mathrm{cm}. \tag{5.8}$$
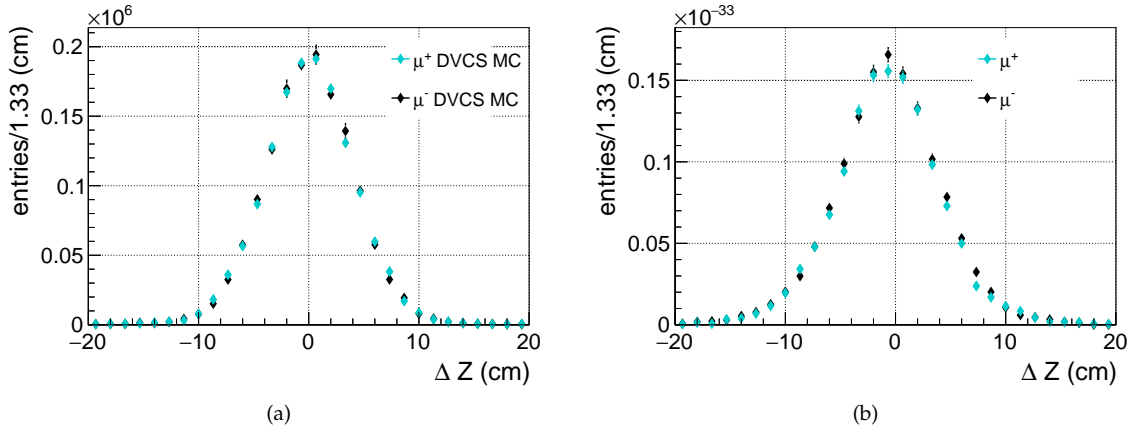
Figure 5.4: Distribution of the exclusivity variable ΔZ seperated for μ^+ and μ^- for a DVCS Monte-Carlo sample (a) and data (b).

To validate the **four-momentum balance**, the measured four-momentum of the recoil proton and the four-momenta of the remaining particles, measured by the spectrometer, are used to calculate the missing mass squared:

$$M_x^2 = (k + p_p - k' - p_{p',\mathrm{reco}} - q)^2. \tag{5.9}$$

For an exclusive process it is distributed as a peak around zero with a width according to the uncertainties in the reconstruction of the four momenta. For a DVCS Monte-Carlo and the data, the distributions are shown in Figure 5.5a and 5.5b. The uncertainties in the reconstruction are very similar for the Monte-Carlo data and the data, leading to similar widths of the corresponding distributions. To remove those events with large uncertainties, a limit of:

$$|M_x^2| < 0.3\,(\mathrm{GeV}/c^2)^2 \tag{5.10}$$

is chosen.

(a)   (b)
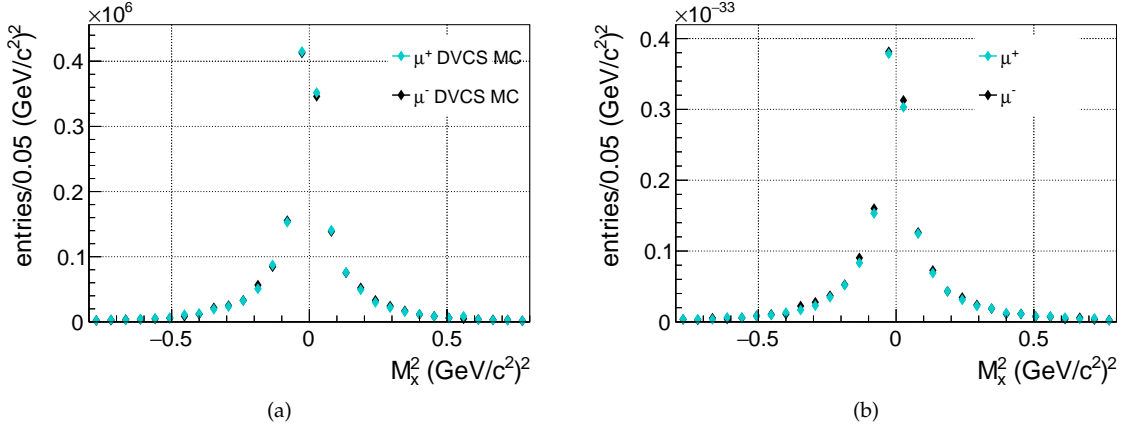
Figure 5.5: Distribution of the exclusivity variable M_x^2 seperated for μ^+ and μ^- for a DVCS Monte-Carlo sample (a) and data (b).

After applying all the previously mentioned selection criteria, a kinematic fit is performed on the remaining candidates for exclusive photon events. All the details on the kinematic fit, including studies on its quality and its impact on the event kinematics are discussed in Section 5.2.
The fitted kinematics are also used when restricting the kinematic region. The lower limit on Q^2 and the limits on y are chosen according to the requirements for DIS events, as previously discussed in Section 4.5.1. Following the discussion in Section 2.7, the considered ν range is between $10\,\text{GeV}$ and $144\,\text{GeV}$. For $|t|$ the lower limit is given by the limitations in the measurement of recoil protons by the proton recoil detector (see Sec. 3.1.4). The upper limit is due to requirements by the factorization in DVCS as mentioned in Section 2.4.1.

In a final step all events with more then one valid combination of muons, proton and real photons are rejected. The obtained data sample still implies a contamination due to the decay of neutral pions. Its contribution is determined and removed from the data sample. The details on this analysis are discussed in Section 5.3.2. The $\phi_{\gamma*\gamma}$-distributions of the data events seperated for μ^+ and μ^- in the reference, interference and extraction region are shown in Figures 5.6a, 5.6b and 5.6c. These distributions are normalized to the corresponding luminosity. A good agreement is obtained. A more detailed discussion of these distributions follows in Section 5.3.1 and 5.4.2 after determining the Bethe-Heitler contribution and π^0-background contamination. A summary of kinematic distributions in data separately for the ν-regions and using the cumulated statistics for μ^+ and μ^- can be found in Appendix A.2.

(a)

(b)

(c)
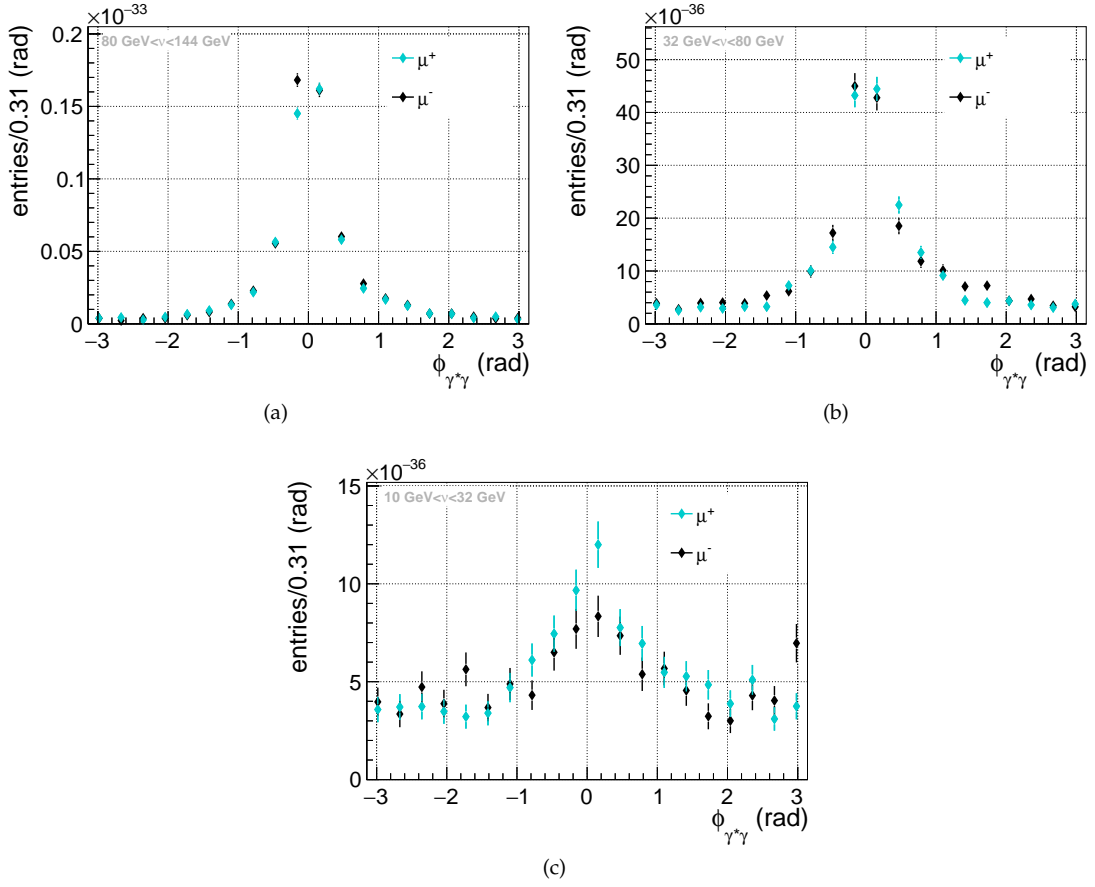
Figure 5.6: $\phi_{\gamma*\gamma}$-distributions for data seperately for μ^+ and μ^- in the reference (a), interference (b) and extraction region (c).

5.2 | The kinematic fit

In exclusive measured processes a kinematic fit can be applied to improve the estimators of the reconstructed kinematics. Here, the well measured kinematic quantities are used to constrain those with larger uncertainties. These quantities are related to the kinematics of the particles and specify a set of constrains like e.g. the momentum and energy conversation. The kinematic quantities and constrains are used to formulate a Lagrange function, which is minimized using the Lagrange multiplier method. A detailed description of the mathematical framework is given in Reference [37].

The formalism of the Lagrange function for exclusive photon production and the constrains are discussed in Sections 5.2.1 and 5.2.2. At COMPASS the kinematic fit was first implemented and applied by Philipp Jörg when analysing the 2012 data sample [114]. The framework is based on a public available software [83], which provides the minimisation procedure and is modified according to the COMPASS requirements. It was further developed by Brian Ventura and is applied in the 2016 analysis.

5.2.1 | The kinematic fit for exclusive photon production

The Lagrange function has the form:

$$L(\vec{k}, \vec{\lambda}) = \chi^2(\vec{k}) + 2\sum_{i=1}^{N} \lambda_i g_i(\vec{k}, \vec{h}). \tag{5.11}$$

Here $\vec{k}$ and $\vec{h}$ are the vectors of measured and unmeasured quantities in the exclusive photon production process, $g_i(\vec{k}, \vec{h})$ refers to a specific constrain i out of a total of number of N constraints, λ_i are the corresponding Lagrange multipliers and $\chi^2(\vec{k})$ a least square function.

The measured quantities are summarized in Table 5.3. Beside the listed quantities, also the target proton is a measured quantity and considered to be at rest ($\vec{p}_p = \vec{0}$).

	Quantities	Description
Incoming and scattered muon	$X_{\mu,\mu'}$	X-coord. of the muon track at the Z-position of the vertex
	$Y_{\mu,\mu'}$	Y-coord. of the muon track at the Z-position of the vertex
	$p_{X\mu,\mu'}$	X-component of the muon momentum at the vertex position
	$p_{Y\mu,\mu'}$	Y-component of the muon momentum at the vertex position
	$p_{Z\mu,\mu'}$	Z-component of the muon momentum at the vertex position
Real photon	X_γ	X-coord. of the cluster at the Z-position of the ECAL
	Y_γ	Y-coord. of the cluster at the Z-position of the ECAL
	E_γ	Cluster energy
Recoil proton	$\Phi_{A,B}$	Azimuthal angle of the recoil proton in ring A and B
	$r_{A,B}$	Radius of the hit in ring A and B with respect to the ring center
	$Z_{A,B}$	Z-position of the hit in ring A and B
	$p_{p'}$	Magnitude of the momentum of the recoil proton

Table 5.3: Measured quantities as considered by the kinematic fit.

The vector of measured quantities is given as:

$$\vec{k} = (\vec{p}_p, \vec{a}_\gamma, |\vec{p}_\gamma|, \vec{a}_\mu, \vec{p}_\mu, \vec{a}_{\mu'}, \vec{p}_{\mu'}, r_A, \Phi_A, Z_A, r_B, \Phi_B, Z_B, |\vec{p}_{p'}|). \tag{5.12}$$

Here $\vec{a}$ and $\vec{p}$ correspond to the position and momentum vectors of the particles or clusters.

The unmeasured quantities are listed in Table 5.4. and the corresponding vector is given as:

$$\vec{h} = (\vec{a}_{\text{vtx}}, \Theta_\gamma, \Phi_\gamma, \Theta_{p'}, \Phi_{p'}). \tag{5.13}$$

Note that the vertex coordinates are considered to be an unmeasured quantity, despite of the fact that the vertex position is reconstructed from the spectrometer measurement. Nevertheless the reconstructed vertex position is used to formulate a constrain (see Sec. 5.2.2.2).

During the minimization procedure, the fit calculates corrections $\Delta\vec{k}$ to the measured quantities in a way that the corrected quantities are expressed as:

$$\vec{k}^{fit} = \vec{k} + \Delta\vec{k}.$$

	Quantities	Description
Vertex	X_{vtx}	X-coord. of the vertex
	Y_{vtx}	Y-coord. of the vertex
	Z_{vtx}	Z-coord. of the vertex
Real photon	Φ_γ	Azimuthal angle of the photon
	Θ_γ	Polar angle of the photon
Recoil proton	$\Phi_{p'}$	Azimuthal angle of the recoil proton
	$\Theta_{p'}$	Polar angle of the recoil proton

Table 5.4: Unmeasured quantities as considered by the kinematic fit.

Using $\Delta\vec{k}$ the least square function is written as [114, p. 49]:

$$\chi^2(\vec{k}) := \Delta\vec{k}^T \hat{C}^{-1} \Delta\vec{k}. \tag{5.14}$$

Here $\hat{C}$ denotes the corresponding covariance matrix to the measured quantities. A detailed description of the composition of this matrix is in Reference [114, p. 52].

The minimization of the least square function with respect to the constrains also minimizes the Lagrange function (see Eq. 5.11), by the minimum χ^2 method. Here, the following set of non-linear equations has to be solved:

$$\frac{\partial L(\vec{k},\vec{\lambda})}{\partial \lambda_i} = 0 \text{ with } i \in N, \tag{5.15}$$

$$\frac{\partial L(\vec{k},\vec{\lambda})}{\partial k_j} = 0 \text{ with } k_j \in \vec{k}, \tag{5.16}$$

$$\frac{\partial L(\vec{k},\vec{\lambda})}{\partial h_l} = 0 \text{ with } h_l \in \vec{h}. \tag{5.17}$$

5.2.2 | Constraints for the kinematic fit

In total 14 constraints are used, which are either formulated according to the energy and momentum conservation or by the particles originating from a common vertex. Considering the 7 unmeasured quantities, there are 7 degrees of freedom (ndf=14-7).

5.2.2.1 | Energy and momentum conversation

The energy and momentum conversation is used to formulate four constrains in total:

$$g_1 = (\vec{p}_\mu^{\text{fit}})_X - (\vec{p}_{\mu'}^{\text{fit}})_X - (\vec{p}_\gamma^{\text{fit}})_X - (\vec{p}_{p'}^{\text{fit}})_X = 0,$$

$$g_2 = (\vec{p}_\mu^{\text{fit}})_Y - (\vec{p}_{\mu'}^{\text{fit}})_Y - (\vec{p}_\gamma^{\text{fit}})_Y - (\vec{p}_{p'}^{\text{fit}})_Y = 0,$$

$$g_3 = (\vec{p}_\mu^{\text{fit}})_Z - (\vec{p}_{\mu'}^{\text{fit}})_Z - (\vec{p}_\gamma^{\text{fit}})_Z - (\vec{p}_{p'}^{\text{fit}})_Z = 0,$$

$$g_4 = E_\mu^{\text{fit}} + m_p c^2 - E_{\mu'}^{\text{fit}} - E_\gamma^{\text{fit}} - E_{p'}^{\text{fit}} = 0$$

The superscript 'fit' indicates that the constraints have to be fulfilled for the quantities corrected by the kinematic fit.

5.2.2.2 | Vertex constraints

To formulated the vertex constrains the tracks are assumed to follow a straight line:

$$\vec{r}(\kappa) = \vec{r}' + \kappa\vec{p},$$

which originates from the vertex. Here $\vec{r}'$ is a known point of the track, $\vec{p}$ the momentum of the particle and κ a free parameter. Following this, the constraints for each coordinate are expressed as:

$$Z = Z' + \kappa\vec{p}_Z \Rightarrow \kappa\vec{p}_Z = Z - Z',$$
$$X = X' + \kappa\vec{p}_X \Rightarrow X\vec{p}_Z = X'\vec{p}_Z + \kappa\vec{p}_X\vec{p}_Z,$$
$$\Rightarrow X\vec{p}_Z = X'\vec{p}_Z + \vec{p}_X(Z - Z'),$$
$$\Rightarrow \vec{p}_Z(X - X') + \vec{p}_X(Z - Z') = 0,$$
$$Y = Y' + \kappa\vec{p}_Y \Rightarrow \vec{p}_Z(Y - Y') + \vec{p}_Y(Z - Z') = 0.$$

Therefore, the constraints for the incoming muon, the scattered muon and the real photon using their measured X and Y-positions as well as their momenta are:

$$g_5 = (\vec{p}_\mu^{\text{fit}})_Z(X_{\text{vtx}} - X_\mu^{\text{fit}}) - (\vec{p}_\mu^{\text{fit}})_X(Z_{\text{vtx}} - Z_\mu^{\text{fit}}) = 0,$$
$$g_6 = (\vec{p}_\mu^{\text{fit}})_Z(Y_{\text{vtx}} - Y_\mu^{\text{fit}}) - (\vec{p}_\mu^{\text{fit}})_Y(Z_{\text{vtx}} - Z_\mu^{\text{fit}}) = 0,$$
$$g_7 = (\vec{p}_{\mu'}^{\text{fit}})_Z(X_{\text{vtx}} - X_{\mu'}^{\text{fit}}) - (\vec{p}_{\mu'}^{\text{fit}})_X(Z_{\text{vtx}} - Z_{\mu'}^{\text{fit}}) = 0,$$
$$g_8 = (\vec{p}_{\mu'}^{\text{fit}})_Z(Y_{\text{vtx}} - Y_{\mu'}^{\text{fit}}) - (\vec{p}_{\mu'}^{\text{fit}})_Y(Z_{\text{vtx}} - Z_{\mu'}^{\text{fit}}) = 0,$$
$$g_9 = (\vec{p}_\gamma^{\text{fit}})_Z(X_{\text{vtx}} - X_\gamma^{\text{fit}}) - (\vec{p}_\gamma^{\text{fit}})_X(Z_{\text{vtx}} - Z_\gamma^{\text{fit}}) = 0,$$
$$g_{10} = (\vec{p}_\gamma^{\text{fit}})_Z(Y_{\text{vtx}} - Y_\gamma^{\text{fit}}) - (\vec{p}_\gamma^{\text{fit}})_Y(Z_{\text{vtx}} - Z_\gamma^{\text{fit}}) = 0.$$

In case of the recoil proton the X and Y-positions are not directly measured but can be calculated using the available information of the azimuthal angles and the radii of the hits in ring A and B:

$$\vec{r}_A = (r_A \cos\Phi_A, r_A \sin\Phi_A, Z_A),$$
$$\vec{r}_B = (r_B \cos\Phi_B, r_B \sin\Phi_B, Z_B).$$

The constraints on the recoil proton are formulated as extrapolations from the hit position in the corresponding ring to the position of the vertex. Considering this the constraints are:

$$g_{11} = (\vec{p}_{p'})_Z((\vec{r}_A)_X - X_{\text{vtx}}) - (\vec{p}_{p'})_X((\vec{r}_A)_Z - Z_{\text{vtx}}) = 0,$$
$$g_{12} = (\vec{p}_{p'})_Z((\vec{r}_A)_Y - Y_{\text{vtx}}) - (\vec{p}_{p'})_Y((\vec{r}_A)_Z - Z_{\text{vtx}}) = 0,$$
$$g_{13} = (\vec{p}_{p'})_Z((\vec{r}_B)_X - X_{\text{vtx}}) - (\vec{p}_{p'})_X((\vec{r}_B)_Z - Z_{\text{vtx}}) = 0,$$
$$g_{14} = (\vec{p}_{p'})_Z((\vec{r}_B)_Y - Y_{\text{vtx}}) - (\vec{p}_{p'})_Y((\vec{r}_B)_Z - Z_{\text{vtx}}) = 0.$$

5.2.3 | Efficiency and quality of the fit

The kinematic fit and the restriction on χ^2_{red} are not only applied, when selecting data but also in the selection of the Bethe-Heitler and the π^0 Monte-Carlo samples. The fit is performed after the event fulfills the requirements formulated by the exclusivity conditions. At that stage the topology of the events corresponds to those of an exclusive photon event. Hence, the fit is expected to converge for most of those events. In data this is the case for 98.7% of them. For the Bethe-Heitler Monte-Carlo sample the

efficiency of the fit is increased to about 99.5%, which is expected due to the event topology corresponding to the hypotheses of the fit. For the Monte-Carlo samples for exclusive and inclusive produced π^0 the efficiency of the fit drops to about 98%, respectively 91%.

To illustrate the impact of the restriction on χ^2_{red} applied in the event selection, the corresponding distribution for all samples separately for each ν-region are shown in Figure 5.7a, 5.7b and 5.7c. The Monte-Carlo samples are normalized to the data according to the discussion in Sections 5.3.1 and 5.3.2. In the reference and interference region, the data and Monte-Carlo distributions show a similar decrease, while in the extraction region a clear discrepancy is visible. While the Bethe-Heitler sample only has small values of χ^2_{red}, in data also higher values are obtained. This hints to an larger fraction of events, which deviate from the exclusive photon event toplogy.
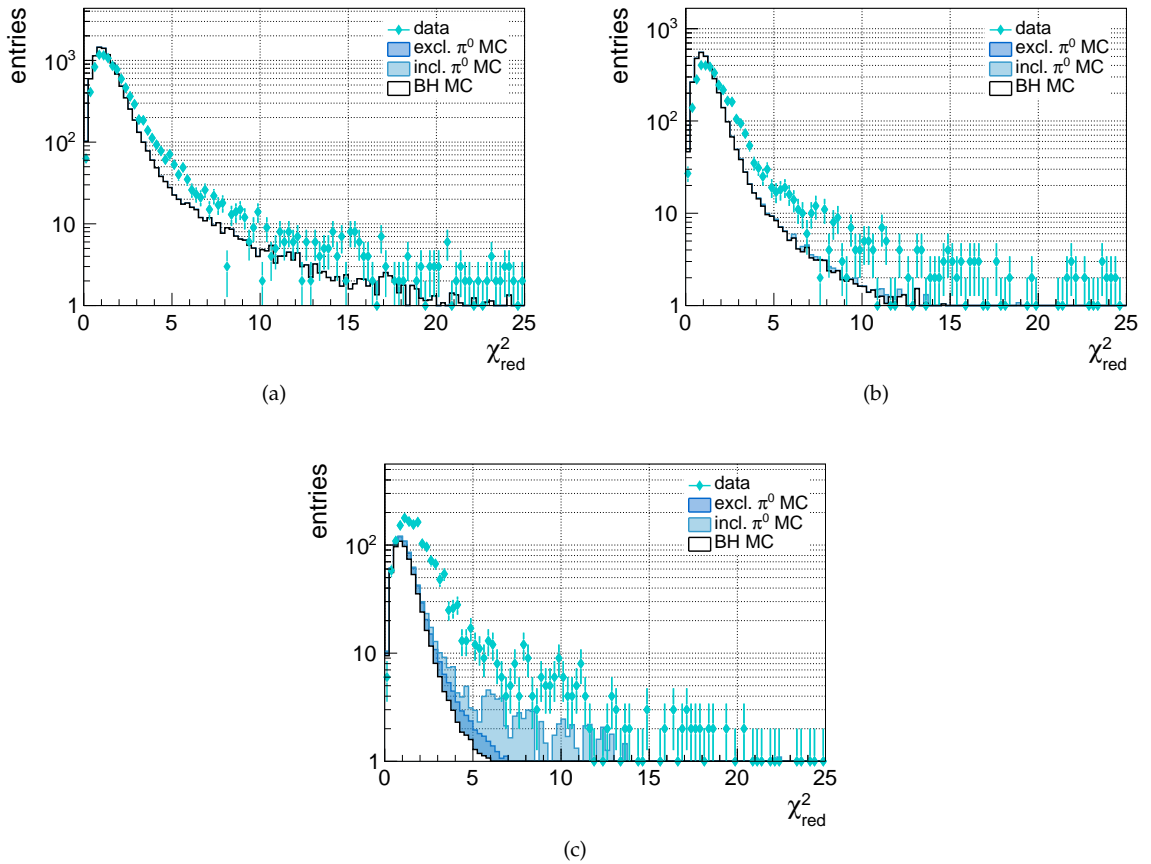
Figure 5.7: χ^2_{red}-distributions obtained for data, BH Monte-Carlo and the exclusive invisible π^0 (HEP-GEN) and inclusive invisible π^0 (LEPTO) Monte-Carlo samples separately for the reference (a), interference (b) and extraction region (c).

The number of exclusive photon events before and after applying the restriction on χ^2_{red} for the data and the Monte-Carlo samples are summarized in Table 5.5. The fraction of removed events is smallest in case of the Bethe-Heitler Monte-Carlo sample and highest for the invisible π^0 Monte-Carlo samples. This is consistent with the expected similarity of the event topologies to the topology assumed by the fit.

To prevent any bias by requiring a restriction on χ^2_{red}, which is too tight and might affect the analysis, it was decided to restrain to $\chi^2_{\text{red}} < 10$. The impact of this restriction is discussed in Section 7.2.2.4 as part of the systematic studies.

ν-region	Sample	no cut	$\chi^2_{\text{red}} < 10$	fraction of removed events (%)
reference	data	9874	9423	4.8
(80 GeV$< \nu <$144 GeV)	BH MC	9691.5	9533	1.6
	inv. π^0	0.51	0.68	
interference	data	3674	3415	7.0
(32 GeV$< \nu <$80 GeV)	BH MC	3382.8	3311.4	2.1
	inv. π^0	17.9	14.3	20.1
extraction	data	1851	1702	8.0
(10 GeV$< \nu <$32 GeV)	BH MC	645.1	631.5	2.1
	inv. π^0	217.5	159.4	26.7

Table 5.5: Summary of the removal ratio when applying a cut on χ^2_{red} for all the data samples.

5.2.4 | Impact of the fit on kinematic distributions in data

The impact of the fit is best illustrated by a direct comparison between the fitted and non fitted data distributions. The kinematic distributions for ν, Q^2, x_{Bj}, $\phi_{\gamma*\gamma}$ and $|t|$ using the available sample for the combined μ^+ and μ^- data are shown in Figures 5.8a to 5.8e (top). Here, the distributions are normalized to the integrated luminosity for μ^+ and μ^-. As can be seen in the ratio of the distributions (bottom), except for the $|t|$-distribution, the fit does not change their shapes. At large values of $|t|$ the change is due to an improvement of the t-resolution by the kinematic fit compared to the reconstruction by the proton recoil detector. This can be illustrated by directly comparing the t-resolution obtained by the proton recoil detector, to the one predicted by the spectrometer measurement and the one after applying the kinematic fit. For this study an exclusive photon Monte-Carlo sample is used. The t-resolution is determined by the difference between the reconstructed values of t to the generated ones. Their relative t-resolutions $\sigma_t/|t^{\text{gen}}|$ as a function of $|t^{\text{gen}}|$ are shown in Figure 5.9. The spectrometer prediction t^{spec} is calculated using the four momentum balance in exclusive photon production. Performing the detailed calculation given in Reference [114], t^{spec} is calculated as:

$$t^{\text{spec}} = -Q^2 - 2E_\gamma(\nu - \sqrt{\nu^2 + Q^2}\cos\theta_{\gamma*\gamma}) \tag{5.18}$$

$$= \frac{-Q^2 - 2\nu(\nu - \sqrt{\nu^2 + Q^2}\cos\theta_{\gamma*\gamma})}{1 + \frac{1}{M_p}(\nu - \sqrt{\nu^2 + Q^2}\cos\theta_{\gamma*\gamma})}. \tag{5.19}$$

Here $\theta_{\gamma*\gamma}$ is the angle between the virtual and the real photon. For the proton recoil detector it can be shown that according to relation:

$$\frac{\sigma_t}{|t|} = (1 + \frac{M_p}{E_p})\frac{\sigma_p}{p} \approx 2\frac{\sigma_p}{p} \text{ at small } |t|, \tag{5.20}$$

the t-resolution in the TOF measurement is about two times the resolution of the proton momentum. In comparison the kinematic fit results in a constant resolution of about 5% over the full $|t|$-range. The

(a)

(b)   (c)

(d)   (e)
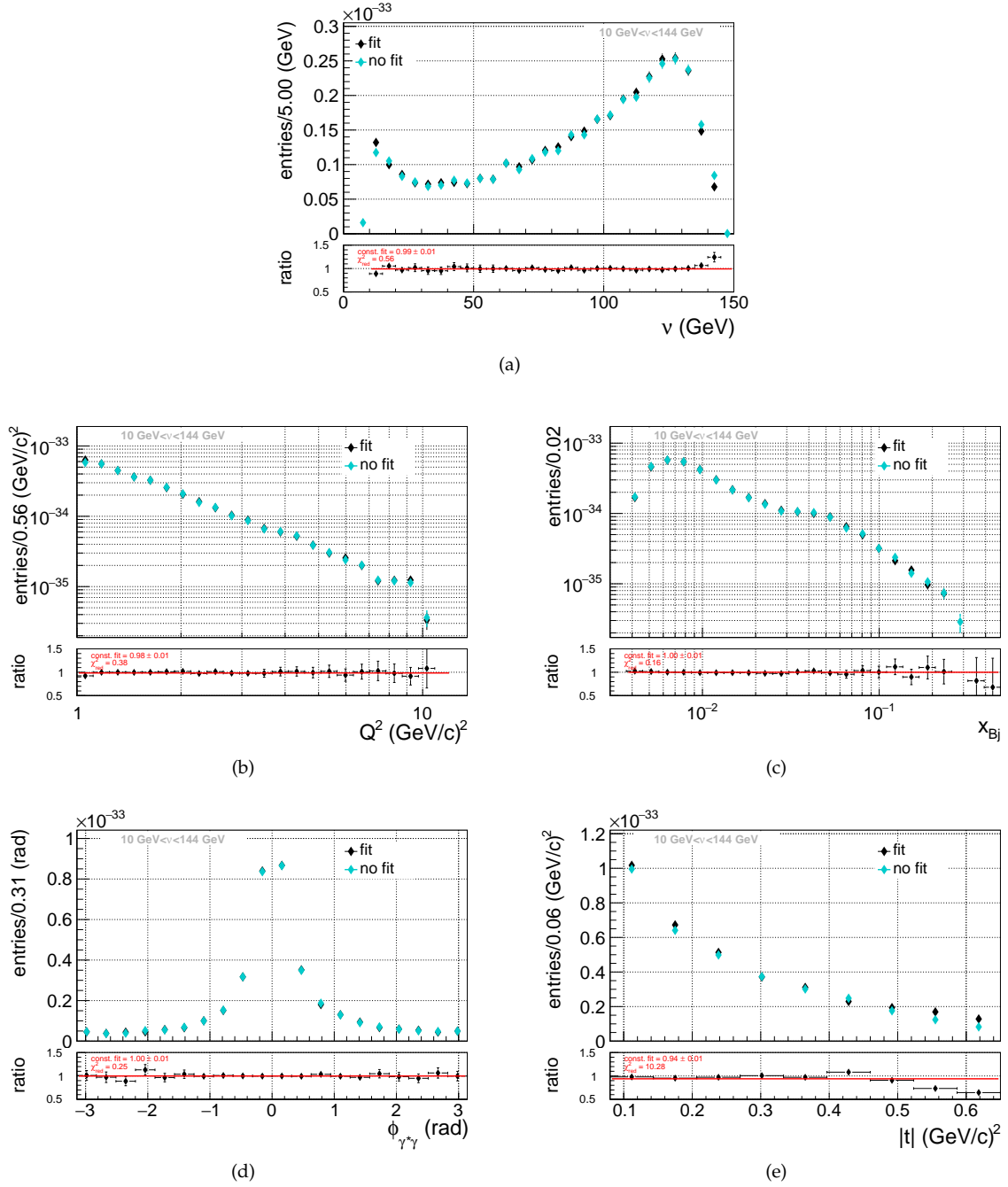
Figure 5.8: (a) χ^2_{red}-distribution for data events, which fulfill all selection criteria for exclusive photon events, beside the limit in the reduced χ^2.
(b)-(f) Kinematic distributions (top) for ν, Q^2, x_{Bj}, $\phi_{\gamma*\gamma}$ and $|t|$ with the fit (black) and without the fit (cyan) applied. The corresponding ratio of the distribution is shown at the bottom and fitted using a constant fit (red).

131

resolution of the proton recoil detector decreases for larger values of $|t|$, which is in agreement to the observation discussed above. For the spectrometer prediction, the resolution decreases drastically with smaller values of $|t|$.
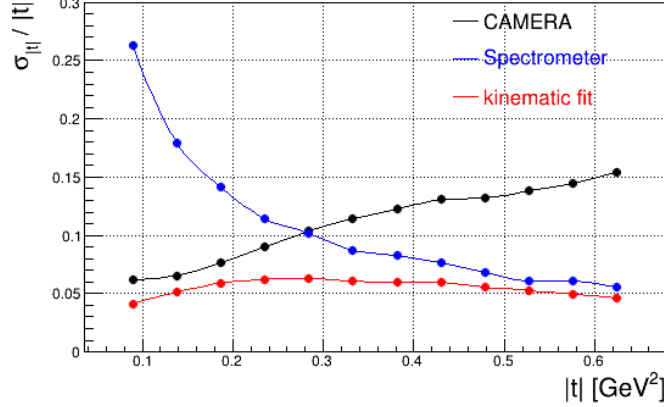
Figure 5.9: $|t|$-resolution as a function of the generated $|t|$ achieved by the proton recoil detector, the spectrometer prediction and the kinematic fit studied using an exclusive photon Monte-Carlo sample. The resolution of the kinematic fit is best and also most stable with respect to the $|t|$ values compared to the other two methods, which show a strong t-dependence. Figure taken from Ref. [165].

5.2.5 | Impact of the fit on data and the Monte-Carlo distributions

The impact of the fit on kinematic distributions in data was discussed in Section 5.2.4. In this Section this study is extended to also review the impact of the fit on the Bethe-Heitler and invisible π^0 Monte-Carlo samples. For the measured quantities, which are summarized in Table 5.3, this is done by studying the so called pulls [52] (see Sec. 5.2.5.1). The impact on x_{Bj}, Q^2, $\phi_{\gamma*\gamma}$, t and ν is discussed in Section 5.2.5.2.

5.2.5.1 | Pull distributions

The pulls to the measured quantities are calculated as:

$$\frac{\Delta k_i}{\sigma_{k_i}} = \frac{k_i^{\text{meas}} - k_i^{\text{fit}}}{= \sqrt{C_{k_i}^{\text{meas}} - C_{k_i}^{\text{fit}}}}. \tag{5.21}$$

Here, σ_{k_i} refers to the square root of the difference between the uncertainties of the corresponding measured and fitted quantities, which are taken from the covariance matrix C. The covariance matrix of the measured values C^{meas} is determined by the vertex or track fitting during the reconstruction, while the one denoted as C^{fit} is obtained from the kinematic fit.

The pull distributions, which are shown and discussed in the following, are obtained in the extraction region. Here, the points refer to the data distribution. The light blue histograms show the corresponding distributions extracted from the exclusive photon Monte-Carlo sample. This sample includes the contributions from Bethe-Heitler, DVCS and their interference. The event weights used for the exclusive photon Monte-Carlo are calculated as discussed in Section 6.1 and the Monte-Carlo is scaled to the data

according to the discussion in Section 5.3.1. The invisible π^0 contamination, including the inclusive and exclusive contributions is shown in dark blue and normalized to the data according to Equation 5.25 in Section 5.3.2. In case the quantities are Gaussian distributed, a standard Gaussian distribution of the pulls around zero is expected. For comparison this is indicated as a dashed green line. The means (μ) and standard deviations (σ) of the histograms are listed in the Figures on the left hand side. In the following only those distributions are shown, which are necessary for the discussion. The full set of pulls is shown in the Appendix A.3.

Figure 5.10a and 5.10b show the pull distributions for the X and Y-coordinate of the incoming muon track. Comparing the data to the exclusive photon Monte-Carlo sample, the corrections to the data are larger. For the X-coordinate in data a slight asymmetry around zero is visible, while the Monte-Carlo is symmetrical distributed around zero. In case of the pull distributions for the Y-component of the muon momenta, displayed in Figures 5.10c and 5.10d, they both have comparable widths, which are in agreement with the standard Gaussian. The same applies for the X-component of the momentum, that is not explicitly shown here. For the Z-component of the momentum, the corrections are slightly larger (see Fig. 5.10e and 5.10f). A slight shift of the data and the π^0 Monte-Carlo is visible in case of the incoming muon, while for the scattered muon a slight asymmetry in data and the π^0 Monte-Carlo is observed.

The pull distributions for the X-coordinate of the ECAL clusters are shown in Figure 5.11a. The corrections due to the fit are normal distributed around zero, but with a larger deviation in the widths for data and π^0 Monte-Carlo compared to the standard Gaussian. The corresponding corrections on the cluster energies are illustrated in Figure 5.11b. A large deviation from the expected standard distribution of the Gaussian is visible for all samples. The distribution for both Monte-Carlo samples are slightly asymmetric and in case of the π^0 Monte-Carlo, also shifted with respect to zero.

Figure 5.12a, 5.12b and 5.12c display the pull distributions for the azimuthal angle, the radial distance from the center and the Z-positions of the hits in ring B. A deviation from the expected Gaussian like shape is visible for the $\Delta\Phi_{\text{ring B}}$. This is due to the large Φ-resolution caused by the widths of the scintillator elements. Therefore a comparison to a Gaussian is not suitable in that case. For $\Delta r_{\text{ring B}}$ and $\Delta Z_{\text{ring B}}$ a shift of the distributions for the data and π^0 Monte-Carlo is visible, while for the π^0 Monte-Carlo also a clear asymmetry is noticeable. This also accounts for the pull distributions of the proton momenta shown in Figure 5.12d. This asymmetry might be related to the observed behavior of the relative t-resolution achieved by the fit compared to the measurement of the proton recoil detector (see Fig. 5.9).

In summary, most pulls are comparable with the expected normal distribution, which means that the fit provides reasonable corrections, especially for data and the exclusive photon Monte-Carlo. Larger deviations can be expected for the invisible π^0 Monte-Carlo sample due to their deviations from the event topology assumed by the fit.
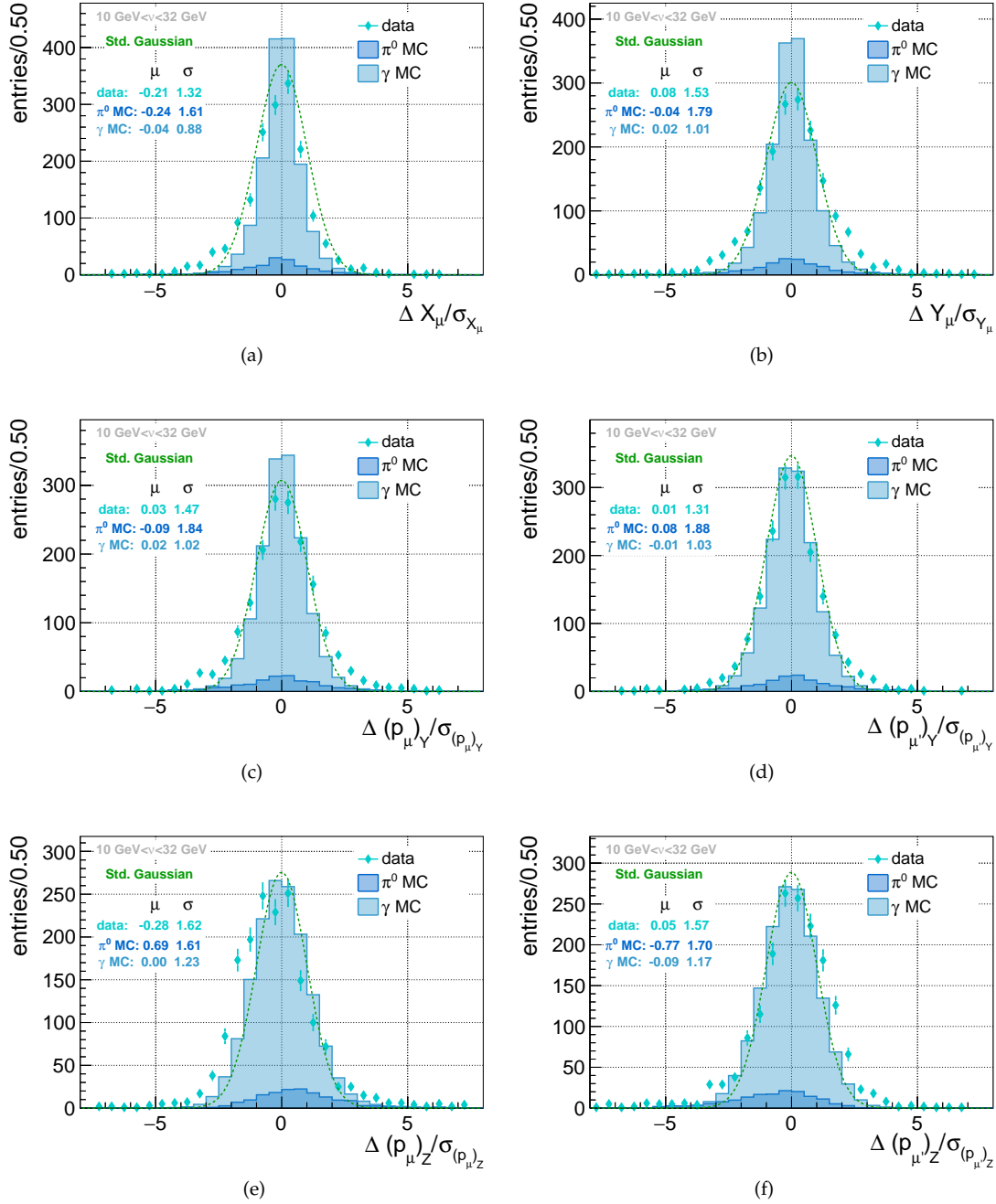
Figure 5.10: Pull distributions for the X-coordinate of the incoming (a) and scattered muon (b) track at the Z-position of the vertex and the Y and Z-component of momentum for the incoming (c and e) and the scattered muon (d and f).
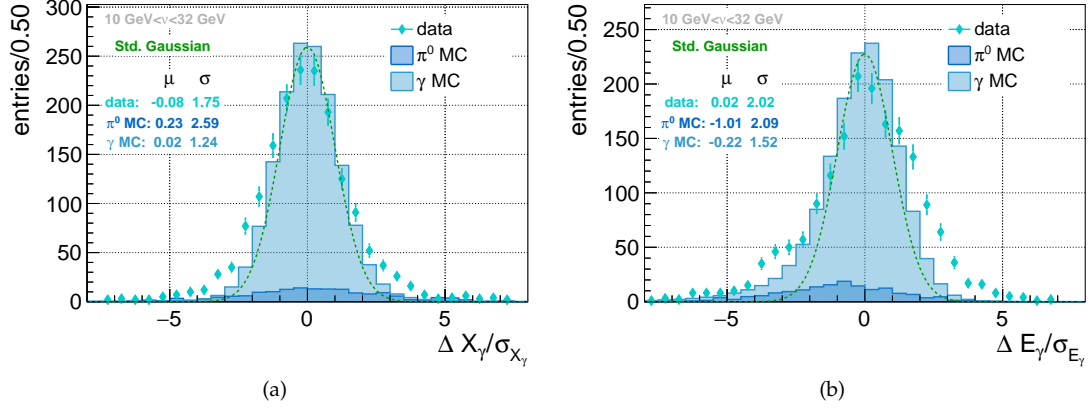
Figure 5.11: Pull distributions for the X-coordinate (a) and the energy (b) of the ECAL cluster.
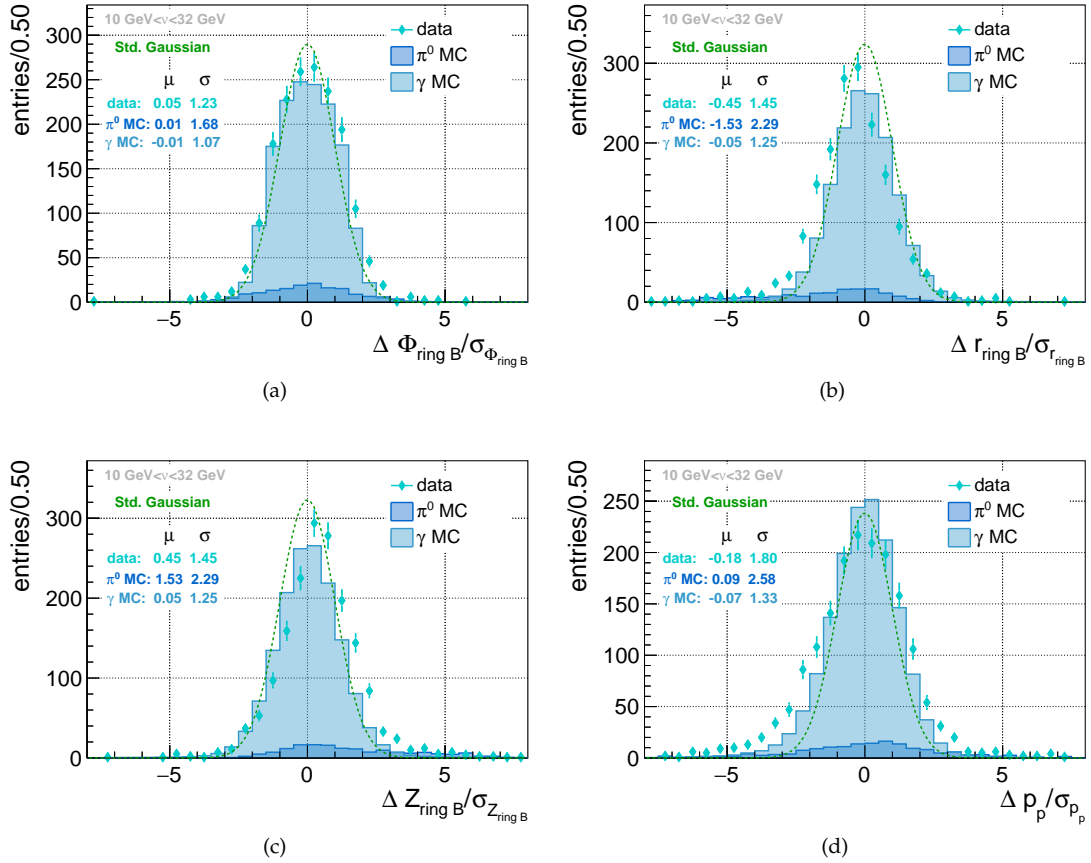
Figure 5.12: Pull distributions of the azimuthal angle (a), the radial distance (b) and the Z-position of the hits in ring B, and momentum of the recoil proton (d).

5.2.5.2 | Impact of the kinematic fit on the kinematic dependence of the differential cross section

As discussed in Section 2.7 the DVCS cross section is extracted in the ν-region between $10\,\mathrm{GeV}$ and $32\,\mathrm{GeV}$ in bins of the kinematic variables Q^2, ν, $|t|$ and $\phi_{\gamma*\gamma}$. In Section 5.2.4 it was seen that by applying the kinematic fit on data, only the shape of the $|t|$-distribution changed, especially at large values of $|t|$. In this Section a study is presented, which compares the impact of the fit in data to the impact it has on the exclusive photon and π^0 Monte-Carlo samples. The principle of this study is similar to the pull distributions discussed in the previous Section. Here, the differences between the reconstructed and fitted values are calculated and divided by the reconstructed kinematic. These relative differences in the data, the exclusive photon and invisible π^0 Monte-Carlo samples are compared separately in each ν-region. The Monte-Carlo samples are normalized according to the discussions in Section 5.3.1 and 5.3.2.

Figure 5.13a, 5.13b and 5.13c show the relative difference of ν in the reference, interference and extraction region. The corrections to ν in the reference region are very small (below 2%). The asymmetry of the distributions to larger relative values indicates that the fit rather corrects to smaller vales of ν. This applies also to the shift of the data distribution with respect to the Monte-Carlo distribution. In the interference region the corrections are slightly larger as compared to the reference region (below 5%), but the distributions are more symmetrically distributed around zero. In the extraction region the corrections on ν are larger, up to about 20%. For the data and the exclusive photon Monte-Carlo sample, the fit tends to correct to higher values of ν, while for the π^0 Monte-Carlo sample corrections to lower values of ν are preferred. The behaviour of the corrections for data and exclusive photon Monte-Carlo are similar and as previously shown in Section 5.2.4 the shape of the ν-distribution is not significantly altered by the fit. The observed corrections on the $\phi_{\gamma*\gamma}$ values, shown in Figure 5.14a, 5.14b and 5.14c are larger then for ν, but symmetrical distributed around zero. For the data and exclusive photon Monte-Carlo sample the corrections are very similar. Also here they grow larger with decreasing ν (from the reference to the extraction region). As the shape of the distribution in data is not altered when comparing the measured and the fitted kinematics, the same is expected for the distribution in Monte-Carlo. For Q^2, shown in Figure 5.15a, 5.15b and 5.15c, the corrections are small (below 5%). In contrast to the other kinematic variables, here the corrections getting smaller with decreasing ν values. The fit tends to slightly correct to larger values of Q^2, which is indicated by the asymmetric distributions in direction of negative values. The correction observed for x_{Bj}, as displayed in Figure 5.16a, 5.16b and 5.16c increase from below 10% to 20%, when comparing the different ν-regions going from larger values to smaller ones. In the reference region the asymmetric shape of the distributions indicate a preference to correct to larger x_{Bj} values, while in the extraction region the opposite is observed. As the $|t|$-distribution is the only one experiencing considerable changes in the shape in data, its comparison to the Monte-Carlo samples is of particular interest. In all ν-regions the corrections are large, which is expected following the discussion in Section 5.2.4 on the improvement of the t-resolution by the fit. In all regions the distributions extracted from data and the exclusive photon Monte-Carlo sample are comparable, so a different impact on data and Monte-Carlo is not expected.

All the previously discussed observations show that the fit contributes some considerable changes to the kinematic variables, which are comparable between data and Monte-Carlo. The studies on the fit efficiency, its quality as well as the pull distributions further show a reliable performance of the fit. As conclusion, it was decided to use the kinematic values obtained by the fit in the analysis of the exclusive photon production.
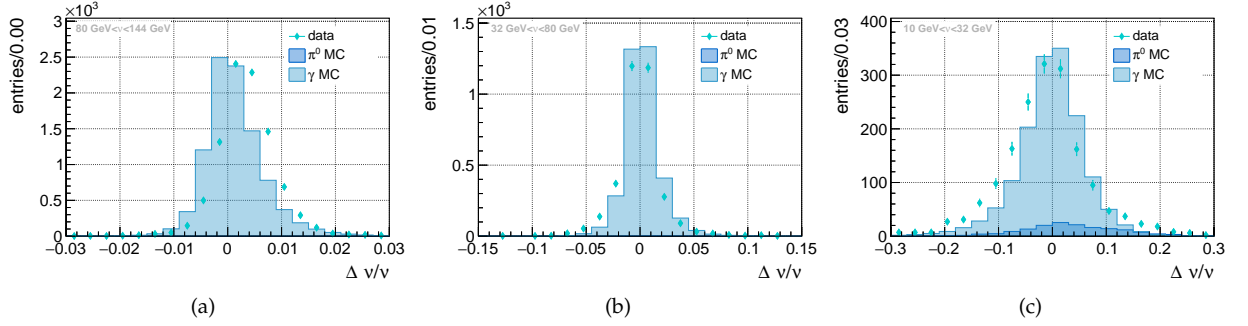
Figure 5.13: Difference between the measured and fitted value of ν relative to the measured value.

Figure 5.14: Difference between the measured and fitted value of $\phi_{\gamma\gamma*}$ relative to the measured value.
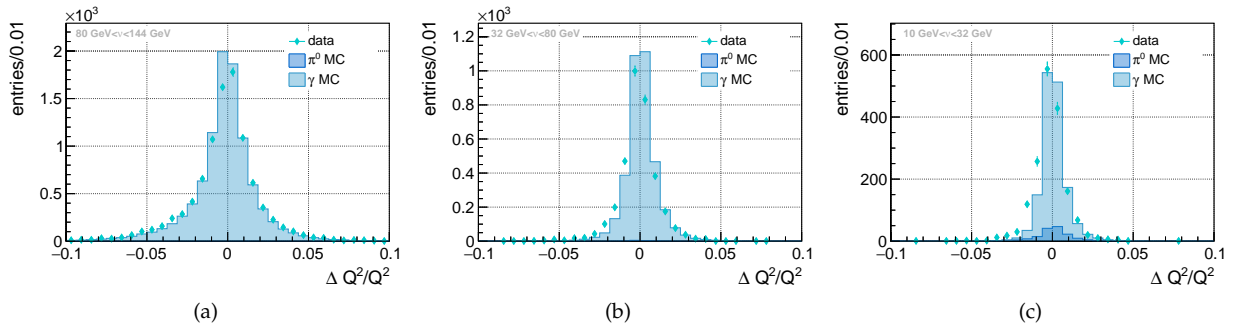
Figure 5.15: Difference between the measured and fitted value of Q^2 relative to the measured value.
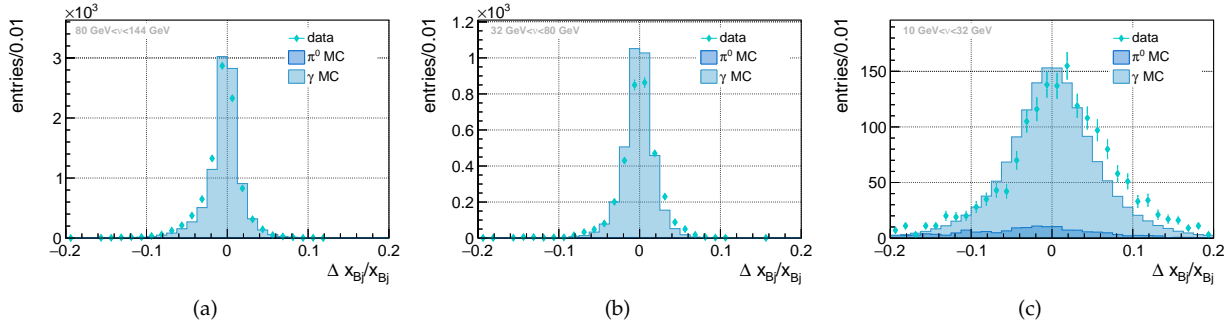
Figure 5.16: Difference between the measured and fitted value of x_{Bj} relative to the measured value.
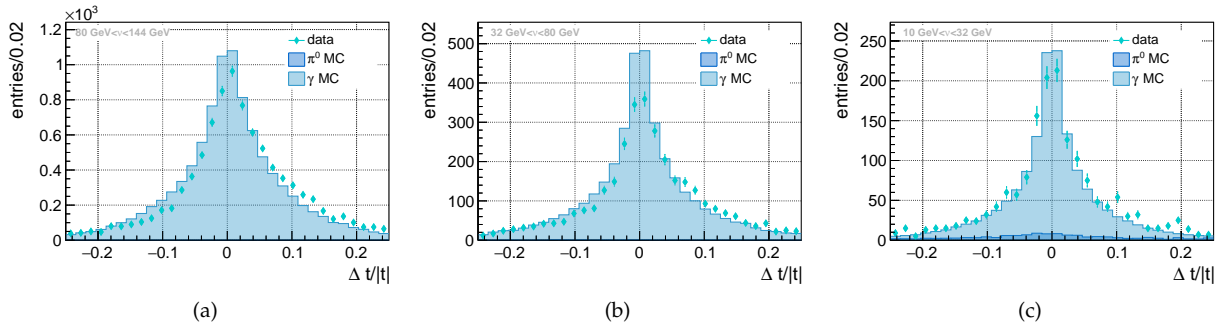
Figure 5.17: Difference between the measured and fitted value of $|t|$ relative to the measured value.

5.3 | Determination of the Bethe-Heitler contribution and the π^0-background contamination

The exclusive photon event sample includes beside of the DVCS also a contribution by Bethe-Heitler and a background contamination due to the decay of neutral pions. To extract the pure DVCS contribution to the exclusive photon production cross section, those have to be determined and subtracted.
The details for determining the Bethe-Heitler contribution using a Monte-Carlo sample for exclusive photons (see Sec. 3.2.1) are discussed in Section 5.3.1. A method to determine the π^0-background contamination is summarized in Section 5.3.2.

5.3.1 | The Bethe-Heitler contribution

The Bethe-Heitler is a pure QED process, therefore its cross section can be calculated using the well known elastic form factors in lepton-proton scattering. To determine its contribution to the exclusive photon data sample, the HEPGEN Monte-Carlo introduced in Section 3.2.1 is used. This sample is obtained by applying the selection criteria discussed in Section 5.1, except some modifications, which

are needed as for e.g. a certain timing information is not available for Monte-Carlo data. Thus, the following criteria are not applied in the selection:

- rejection of bad spills,

- event within time in spill window,

- meantime of track,

- number of hits in BMS.

Those criteria refer mainly to the incoming muon. As it was mentioned in Section 3.2.2 those are not simulated but their parameters are extracted from data and used in the simulation.
To obtain the Bethe-Heitler Monte-Carlo sample, each event is weighted by ω_{PAM}, which is the weight corrected for the lepton mass as introduced in Section 3.2.2.1. In the following this Monte-Carlo sample will be referred to as Bethe-Heitler Monte-Carlo (BH MC).

To illustrate the contribution of the Bethe-Heitler, Figure 5.18a, 5.18b and 5.18c show the $\phi_{\gamma*\gamma}$-distributions in data and the Bethe-Heitler Monte-Carlo in the reference, interference and extraction region. A strong $\phi_{\gamma*\gamma}$-dependence of the Bethe-Heitler is observed in all ν-regions. Especially in the reference region, where the Bethe-Heitler process is dominant, a good agreement between the data and the Bethe-Heitler is obtained (98.8%±1%). In the extraction region the difference between the data and the Monte-Carlo hints to the events used for determining the DVCS cross section. These distributions still include the contamination by the invisible π^0-background, which is discussed in Section 5.3.2.2.

The Bethe-Heitler Monte-Carlo distributions are scaled by the ratio of the data luminosity $\mathcal{L}$ to the Monte-Carlo luminosity $\mathcal{L}_{\mathrm{MC}}$:

$$c_{\mathrm{BH}} = \frac{\mathcal{L}}{\mathcal{L}_{\mathrm{MC}}}. \tag{5.22}$$

It is calculated according to:

$$\mathcal{L}_{\mathrm{MC}} = \frac{\sum\limits_{i=1}^{N_{\mathrm{gen}}} \omega_i^{\mathrm{DVCS}}}{\sigma_{\mathrm{MC}}^{\mathrm{DVCS}}}. \tag{5.23}$$

Here, N_{gen} refers to the number of generated events , ω_i to weight of event i and $\sigma_{\mathrm{MC}}^{\mathrm{DVCS}}$ to the integrated Monte-Carlo cross section for the DVCS process in a given phase space ($\Delta Q^2 \Delta \nu \Delta t \Delta \phi_{\gamma*\gamma}$). The use of the DVCS weights and the corresponding cross section in Equation 5.23 is not mandatory. In principle they can be replaced by any of the available processes, introduced in Section 3.2.2.1. Numerically it is favourable to use the DVCS weights, as the Bethe-Heitler weights show larger variations, which could result in large fluctuations in a finite Monte-Carlo sample. Therefore, the numerical integration done to determine $\sigma_{\mathrm{MC}}^{\mathrm{DVCS}}$ are more stable in case of DVCS.

(a)

(b)

(c)
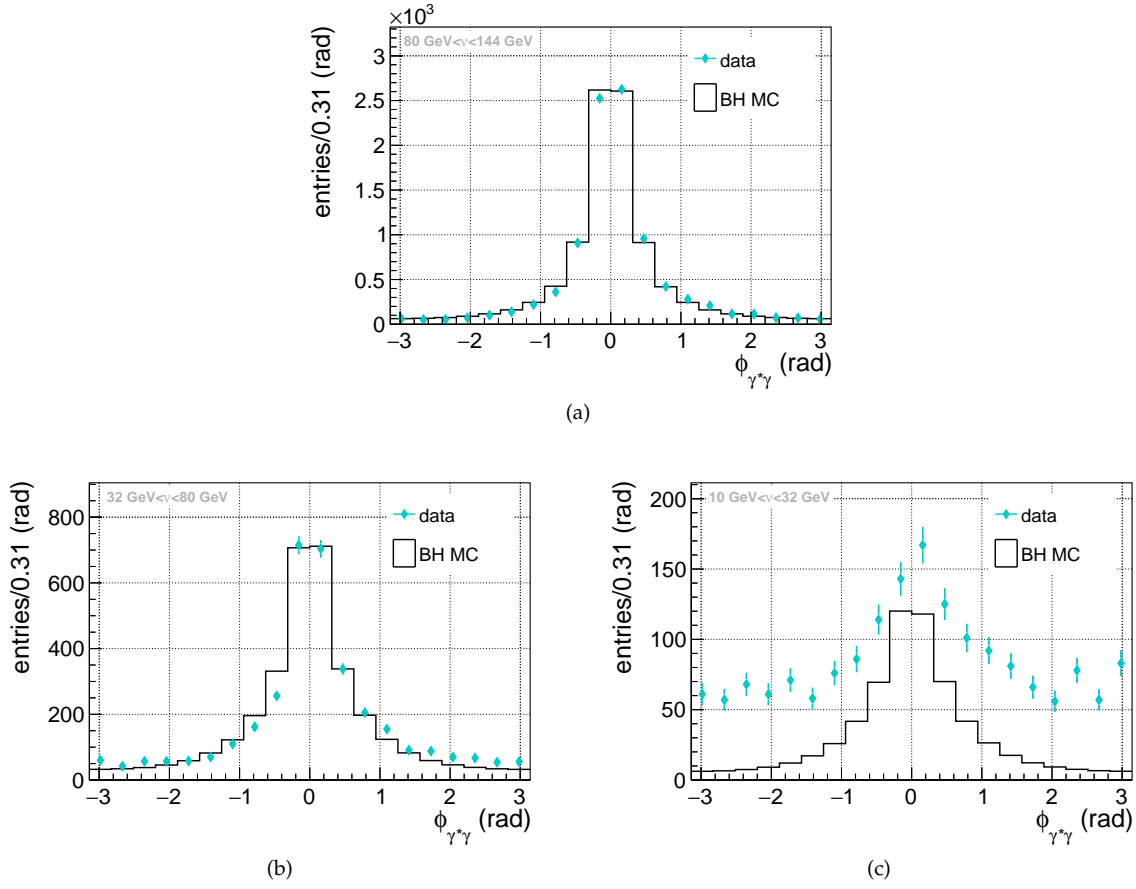
Figure 5.18: $\phi_{\gamma*\gamma}$-distributions for data and Bethe-Heitler Monte-Carlo in the reference (a), interference (b) and extraction region (c).

Using the following phase space when generating the Monte-Carlo events:

- $-\pi \leq \phi_{\gamma*\gamma} \leq \pi$,
- $2\,\text{GeV} < \nu < 170\,\text{GeV}$,
- $0.5\,(\text{GeV}/c)^2 < Q^2 < 80\,(\text{GeV}/c)^2$ and
- $0.001\,(\text{GeV}/c)^2 < t' < 1.2\,(\text{GeV}/c)^2$.

Here, t' is:

$$t' = t - t_{\min},$$

where

$$t_{\min} = -\Delta^2_{\min} = \frac{Q^2}{x_{Bj}} \cdot \frac{\left(\frac{2M_p^2 x_{Bj}^2}{Q^2} - \sqrt{1 + \frac{4M_p^2 x_{Bj}^2}{Q^2}} \right)}{\left(\frac{2M_p^2 x_{Bj}}{Q^2} - \sqrt{1 + \frac{4M_p^2 x_{Bj}^2}{Q^2}} \right)}$$

140

is the minimal squared four-momentum transfer to the proton needed to produce a real photon [27]. In this phase space the integrated Monte-Carlo cross section is $\sigma_{\mathrm{MC}}^{\mathrm{DVCS}} = 9.93938024 \cdot 10^{-34} \mathrm{cm}^2$.

5.3.1.1 | Quality of the Bethe-Heitler Monte-Carlo

The quality of the Bethe-Heitler simulation is illustrated by comparing distributions extracted from data and reconstructed Monte-Carlo in the reference region. Those event samples are obtained by applying the selection criteria summarized in Section 5.1, with the modifications for the Monte-Carlo selection described in the previous Section, on the available statistics in data and Monte-Carlo (see intro to Ch. 4 and Sec. 5.3.1.2). The Monte-Carlo distributions are scaled according to Equation 5.22.

Figure 5.19a to 5.19d show the distributions in ν, x_{Bj}, Q^2 and $|t|$ (top) and the corresponding ratios (bottom), which are fitted assuming a constant value. The result of the fits are indicated as a solid red line. Overall there is a good agreement between the data and the Bethe-Heitler Monte-Carlo distributions with some deviations at large values of ν, Q^2 and x_{Bj}. In Figure 5.20a to 5.20e distributions related to the incoming and scattered muons are shown, namely the energy distribution of the incoming muons and the energy, polar angle, azimuthal angle and transverse momentum distributions of the scattered muons. Here, a very good agreement between both samples is achieved. At large polar angles and large transverse momenta of the scattered muons a small discrepancy is observed affecting only a small number of events. In the energy, polar and azimuthal angle distributions of the real photons, shown in Figures 5.21a to 5.21c only small deviations at large photon energies and polar scattering angles are visible. These are related to the deviations observed at large values of ν. The kinematics of the recoil protons, namely their momentum, transverse momentum and polar angle distributions are displayed in Figures 5.22a, 5.22b and 5.22c. The corresponding ratios show a close to perfect agreement between the data and the Bethe-Heitler Monte-Carlo.

In summary, the data is well reproduced by the simulation for a variety of different kinematic distributions, which are related to the initial and final state particles of the exclusive photon production. This high degree of agreement, which is obtained in the reference region assures to use the Bethe-Heitler Monte-Carlo to subtract its contribution to the exclusive photon cross section in the extraction region.
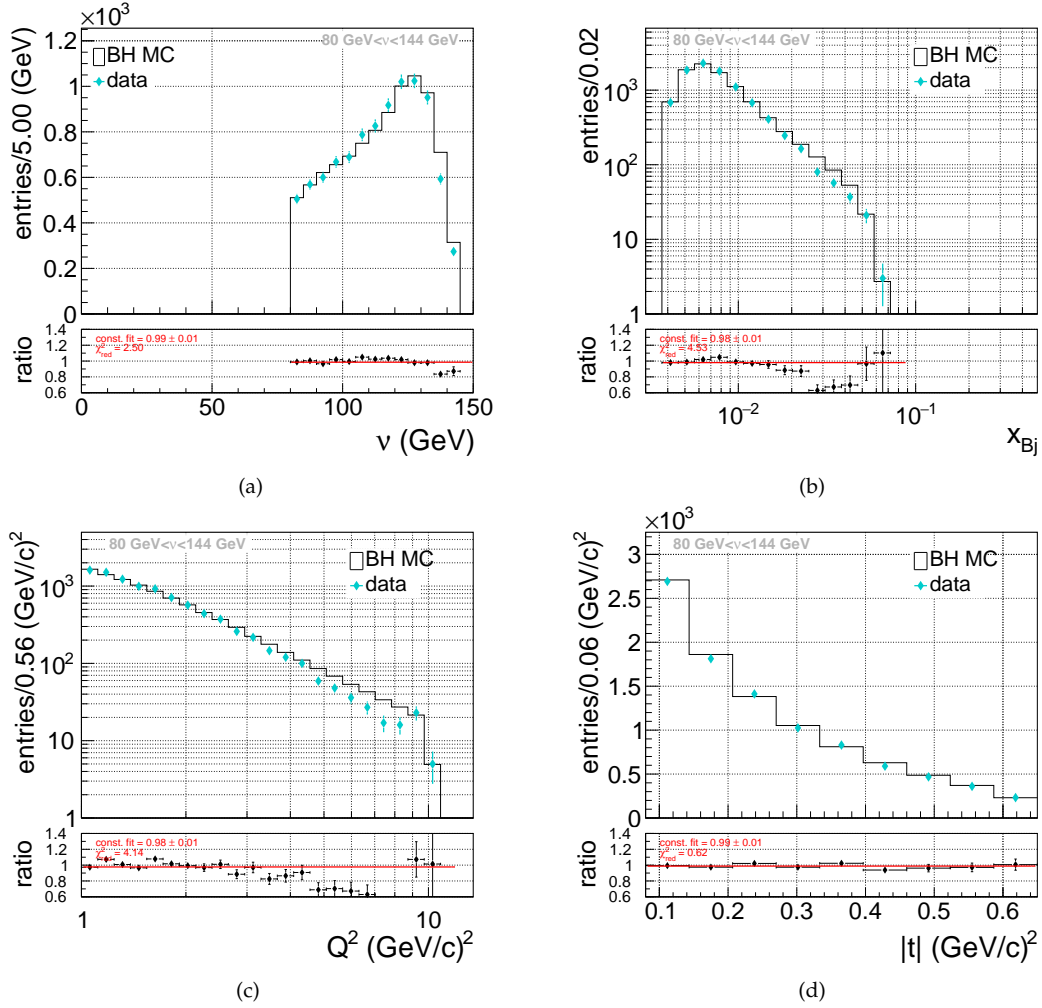
Figure 5.19: Data and Bethe-Heitler Monte-Carlo distributions for ν (a), x_{Bj} (b), Q^2 (c) and $|t|$ (d) in the reference region.
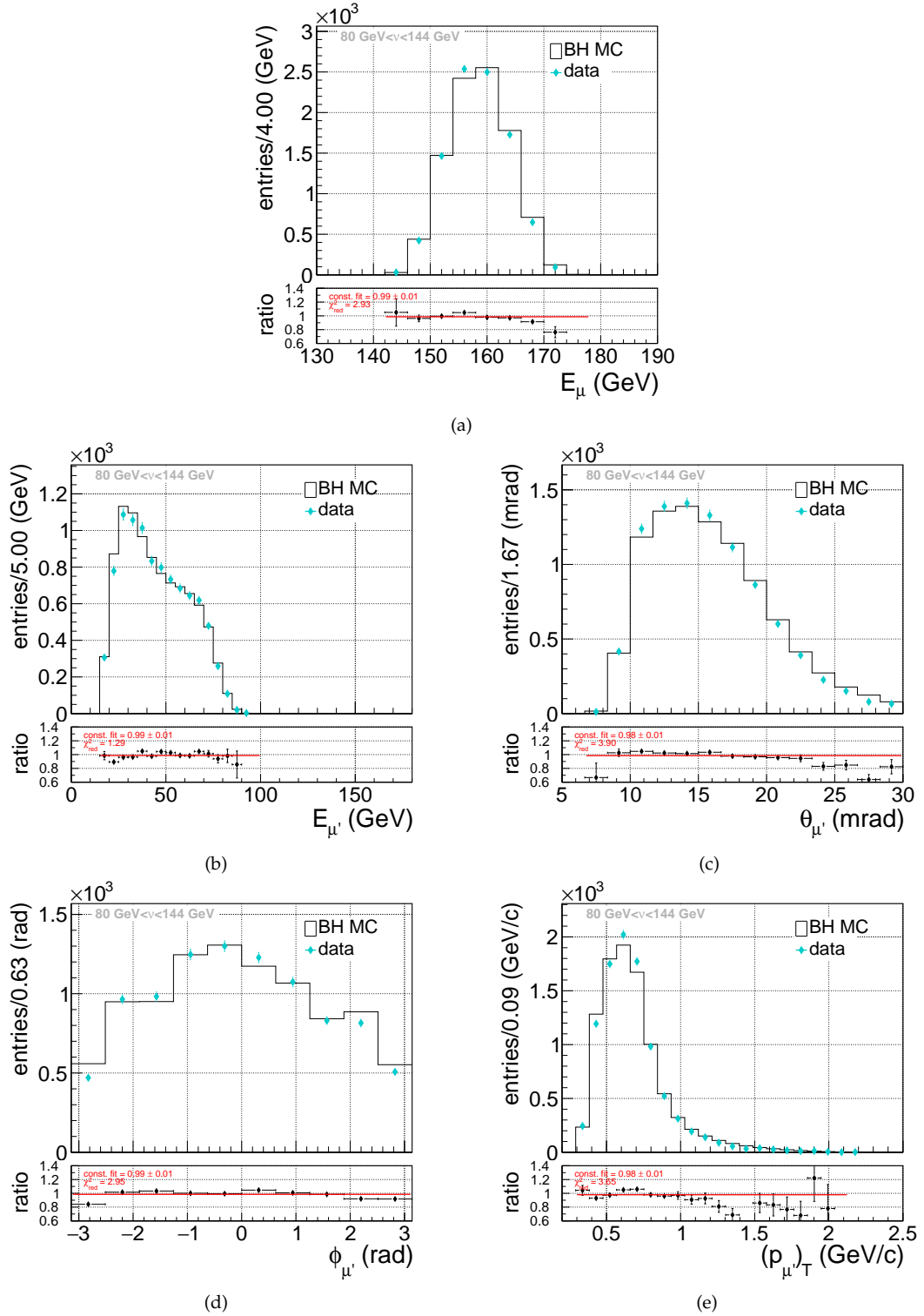
Figure 5.20: Data and Bethe-Heitler Monte-Carlo distributions of the energy of the incoming muons (a) and the energy (b), the polar angle (c), the azimuthal angle (d) and the transverse momentum (e) of the scattered muons in the reference region.

(a)

(b)

(c)
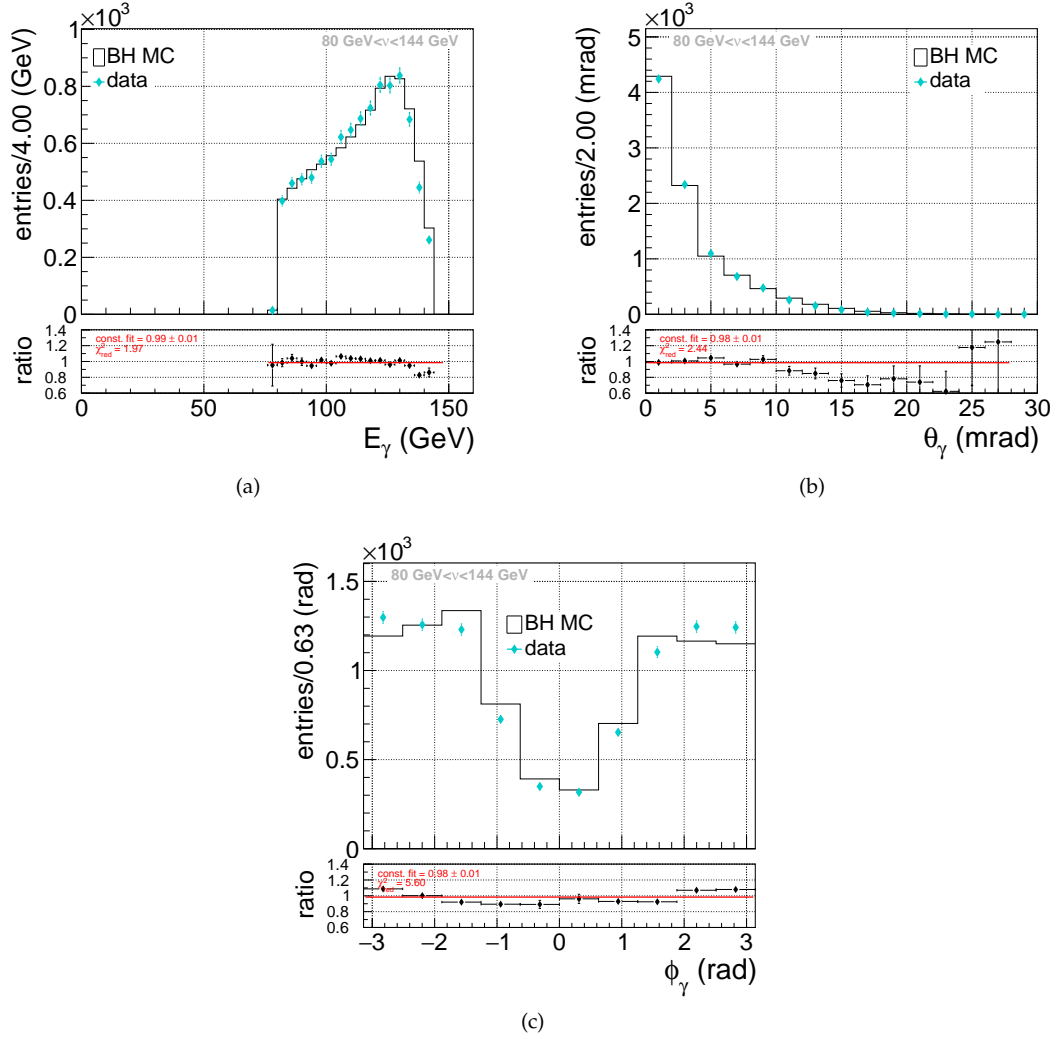
Figure 5.21: Data and Bethe-Heitler Monte-Carlo distributions of the energy (a), the polar angle (b) and the azimuthal angle (c) of the real photon in the reference region.

(a)

(b)

(c)
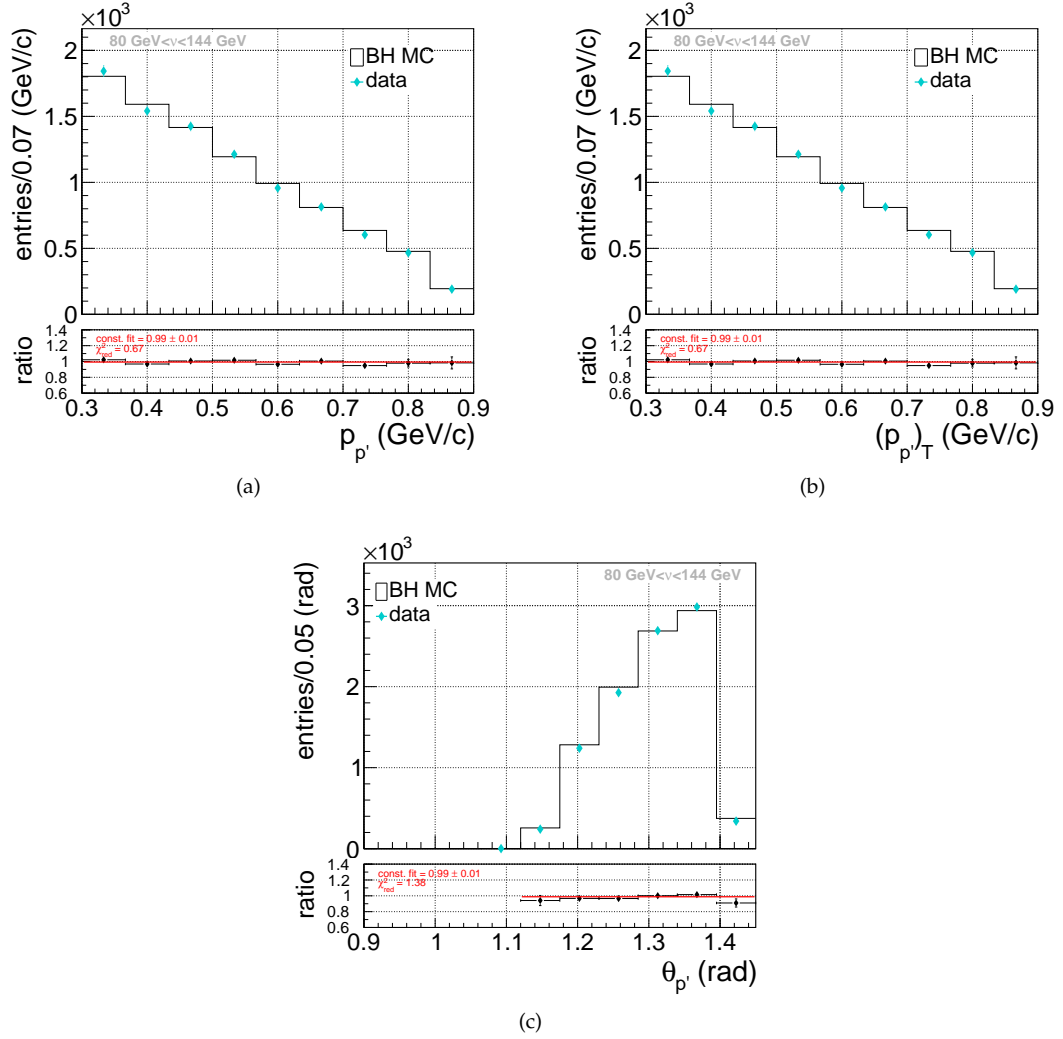
Figure 5.22: Data and Bethe-Heitler Monte-Carlo distributions of the momentum (a), the transverse momentum (b) and the polar angle (c) of the recoil proton in the reference region.

5.3.1.2 | Summary of the available Monte-Carlo statistics for exclusive photon production

The available Monte-Carlo statistics for exclusive photon production is summarized in Table 5.6. Here, N^{gen} is the total number of generated events, N^{rec} is the number of reconstructed events after applying the selection criteria for exclusive photon events and $\mathcal{L}_{\text{MC}}^{\mathcal{P},\pm}$ the integrated Monte-Carlo luminosity separately for μ^+ and μ^- calculated according to Equation 5.23.

Period	N^{gen} (total)	N^{rec} (selection)	$\mathcal{L}_{\text{MC}}^{\mathcal{P},+}/10^{38}$ cm^{-2}	$\mathcal{L}_{\text{MC}}^{\mathcal{P},-}/10^{38}$ cm^{-2}
P04	18 861 335	1 022 437	13.42	13.37
P05	17 926 184	976 543	13.62	11.98
P06	15 243 306	892 114	10.60	11.14
P07	17 947 609	1 039 498	11.96	13.56
P08	19 205 728	1 189 098	12.68	15.09
P09	10 330 951	631 107	9.13	5.58
total	99 515 113	5 750 797	71.41	70.72

Table 5.6: Summary of the statistics of the exclusive photon Monte-Carlo in each period. Here, N^{gen} denotes the total number of generated events and N^{rec} the number of reconstructed events after applying the exclusive photon event selection. The Monte-Carlo luminosity is calculated according to Eq. 5.23.

5.3.2 | The π^0-backgound contamination

For estimating the π^0-background contamination, one has to distinguish between two cases. In the first case both decay photons are detected. Therefore, it is possible to identify and remove these events directly from the data sample. This contribution is referred to as *visible π^0-background* and is discussed in Section 5.3.2.1. In the second case, only the high energy photon is detected. This contamination is called *invisible π^0-background*. It can be determined using dedicated Monte-Carlo samples considering the hard exclusive production channel and the inclusive production channel in DIS for neutral pions. The method used for this determination is discussed in Section 5.3.2.2.

5.3.2.1 | Contribution of visible π^0-background

The visible π^0 events in the exclusive photon sample can be identified by combining the selected high energy photon that has an energy above the DVCS ECAL thresholds to the low energy photons within the same event, which are below the DVCS thresholds. In the search for low energy photons, only those photons are considered, which are either detected in ECAL0 or in ECAL1 and have energies above a low energy threshold, which is specific for each ECAL. These thresholds are chosen to be above the electronic noise level and are determined to be 0.5 GeV for ECAL0 and 0.63 GeV for ECAL1. The fact that ECAL2 is not considered in the search for π^0, as well as the analysis to determine the low energy threshold limits, are discussed in detail in Section 5.3.3.

An event is considered to be a π^0 event, if the invariant mass of the photon pair is within a 2.5σ range around the nominal π^0-mass (M_{π_0}=134.97 MeV/c^2). This results in a selection criteria of:

$$115\,\text{MeV/c}^2 < M_{\gamma\gamma} < 155\,\text{MeV/c}^2. \tag{5.24}$$

The invariant mass spectrum of the photon pairs in the data sample is shown in Figure 5.23. A clear peak at the π^0 mass is visible. The contributions, where the high energy photon is either detected in

ECAL0 or in ECAL1 are indicated in dark and light blue. For fitting the peak a Gaussian is used and displayed as a green solid line.
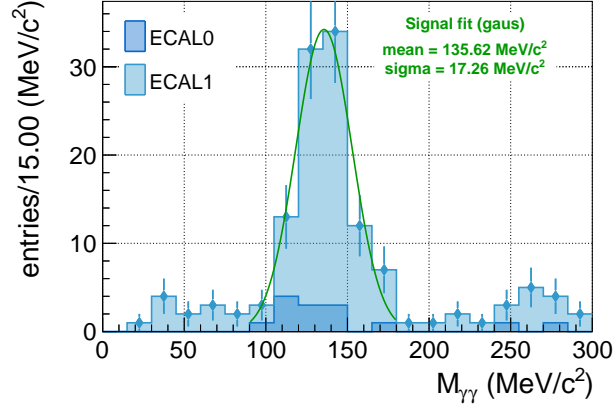
Figure 5.23: $M_{\gamma\gamma}$ spectrum in data seperated by the ECALs.

5.3.2.2 | Contribution of invisible π^0-background

To estimate the contamination of the exclusive photon sample by the invisible π^0-background, two Monte-Carlo simulations are used. One for the hard exclusive and one for the inclusive production of π^0 in DIS (see Sec. 3.2.1). The corresponding reconstructed Monte-Carlo samples for the invisible π^0 contamination are obtained by applying the event selection for exclusive photon production, considering the modifications for simulated data as described in Section 5.3.1.

For normalizing the Monte-Carlo samples, the visible π^0 in data is used in a two step procedure. As a first step, the visible π^0 peaks in the Monte-Carlo samples are separately normalized to the visible π^0 in data. This results in general normalization factors for each Monte-Carlo sample, which are denoted as $c_{\pi^0,\text{HEPGEN}}$ and $c_{\pi^0,\text{LEPTO}}$. As by this general normalization, the yields of both Monte-Carlo contributions are not considered, which leads to an overestimation of the invisible π^0 in the exclusive photon sample. The normalization for the Monte-Carlo samples has to be modified to be:

$$c^{\pi^0} = R_{\text{LEPTO}} \cdot c_{\pi^0,\text{LEPTO}} + (1 - R_{\text{LEPTO}}) \cdot c_{\pi^0,\text{HEPGEN}}. \tag{5.25}$$

Here, R_{LEPTO} denotes to the yield of the inclusive π^0 Monte-Carlo sample. This yield is determined in a related analysis, which is discussed in detail later in this Section. The reason for using the normalization given in Equation 5.25 is that in both cases of π^0 production, the corresponding cross sections are not well known, so a precise determination of the corresponding Monte-Carlo luminosity is not possible. For the inclusive channel the uncertainty in the cross section is due to the not well known fragmentation functions for π^0 in the particular phase space used in the DVCS analysis. The fragmentation functions describe the probability to observe a π^0 in the final state, due to the fragmentation of the target nucleon. The cross section determination for hard exclusive π^0 production is part of recent measurements for studying GPDs in HEMP processes and therefore is not known today.

For determining the yield of the contribution by the HEPGEN and LEPTO Monte-Carlo samples to the invisible π^0 background in the exclusive photon Monte-Carlo sample, a dedicated event selection for exclusive produced π^0 is used. This event selection is similar to the one used for identifying the

exclusive photon events (see Tab. 5.1 and 5.2 in Sec. 5.1), but modified to adjust to the event topology of exclusive π^0 production: $p\mu \to \mu'\pi^0 p' \to \mu'\gamma\gamma p'$. These modifications are summarized as:

- identification of π^0 by selecting photon pairs with a high energy photon above the DVCS thresholds ($E_{\gamma,\text{DVCS thr.}}$=4/5 GeV in ECAL0/1) and a low energy photon below the DVCS threshold, but above the low energy thresholds of $E_{\gamma,\text{low thr.}}$=0.5/0.63 GeV in ECAL0/1.

- The exclusivity conditions (see Sec. 5.1.4) are adjusted to fit the event topology of an exclusive π^0 production:

  - predicted four-momentum and momentum vector of the recoil proton:

  $$p_{p',\text{pred}} = k + p_p - k' - p_{\pi^0},$$
  $$\vec{p}_{p',\text{pred}} = \vec{k} - \vec{k}' - \vec{p}_{\pi^0}.$$

  - four momentum balance:

  $$M_x^2 = (k + p_p - k' - p_{p',\text{reco}} - p_{\pi^0})^2.$$

- No kinematic fit is performed and the selection criteria based on the event kinematics are applied on the reconstructed kinematics by the measurements of the spectrometer and the proton recoil detector.

The relative contributions of the two Monte-Carlo samples are determined by comparing kinematic distributions obtained from the Monte-Carlo samples to the same distributions in data. Suitable for this comparison are the distributions of the exclusivity variables as introduced in Section 5.1.4. For this distributions, it is expected to have a clear visible separation between the exclusive and inclusive contribution. The exclusive produced π^0 should mainly contribute to the central region of the peaks, while in case of inclusive production it is expected to have a much broader distribution, which means a contribution in the periphery of the distributions. The yields are extracted by performing a fitting procedure, in which the combined Monte-Carlo distributions are matched to the corresponding data distribution. For this fit the TFractionFitter [162] toolbox is used, which is provided as part of the ROOT software. This tool is dedicated to "determine the fraction of several types of events contributing to a measured sample" [162] using a binned maximum likelihood approach. In this procedure also the statistics of each sample in each bin are considered, leading to additional parameters in the fit. For more details on the fitting procedure see Reference [24].

The results of the fitting procedure for each exclusivity variable are shown in Figure 5.24 to 5.27. On the left side, a comparison of the data distribution and the distribution obtained from the fit is shown. In all four cases, the data is well described by the fit. The right side shows the normalized distributions of the exclusive (light blue) and inclusive (dark blue) produced π^0 Monte-Carlo samples, which are normalized to the visible π^0 peak in data and scaled by the yields determined by the fit. The sum of both samples is illustrated as the black histogram and compared to the distribution obtained by the fit (cyan data point). The fact that the distribution obtained by the combined Monte-Carlo samples does not perfectly match the distribution obtained by the fit is due the fit considering the amount of statistics in each bin during the maximization of the likelihood function. The best agreement between the combined Monte-Carlo sample and the fit is obtained for M_X^2 and $\Delta(p_{p'})_T$ (see Fig. 5.26 and 5.25). For the ΔZ-distribution shown in Figure 5.27, the distributions obtained from the inclusive and exclusive produced π^0 Monte-Carlo samples are very similar. Both show a clear peak around zero, which makes it hard to distinguish between both contributions. Hence, the fit finds a description of the data by only using the inclusive distribution, but with large deviations between the distribution obtained by the fit and the normalized Monte-Carlo samples.

(a)   (b)
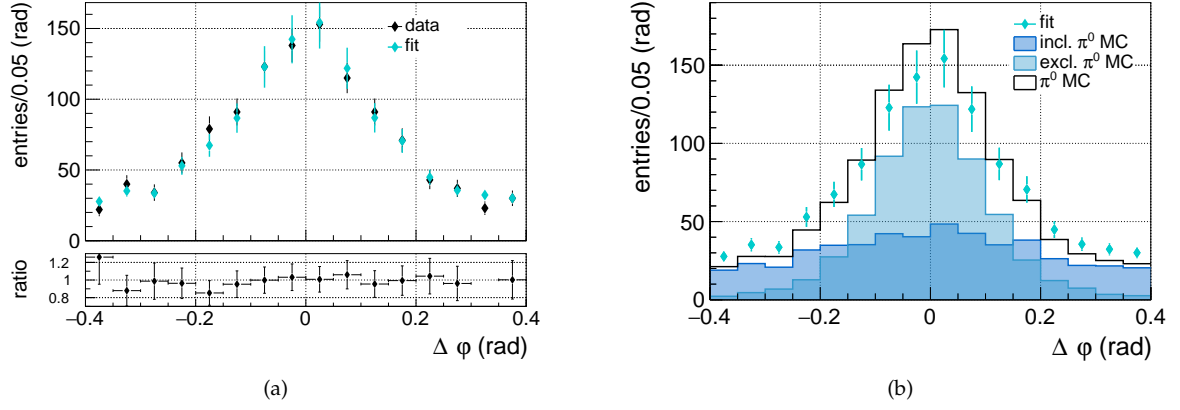
Figure 5.24: (a) Comparison of the $\Delta\phi$-distribution in data (cyan) and the fit (black) of the exclusive and inclusive π^0 Monte-Carlo sample.
(b) Normalized and scaled $\Delta\phi$-distribution of the exclusive (light blue), inclusive (drak blue) and the sum of both π^0 Monte-Carlo (black) sample in comparison to the fit (cyan).

(a)   (b)
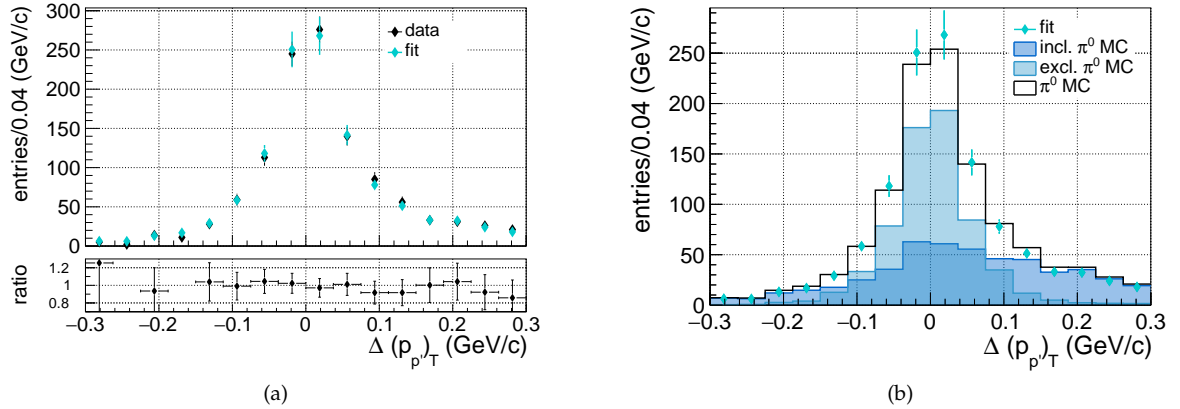
Figure 5.25: (a) Comparison of the Δp_T-distribution in data (cyan) and the fit (black) of the exclusive and inclusive π^0 Monte-Carlo sample.
(b) Normalized and scaled Δp_T-distribution of the exclusive (light blue), inclusive (dark blue) and the sum of both π^0 Monte-Carlo (black) sample in comparison to the fit (cyan).

(a)   (b)
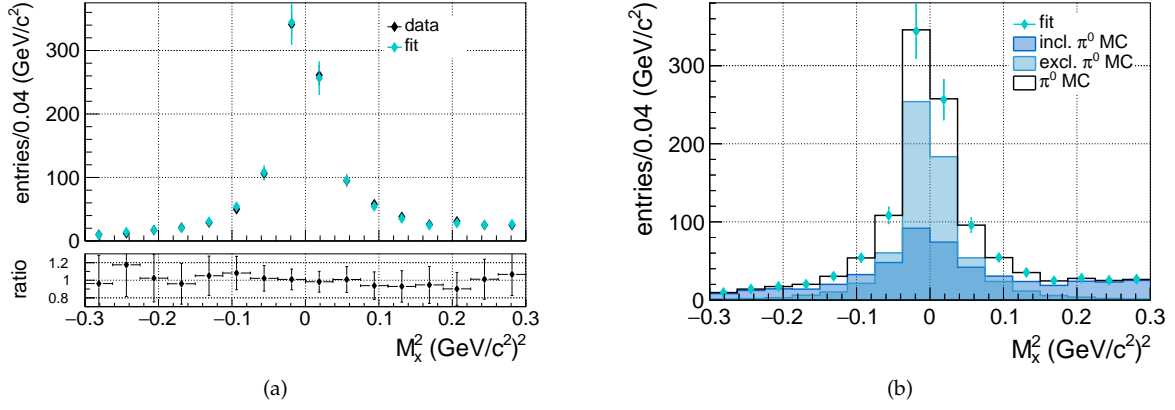
Figure 5.26: (a) Comparison of the M_X^2-distribution in data (cyan) and the fit (black) of the exclusive and inclusive π^0 Monte-Carlo sample.
(b) Normalized and scaled M_X^2-distribution of the exclusive (light blue), inclusive (dark blue) and the sum of both π^0 Monte-Carlo (black) sample in comparison to the fit (cyan).

(a)   (b)
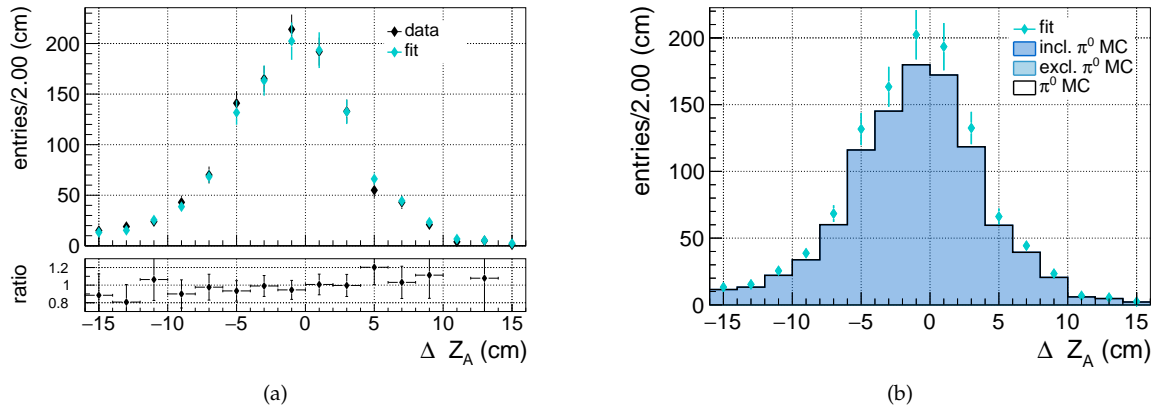
Figure 5.27: (a) Comparison of the ΔZ-distribution in data (cyan) and the fit (black) of the exclusive and inclusive π^0 Monte-Carlo sample.
(b) Normalized and scaled ΔZ-distribution of the exclusive (light blue), inclusive (dark blue) and the sum of both π^0 Monte-Carlo (black) sample in comparison to the fit (cyan).

The fit results on the determined yield of LEPTO (R_{LEPTO}) are summarized in Table 5.7 and illustrated in Figure 5.28.

	M_X^2	$\Delta(p_{p'})_T$	$\Delta\phi$	ΔZ
R_{LEPTO}	44.4±4.5%	36.9±3.8%	59.9±5.4%	99.9±3.7%

Table 5.7: Summary of the results and the statistical uncertainty as determined by the fit for R_{LEPTO} in the different data samples for all exclusivity variables.

As discussed previously the agreement between the distribution obtained by the fit and the one obtained by combining the normalized and scaled π^0 Monte-Carlo samples is best for M_X^2 and $\Delta(p_{p'})_T$. Here, the fit also produces comparable results of the Monte-Carlo yields. Besides the obvious deviation of the results obtained from the ΔZ-distribution, also for the $\Delta\phi$-distribution a larger value for the relative contribution of the inclusive π^0 Monte-Carlo sample is obtained. Comparing this distribution to the distributions of M_X^2 and $\Delta(p_{p'})_T$, it is much broader and has a higher relative number of events in the periphery of the distribution. An alternative approach was performed by Po-Ju Lin using a minimal least square approach. The results of this method, when fitting each variable separately or using a combined fit for all variables are illustrated in Figure 5.28 by the dark blue points and the horizontal line respectively. This method produces comparable results, but deviates for $\Delta(p_{p'})_T$ and ΔZ. For more details on this method see Reference [121].
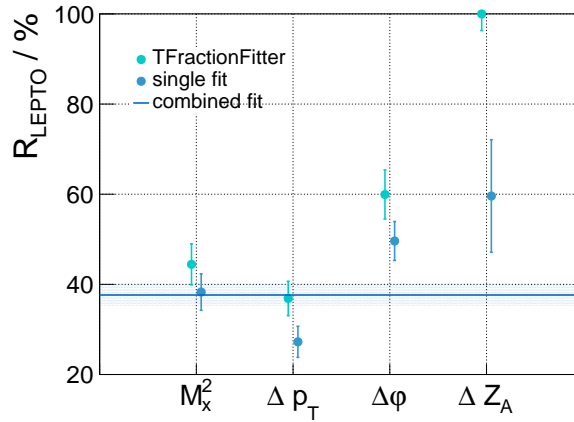
Figure 5.28: Results on the relative fraction of the LEPTO π^0 Monte-Carlo (R_{LEPTO}) for all exclusivity variables.

Extended studies on the consistency of the analysis were performed by also considering events, which have more than one combination of vertex, proton and π^0 candidates that fulfill all selection criteria. For those events it is expected to increase the amount of inclusive produced π^0, as the exclusive sample is considered to be more clean and therefore includes less of those ambiguous events. Performing this study confirmed the expected results, leading to about 10-15% higher values for the relative contribution of the inclusive π^0 Monte-Carlo. If only those ambiguous events are used, the fit predicted a R_{LEPTO} between 90-100%. In an additional study the ECAL thresholds for the high energy photon are reduced to the thresholds used in the analysis of hard exclusive π^0 production ($E_{\gamma,\pi^0\,\text{thr.}}$=1/2 GeV in

ECAL0/1). Here, the values for R_{LEPTO} are increased by about 10% with respect to the results obtained using the DVCS ECAL thresholds.

Due to the different results of the fit depending on the exclusive variables, it was decided to conclude on a relative contribution of the inclusive produced π^0 Monte-Carlo of R_{LEPTO}=40% with an uncertainty of $\pm 10\%$. Its impact on the result of the $|t|$-dependent DVCS cross section is part of the systematic studies presented in Section 7.2.2.3.

Figure 5.29a and 5.29b show the visible π^0 events in data compared to the contributions by the exclusive and inclusive π^0 Monte-Carlo. The distributions are either obtained using the dedicated π^0 selection (see Fig. 5.29a) or represent the visible π^0 in the exclusive photon samples (see Fig. 5.29b) using the available data and Monte-Carlo statistics. The corresponding Monte-Carlo distributions are normalized to the visible π^0 in data and scaled by the relative Monte-Carlo yields. The observed amount of visible π^0 in the exclusive photon data sample is in the order of 80 events.

(a)   (b)
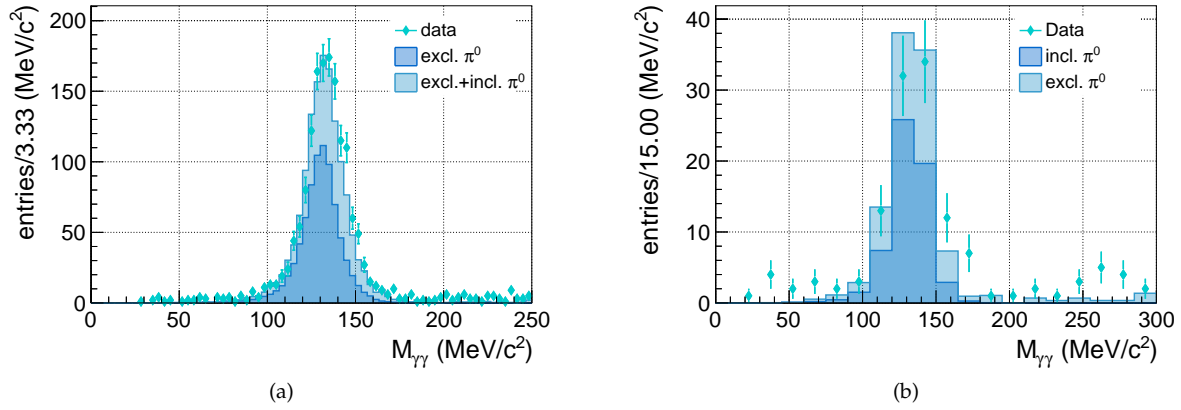
Figure 5.29: (a) $M_{\gamma\gamma}$-spectra for the real data and the normalized and scaled π^0 Monte-Carlo samples using the event selection for exclusive π^0 production.
(b) $M_{\gamma\gamma}$-spectra for the real data and the normalized and scaled Monte-Carlo samples using the event selection for exclusive γ production.

5.3.3 | Study of the low energy ECAL thresholds

The low energy ECAL thresholds have a direct impact on the visible π^0 and therefore on the normalization of the π^0 Monte-Carlo samples. These thresholds should be chosen to be higher than the level of the electronic noise observed in the ECALs. A hint to the level of electronic noise depending on the type of the ECAL cells can be seen in Figure 4.39 in Section 4.8.3. The electronic noise is visible as the vertical band overlaying the signal at low energies. The highest noise level, compared to the noise levels in ECAL1 and ECAL0, is observed for ECAL2 . The distributions are obtained using a very basic selection, therefore the observed noise levels are not directly comparable to the noise observed in the exclusive photon sample.
To determine the noise level in the ECALs, the impact of the low energy threshold settings on the observed visible π^0 in data is studied. In this study the signal to noise ratio (SNR) in the invariant mass spectra of the photon pairs is determined, which are obtained by combining the high energy photon

(above the DVCS threshold) to the low energy photons for different values of the low energy thresh-olds. The SNR is calculated by determining the number of events contributing to the visible π^0 peak and dividing it by the number of background events in the signal region. These numbers are extracted by a fit using a Gaussian for the π^0 signal and a constant fit or first degree polynomial for the back-ground. To allow to study the low energy threshold settings for each ECAL separately, only photon pairs detected in a specific ECAL are used. Figure 5.30a and 5.30b show the invariant mass spectra of photon pairs in ECAL1, using a low energy threshold of either 0.35 GeV or 0.6 GeV. The signal and back-ground fits are indicated as green and blue dashed lines. The corresponding combined fit is displayed as a dashed cyan line. The given number of signal and background events are calculated by the integral of the corresponding fit distributions. For the number of background events in the signal regime only the region of the Gaussian fit is considered in the integration.

(a)   (b)
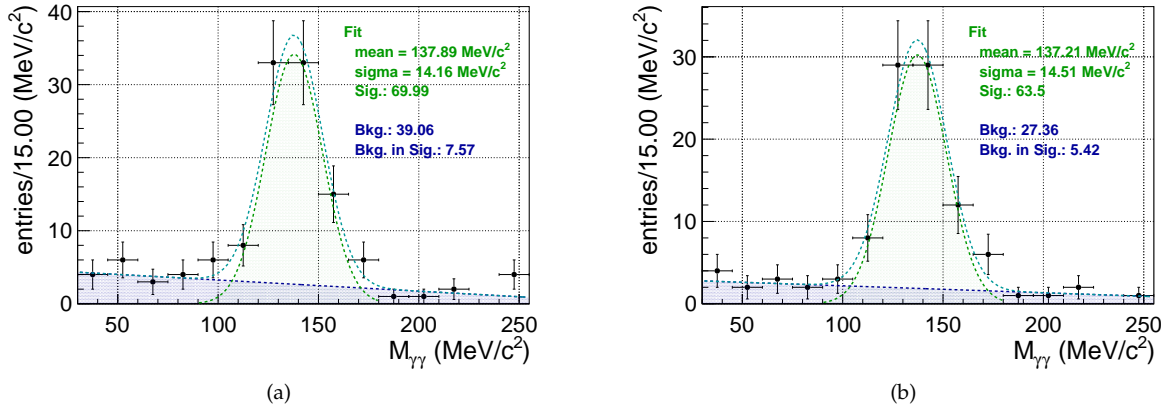
Figure 5.30: (a) $M_{\gamma\gamma}$-spectrum at $E_{\gamma,\text{low thr.}}$=0.35 GeV when only considering photons in ECAL1.
(b) $M_{\gamma\gamma}$-spectrum at $E_{\gamma,\text{low thr.}}$=0.6 GeV when only considering photons in ECAL1.
The spectra are fitted using a Gaussian (green) for the signal and a first degree polynomial (blue) as background to determine the corresponding SNR.

The summary of the SNR study for photon pairs detected in ECAL1 is shown in Figure 5.31a. The SNR increases until a threshold value of about 0.6 GeV and stays rather constant afterwards.
To further review the low energy threshold settings, the visible π^0 in data are compared to the sum of visible and invisible π^0 in the corresponding Monte-Carlo samples. The result of this comparison depending on the low energy threshold settings is displayed in Figure 5.31b. For an easy comparison the diagrams are normalized to the corresponding values at a low energy threshold of 0.3 GeV. For a stable normalization to the visible π^0 in data, the sum of visible and invisible π^0 in the Monte-Carlo samples is expected to be constant. This can be seen for low energy threshold values higher than 0.55 GeV. For lower threshold settings the observed changes in the sums are an artefact of the much higher statistics in Monte-Carlo compared to the one available for data, which affects the normalization. Considering the results of both studies it was decided to chose a low energy threshold setting for ECAL1 of 0.63 GeV.
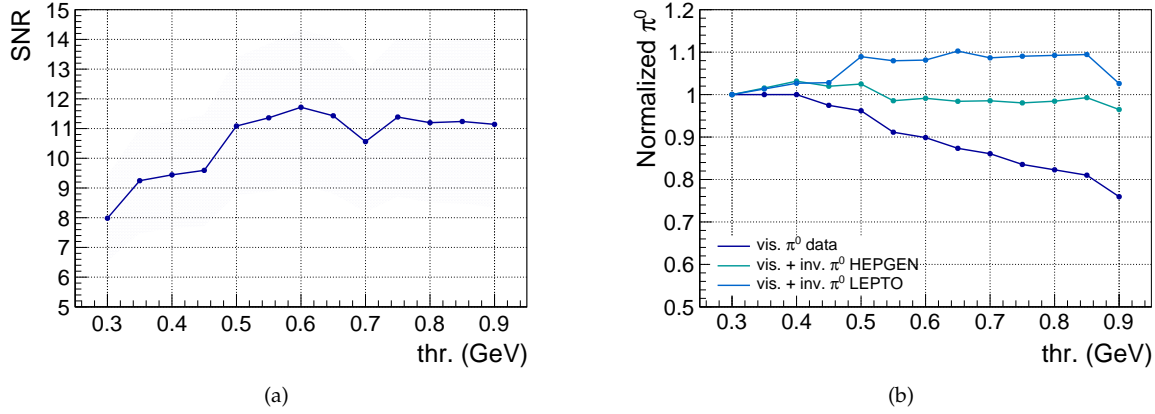
Figure 5.31: (a) Result of the Signal-to-Noise ratio (SNR) of the visible π^0 in data as function of the low energy threshold considering only photons in ECAL1.
(b) Visible π^0 in data and sum of visible and invisible π^0 in the Monte-Carlo samples as function of the low energy threshold considering only photons in ECAL1. The numbers are normalized to the corresponding amount of π^0 at a low energy threshold of 0.3 GeV.

The same study was performed for photon pairs detected in ECAL0 and ECAL2. In case of ECAL0 the amount of observed photon pairs is much smaller compared to those in ECAL1. This can be seen in the invariant mass spectra of the photon pairs at low energy thresholds of 0.3 GeV and 0.5 GeV in Figure 5.32a and 5.32b. The summary of the results of these studies are shown in Figure 5.33a and Figure 5.33b. The available statistics is too small to allow to draw conclusions on the limit of the low energy thresholds. As the noise level in ECAL0 is expected to be low, it was decided to set the low energy threshold to 0.5 GeV, which is above the noise levels indicated in Figure 4.39a in Section 4.8.3.

(a)   (b)
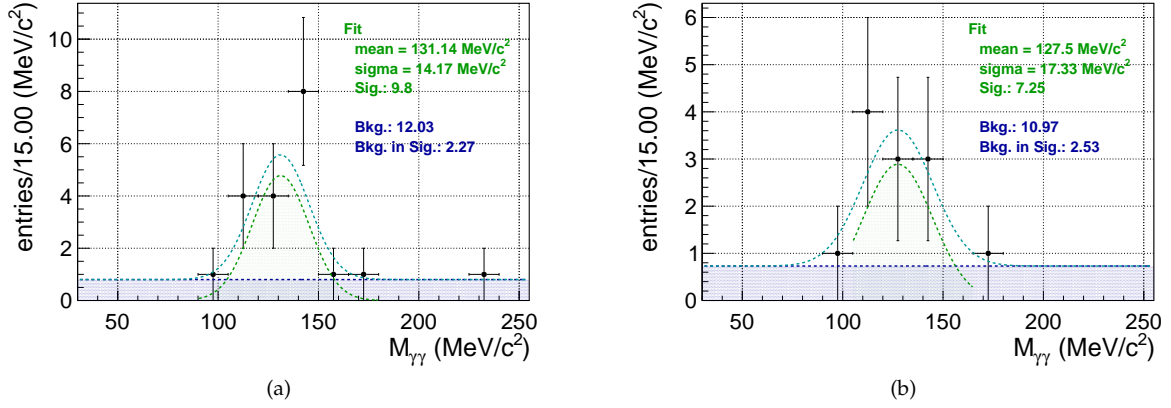
Figure 5.32: (a) $M_{\gamma\gamma}$-spectrum at $E_{\gamma,\text{low thr.}}$=0.3 GeV when only considering photons in ECAL0.
(b) $M_{\gamma\gamma}$-spectrum at $E_{\gamma,\text{low thr.}}$=0.5 GeV when only considering photons in ECAL0.
The spectra are fitted using a Gaussian (green) for the signal and a zero degree polynomial (blue) as background to determine the corresponding SNR.

(a)   (b)
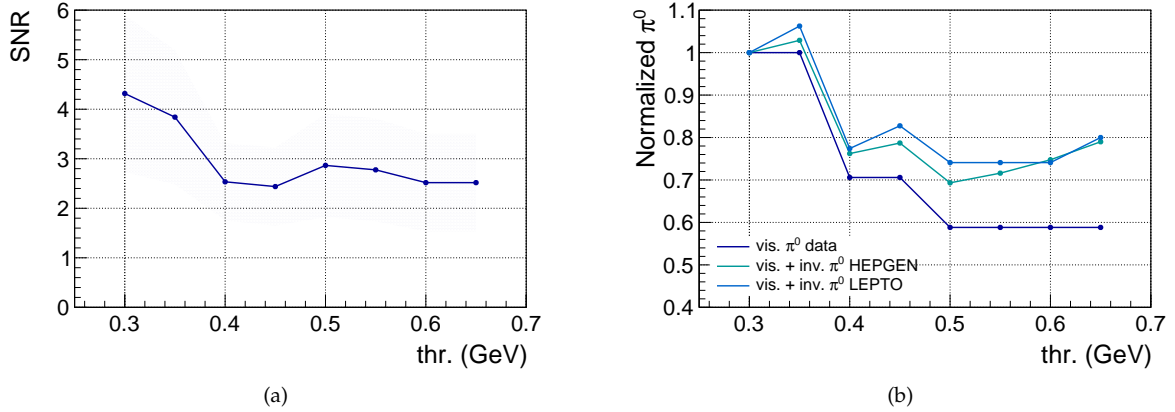
Figure 5.33: (a) Result of the Signal-to-Noise ratio (SNR) of the visible π^0 in data as function of the low energy threshold considering only photons in ECAL0.
(b) Visible π^0 in data and sum of visible and invisible π^0 in the Monte-Carlo samples as function of the low energy threshold considering only photons in ECAL0. The numbers are normalized to the corresponding amount of π^0 at a low energy threshold of 0.3 GeV.

155

The invariant mass spectra of photon pairs detected in ECAL2 for low energy thresholds of 1.0 GeV and 3.0 GeV are shown in Figure 5.34a and 5.34b. The spectra show a considerable amount of noise, but no clear hint to π^0 events. Extending this study to also allow low energy photons in ECAL0 and ECAL1, one obtains the distributions shown in Figure 5.34c and 5.34d. As in both cases no clear hint to π^0 in ECAL2 is visible, it is not used for determining the π^0 background contamination.
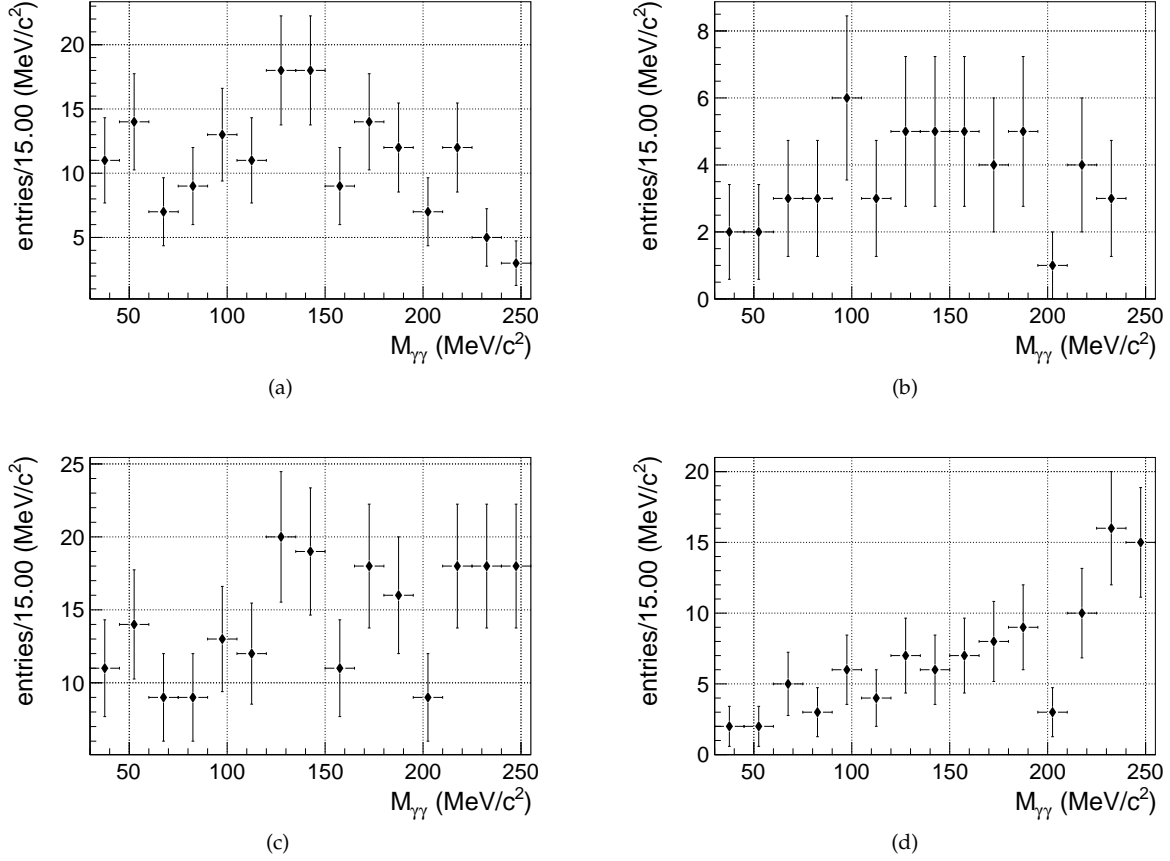
Figure 5.34: $M_{\gamma\gamma}$-spectra of detected photon pairs for $E_{\gamma,\mathrm{low\ thr.}}$=1.0 GeV and $E_{\gamma,\mathrm{low\ thr.}}$=3.0 GeV when only considering photon pairs detected in ECAL2 (a) and (b) or when also considering low energy photons in ECAL0 and ECAL1 (c) and (d).

5.4 | The DVCS data sample

This Section comprises the results of the previous studies to identify the different contributions to the exclusive photon data sample. These contributions are summarized in detail in Section 5.4.1. A detailed discussion of the corresponding kinematic distributions, especially those of the identified DVCS events is in Section 5.4.2.

5.4.1 | Summary of the contributions to the exclusive photon sample

The total number of events in data, the contributions by the Bethe-Heitler and the visible and invisible background contamination due to exclusive and inclusive produced π^0 in each ν-region are summarized in Table 5.8. A detailed listing separately for each period of data tanking is in Table 5.9.

The exclusive photon events are extracted using the selection criteria introduced in Section 5.1. The included contribution by Bethe-Heitler is determined by a dedicated Bethe-Heitler Monte-Carlo sample for each period, which is scaled to the data as discussed in Section 5.3.1. For the inclusive and exclusive produced π^0, only Monte-Carlo samples for period 09 are available. The corresponding background contamination are determined according to Section 5.3.2. The differences in the visible and invisible π^0 contamination in each period is due to the different normalization to the visible π^0 in data.

About 64.8% of the selected events in data are in the reference region, where the contribution to the observed cross section is dominated by the Bethe-Heitler. Here, an agreement of 98.8% between data and Bethe-Heilter is obtained. A fraction of about 23.5% of the selected events is in the interference region and 11.7% of the events are in the extraction region. In this region about 37.1% of these events are due to the Bethe-Heitler contribution and another 9.4% are due to the invisible π^0 background contamination. Subtracting these from the 1701 observed exclusive photon events, about 910 data events are identified as being produced in DVCS.

Type	reference	interference	extraction
data	9423	3415	1701
vis. π^0 data	0	7	85
BH MC	9532.9	3311.4	631.5
excl. vis. π^0	0.0	2.1	48.3
excl. inv. π^0	0.0	5.8	76.1
incl. vis. π^0	0.0	2.4	31.6
incl. inv. π^0	0.0	8.5	83.3

Table 5.8: Summary of the number of exclusive photon events in data, the Bethe-Heitler contribution by the Bethe-Heitler Monte-Carlo and the visible and invisible π^0 in the exclusive and inclusive π^0 Monte-Carlo sample.

Period	Type	reference	interference	extraction
P04	data	1523	561	292
	vis. π^0 data	0	1	19
	BH MC	1595.3	570.6	108.3
	excl. inv. π^0	0.0	1.4	17.9
	incl. inv. π^0	0.0	2.0	21.8
P05	data	1331	545	232
	vis. π^0 data	0	3	7
	BH MC	1392.8	493.2	94.9
	excl. inv. π^0	0.0	0.7	8.9
	incl. inv. π^0	0.0	1.0	9.8
P06	data	1485	549	241
	vis. π^0 data	0	1	11
	BH MC	1469.2	480.4	91.6
	excl. inv. π^0	0.0	0.8	10.8
	incl. inv. π^0	0.0	1.2	11.8
P07	data	1796	595	276
	vis. π^0 data	0	0	12
	BH MC	1842.4	608.3	114.0
	excl. inv. π^0	0.0	0.8	10.8
	incl. inv. π^0	0.0	1.2	11.8
P08	data	1818	671	378
	vis. π^0 data	0	1	19
	BH MC	1770.7	633.3	122.8
	excl. inv. π^0	0.0	1.4	17.9
	incl. inv. π^0	0.0	2.0	19.6
P09	data	1470	494	282
	vis. π^0 data	0	1	10
	BH MC	1462.5	525.7	100.0
	excl. inv. π^0	0.0	0.8	9.6
	incl. inv. π^0	0.0	1.1	10.8

Table 5.9: Summary of the number of exclusive photon events in data, the Bethe-Heitler contribution by the Bethe-Heitler Monte-Carlo and the invisible π^0 in the exclusive and inclusive π^0 Monte-Carlo sample separately for each period.

5.4.2 | Kinematic distributions of the DVCS contribution

The Figures presented in this Section are illustrating the kinematic distributions of the identified DVCS events. These events correspond to the cumulated μ^+ and μ^- distributions of the Bethe-Heitler contribution and invisible π^0 contamination extracted from the Monte-Carlo samples. These distribution are scaled/normalized following the discussions in Sections 5.3.1 and 5.3.2.

In Figures 5.35a, 5.35b and 5.35c the ν, x_{Bj} and Q^2-distributions are shown considering a ν-region between 10 GeV and 144 GeV. The excess of events in data compared to the Monte-Carlo distributions indicates clearly the presence of DVCS events at ν-values smaller than $\lesssim 40$ GeV and x_{Bj} values larger than 0.03. In Q^2 the events are equally distributed over the considered Q^2-region between $1\,(\text{GeV}/c)^2$ and $10\,(\text{GeV}/c)^2$. The $|t|$-distribution for events in the extraction region, shown in Figure 5.35d, indicate a clear decrease of the DVCS cross section with $|t|$. In Figure 5.36a to 5.36e the energy distribution of
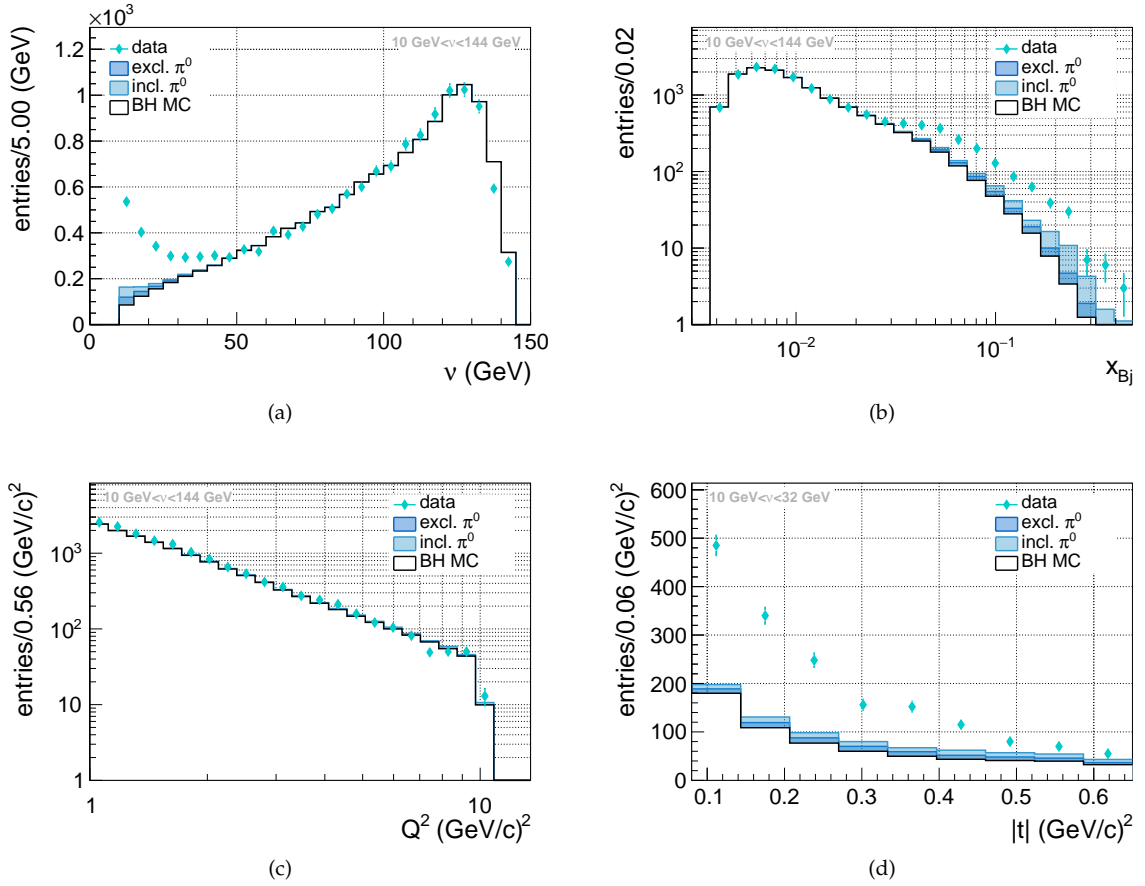
Figure 5.35: ν, x_{Bj}, Q^2 and $|t|$-distributions for data, the Bethe-Heitler contribution and the invisible π^0 contamination.

the incoming muons and the energy, polar angle, azimuthal angle and transverse momentum distribution of the scattered muons are shown. For most of the distributions, the DVCS events are relatively uniformly distributed over the spectra. An exception is seen in the energy distributions of the scattered muon, where the excess of events at high energies reflects the substantial DVCS contribution at small

values of ν. These events correspond to relatively small polar scattering angles, which can be spotted in Figure 5.36c. In the polar angle distribution of the photons, as displayed in Figure 5.37a, the DVCS

(a)

(b)

(c)

(d)

(e)
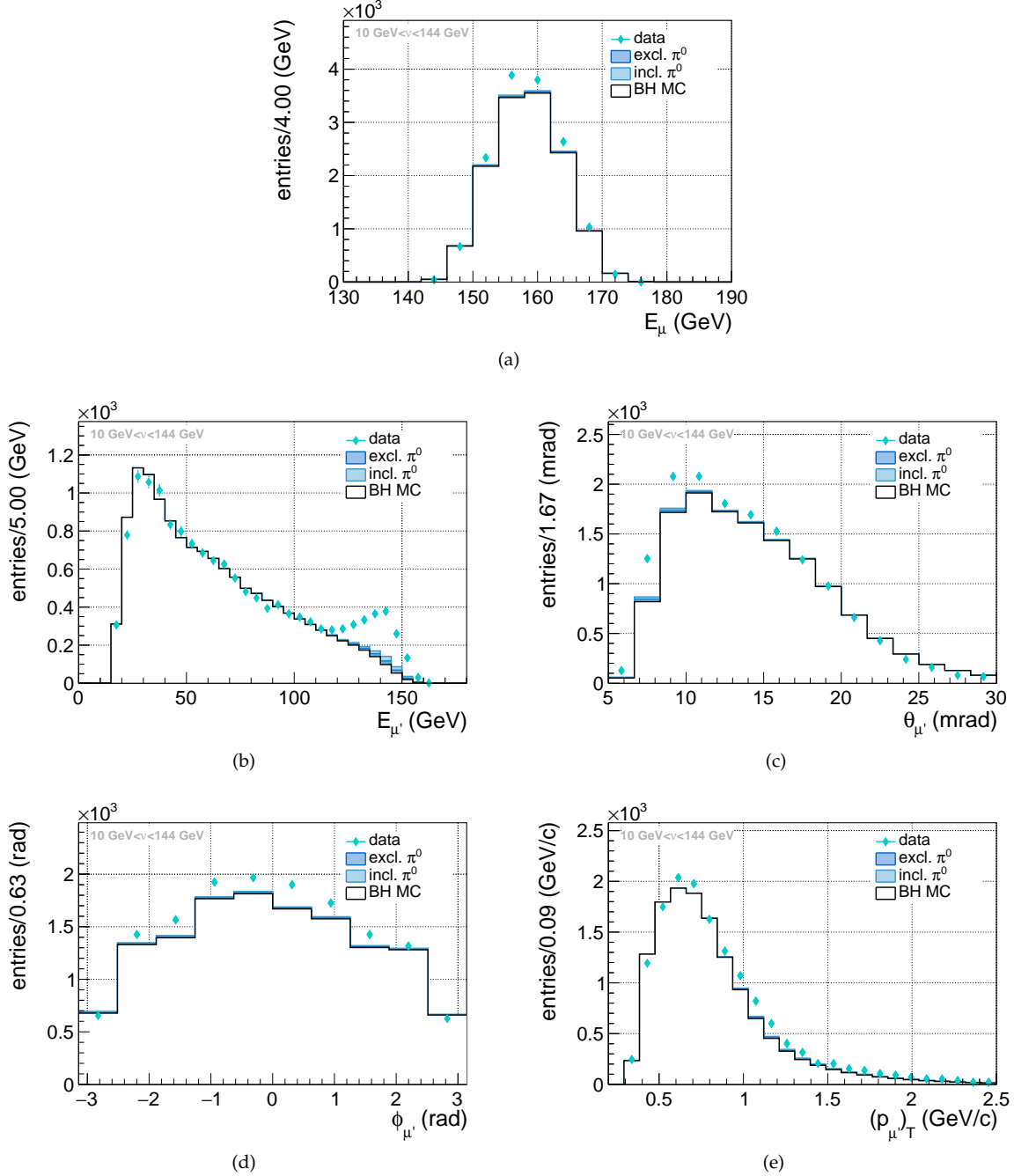
Figure 5.36: Data and Bethe-Heitler Monte-Carlo distributions of the energy of the incoming muons (a) and the energy (b), the polar angle (c), the azimuthal angle (d) and the transverse momentum (e) of the scattered muons in all ν-regions.

events distribute uniformly over the spectrum. For the azimuthal angle distribution, shown in Figure 5.37b, a separation of the DVCS is clearly visible with an excess of data events at large angles, while the small angles are dominated by the Bethe-Heitler contribution. The photon energy distributions for photons in ECAL0, ECAL1 or ECAL2 are shown in Figures 5.37c, 5.37d and 5.37e. Nearly all photons detected in ECAL2 are photons with high energies produced by the Bethe-Heitler. The DVCS photons are produced with lower energies and are detected in ECAL0 and ECAL1.

The distributions of the momenta, the transverse momenta and the polar angle of the recoil proton are displayed in Figures 5.38a, 5.38b and 5.38c. In the momentum and transverse momentum distributions, the observed excess of events is largest at small momenta and decreases to higher momenta, which reflects the observation discussed previously for the $|t|$-distribution. In the polar angle distribution the events are relatively uniformly distributed over the spectrum.

The $\phi_{\gamma*\gamma}$-distributions in the reference, interference and extraction region are shown in Figures 5.39a, 5.39b and 5.39c. In the reference region the data is dominated by the Bethe-Heitler contribution, which has a strong angular dependence and is symmetrical distributed around zero. In data an asymmetry between positive and negative angles is visible. This asymmetry is underlined by calculating the difference of the data and the Monte-Carlo contributions (Bethe-Heitler and invisible π^0) in each bin, displayed in the bottom graph. The observed modulation in $\phi_{\gamma*\gamma}$ around zero is due to the expected $\phi_{\gamma*\gamma}$-dependent and interference contributions to the cross section, which are not present in the Bethe-Heitler Monte-Carlo (see Sec. 2.5.1). For the interference region the situation is similar. Also here a large contribution of Bethe-Heitler and a $\phi_{\gamma*\gamma}$-modulation in the bottom graph is visible. In the periphery regions of the distribution a larger excess of events is visible when comparing the data to the Monte-Carlo contributions, then what is observed in the reference region. In the extraction region a considerably contamination of invisible π^0 is present. The difference between the data and Monte-Carlo distributions show nearly no $\phi_{\gamma*\gamma}$-modulation. This indicates that the DVCS contribution only has a weak $\phi_{\gamma*\gamma}$-dependence, so the events are rather uniformly distributed over the spectrum. The clear offset in the difference hints to the $\phi_{\gamma*\gamma}$ independent contribution to the pure DVCS cross section described by the coefficient c_0^{DVCS} (see Eq. 2.58 in Sec. 2.5.1). The Fourier coefficients by the DVCS and interference contributions to the observed DVCS cross section (see Sec. 2.5.3) are studied in Section 7.3.

(a)

(b)

(c)

(d)

(e)
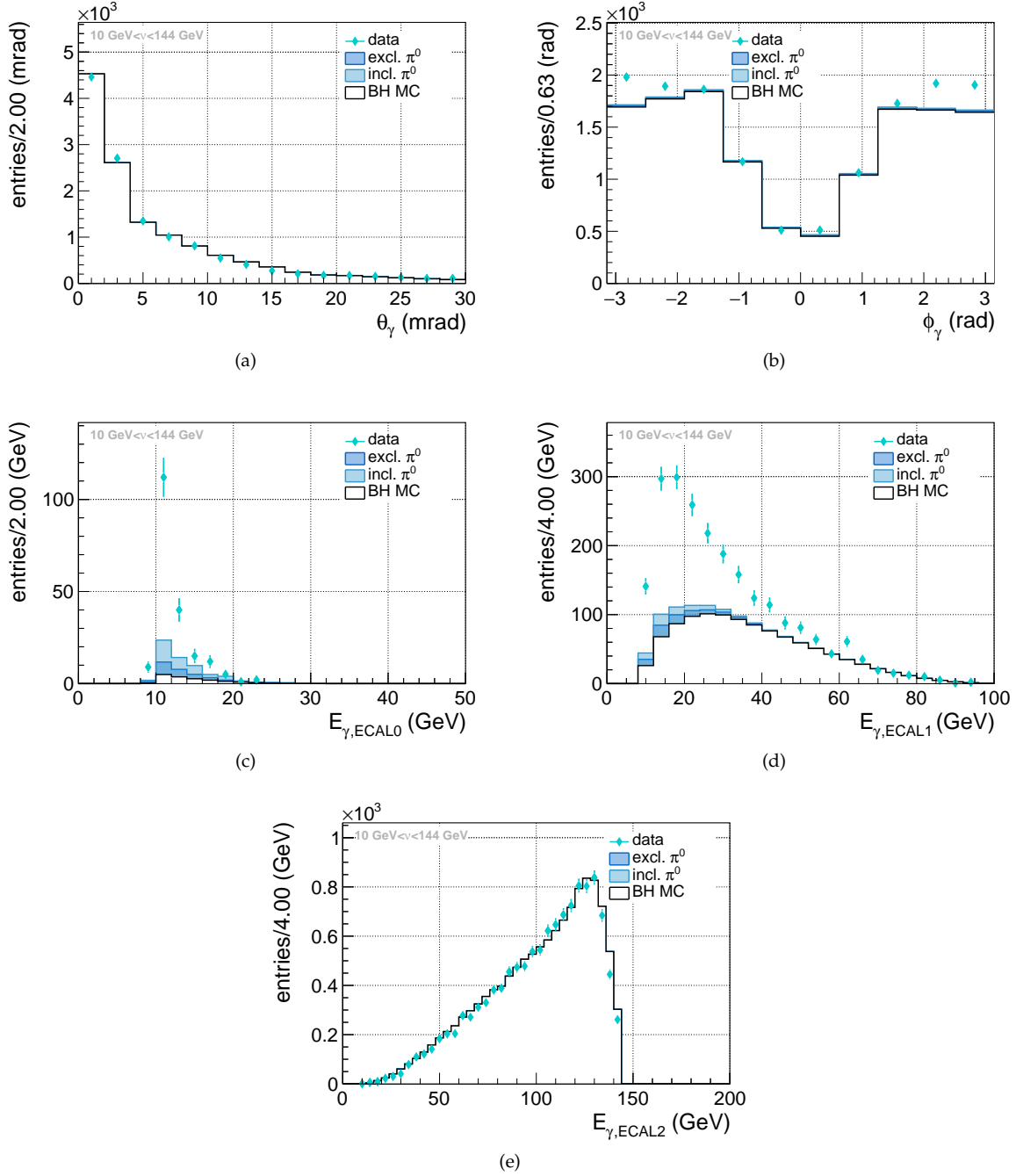
Figure 5.37: Distributions of the energy, the polar and the azimuthal angle (E, θ, ϕ) for the exclusive photon (γ) events for data, Bethe-Heitler and the invisible π^0 contamination in all ν-regions. The energy distribution is separately shown for each ECAL.

(a)

(b)

(c)
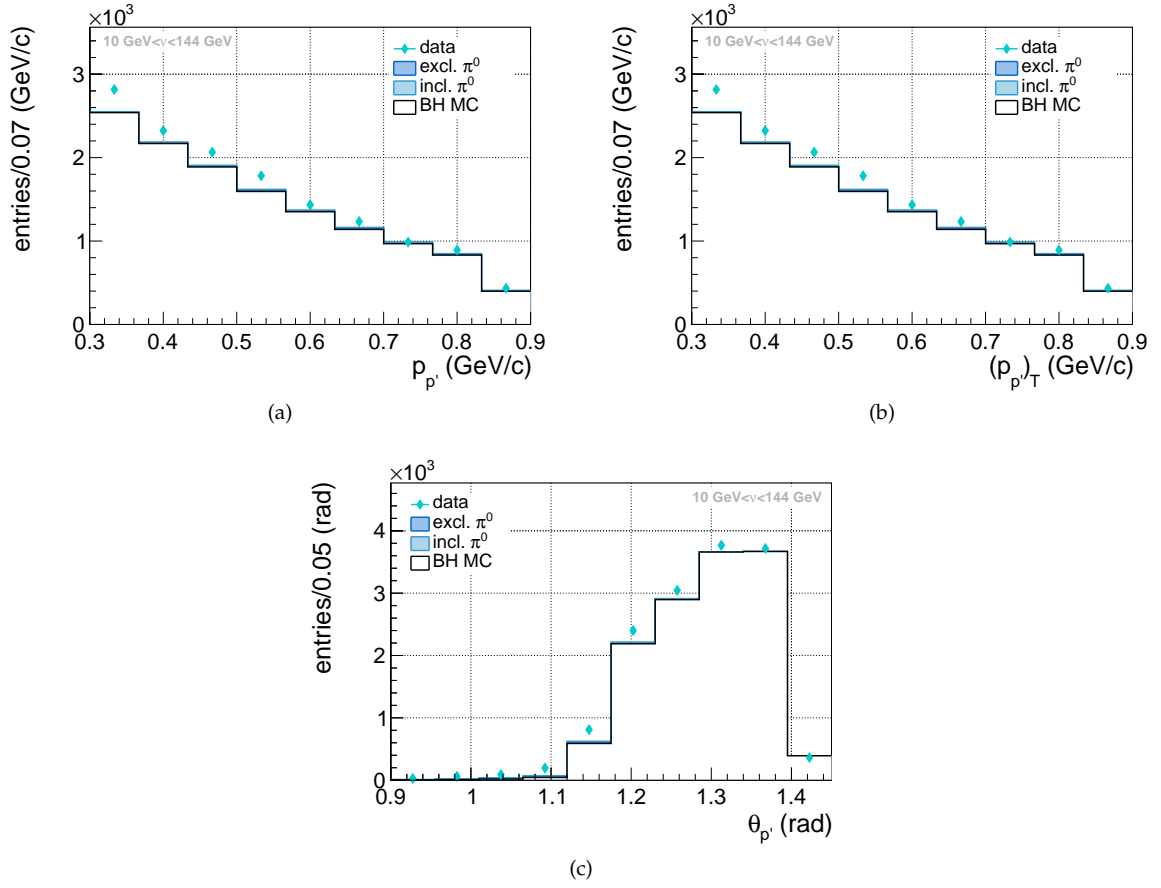
Figure 5.38: Distributions of the momentum, the transverse momentum and the polar angle $(p, (p)_T, \theta)$ of the recoil proton (p') for data, Bethe-Heitler and the invisible π^0 contamination in all ν-regions.

(a)

(b)

(c)
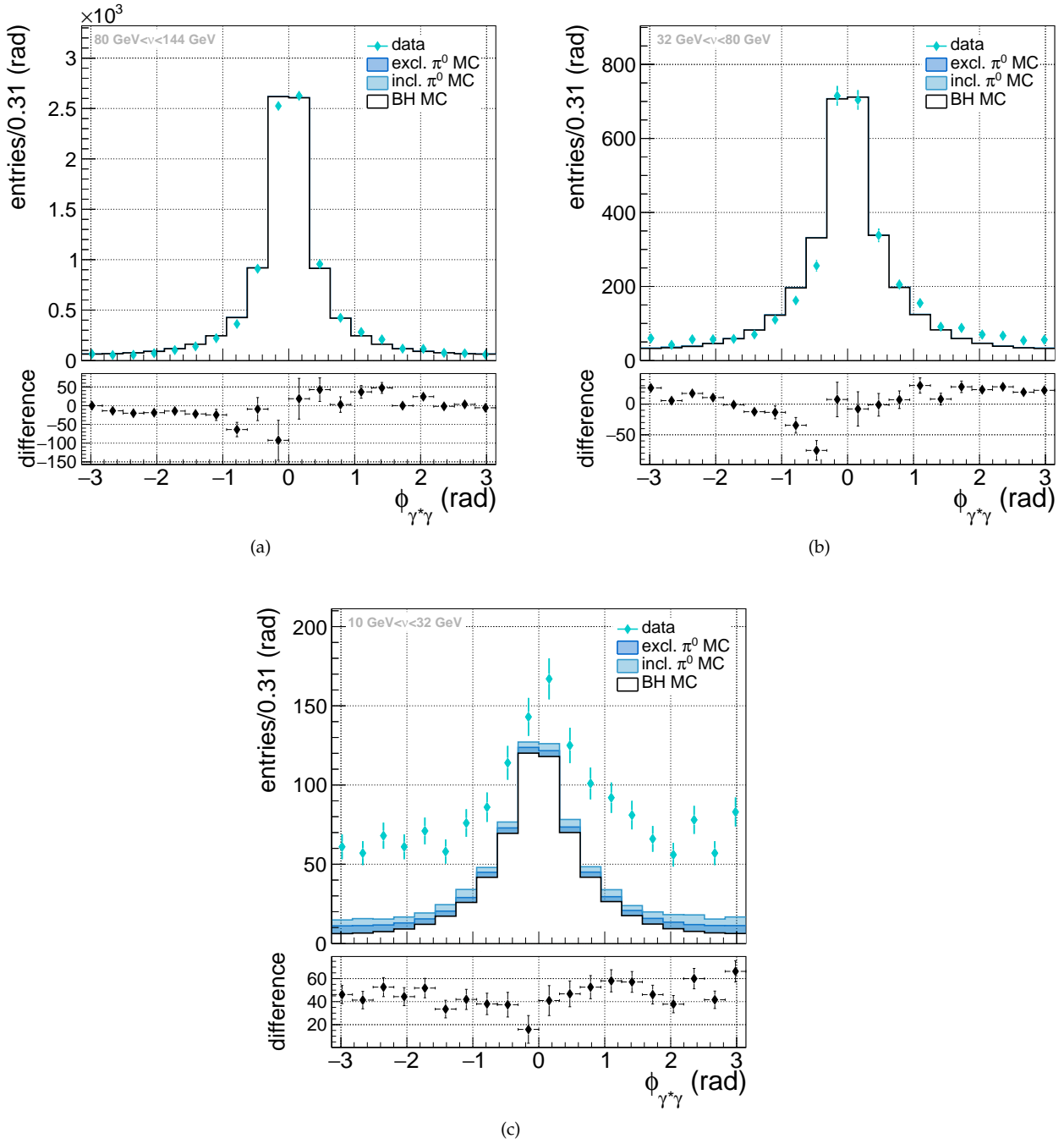
Figure 5.39: $\phi_{\gamma\gamma*}$-distributions for data, Bethe-Heitler and the invisible π^0-contamination in each ν-region (top). Difference between the data and the cumulated Monte-Carlo distributions (bottom).
The visible modulation in the data-Monte-Carlo differences in the reference (a) and interference (b) region hint to the $\phi_{\gamma*\gamma}$-dependence of the cross section for exclusive photon production.
In the extraction region (c), the average of the difference over the full spectrum hints to the c_0^{DVCS} term contributing to the pure DVCS in the cross section for exclusive photon events.

The acceptance for exclusive photon events

A correction of the spectrometer acceptance is mandatory, when calculating a cross section. The acceptance is determined by comparing the generated events of a Monte-Carlo sample, which represent the pure physics events to the same sample of events, but considering the response of the apparatus. This response includes the simulation of the particle propagation through the spectrometer and the corresponding detector responses for the specific events selected by the applied selection criteria.
A good description of the data by the Monte-Carlo is thereby crucial for an accurate acceptance determination. To illustrate the agreement between data and Monte-Carlo, the study to review the quality of the Bethe-Heitler Monte-Carlo (see Sec. 5.3.1.1) is extended to include also the DVCS and interference contribution. This study is presented in Section 6.1. The calculation of the acceptance and its detailed study in the extraction region is presented in Section 6.2.

6.1 | Monte-Carlo description of the exclusive photon data sample

As discussed in Section 3.2.2.1, HEPGEN provides not only weights for the Bethe-Heitler, but also includes a model to describe the interference and the DVCS contributions. If the cross sections of all these processes are known, the corresponding event weight is given by the sum of the corresponding event weights. As only the Bethe-Heitler weights are known precisely, a more general ansatz introduces a scale parameter (X) to the DVCS contribution. Hence, the ansatz for the total event weight for exclusive photon production reads as:

$$\omega = \omega_{\text{PAM}} + \sqrt{X \cdot \kappa_{\text{slope}}} \cdot \omega_{\text{INT}} + X \cdot \kappa_{\text{slope}} \cdot \omega_{\text{DVCS}}. \tag{6.1}$$

Here, an additional factor κ_{slope} is introduced, which corrects for the difference in the t-slope observed in data and the one used when generating the Monte-Carlo. In this case it is given by:

$$\kappa_{\text{slope}} = \frac{e^{-B_0|t|}}{e^{-B_{\text{MC}}|t|}} = \frac{e^{-6.44|t|}}{e^{-4.48|t|}}. \tag{6.2}$$

Here, B_0 denotes the value of the slope parameter, which is extracted in Section 7.2.1 and B_{MC} the slope parameter used in the simulation. The factor for ω_{INT} comes from the contribution of the DVCS amplitude to the interference and its relation to the cross section ($\propto \omega_{\text{DVCS}}$). The scaling parameter X is chosen to provide the best agreement between data and the cumulated distributions of the exclusive

photon Monte-Carlo and the invisible π^0 contamination in the extraction region ($10\,\text{GeV}< \nu <32\,\text{GeV}$). As illustrated in Figure 6.1 the best agreement is obtained when choosing X equal to 0.68. The ratio between the data and the Monte-Carlo is shown at the bottom of Figure 6.1 and fitted by a constant. A good agreement in the extraction and reference region is obtained, while deviations in the interference region are visible.
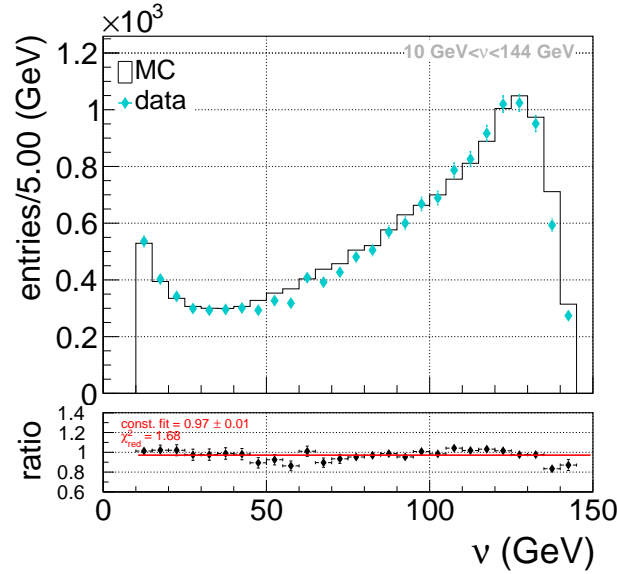
Figure 6.1: Comparison of the ν-distribution (top) between data (cyan) and the cumulated Monte-Carlo (black) considering all ν-regions. The ratio between data and Monte-Carlo (bottom) is fitted assuming a constant.

In Figures 6.2, 6.3 and 6.4 the comparison of Q^2, x_{Bj} and $|t|$-distributions in data and the Monte-Carlo samples are shown. On the left hand side all ν-regions are considering, while on the right hand side the distributions are only shown in the extraction region. Here, the ratio fits are comparable with one, while for the full ν-region the ratio estimated by the constant fit is about 0.97. This deviation is mainly caused by a slight overestimation of the Monte-Carlo in the interference region. Further comparison related to the kinematics of the incoming and scattered muon, the real photon and the recoil proton can be found in the Appendix A.4.

(a)   (b)
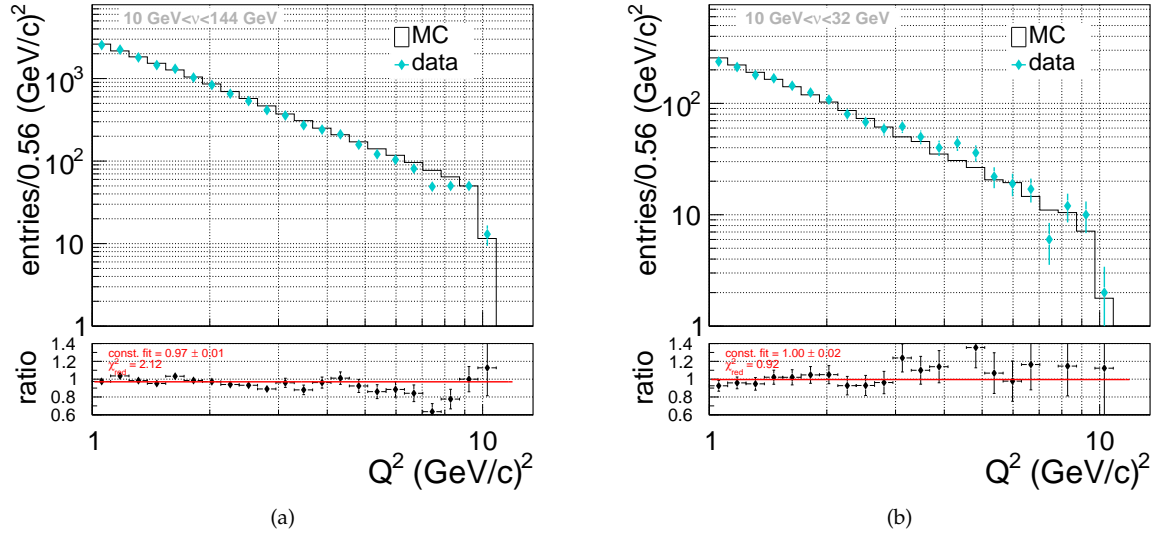
Figure 6.2: Comparison of the Q^2-distribution (top) between data (cyan) and the cumulated Monte-Carlo (black) considering all ν-regions (a) and only the extraction region (b). The ratio between data and Monte-Carlo (bottom) is fitted assuming a constant.

(a)   (b)
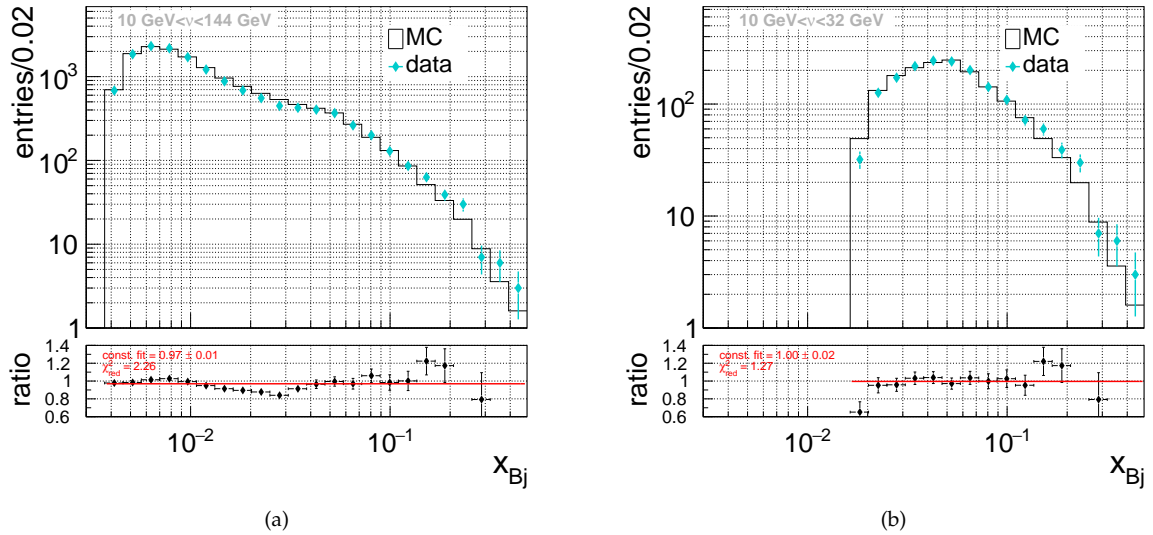
Figure 6.3: Comparison of the x_{Bj}-distribution (top) between data (cyan) and the cumulated Monte-Carlo (black) considering all ν-regions (a) and only the extraction region (b). The ratio between data and Monte-Carlo (bottom) is fitted assuming a constant.

167

(a)   (b)
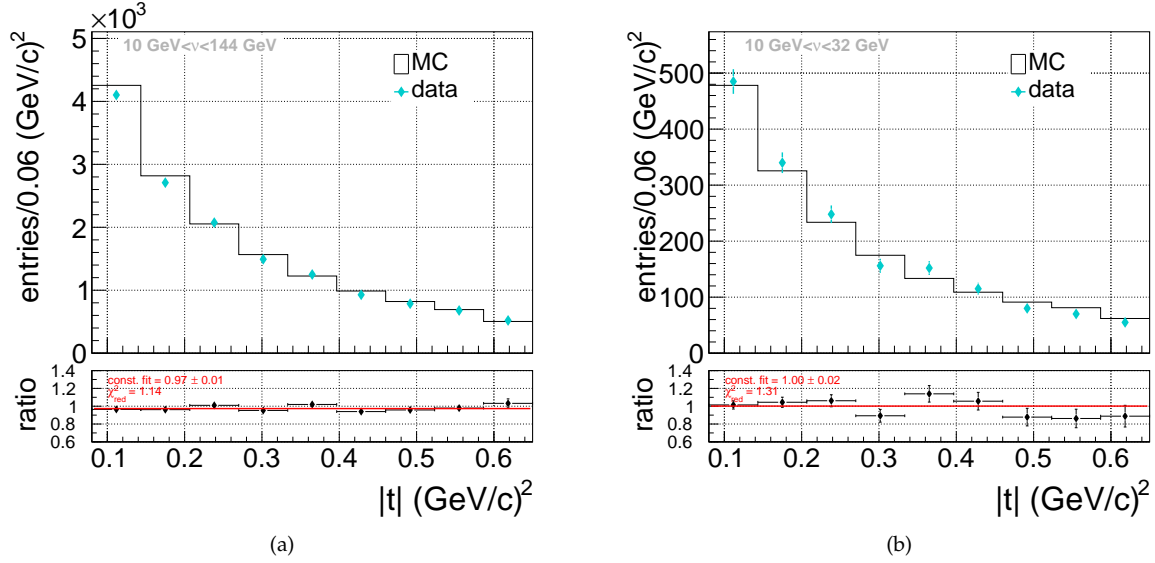
Figure 6.4: Comparison of the $|t|$-distribution (top) between data (cyan) and the cumulated Monte-Carlo (black) considering all ν-regions (a) and only the extraction region (b). The ratio between data and Monte-Carlo (bottom) is fitted assuming a constant.

6.2 | Determination and study of the acceptance

The response of the apparatus is represented by the reconstructed HEPGEN Monte-Carlo events, which pass the event selection for exclusive photon production (see Tab. 5.1 and 5.2 in Sec. 5.1) with the corresponding modifications for Monte-Carlo events discussed in Section 5.3.1. The generated events should represent the base line of physics events used in the analysis. Here, this is given by all the incoming muons, which fulfill the selection criteria used when determining the flux. Hence, all generated events are neglected, which could not be reconstructed applying this criteria.

Figure 6.5a and 6.5b show the Q^2-ν-distribution and Q^2-$|t|$-distribution of reconstructed DVCS Monte-Carlo events. The black lines indicate a four dimensional binning in Q^2, ν, $|t|$ and $\phi_{\gamma*\gamma}$, where the corresponding phase space elements are given as:

$$\Delta\Omega = \Delta Q^2 \Delta\nu \Delta|t| \Delta\phi_{\gamma*\gamma}.$$

Here, the Δ indicates the width of the bins in the corresponding variable. The acceptance is studied in this phase space using the following binning:

- 11 bins of width $\Delta\nu =2$ GeV in ν between 10 GeV and 32 GeV,

- 9 bins of width $\Delta Q^2=1$ (GeV/c)^2 in Q^2 between 1 (GeV/c)^2 and 10 (GeV/c)^2,

- 4 bins in $|t|$ with a variable range: $[0.08,0.136]$, $]0.136,0.219]$, $]0.219,0.36]$, $]0.36,0.64]$ in (GeV/c)^2 and

- 8 bins of width $\Delta\phi_{\gamma*\gamma}=\pi/4$ rad between $-\pi$ and π.

The binning in $|t|$ is chosen in order that each bin includes approximately the same amount of events, while for the other kinematic variables the bins are equidistant.
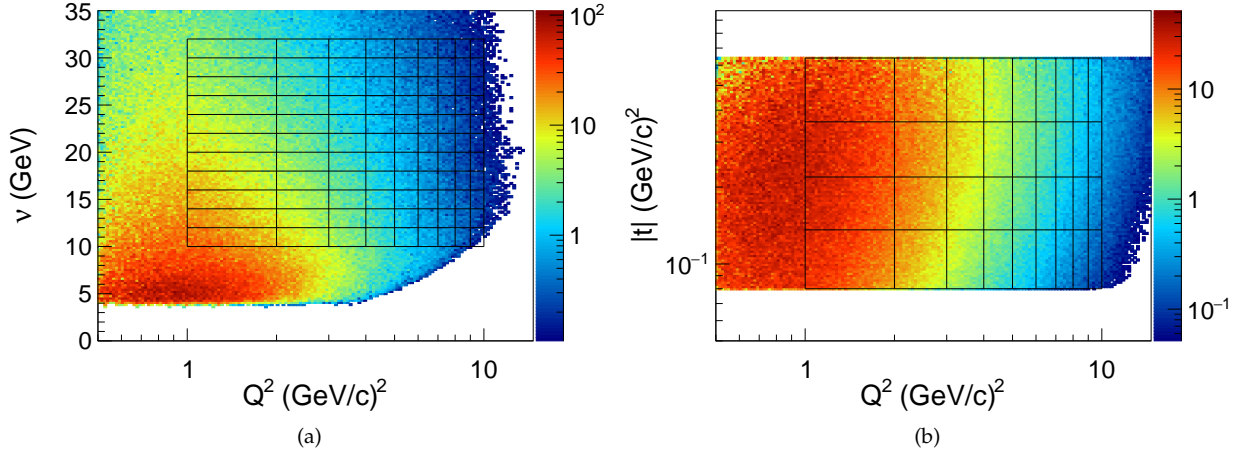
Figure 6.5: Q^2-ν-distribution (a) and Q^2-$|t|$-distribution (b) of reconstructed DVCS Monte-Carlo events. The black lines indicate the borders of the corresponding 9 bins in Q^2, 11 bins in ν and 4 bins in $|t|$.

In each bin the acceptance A is calculated as the ratio of the sum of reconstructed event weights η_{rec} in a phase space element $\Delta\Omega$ and the sum of generated event weights η_{gen} in the same phase space element:

$$A(\Delta\Omega) = \frac{\eta_{rec}(\Delta\Omega_{rec})}{\eta_{gen}(\Delta\Omega_{gen})}. \tag{6.3}$$

A generated Monte-Carlo event is allocated to a phase space element based on its generated kinematic, while its reconstruction uses the kinematics after applying the kinematic fit. By this the migration of events between the phase space elements, due to the reconstruction, are considered by the acceptance correction.

The result of the acceptance is presented in Figure 6.6 separately for the positively (red) and negatively (black) charged incoming muons using the statistics of the exclusive photon Monte-Carlo available for period 09. The $\phi_{\gamma*\gamma}$-dependence of the acceptance is shown in bins of Q^2 (horizontal axis) and ν (vertical axis) while averaging over $|t|$. The acceptance is very similar for both incoming muon charges averaging at about 40% for Q^2 smaller than 5 (GeV/c)^2 and showing only a weak dependence on $\phi_{\gamma*\gamma}$. A clear $\phi_{\gamma*\gamma}$-dependence is visible in the regime of high Q^2 and small ν (<20 GeV), which is caused by the geometrical acceptance of the ECALs. The ν-dependence of the acceptance is shown in Figure 6.7 in bins of Q^2 and $|t|$ and averaged over $\phi_{\gamma*\gamma}$. For Q^2 below 5 (GeV/c)^2 a weak ν-dependence is observed. In the regime of larger Q^2 and small $|t|$ the acceptance decreases with small values of ν.
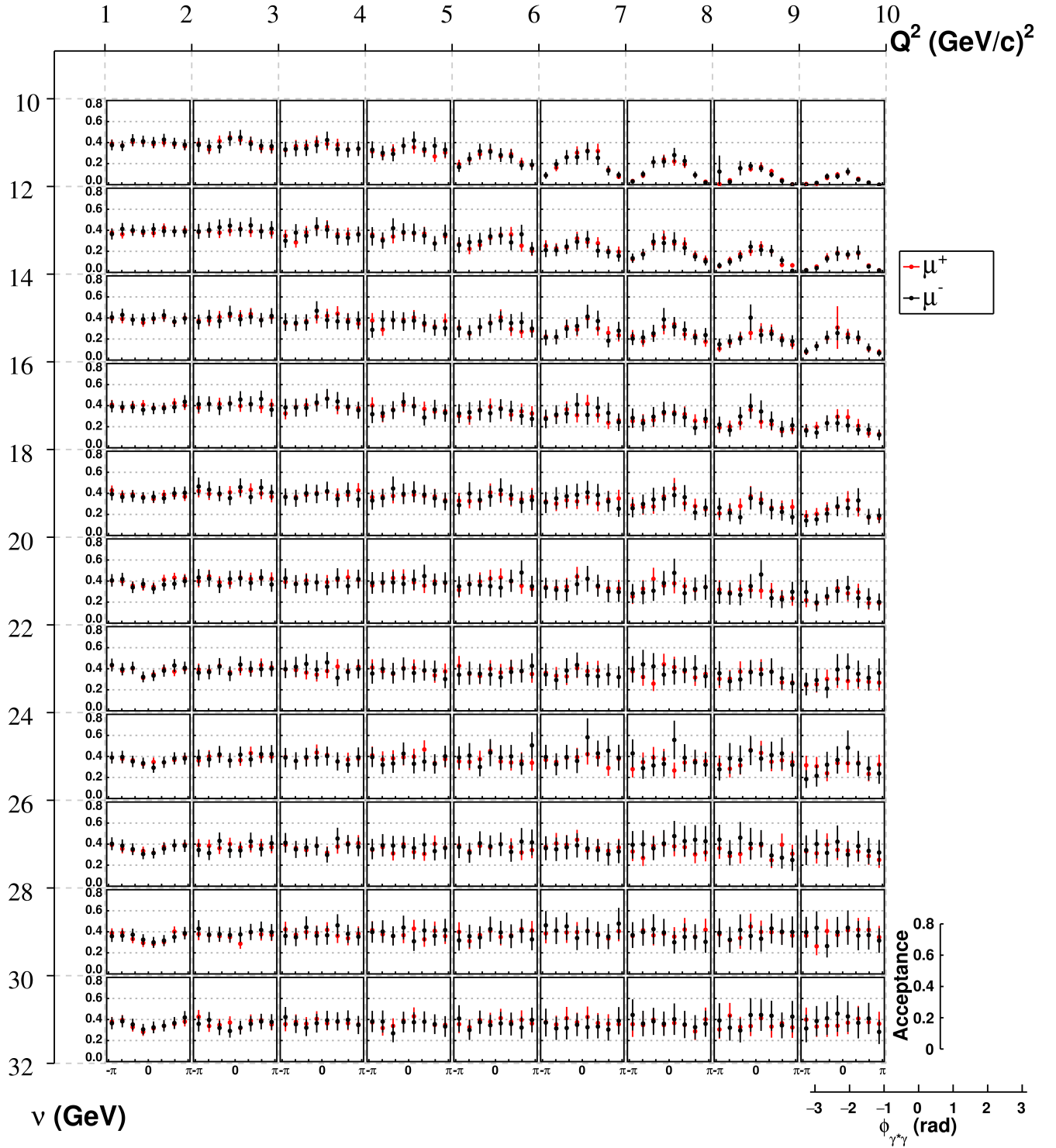
Figure 6.6: Acceptance as a function of $\phi_{\gamma*\gamma}$ in bins of Q^2 and ν separately for μ^+ (red) and μ^- (black). The horizontal axis represents the Q^2-bins (9 bins), while the vertical one represents the ν-bins (11 bins). The acceptance is averaged over $|t|$.
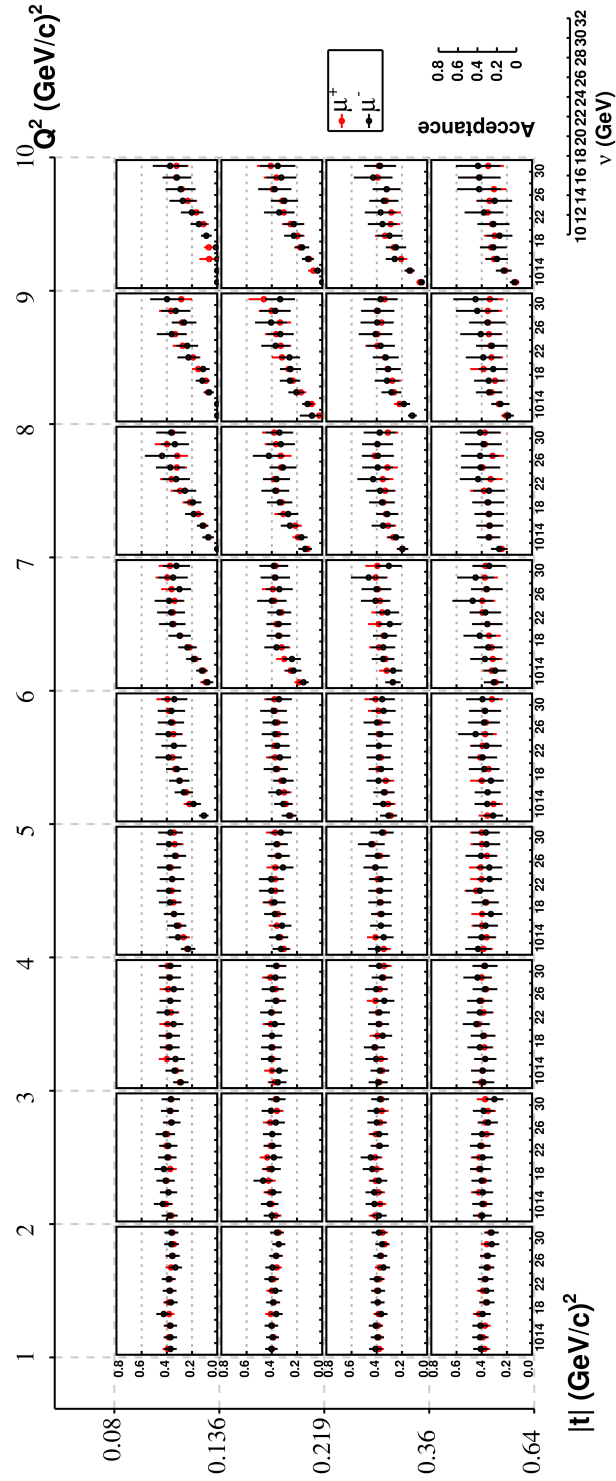
Figure 6.7: Acceptance as a function of ν in bins of Q^2 and $|t|$ separately for μ^+ (red) and μ^- (black). The horizontal axis represents the Q^2-bins (9 bins), while the vertical one represents the $|t|$-bins (4 bins). The acceptance is averaged over $\phi_{\gamma*\gamma}$.

The study of the acceptance in a wide kinematic range allows to draw conclusions on the kinematic regime considered for the extraction of the DVCS cross section. To calculate the $|t|$-dependence of the DVCS cross section an integration over $\phi_{\gamma*\gamma}$ (see Sec. 7.1) is performed. Due to this the considered kinematic range can be limited to a range, where the acceptance shows only a weak dependence on $\phi_{\gamma*\gamma}$ to avoid any potential bias. Therefore, when extracting the DVCS cross section only the region of Q^2 below $5\,(\text{GeV/c})^2$ will be considered. As in this region also only a weak ν-dependence of the acceptance is observed the number of ν-bins can be reduced to 4 equidistant bins.

6.3 | Results of the acceptance

The binning and kinematic regime, which will be used when calculating the DVCS cross section are:

- 4 bins of width $\Delta\nu =5.5$ GeV in ν between 10 GeV and 32 GeV,

- 4 bins of width ΔQ^2=1 $(\text{GeV/c})^2$ in Q^2 between $1\,(\text{GeV/c})^2$ and $5\,(\text{GeV/c})^2$,

- 4 bins in $|t|$ with a variable width: [0.08,0.136],]0.136,0.219],]0.219,0.36],]0.36,0.64] in $(\text{GeV/c})^2$ and

- 8 bins of width $\Delta\phi_{\gamma*\gamma}$=$\pi/4$ rad between $-\pi$ and π.

The acceptance as a function of $\phi_{\gamma*\gamma}$ in bins of Q^2 and ν and separately for each $|t|$-bin are shown in Figure 6.8 and 6.9. In all bins the acceptance is either constant or only shows a weak $\phi_{\gamma*\gamma}$-dependence at average values between 35%-40%.
The statistical errors quoted here are estimated using:

$$\Delta A(\Delta\Omega) = \sqrt{\left(\frac{1}{\eta_{\text{gen}}(\Delta\Omega_{\text{gen}})}\Delta\eta_{\text{rec}}(\Delta\Omega_{\text{rec}})\right)^2 + \left(\frac{\eta_{\text{rec}}(\Delta\Omega_{\text{rec}})}{\eta_{\text{gen}}^2(\Delta\Omega_{\text{gen}})}\Delta\eta_{\text{gen}}(\Delta\Omega_{\text{gen}})\right)^2}. \tag{6.4}$$

For Poisson statistics the uncertainties for the sum of reconstructed and generated weights ($\Delta\eta_{\text{rec}}(\Delta\Omega_{\text{rec}})$ and $\Delta\eta_{\text{gen}}(\Delta\Omega_{\text{gen}})$) are given by the sum of the DVCS weights squared over all events N in the corresponding phase space element:

$$\Delta\eta = \sum^{N(\Delta\Omega)} \omega_{DVCS}^2. \tag{6.5}$$

Here, it is assumed that η_{rec} and η_{gen} are independent, which is not the case, therefore the error estimation is not accurate, but with high enough statistics, a fair estimation of the statistical uncertainties is provided. For calculating a more accurate error one would also have to consider the event migration.

(b)
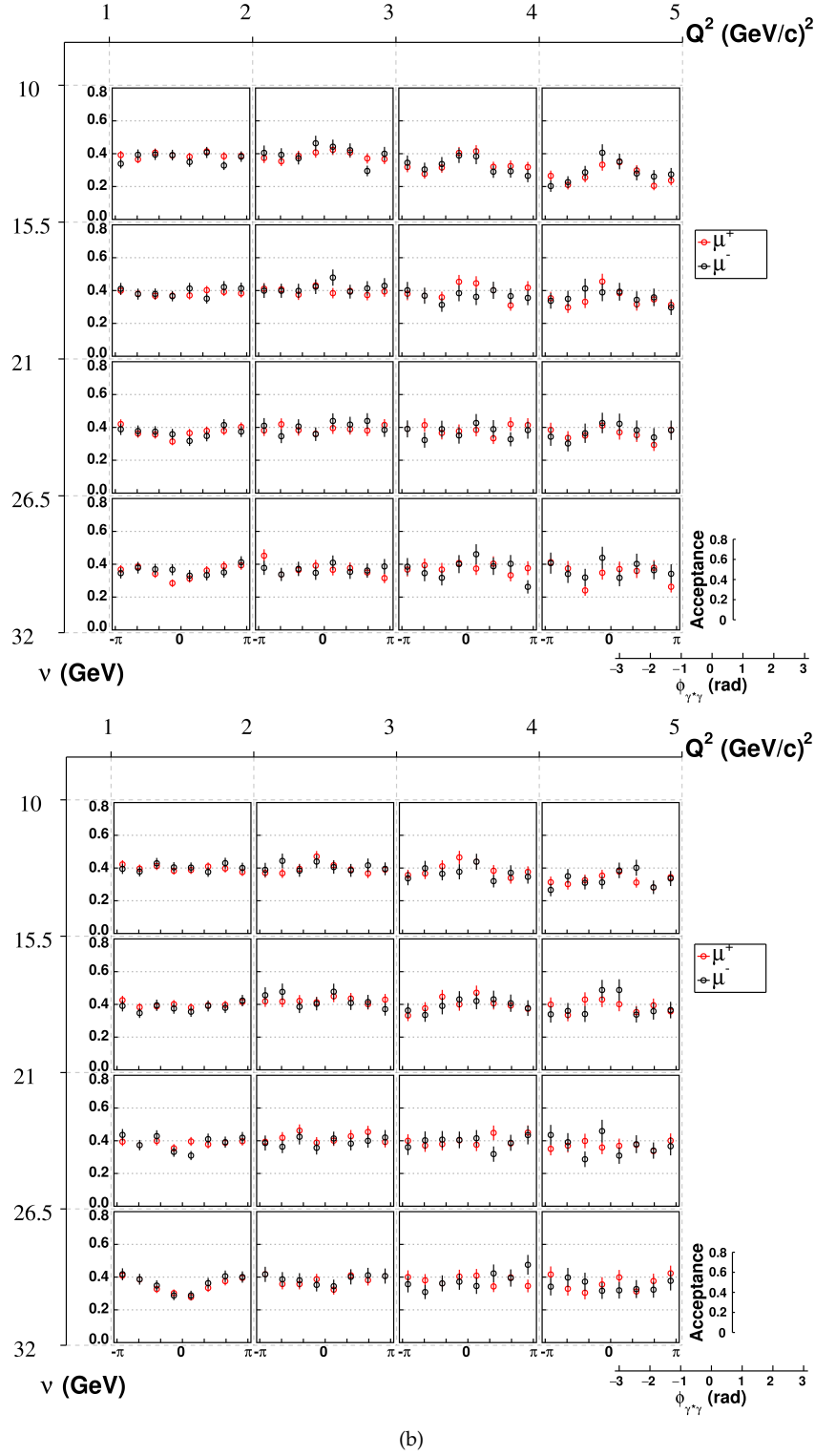
Figure 6.8: Acceptance as a function of $\phi_{\gamma*\gamma}$ in bins of Q^2 and ν for $0.08\,(\text{GeV/c})^2 < |t| < 0.136\,(\text{GeV/c})^2$ (a) and $0.136\,(\text{GeV/c})^2 < |t| < 0.219\,(\text{GeV/c})^2$ (b).
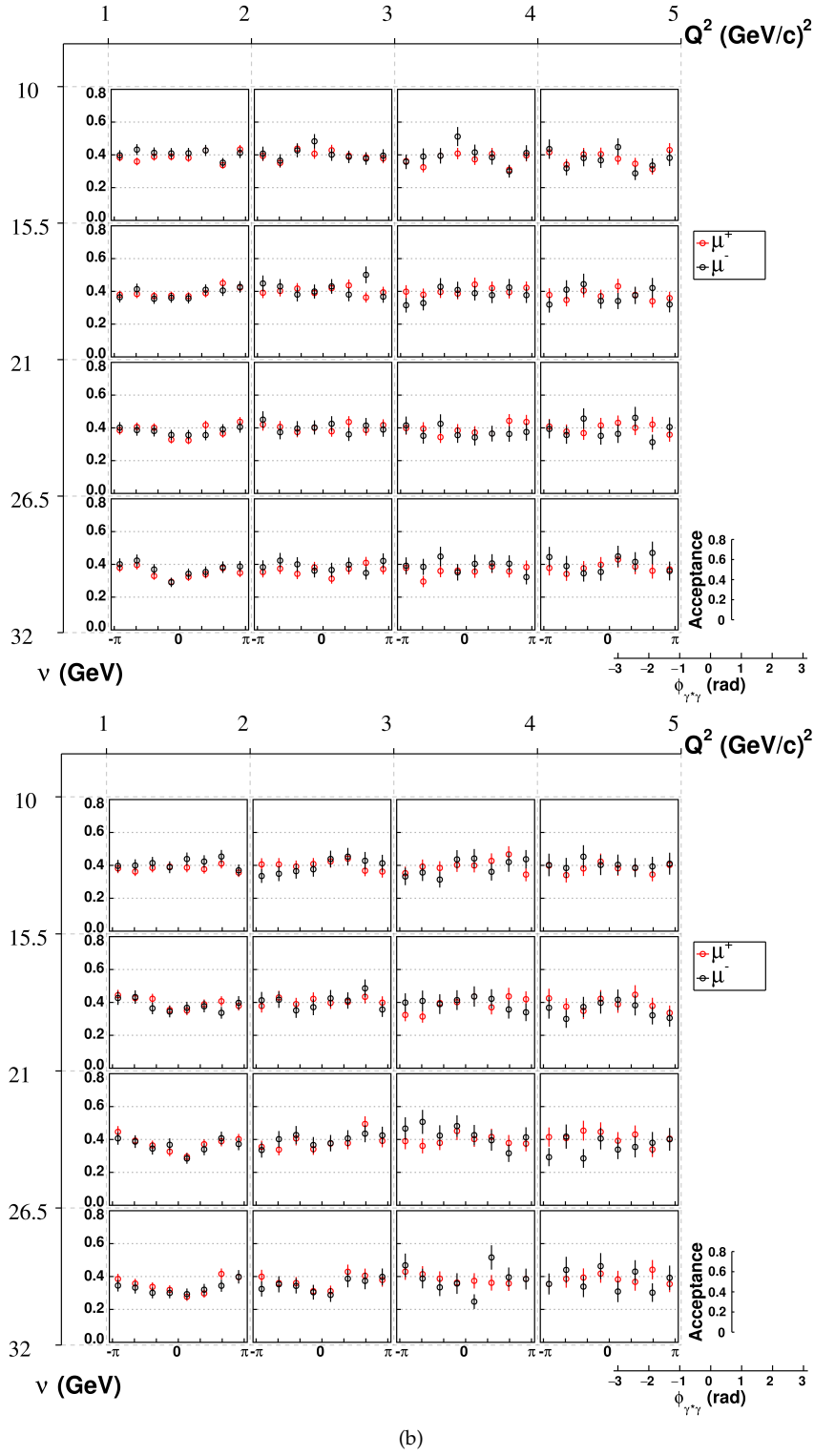
Figure 6.9: Acceptance as a function of $\phi_{\gamma*\gamma}$ in bins of Q^2 and ν for $0.219\,(\mathrm{GeV/c})^2 < |t| < 0.36\,(\mathrm{GeV/c})^2$ (a) and $0.36\,(\mathrm{GeV/c})^2 < |t| < 0.64\,(\mathrm{GeV/c})^2$ (b).

174

The DVCS cross section

As discussed in Section 2.5.1, the measured exclusive photon cross section does include contributions from DVCS, Bethe-Heitler and their interference. Besides those contributions to the cross section also a background contamination by the two photon decay of neutral pions has to be determined (see Sec. 5.3.2). Using all previous results and conclusions, the analysis steps for the cross section extraction are:

- The exclusive photon events are selected according to the event selection summarized in Table 5.1 and 5.2 (see Sec. 5.1).

- The visible π^0 contamination is directly removed from the data sample using to the method discussed in Section 5.3.2.1.

- The determination of the Bethe-Heitler contribution and the invisible π^0 contamination relies on dedicated Monte-Carlo samples. Here the same exclusive photon selection as for the data is applied, except for the modifications discussed in Section 5.3.1. Their contributions are subtracted from the measured cross section of exclusive photon production and are determined as:

  – The Bethe-Heitler contribution is determined using a Bethe-Heitler Monte-Carlo sample, which is normalized by the Monte-Carlo cross section (see Sec. 5.3.1).

  – For the determination of the invisible π^0 contamination, two dedicated Monte-Carlo samples are used. One sample for the hard exclusive π^0 production (HEPGEN π^0 MC) and the other one for the inclusive π^0 production in DIS (LEPTO π^0 MC). Both contributions are normalized to the visible π^0 in data and their corresponding shares as determined in Section 5.3.2.2.

- The DVCS cross section is extracted in a four dimensional binning of Q^2, ν, $|t|$ and $\phi_{\gamma*\gamma}$ and restricted to a region where a substantial DVCS contribution is expected (ν between 10 GeV and 32 GeV, high x_{Bj} see Sec. 2.4.1.1).

The details on the determination of the DVCS cross section and its $|t|$-dependence are described in Section 7.1. In Section 7.2 the extraction of the slope parameter and its interpretation are presented, including a detailed study of the systematic uncertainties. The $\phi_{\gamma*\gamma}$-modulation of the DVCS cross section is analysed in Section 7.3, showing a first approach to extract the values of the Fourier coefficients (see Eq. 2.65 and 2.66 in Sec. 2.5.3).

7.1 | Extraction method of the DVCS cross section

The differential DVCS cross section separately for each charge of the incoming lepton ($\pm$) in the phase space element $\Delta\Omega_{ijkl} = \Delta|t|_i\Delta\phi_{\gamma*\gamma_j}\Delta Q_k^2\Delta\nu_l$ is calculated as:

$$\left\langle \frac{d\sigma_{\text{DVCS}}^{\mu p\to\mu'\gamma p'}}{d\Omega} \right\rangle_{ijkl}^{\pm} = \left\langle \frac{d\sigma_{\text{data}}^{\mu p\to\mu'\gamma p'}}{d\Omega} \right\rangle_{ijkl}^{\pm} - \left\langle \frac{d\sigma_{\text{BH}}^{\mu p\to\mu'\gamma p'}}{d\Omega} \right\rangle_{ijkl}^{\pm} - \left\langle \frac{d\sigma_{\text{inv. }\pi^0}^{\mu p\to\mu'\gamma p'}}{d\Omega} \right\rangle_{ijkl}^{\pm}. \tag{7.1}$$

Here, the binning is chosen as discussed in Section 6.3. The different terms correspond to the observed cross section for exclusive photon production obtained from the data, which is subtracted by the cross section contributions of the Bethe-Heitler and the invisible π^0 contamination. As these cross sections are for the muon-proton scattering ($\mu p \to \mu'\gamma p'$), they need to be converted to the cross section for virtual photon-proton scattering ($\gamma * p \to \gamma p$). This conversion is provided by the transverse virtual photon flux factor as discussed in Section 2.1.3.3. Here, $\Gamma(Q^2, \nu)$ is given as [16]:

$$\Gamma(Q^2, \nu) = \frac{\alpha}{2\pi}\frac{(1 - x_{Bj})}{Q^2 y E_\mu}\left[y^2\left(1 - \frac{2m_\mu^2}{Q^2}\right) + \frac{2}{1 + \frac{Q^2}{\nu^2}}\left(1 - y - \frac{Q^2}{4E_\mu^2}\right)\right]. \tag{7.2}$$

The additional term with respect to Equation 2.24 in Section 2.1.3.3 is due to the muon mass m_μ not being neglected. One should note that, when applying this factor it has to be ensured that the longitudinal components of the virtual photon can be neglected. For DVCS this is the case in LO and twist-2, when the cross section is dominated by c_0^{DVCS} [16].

Using Equation 2.25 in Section 2.1.3.3, the DVCS cross section for virtual photon-proton scattering reads as:

$$\left\langle \frac{d\sigma_{\text{DVCS}}^{\gamma^* p\to\gamma p'}}{d\Omega} \right\rangle_{ijkl}^{\pm} = \left\langle \frac{1}{\Gamma}\frac{d\sigma_{\text{data}}^{\mu p\to\mu'p'\gamma}}{d\Omega} \right\rangle_{ijkl}^{\pm} - \left\langle \frac{1}{\Gamma}\frac{d\sigma_{\text{BH}}^{\mu p\to\mu'p'\gamma}}{d\Omega} \right\rangle_{ijkl}^{\pm} - \left\langle \frac{1}{\Gamma}\frac{d\sigma_{\text{inv. }\pi^0}^{\mu p\to\mu'p'\gamma}}{d\Omega} \right\rangle_{ijkl}^{\pm}. \tag{7.3}$$

From the measured event sample, the cross section is obtained using:

$$\sigma = \frac{N}{\mathcal{L}\cdot A}, \tag{7.4}$$

where N is the number of measured events, $\mathcal{L}$ the integrated luminosity and A the acceptance. Using Equation 7.3 and 7.4 one obtains:

$$\left\langle \frac{d\sigma_{\text{DVCS}}^{\gamma^* p\to\gamma p'}}{d\Omega} \right\rangle_{ijkl}^{\pm} = \frac{1}{\mathcal{L}^{\pm}\Delta|t|_i\Delta\phi_{\gamma*\gamma_j}\Delta Q_k^2\Delta\nu_l}\sum_{p\in\mathcal{P}}\left(A_{ijkl}^{p,\pm}\right)^{-1}\left[\sum_{e=1}^{N_{ijkl}^{\text{data}\,p,\pm}}\frac{1}{\Gamma(Q_e^2, \nu_e)} - \right. \tag{7.5}$$

$$\left. c_{BH}^{p,\pm}\sum_{e=1}^{N_{ijkl}^{\text{BH}\,p,\pm}}\frac{(\omega_{\text{PAM}})_e}{\Gamma(Q_e^2, \nu_e)} - c_{\pi^0}^{p,\pm}\sum_{e=1}^{N_{ijkl}^{\text{inv. }\pi^0 p,\pm}}\frac{(\omega_{\pi^0})_e}{\Gamma(Q_e^2, \nu_e)}\right],$$

which is the detailed expression to calculate the DVCS cross section. Here, $\mathcal{L}^{\pm}$ is the integrated luminosity over all periods of data taking separately for μ^+ and μ^-:

$$\mathcal{L}^{\pm} = \sum_{p\in\mathcal{P}}\mathcal{L}^{p,\pm},$$

$c_{\text{BH}}^{p,\pm}$ the scaling factor for the Bethe-Heitler Monte-Carlo as discussed in Section 5.3.1

$$c_{\text{BH}}^{p,\pm} = \frac{\mathcal{L}^{p,\pm}}{\mathcal{L}_{MC}^{p,\pm}},$$

and the last term corresponds to the invisible π^0 background contamination, which in detail reads as:

$$c_{\pi^0}^{p,\pm} \sum_{e=1}^{N_{ijkl}^{\text{inv. }\pi^0 p,\pm}} \frac{(\omega_{\pi^0})_e}{\Gamma(Q_e^2, \nu_e)} = c_{\pi^0_{\text{LEPTO}}}^{p,\pm} \cdot R_{\text{LEPTO}} \sum_{e=1}^{N_{ijkl}^{\text{inv. }\pi^0_{\text{LEPTO}} p,\pm}} \frac{1}{\Gamma(Q_e^2, \nu_e)} +$$

$$c_{\pi^0_{\text{HEPGEN}}}^{p,\pm} \cdot (1 - R_{\text{LEPTO}}) \sum_{e=1}^{N_{ijkl}^{\text{inv. }\pi^0_{\text{HEPGEN}} p,\pm}} \frac{(\omega_{\pi^0})_e}{\Gamma(Q_e^2, \nu_e)} \text{ (see Eq. 5.25 in Sec. 5.3.2.2).}$$

The normalization factors are given, as discussed in Section 5.3.2.2, as:

$$c_{\pi^0_{\text{LEPTO}}}^{p,\pm} = \frac{N_{\text{vis. }\pi^0}^{\text{data}p,\pm}}{N_{\text{vis. }\pi^0}^{\text{LEPTO}p,\pm}},$$

and

$$c_{\pi^0_{\text{HEPGEN}}}^{p,\pm} = \frac{N_{\text{vis. }\pi^0}^{\text{data}p,\pm}}{N_{\text{vis. }\pi^0}^{\text{HEPGEN}p,\pm}}.$$

The first sum in Equation 7.5 refers to a sum over all analysed periods p (see Tab. 4.1 in the introduction to Ch. 4). The following terms correspond to sums over all events N in data, the Bethe-Heitler Monte-Carlo and the invisible π^0 Monte-Carlo samples. Here, each event is weighted by the inverse of the transverse virtual photon flux factor, which is calculated based on its kinematic. In case of the HEPGEN Monte-Carlo samples, the Monte-Carlo weights of the corresponding physics processes are used. The first factor in Equation 7.5 includes the integrated luminosity and the widths of the kinematic bins in $\Delta\Omega_{ijkl}$.

To obtain the cross section in each bin of $|t|_i$ and $\phi_{\gamma*\gamma j}$, the weighted average of the four dimensional differential cross section over all Q^2 and ν-bins is calculated as:

$$\left\langle \frac{d\sigma_{\text{DVCS}}^{\gamma^* p \to \gamma p'}}{d|t| d\phi_{\gamma*\gamma}} \right\rangle_{ij}^{\pm} = \frac{\sum\limits_{k,l} \left\langle \frac{d\sigma_{\text{DVCS}}^{\gamma^* p \to \gamma p'}}{d\Omega} \right\rangle_{ijkl}^{\pm} \Delta Q_k^2 \Delta \nu_l}{\sum\limits_{k,l} \Delta Q_k^2 \Delta \nu_l}. \tag{7.6}$$

Using the method discussed in Section 2.5.3, the $|t|$-dependent DVCS cross section $d\sigma/d|t|$ separately for μ^+ and μ^- is obtained by integrating Equation 7.6 over $\phi_{\gamma*\gamma}$:

$$\left\langle \frac{d\sigma_{\text{DVCS}}^{\gamma^* p \to \gamma p'}}{d|t|} \right\rangle_i^{\pm} = \sum_j \Delta\phi_{\gamma*\gamma, j} \left\langle \frac{d\sigma_{\text{DVCS}}^{\gamma^* p \to \gamma p'}}{d|t| d\phi_{\gamma*\gamma}} \right\rangle_{ij}^{\pm}. \tag{7.7}$$

For the beam charge independent DVCS cross section, the average over both charges and polarizations of the incoming muons is calculated:

$$\left\langle \frac{d\sigma^{\gamma^* p \to \gamma p'}_{\text{DVCS}}}{d|t|} \right\rangle_i = \frac{1}{2} \left[\left\langle \frac{d\sigma^{\gamma^* p \to \gamma p'}_{\text{DVCS}}}{d|t|} \right\rangle^+_i + \left\langle \frac{d\sigma^{\gamma^* p \to \gamma p'}_{\text{DVCS}}}{d|t|} \right\rangle^-_i \right].$$

(7.8)

Equation 7.8 corresponds to the final $|t|$-dependent DVCS cross section.

From Equation 7.5 and 7.6 and performing the standard propagation of statistical uncertainties, the uncertainties of the differential DVCS cross section in each $|t|$ and $\phi_{\gamma*\gamma}$-bin are calculated as:

$$\left\langle (\Delta\sigma^{\gamma^* p \to \gamma p'}_{\text{DVCS}})^2 \right\rangle^\pm_{ij} = \frac{1}{(\mathcal{L}^\pm \Delta|t|_i \Delta\phi_{\gamma*\gamma,j} \Delta Q^2 \Delta\nu)^2} \sum_{p \in \mathcal{P}} \sum_{k,l} (A^{p,\pm}_{ijkl})^{-2} \Bigg\{ \left[\Delta D_{ijkl} + \Delta A^{p,\pm}_{ijkl} \right] +$$

(7.9)

$$(c^{p,\pm}_{\text{BH}})^2 \left[\Delta B_{ijkl} + \Delta A^{p,\pm}_{ijkl} \right] + (c^{p,\pm}_{\pi^0_{\text{LEPTO}}})^2 \cdot R_{\text{LEPTO}} \left[\Delta L_{ijkl} + \Delta A^{p,\pm}_{ijkl} \right] +$$

$$(c^{p,\pm}_{\pi^0_{\text{HEPGEN}}})^2 \cdot (1 - R_{\text{LEPTO}}) \left[\Delta H_{ijkl} + \Delta A^{p,\pm}_{ijkl} \right] \Bigg\}.$$

Here, the following abbreviations correspond to the data, the Bethe-Heitler Monte-Carlo and the invisible π^0 Monte-Carlo samples:

$$\Delta D_{ijkl} = \sum_{e=1}^{N^{\text{data}\,p,\pm}_{ijkl}} \left(\frac{1}{\Gamma(Q^2_e, \nu_e)} \right)^2,$$

$$\Delta B_{ijkl} = \sum_{e=1}^{N^{\text{BH}\,p,\pm}_{ijkl}} \left(\frac{(\omega_{PAM})_e}{\Gamma(Q^2_e, \nu_e)} \right)^2,$$

$$\Delta L_{ijkl} = \sum_{e=1}^{N^{\text{inv. }\pi^0_{\text{LEPTO}}\,p',\pm}_{ijkl}} \left(\frac{1}{\Gamma(Q^2_e, \nu_e)} \right)^2,$$

$$\Delta H_{ijkl} = \sum_{e=1}^{N^{\text{inv. }\pi^0_{\text{HEPGEN}}\,p',\pm}_{ijkl}} \left(\frac{(\omega_{\pi^0})_e}{\Gamma(Q^2_e, \nu_e)} \right)^2.$$

The expression $\Delta A^{p,\pm}_{ijkl}$ is the statistical uncertainty of the acceptance as calculated according to Equation 6.4 in Section 6.3.

The uncertainties of the DVCS cross section for each $|t|$-bin are calculated analog to Equation 7.7 and 7.8 as:

$$\left\langle (\Delta\sigma^{\gamma^* p \to \gamma p'}_{\text{DVCS}})^2 \right\rangle^\pm_i = \sum_j \Delta\phi^2_{\gamma*\gamma,j} \cdot \left\langle (\Delta\sigma^{\gamma^* p \to \gamma p'}_{\text{DVCS}})^2 \right\rangle^\pm_{ij},$$

(7.10)

and for the charge averaged DVCS cross section as:

$$\left\langle \Delta\sigma^{\gamma^* p \to \gamma p'}_{\text{DVCS}} \right\rangle_i = \frac{1}{2} \sqrt{ \left\langle (\Delta\sigma^{\gamma^* p \to \gamma p'}_{\text{DVCS}})^2 \right\rangle^+_i + \left\langle (\Delta\sigma^{\gamma^* p \to \gamma p'}_{\text{DVCS}})^2 \right\rangle^-_i }.$$

(7.11)

The results of the charge seperated and charge averaged DVCS cross section for each $|t|$-bin and their statistical uncertainties are summarized in Table 7.1.

$|t|$-bin	[0.08,0.136]	]0.136,0.219]	]0.219,0.36]	]0.36,0.64]
$d\sigma^+/d|t|$	26.8	17.6	11.0	2.9
stat. error	4.2	2.6	1.6	0.7
$d\sigma^-/d|t|$	30.2	19.2	7.3	2.3
stat. error	4.5	3.1	1.5	0.7
$d\sigma/d|t|$	28.5	18.4	9.2	2.6
stat. error	3.1	2.0	1.1	0.5

Table 7.1: Values of $\left\langle d\sigma_{\mathrm{DVCS}}^{\gamma^* p \to \gamma p'}/d|t| \right\rangle^{\pm}$ and $\left\langle d\sigma_{\mathrm{DVCS}}^{\gamma^* p \to \gamma p'}/d|t| \right\rangle$ in nb/(GeV/c)^2 and their statistical uncertainties.

7.2 | Study of the |t|-slope

Using the extracted cross section values, the $|t|$-dependence of the dominant contribution c_0^{DVCS} (see Sec. 2.5.3) to the charge spin cross section sum can be studied. This method used to analyse the $|t|$-dependence and determine the slope parameter is presented in Section 7.2.1. The study of systematic effects and uncertainties on the extraction of the cross section and the slope parameter is discussed in Section 7.2.2 . The final results on the slope parameter including the systematic uncertainties, an interpretation of the obtained results and a comparison to the results obtained in 2012 are presented in Section 7.2.3.

7.2.1 | The |t|-slope

The DVCS cross section in bins of $|t|$ and their statistical uncertainties are shown in Figure 7.1. To extract the slope parameter B, a binned maximum log-likelihood fit is performed assuming an exponential ansatz of the form: $e^{-B|t|}$. The log-likelihood function is defined as:

$$\log L(B) = \sum_{i=1}^{4} \sigma_i \log l_i(B), \tag{7.12}$$

with:

$$l_i(B) = \sigma_{\mathrm{tot}} \int_{t_i^{\mathrm{min}}}^{t_i^{\mathrm{max}}} \frac{1}{N} e^{-B|t|} dt. \tag{7.13}$$

Here, i denotes the index of the corresponding $|t|$-bin, σ_i is the extracted DVCS cross section in $|t|$-bin i:

$$\sigma_i = \left\langle \frac{d\sigma_{\mathrm{DVCS}}^{\gamma^* p \to \gamma p'}}{d|t|} \right\rangle_i \cdot \Delta t_i,$$

and σ_{tot} is the cross section sum over all $|t|$-bins:

$$\sigma_{\mathrm{tot}} = \sum_{i=1}^{4} \sigma_i.$$
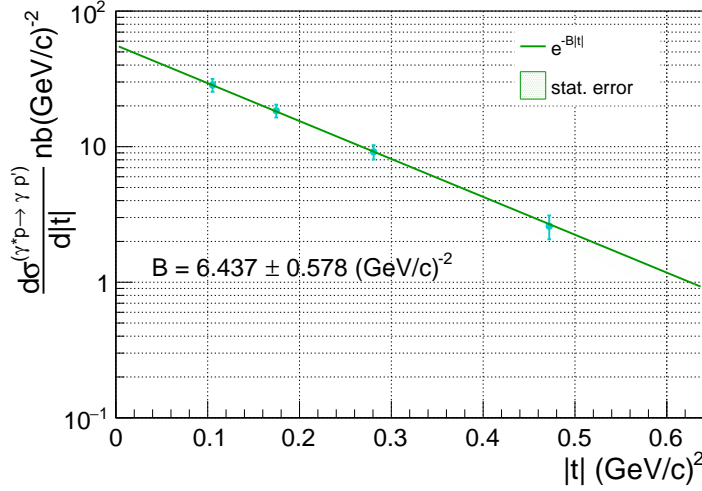
Figure 7.1: DVCS cross section extracted in 4 bins of $|t|$ with the corresponding statistical errors (cyan points). The $|t|$-dependence is described by a maximum log-likelihood fit using an exponential ansatz of the form: $e^{-B|t|}$. The fit and the statistical uncertainties are shown in green.

The normalization N is given by the integral of the exponential over the full $|t|$-range:

$$N = \int_{0.08\,(\text{GeV}/\text{c})^2}^{0.64\,(\text{GeV}/\text{c})^2} e^{-B|t|} dt.$$

The statistical uncertainty of the slope parameter is determined by the same fitting procedure, but instead of using the DVCS cross section values, the corresponding statistical uncertainties are fitted. This procedure was already used when analysing the 2012 data (see Ref. [114]) and verified using a toy Monte-Carlo. This method accounts for the fact that in the cross section calculation a sum of weights instead of a common sum of events is used [119].

The result and statistical uncertainty of the slope parameter are shown in Figure 7.1. Here, the relative statistical uncertainty is about 9%. The high number of floating point is kept to better evaluate the impacts of the following systematic studies.

7.2.2 | Systematic effects and uncertainties

The extracted DVCS cross section and therefore the B parameter can be affected by various systematic effects. In the following the studies, which were performed to quantify their impacts on the results, are presented.

7.2.2.1 | Variations of the Bethe-Heitler contribution

The Bethe-Heitler contribution, which is subtracted from the measured cross section for exclusive photon production, is varied by changing the scaling factor c_{BH} (see Sec. 5.3.1) of the Bethe-Heitler Monte-Carlo. This variation is between 76% and 124% of its present value in steps of 2%. The differences of the DVCS cross section in each $|t|$-bin and the slope parameter with respect to their current values (σ_{0,t_i}, B_0) as a function of the variation of the scaling factor (f) are shown in Figure 7.2a to 7.2e. The error band

indicates the corresponding statistical uncertainties.

As discussed in Section 5.3.1, the agreement of the data and the Bethe-Heitler in the reference region is very good at a ratio of about 99%. For the contribution of the Bethe-Heitler Monte-Carlo in the extraction region an uncertainty of $\pm 4\%$ is assumed, which is in the order of fluctuations observed in the acceptance study. Using this systematic uncertainty on c_{BH} leads to an relative systematic uncertainty on the DVCS cross section and the slope parameter as summarized in Table 7.5 and 7.6.

(a)

(b)

(c)

(d)

(e)
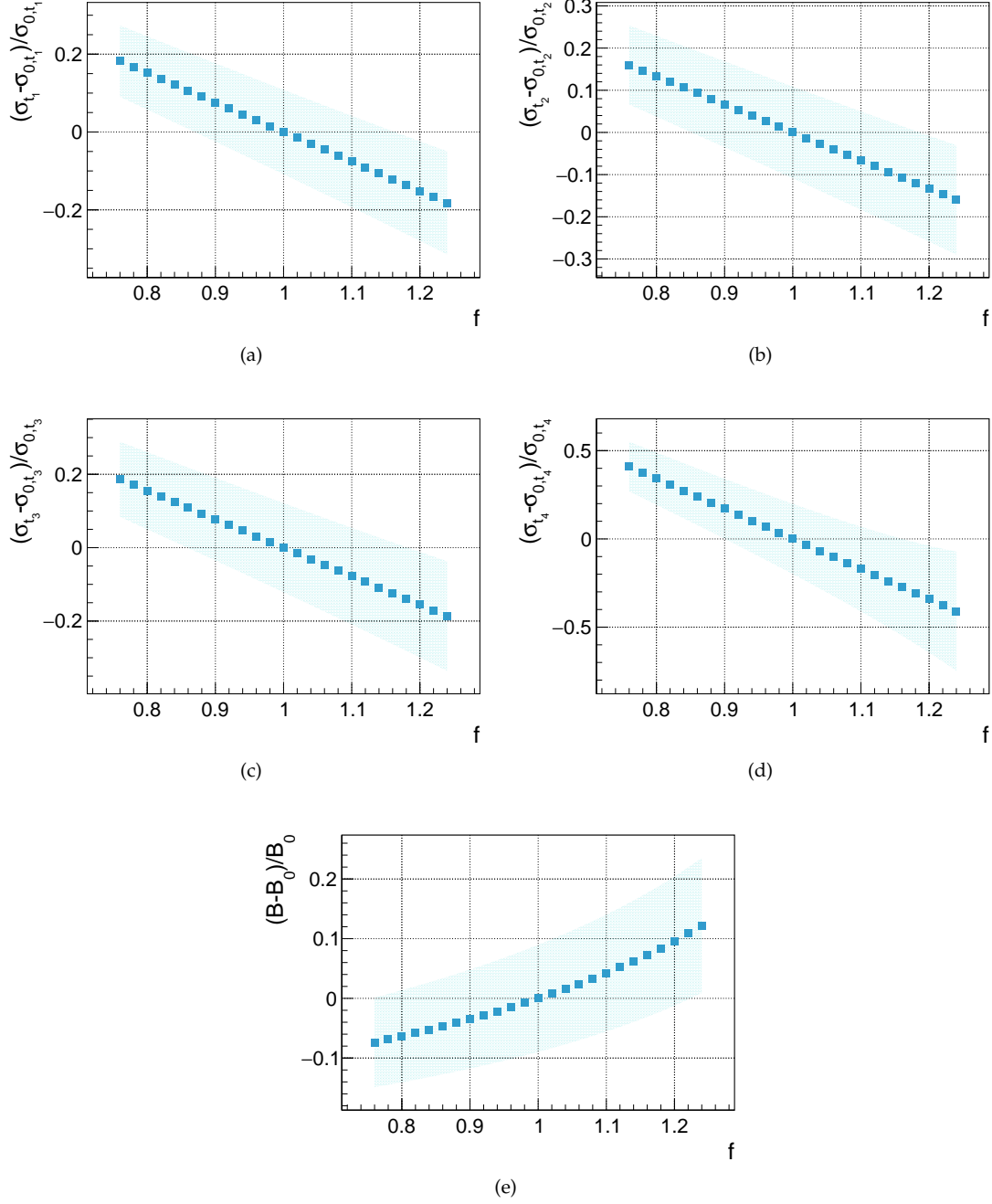
Figure 7.2: Values of $d\sigma_{\text{DVCS}}^{\gamma^* p \to \gamma p'}/d|t|$ with respect to their current values for $0.08 < |t|\,(\text{GeV/c})^2 < 0.136$ (a), $0.136 < |t|\,(\text{GeV/c})^2 < 0.219$ (b), $0.219 < |t|\,(\text{GeV/c})^2 < 0.36$ (c) and $0.36 < |t|\,(\text{GeV/c})^2 < 0.64$ (d) and B (e) as a function of the BH contribution scaled by a factor f.

7.2.2.2 | Variations of the visible π^0 contamination

As discussed in Section 5.3.2, the visible π^0 contamination in data is used to normalize the Monte-Carlo samples for hard exclusive and inclusive π^0 production. Here, also the small number of the observed visible π^0 in data was mentioned (85 events), which can lead to large fluctuations of the normalization. To quantify its impact on the results of the DVCS cross section and the slope parameter the normalization factors for both Monte-Carlo samples ($c_{\pi^0_{\mathrm{HEPGEN}}}$ and $c_{\pi^0_{\mathrm{LEPTO}}}$) are varied in 5% steps between 60% and 140% of their current values. This is displayed in Figure 7.3a to 7.3e.

To find an estimator for the systematic uncertainties of the normalization factors, a study of the visible π^0 and its dependence on the low energy threshold settings of the ECALs is performed, which is similar to the one presented in Section 5.3.3. The extraction of the DVCS cross section and the analysis of the |t|-slope is done for two additional sets of low energy thresholds, once for small values $E_{\gamma,\mathrm{low\ thr.}}$=0.3/0.3 GeV in ECAL0/1 and once for large values $E_{\gamma,\mathrm{low\ thr.}}$=0.5/1.0 GeV in ECAL0/1. The small threshold values correspond to those used in the analysis of the 2012 data. The relative differences $D_{\mathrm{rel.}}$ for the DVCS cross section in each |t|-bin and on the slope parameter with respect to their current values are summarized in Table 7.2.

	on $d\sigma_{\mathrm{DVCS}}^{\gamma^* p \to \gamma p'}/d|t|$				on B
|t|-bin	[0.08,0.136]	]0.136,0.219]	]0.219,0.36]	]0.36,0.64]	
$D_{\mathrm{rel.}}$/% for $E_{\gamma,\mathrm{low\ thr.}}$=0.3/0.3 GeV	0.3	-0.4	-0.2	2.4	-0.8
$D_{\mathrm{rel.}}$/% for $E_{\gamma,\mathrm{low\ thr.}}$=0.5/1.0 GeV	2.4	-0.8	-1.1	-4.2	2.7

Table 7.2: Observed relative differences of the DVCS cross section and the slope parameter for different combinations of the low energy thresholds of ECAL0/1.

Comparing these results to the impact of the modified normalization to the visible π^0 in Figure 7.3a to 7.3e, they correspond to a systematic uncertainty of the normalization down to about 5% and up to 15%. These lead to the systematic uncertainties of the DVCS cross section and the slope parameter, as summarized in Table 7.5 and 7.6.
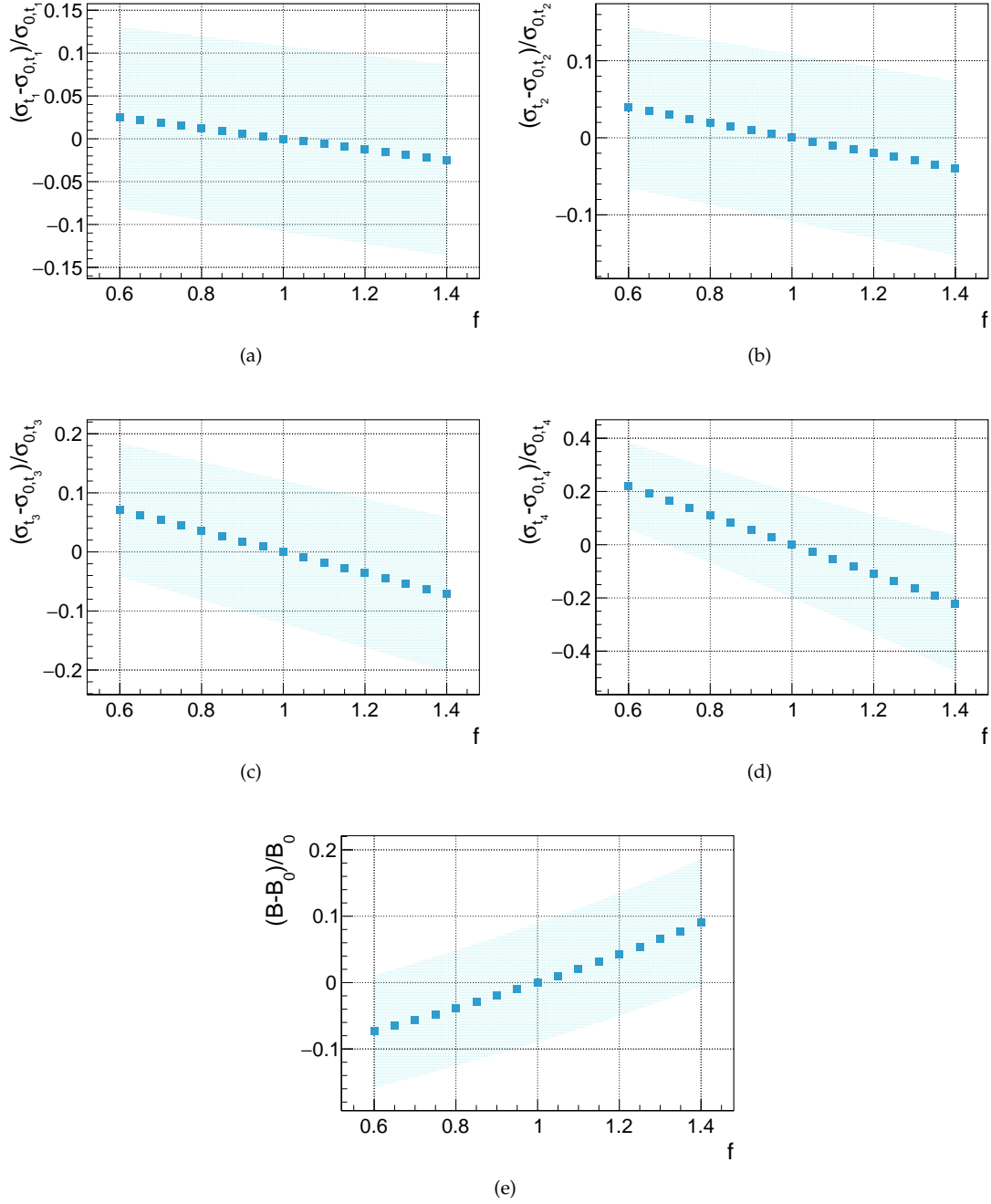
Figure 7.3: Values of $d\sigma_{\mathrm{DVCS}}^{\gamma^* p \to \gamma p'}/d|t|$ with respect to their current values for $0.08 < |t|\,(\mathrm{GeV/c})^2 < 0.136$ (a), $0.136 < |t|\,(\mathrm{GeV/c})^2 < 0.219$ (b), $0.219 < |t|\,(\mathrm{GeV/c})^2 < 0.36$ (c) and $0.36 < |t|\,(\mathrm{GeV/c})^2 < 0.64$ (d) and B (e) as a function of the vis. π^0 contamination scaled by a factor f.

7.2.2.3 | Variations of the ratio between the π^0 Monte-Carlo samples

As discussed in Section 5.3.2.2, the ratio between the Monte-Carlo samples for hard exclusive and inclusive π^0 production was determined to be R_{LEPTO}=40% with an estimated uncertainty of ± 10%. Figure 7.4a to 7.4e shows the relative differences of the determined DVCS cross section and the slope parameter as a function of R_{LEPTO} between 0% and 100% in steps of 5%.

The corresponding relative systematic uncertainties are summarized in Table 7.5 and 7.6.

(a)

(b)

(c)

(d)

(e)
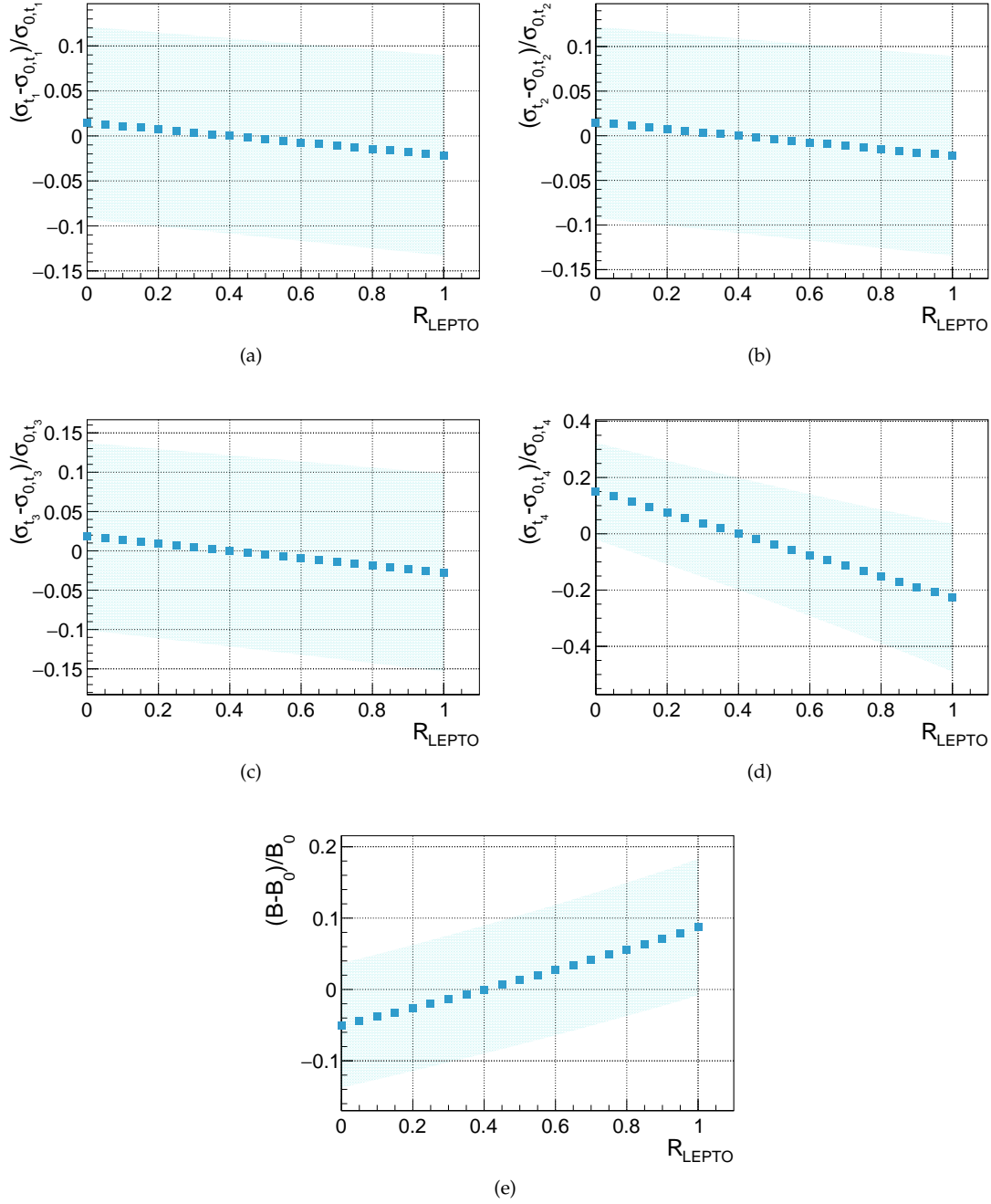
Figure 7.4: Values of $d\sigma_{\mathrm{DVCS}}^{\gamma^* p \to \gamma p'}/d|t|$ with respect to their nominal values for $0.08 < |t|\,(\mathrm{GeV/c})^2 < 0.136$ (a), $0.136 < |t|\,(\mathrm{GeV/c})^2 < 0.219$ (b), $0.219 < |t|\,(\mathrm{GeV/c})^2 < 0.36$ (c) and $0.36 < |t|\,(\mathrm{GeV/c})^2 < 0.64$ (d) and B (e) as a function of R_{LEPTO}.

7.2.2.4 | Variations of the χ^2 limit of the kinematic fit

Figure 7.5a to 7.5e show the relative difference of the DVCS cross section and the slope parameter as a function of different values for the χ^2 limit of the kinematic fit, which is applied in the selection of the exclusive photon events. Compared to the limit used in the event selection ($\chi^2 < 10$), a tighter limit leads to large differences in the cross sections and the slope parameter, while for a more relaxed limit only small differences are observed. For an estimation of the systematic uncertainty a limit of $\chi^2 < 16$ is assumed, which leads to a slope parameter, that is about 1.5% smaller and values of the cross sections that are about 4.8%, 1.3%, 3.3% and 8.1% larger in each $|t|$-bin compared to their current values.

(a)

(b)

(c)

(d)

(e)
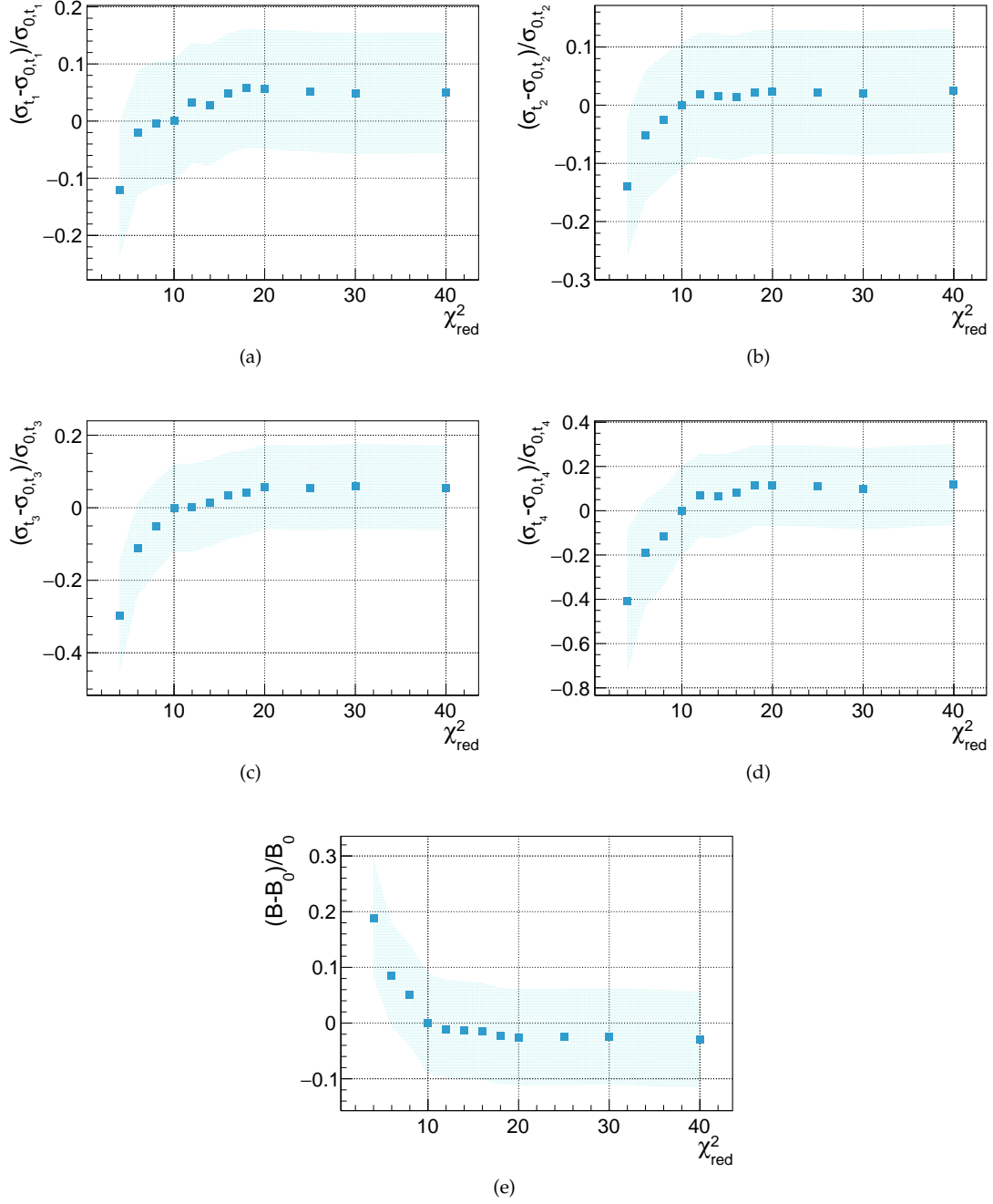
Figure 7.5: Values of $d\sigma_{\mathrm{DVCS}}^{\gamma^* p \to \gamma p'}/d|t|$ with respect to their current values for $0.08 < |t|\,(\mathrm{GeV/c})^2 < 0.136$ (a), $0.136 < |t|\,(\mathrm{GeV/c})^2 < 0.219$ (b), $0.219 < |t|\,(\mathrm{GeV/c})^2 < 0.36$ (c) and $0.36 < |t|\,(\mathrm{GeV/c})^2 < 0.64$ (d) and B (e) as a function of the limit on χ^2_{red}.

7.2.2.5 | Effect of radiative corrections

A calculation of the radiative effects for COMPASS kinematics was performed for the analysis of 2012 data. These provide corrections to the measured DVCS cross section to obtain the cross sections for the one-photon-exchange approximation [114]. In 2012, the DVCS cross section was determined in the same kinematic regime, but with a different $|t|$-binning. There, four equidistant $|t|$-bins where used with $\Delta|t| = 0.14\,(\text{GeV/c})^2$. The corrections to the cross section values are adjusted according to the binning used in 2016. A summary of the reduction of the cross section values in 2012 and the adjusted values for 2016 is given in Table 7.3.

	σ_{t_1}	σ_{t_2}	σ_{t_3}	σ_{t_4}
rel. sys. error $\downarrow$/% (2012)	5.8	4.7	4.1	3.6
rel. sys. error $\downarrow$/% (2016)	2.3	3.5	4.7	7.7

Table 7.3: Relative reduction of the cross section sums estimated for 2012 and the adjusted reduction rate for 2016.

The extracted slope with the reduced values for the DVCS cross section is shown in Figure 7.6. Compared to the current value of the slope parameter an increase of about 2.4% is observed.
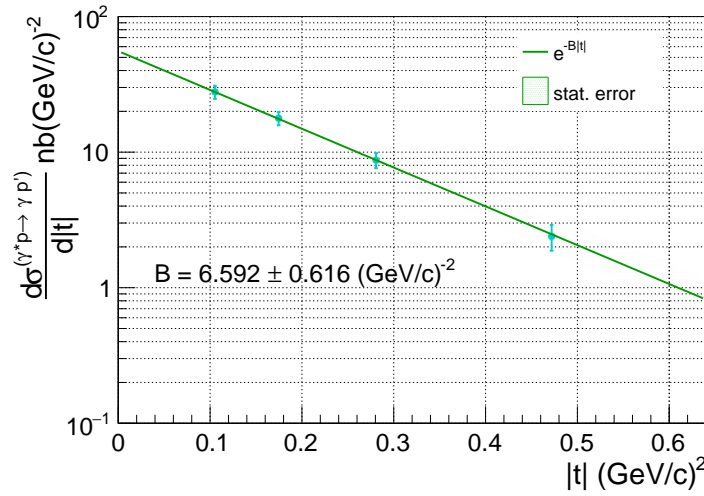
Figure 7.6: Extracted slope using the reduced values of the DVCS cross section as given in Table 7.3. The slope parameter is about 2.4% larger than its current value.

7.2.2.6 | Effect of the binning in $|t|$ and ν

To study the effect of the binning in $|t|$ and ν, the analysis was repeated using different combinations of the 2012 and 2016 binning. As mentioned already in Section 7.2.2.5, in 2012 four equidistant bins were used in $|t|$ with $\Delta|t| = 0.14\,(\text{GeV/c})^2$ and 11 equidistant bins in ν with $\Delta\nu = 2\,\text{GeV}$.
Figure 7.7a shows the DVCS cross section and the corresponding extraction of the slope parameter using the 2012 $|t|$-binning and 2016 ν-binning. For the DVCS cross section in the last $|t|$-bin, a deviation with

respect to the corresponding values in the other bins can be observed, which is caused by the relatively small statistics of the data sample. To compensate for this effect the study is also performed when merging the last two |t|-bins (3 |t|-bins (2012)). The result of the DVCS cross section and the slope parameter using only this |t|-binning and 2016 ν-binning is shown in Figure 7.7b. By only using 3 bins a value for the slope parameter close to the current one is obtained, which allows to draw the conclusion that the deviation observed in the first case is mainly caused by the small statistics. A summary of the
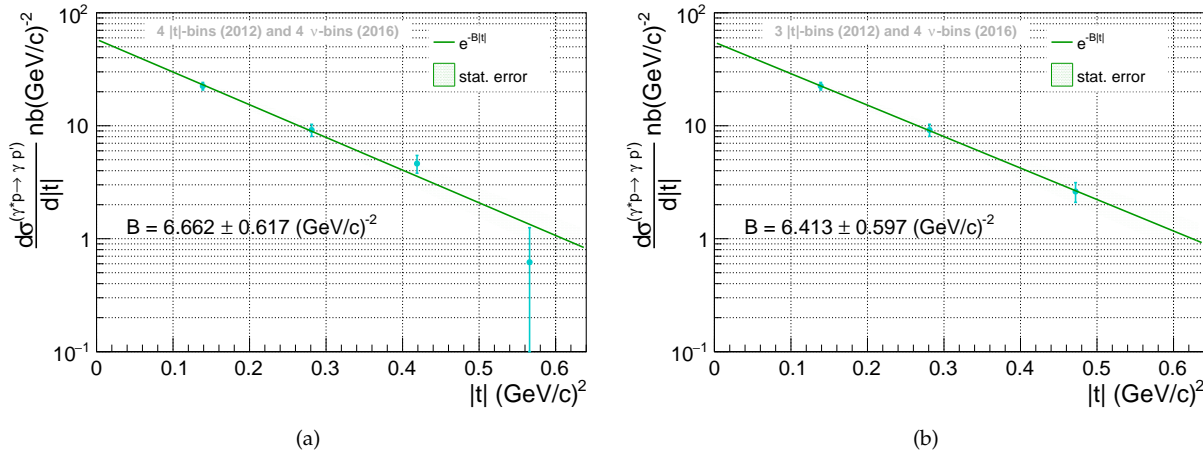
Figure 7.7: DVCS cross section and extracted slope parameter using the 2016 binning in ν and the 2012 binning in |t| (a). (b) Values extracted with the same binning, but the two last |t|-bins are merged.

extracted slope parameters and the relative difference to the current value using different combinations of the binning is given in Table 7.4. The corresponding illustrations of the DVCS cross section and the slope parameter, which are not shown in this Section, can be found in Appendix A.5.

For the same binning in |t| and ν as was used in the 2012 analysis, a slope parameter, which is about 1.8% higher with respect to the current value is obtained. To further investigate the impact of the |t|-binning on the slope parameter, a study is performed where the number of |t|-bins is increased to five and an equidistant (5 |t|-bins (2012)) or an equistatistic (5 |t|-bins (2016)) |t|-binning is used. In both cases a larger value (4.2% and 5.1%) for the slope parameter is obtained, but with visible fluctuations of the data points with respect to the slope extracted by the fit (see Fig. 7.8a and 7.8b).

In summary the chosen ν-binning only has a minor effect on the obtained value of the slope parameter. While for the binning in |t| a considerably impact is observed, which leads in most cases to a larger value of the slope parameter. The small effect of the ν-binning is expected due to the nearly constant acceptance. Using more bins in |t| introduces statistical fluctuations to the values of the DVCS cross section, which have an impact on the fit used to extract the slope parameter. Assuming that most of the observed deviations is due to statistical fluctuations, a relative systematic uncertainty of 2.5% to larger values and 0.5% to smaller values of the slope parameter is estimated.
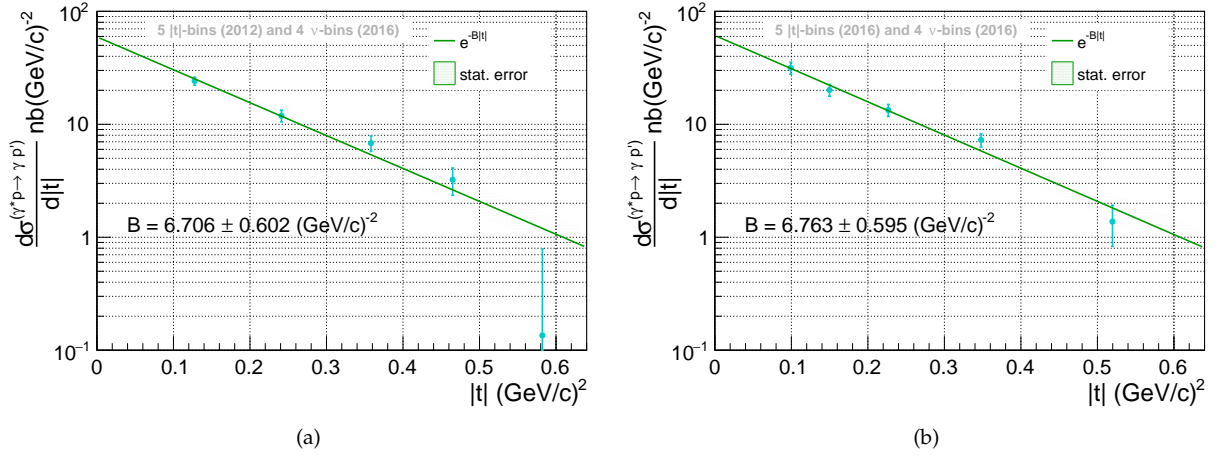
Figure 7.8: (a) DVCS cross section and extracted slope parameter using the 2016 binning in ν and the 5 equidistant bins in $|t|$. (b) DVCS cross section and extracted slope parameter using the 2016 binning in ν and the 5 equistatistic bins in $|t|$.

$B_0 = 6.437 \, (\mathrm{GeV/c})^{-2}$	$B/ \, (\mathrm{GeV/c})^{-2}$	$(B - B_0)/B_0/\%$
4 $|t|$-bins (2012) and 4 ν-bins (2016)	6.662	3.5
3 $|t|$-bins (2012) and 4 ν-bins (2016)	6.413	-0.4
4 $|t|$-bins (2016) and 11 ν-bins (2012)	6.397	-0.6
4 $|t|$-bins (2012) and 11 ν-bins (2012)	6.552	1.8
3 $|t|$-bins (2012) and 11 ν-bins (2012)	6.292	-2.3
5 $|t|$-bins (2012) and 4 ν-bins (2016)	6.706	4.2
5 $|t|$-bins (2016) and 4 ν-bins (2016)	6.763	5.1

Table 7.4: Summary of the values of the slope parameter and the relative differences to its current value, using different combinations of ν and $|t|$-binning.

7.2.2.7 | Statistical fluctuations of the DVCS cross section

As show in Section 7.2.1 Figure 7.1, the data points show no statistical fluctuations with respect to the slope derived from the fit. To exclude the possibility of any systematic effect by the considered data periods, Figure 7.9 shows the DVCS cross section in each $|t|$-bin derived when only considering a single period (shades of blue) in comparison to the sum of all periods (cyan) and the corresponding fit of the slope. For the purpose of display, the $|t|$-values of the data points for the single periods are slightly shifted. Nearly all extracted DVCS cross section values are comparable within their statistical uncertainty to the one extracted for the sum of all periods. Only in the last $|t|$-bin, a larger deviation is visible for the one derived for period 05. In summary, no deviations hinting to a systematic effect are observed.
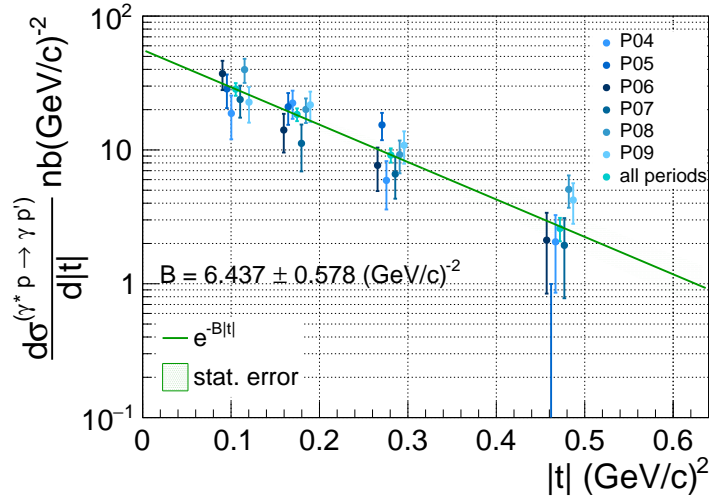
Figure 7.9: DVCS cross section values using the full available 2016 data statistics (cyan) in comparison to the values obtained when only considering a single data taking period (shades of blue).

7.2.2.8 | Summary of the systematic uncertainties

Table 7.5 and 7.6 summarize the relative uncertainties determined by the systematic studies that are used for the values of the DVCS cross section (see Tab. 7.1 in Sec. 7.2.1) and the slope parameter (see Fig. 7.1 in Sec. 7.2.1). The total systematic uncertainties are obtained by adding the listed contributions in quadrature.

	DVCS cross section				
	$|t|$-bin	[0.08,0.136]	]0.136,0.219]	]0.219,0.36]	]0.36,0.64]
BH	rel. sys. error ↑/%	3.0	2.7	3.1	6.8
contrib.	rel. sys. error ↓/%	3.0	2.7	3.1	6.8
vis. π^0	rel. sys. error ↑/%	0.9	1.5	2.7	8.3
contrib.	rel. sys. error ↓/%	0.3	0.5	0.9	2.8
R_{LEPTO}	rel. sys. error ↑/%	0.4	0.4	0.5	3.8
	rel. sys. error ↓/%	0.4	0.4	0.5	3.8
χ^2_{red}	rel. sys. error ↑/%	4.8	1.3	3.3	8.1
rad. corr.	rel. sys. error ↓/%	2.3	3.5	4.7	7.7
Σ	rel. sys. error ↑/%	5.7	3.4	5.3	14.0
	rel. sys. error ↓/%	3.8	4.5	5.7	11.3

Table 7.5: Summary of the relative systematic uncertainties of $\left\langle d\sigma_{DVCS}^{\gamma^* p \to \gamma p'} / d|t| \right\rangle$ in each $|t|$-bin. The bottom line is the total systematic uncertainty, which is obtained by adding the listed uncertainties in quadrature.

192

	Slope parameter	
BH	rel. sys. error ↑/%	1.6
contrib.	rel. sys. error ↓/%	1.5
vis. π^0	rel. sys. error ↑/%	3.1
contrib.	rel. sys. error ↓/%	1.2
R_{LEPTO}	rel. sys. error ↑/%	1.3
	rel. sys. error ↓/%	1.3
χ^2_{red}	rel. sys. error ↓/%	1.5
rad. corr.	rel. sys. error ↑/%	2.4
binning	rel. sys. error ↑/%	2.5
	rel. sys. error ↓/%	0.5
Σ	rel. sys. error ↑/%	5.1
	rel. sys. error ↓/%	2.8

Table 7.6: Summary of the relative systematic uncertainties of the slope parameter. The bottom line is the total systematic uncertainty, which is obtained by adding the listed uncertainties in quadrature.

7.2.3 | Summary, interpretation and comparison of the results

The final result for the slope parameter is:

$$B = 6.4 \pm 0.6|_{\text{stat}} {}^{+0.3}_{-0.2}|_{\text{sys}}\,(\text{GeV/c})^{-2},$$

at an average kinematic of:

$$\langle Q^2 \rangle = 1.8\,(\text{GeV/c})^2, \ \langle v \rangle = 17.9\,(\text{GeV}), \ \langle x_{Bj} \rangle = 0.060, \ \langle \xi \rangle = 0.033 \ \text{and} \ \langle W \rangle = 5.7\,(\text{GeV/c}^2).$$

Figure 7.10 shows the DVCS cross section and the fit of the slope including the statistical and systematic uncertainties. The uncertainties are added in quadrature to determine the total uncertainty.

Using Equation 2.72 in Section 2.5.3 and considering the approximation for $\xi \approx \frac{x_{Bj}}{2-x_{Bj}}$ given by Equation 2.44 in Section 2.4.1.1, the averaged square of the impact parameter is calculated as:

$$\langle b_\perp^2(x) \rangle = 2\hbar^2 \left(\frac{1+\xi}{1-\xi} \right) B(x) \approx 2\hbar^2 \left(\frac{B}{1-x_{Bj}} \right). \tag{7.14}$$

At $x = \xi \simeq x_{Bj}/2$, $\langle b_\perp^2(x) \rangle$ is equal to the transverse extension of partons in the proton (see Sec. 2.5.3). For the current value of B and $\langle x_{Bj} \rangle = 0.060$ Equation 7.14 results in:

$$\langle b_\perp^2(x = x_{Bj}/2) \rangle \sim \langle r_\perp^2(x = x_{Bj}/2) \rangle \approx 0.53 \pm 0.05|_{\text{stat}} {}^{+0.03}_{-0.02}|_{\text{sys}}\,\text{fm}^2.$$

Figure 7.11 shows a comparison of this result to the one obtained when analysing the 2012 COMPASS data [16] (red star) and results obtained by the H1 [2, 4] (blue triangles) and ZEUS [175] (green circle) experiment at HERA, which used the same method to determine the DVCS cross section and extract the slope parameter. The axis on the right hand side indicates the value of the squared impact parameter
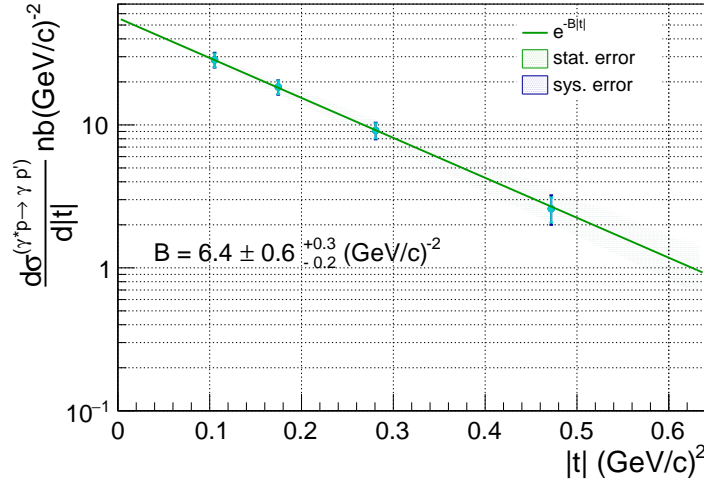
Figure 7.10: Values of the DVCS cross section in each $|t|$-bin and the slope extracted by the fit, including the statistic and systematic uncertainties. The inner error bars represent the statistical uncertainty, while for the outer error bars the statistical and systematic uncertainties are added in quadrature.
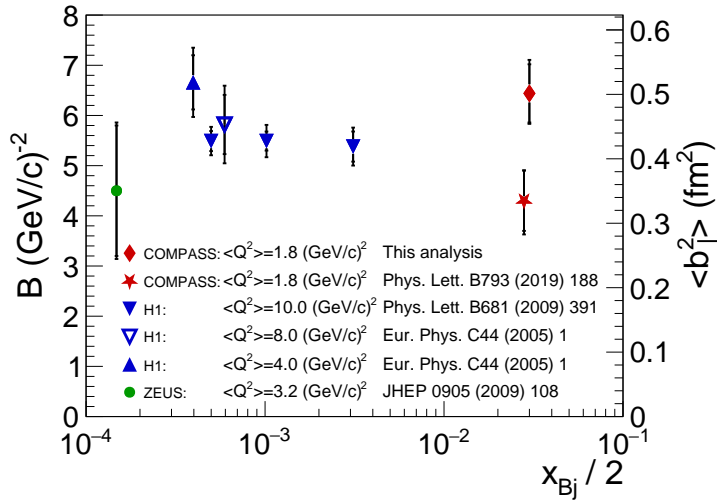
Figure 7.11: Comparison of the results on the slope parameter at the corresponding average x_{Bj}-values obtained by COMPASS using the 2016 data set (red diamond), to results obtained by COMPASS using the 2012 data set [16] (red star), H1 [2, 4] (blue triangles) and ZEUS [175] (green solid circle). The inner error bars represent the statistical uncertainty, while for the outer error bars the statistical and systematic uncertainties are added in quadrature.

using the approximation $\langle b_\perp^2 \rangle \approx 2\hbar^2 B$.

For the two COMPASS results, despite of being extracted at a very similar average kinematic, a deviation of about 2.5σ is visible. The 2016 result is obtained using an improved analysis method, which

includes additional criteria in the exclusive photon event selection and a more accurate Monte-Carlo simulation. In the 2012 analysis, a discrepancy between the data that was taken with opposite beam polarization was observed, which are in the 2016 data in good agreement. Beside the analysis steps, also the detector systems crucial to the measurement, namely ECAL0 and the proton recoil detector were improved after the 2012 data taking. The work on a detailed comparison of the 2012 and 2016 data, the event selection and analysis steps is still ongoing.

The H1 and ZEUS results are obtained in the gluon region at higher average values of Q^2 and much smaller x_{Bj}. Therefore, the measurements are more sensitive to higher order effects like the one and two gluon exchange, which might bias the comparison to the COMPASS results. The H1 measurements indicate an increase of the slope parameter with decreasing Q^2, which is in agreement with the larger value of the slope parameter obtained in the COMPASS 2016 analysis.

A similar behaviour can be observed, when performing the COMPASS analysis of the 2016 data separately in two x_{Bj} regimes. The results of this analysis are shown in Figure 7.12. Its corresponding DVCS cross sections and the fits of the slopes are illustrated in Appendix A.6. The result for $\langle x_{Bj} \rangle = 0.04$ is indicated by the solid red diamond and the result obtained for $\langle x_{Bj} \rangle = 0.09$ by the open diamond. Due to the fixed target measurement, the results are obtained at two different average values of Q^2. The statistic uncertainties are to large to draw any final conclusions, but a trend to larger values of the slope parameter with decreasing Q^2 is visible.
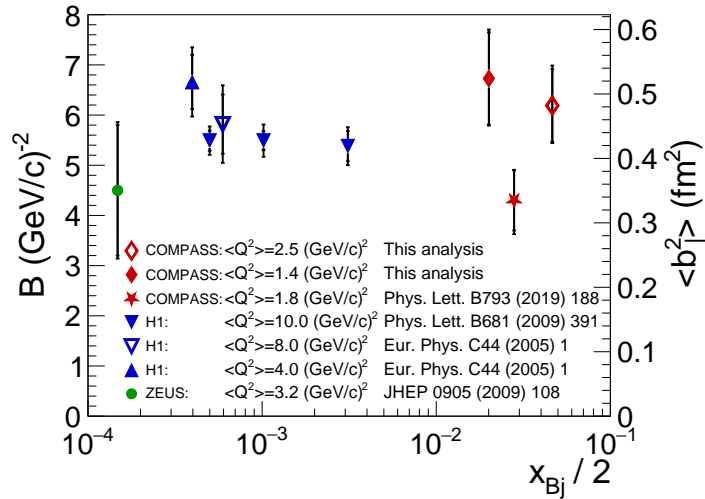
Figure 7.12: Comparison of the result on the slope parameters obtained by COMPASS using the 2016 data set and two intervals in x_{Bj} (red diamond), to results obtained by COMPASS using the 2012 data set [16] (red star), H1 [2, 4] (blue triangles) and ZEUS [175] (green circle). The inner error bars represent the statistical uncertainty, while for the outer error bars the statistical and systematic uncertainties are added in quadrature.

Figure 7.13a and 7.13b show the same data as discussed above, but with the predictions of the evolution of the x_{Bj}-dependence of the slope parameter by the KM15 [116, 118] and GK model [84, 85, 87], for an average Q^2 of 10.0 (GeV/c)^2 and 1.8 (GeV/c)^2. In case of the KM15-ImH, only the imaginary part of the GPD H is used. The two models differ in their predicted Q^2 evolution. While the KM15 model predicts an increase of B for larger values of Q^2, the GK model predicts an increasing value of B with decreasing Q^2. The KM15-ImH and GK model prediction for an average Q^2 of 1.8 (GeV/c)^2 both favour the result obtained in the 2016 COMPASS analysis.
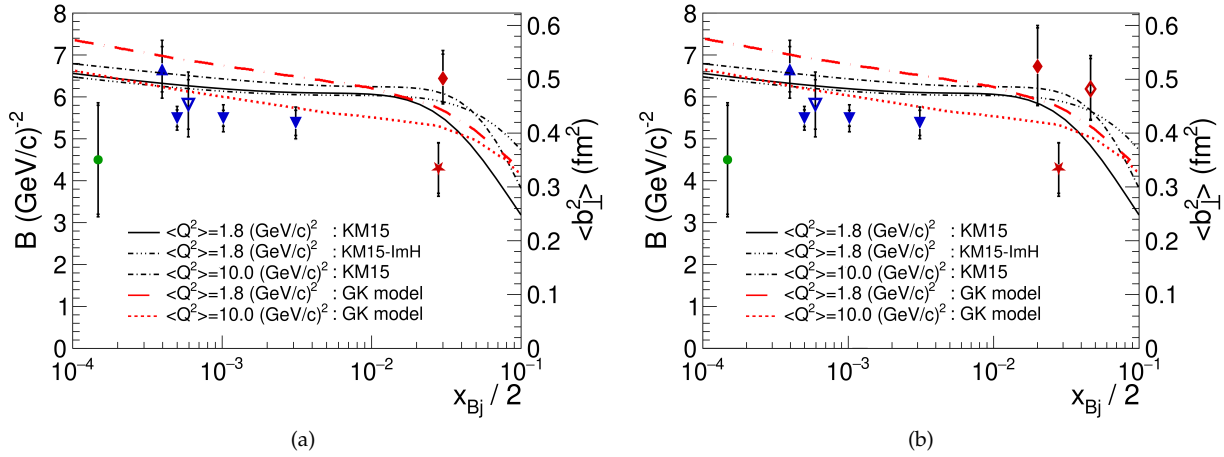
Figure 7.13: (a) and (b) show the same data points as shown in Figure 7.11 and 7.12, but overlaid with the prediction of the x_{Bj} evolution of the slope parameter at an average Q^2 of 10.0 (GeV/c)^2 and 1.8 (GeV/c)^2 using the KM15 [116, 118] and the GK model [84, 85, 87].

7.3 | Study of the ϕ modulation of the DVCS cross section

As discussed in Section 2.5.3, the Fourier coefficients can be extracted by studying the $\phi_{\gamma*\gamma}$-dependence of the virtual-photon proton cross section $d^2\sigma_{\text{DVCS}}^{\gamma*p\to\gamma p'}/d|t|d\phi_{\gamma*\gamma}$. Figure 7.14a to 7.14d show the DVCS cross section as a function of $\phi_{\gamma*\gamma}$ for each $|t|$-bin. The corresponding $\phi_{\gamma*\gamma}$-modulations are fitted by the function:

$$f(\phi_{\gamma*\gamma}) = c_0 + c_1\cos(\phi_{\gamma*\gamma}) + c_2\cos(2\phi_{\gamma*\gamma}) + s_1\sin(\phi_{\gamma*\gamma}) + s_2\sin(2\phi_{\gamma*\gamma}), \tag{7.15}$$

which is chosen as discussed in Section 2.5.3. The coefficients c_0, c_1 and c_2 refer to DVCS related coefficients in Equation 2.65 and s_1 and s_2 to interference related coefficients in Equation 2.66.

The results of the fits are summarized in Table 7.7. Except for the result of c_0, the results for c_1, c_2, s_1 and s_2 are compatible with zero within 2σ. Comparing the fit for c_0 with the mean values given in the bottom line of Table 7.7, an agreement better than 4% is obtained. The mean values are calculated using the values of the DVCS cross section given in Table 7.1 in Section 7.2.1 as: $\langle d\sigma_{\text{DVCS}}^{\gamma*p\to\gamma p'}/d|t|2\pi\rangle$. This agreement shows that c_0 is dominant, which supports interpretations of the slope parameter being strongly related to the transverse extensions of patrons in the proton (see Sec. 2.5.3). For a more accurate determination of the remaining coefficients, a larger data sample is needed for e.g. by including the 2017 data.

$|t|$-bin	[0.08,0.136]	]0.136,0.219]	]0.219,0.36]	]0.36,0.64]
c_0	4.34±0.48	2.87±0.31	1.46±0.17	0.42±0.08
c_1	-0.34±0.72	-0.89±0.45	-0.05±0.25	-0.12±0.12
c_2	1.28±0.66	-0.24±0.44	-0.27±0.24	-0.18±0.11
s_1	1.38±0.62	0.17±0.44	0.06±0.24	0.18±0.10
s_2	0.08±0.67	0.79±0.45	-0.34±0.24	0.29±0.10
c_0	4.53±0.49	2.93±0.32	1.46±0.18	0.42±0.08

Table 7.7: Summary of the fit results on the $\phi_{\gamma*\gamma}$-modulation of $d\sigma_{\text{DVCS}}^{\gamma*p\to\gamma p'}/d|t|d\phi_{\gamma*\gamma}$ in each $|t|$-bin. Mean values calculated from results on the DVCS cross section as: $\langle d\sigma_{\text{DVCS}}^{\gamma*p\to\gamma p'}/d|t|2\pi\rangle$ (bottom line).

(a)

(b)

(c)

(d)
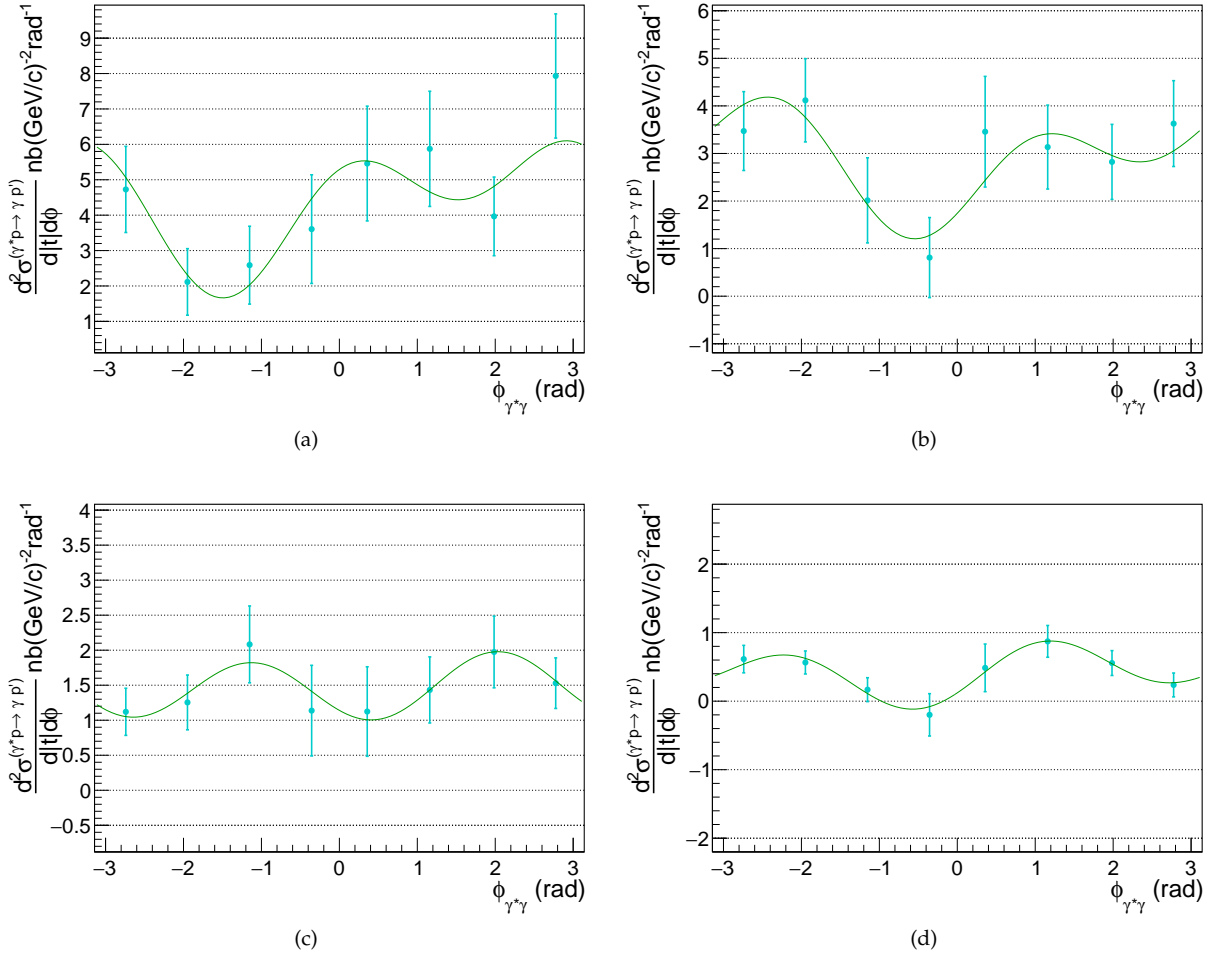
Figure 7.14: $d\sigma_{\text{DVCS}}^{\gamma*p\to\gamma p'}/d|t|d\phi_{\gamma*\gamma}$ as a function of $\phi_{\gamma*\gamma}$ for $0.08 < |t|\,(\text{GeV/c})^2 < 0.136$ (a), $0.136 < |t|\,(\text{GeV/c})^2 < 0.219$ (b), $0.219 < |t|\,(\text{GeV/c})^2 < 0.36$ (c) and $0.36 < |t|\,(\text{GeV/c})^2 < 0.64$ (d).

Summary, conclusion and future prospects

Studying the cross section of hard exclusive photon production in *Deeply Virtual Compton Scattering* (DVCS) allows to extract combinations of *Compton Form Factor*s (CFFs), which are used to further constrain the *Generalized Parton Distribution function*s (GPDs). These GPDs provide insights on the nucleon structure, in particular to the extension of partons in the nucleon and its spin composition. Besides of DVCS, GPD related observables are also accessible in other exclusive reactions like *Hard Exclusive Meson Production* (HEMP).

The COMPASS experiment allows to study these reactions in the small x_{Bj} regime of the sea quarks. A pilot run dedicated to measure DVCS and hard exclusive π^0 production was performed in 2012 and followed up by long data taking periods in 2016/17. In these measurements, high energetic (160 GeV) positively and negatively charged muon beams with opposite polarization were scattered off an unpolarized liquid hydrogen target. For an exclusive measurement of the initial and final state particles in exclusive photon production ($p\mu \rightarrow \mu' p' \gamma$) the COMPASS spectrometer was supplemented by a proton recoil detector surrounding the target, which was followed by an additional electromagnetic calorimeters to increase the photon acceptance. The scattering events are selected using a system of trigger hodoscopes, dedicated to the scattered muons. Therefore, not only the exclusive events are being recorded but in general inelastic muon-proton scattering events. The muon flux is determined using a true random trigger allowing for a precision better then 1%.

In order to identify exclusive photon events, a dedicated selection is performed. This selection is improved by using the exclusive measurement and formulating exclusivity conditions. These exclusivity conditions are requirements on the deviation between the measured proton kinematic to its prediction based on the measurement of the remaining particles and restrictions on the missing mass. Additionally a kinematic fit is applied. Its quality is used to further constrain the event selection and improve the resolution on the event kinematics, in particular on the variable $|t|$, which is the square of the four momentum transfer to the proton.

Beside of DVCS events, the exclusive photon sample still includes radiative photons of the so called *Bethe-Heitler* (BH) process and a background contamination by photons originating from the decay of inclusively or exclusively produced π^0. In order to obtain the DVCS cross section, these contributions are subtracted from the data sample. They are determined using dedicated Monte-Carlo samples for exclusive photon production and both π^0 production channel. The exclusive photon Monte-Carlo simulation is also used to determine the spectrometer acceptance. As both, the Bethe-Heitler contribution

and the acceptance, provide large corrections when determining the DVCS cross section a good repro-
duction of the data by the simulation is mandatory. To ensure a sufficient quality of the simulation,
several improvements on descriptions of the detector systems and their efficiencies were made.

The high beam energy at COMPASS allows to analyse the data in three distinct ν-regions. In the
ν-region between 80 GeV and 144 GeV, Bethe-Heitler is the dominant process. In this so called reference
region, an agreement of 98% between the Bethe-Heitler and the data is obtained. A substantial contribu-
tion by the pure DVCS is observed in the region for ν between 10 GeV and 32 GeV, which corresponds
to the region considered for extracting the DVCS cross section (extraction region). In the intermediate
ν-region between 32 GeV and 144 GeV a larger contribution by the interference between the scattering
amplitudes of DVCS and Bethe-Heitler, compared to the pure DVCS contribution is expected.

The DVCS cross section for virtual photon-proton scattering is calculated separately for μ^+ and μ^-
in bins of Q^2, ν, $\phi_{\gamma*\gamma}$ and $|t|$ in the kinematic range of:

$$1\,(\text{GeV/c})^2 < Q^2 < 5\,(\text{GeV/c})^2,\ 10\,\text{GeV} < \nu < 32\,\text{GeV}\ \text{and}\ 0.08\,(\text{GeV/c})^2 < |t| < 0.64\,(\text{GeV/c})^2.$$

In order to obtain, the $|t|$-dependance of the DVCS cross section, the cross section values are summed
over Q^2 and ν, integrated over $\phi_{\gamma*\gamma}$ and averaged over μ^+ and μ^-. An exponential $|t|$-dependance
is observed. The slope parameter B is extracted by a binned maximum log-likelihood fit assuming an
exponential ansatz of the form: $e^{-B|t|}$. Using about two-third of the 2016 data, the slope parameter is
determined to be:

$$B = 6.4 \pm 0.6|_{\text{stat}}{}^{+0.3}_{-0.2}|_{\text{sys}}\,(\text{GeV/c})^{-2},$$

at an average kinematics of:

$$\langle Q^2 \rangle = 1.8\,(\text{GeV/c})^2,\ \langle \nu \rangle = 17.9\,(\text{GeV}),\ \langle x_{Bj} \rangle = 0.060\ \text{and}\ \langle W \rangle = 5.7\,(\text{GeV/c}^2).$$

Using the fact that due to the $\phi_{\gamma*\gamma}$ integration only the pure DVCS contribution c_0 remains, which is
dominated by the imaginary part of the CFF $\mathcal{H}$, the slope parameter is related to the impact parameter
$b_\perp$. The impact parameter is determined to be:

$$\langle b_\perp^2 (x = x_{Bj}/2) \rangle \approx 2\hbar^2 \left(\frac{B}{1 - x_{Bj}} \right) = 0.53 \pm 0.05|_{\text{stat}}{}^{+0.03}_{-0.02}|_{\text{sys}}\,\text{fm}^2.$$

At small x_{Bj} values, where $x = \xi \simeq x_{Bj}/2$ holds, the impact parameter gives an approximate value for
the transverse extension of partons in the proton.
Comparing the determined slope parameter to its value obtained in the analysis of 2012 data, a differ-
ence of about 2.5σ is observed. The reason for this discrepancy is not yet resolved, but further investi-
gations are ongoing.

In addition to the 2016 data, the measurement at COMPASS also provides the 2017 data set, which is
not considered in the present analysis, but will contribute a two to three times higher statistics compared
to the 2016 data sample. With the higher statistics it will be possible to extract the slope parameter in
multiple x_{Bj} intervals. This would provide the possibility to obtain the evolution of $\langle b_\perp \rangle$ with x_{Bj} in
the sea quark regime. The high statistics data sample will also allow to study the $\phi_{\gamma*\gamma}$-modulation
of the cross section sum, hence the interference contribution and extract the charge spin cross section
difference, which makes it possible to access the real part of the CFF $\mathcal{H}$.

Bibliography

[1]   G. Aad et al. "Observation of a new particle in the search for the Standard Model Higgs boson with the ATLAS detector at the LHC." In: *Physics Letters B* 716.1 (2012), pp. 1–29. DOI: `10.1016/j.physletb.2012.08.020`. URL: `https://doi.org/10.1016%2Fj.physletb.2012.08.020`.

[2]   F.D. Aaron et al. "Measurement of deeply virtual Compton scattering at HERA." In: *The European Physical Journal C* 44.1 (2005), 1–11. ISSN: 1434-6052. DOI: `10.1140/epjc/s2005-02345-3`. URL: `http://dx.doi.org/10.1140/epjc/s2005-02345-3`.

[3]   F.D. Aaron et al. "Measurement of deeply virtual Compton scattering and its t-dependence at HERA." In: *Physics Letters B* 659.4 (2008), 796–806. ISSN: 0370-2693. DOI: `10.1016/j.physletb.2007.11.093`. URL: `http://dx.doi.org/10.1016/j.physletb.2007.11.093`.

[4]   F.D. Aaron et al. "Deeply virtual Compton scattering and its beam charge asymmetry in e±p collisions at HERA." In: *Physics Letters B* 681.5 (2009), 391–399. ISSN: 0370-2693. DOI: `10.1016/j.physletb.2009.10.035`. URL: `http://dx.doi.org/10.1016/j.physletb.2009.10.035`.

[5]   P. Abbon, E. Albrecht, and V.Yu. Alexakhin et al. "The COMPASS experiment at CERN." In: *Nuclear Instruments and Methods in Physics Research Section A: Accelerators, Spectrometers, Detectors and Associated Equipment* 577.3 (2007), pp. 455–518. ISSN: 0168-9002. DOI: `10.1016/j.nima.2007.03.026`. URL: `https://www.sciencedirect.com/science/article/pii/S0168900207005001`.

[6]   I. Abt et al. "The H1 detector at HERA." In: *Nuclear Instruments and Methods in Physics Research Section A: Accelerators, Spectrometers, Detectors and Associated Equipment* 386.2 (1997), pp. 310–347. ISSN: 0168-9002. DOI: `https://doi.org/10.1016/S0168-9002(96)00893-5`. URL: `https://www.sciencedirect.com/science/article/pii/S0168900296008935`.

[7]   K. Ackerstaff et al. "The HERMES Spectrometer." In: *Nuclear Instruments and Methods in Physics Research Section A: Accelerators, Spectrometers, Detectors and Associated Equipment* 417.2–3 (1998), 230–265. ISSN: 0168-9002. DOI: `10.1016/s0168-9002(98)00769-4`. URL: `http://dx.doi.org/10.1016/S0168-9002(98)00769-4`.

[8]   M. R. Adams et al. "Proton and deuteron structure functions in muon scattering at 470 GeV." In: *Phys. Rev. D* 54 (5 1996), pp. 3006–3056. DOI: `10.1103/PhysRevD.54.3006`. URL: `https://link.aps.org/doi/10.1103/PhysRevD.54.3006`.

[9]   C. Adloff et al. "Measurement of deeply virtual Compton scattering at HERA." In: *Physics Letters B* 517.1–2 (2001), 47–58. ISSN: 0370-2693. DOI: `10.1016/s0370-2693(01)00939-x`. URL: `http://dx.doi.org/10.1016/S0370-2693(01)00939-X`.

[10] C. Adolph et al. "The spin structure function g1p of the proton and a test of the Bjorken sum rule." In: *Physics Letters B* 753 (2016), pp. 18–28. ISSN: 0370-2693. DOI: `https://doi.org/10.1016/j.physletb.2015.11.064`. URL: `https://www.sciencedirect.com/science/article/pii/S037026931500920X`.

[11] S. Agostinelli et al. "Geant4—a simulation toolkit." In: *Nuclear Instruments and Methods in Physics Research Section A: Accelerators, Spectrometers, Detectors and Associated Equipment* 506.3 (2003), pp. 250–303. ISSN: 0168-9002. DOI: `https://doi.org/10.1016/S0168-9002(03)01368-8`. URL: `https://www.sciencedirect.com/science/article/pii/S0168900203013688`.

[12] A. Airapetian, N. Akopov, Z. Akopov, E. C. Aschenauer, W. Augustyniak, R. Avakian, A. Avetissian, E. Avetisyan, S. Belostotski, and et al. "Inclusive measurements of inelastic electron and positron scattering from unpolarized hydrogen and deuterium targets." In: *Journal of High Energy Physics* 2011.5 (2011). ISSN: 1029-8479. DOI: `10.1007/jhep05(2011)126`. URL: `http://dx.doi.org/10.1007/JHEP05(2011)126`.

[13] A. Airapetian et al. "Measurement of the Beam-Spin Azimuthal Asymmetry Associated with Deeply-Virtual Compton Scattering." In: *Physical Review Letters* 87.18 (2001). ISSN: 1079-7114. DOI: `10.1103/physrevlett.87.182001`. URL: `http://dx.doi.org/10.1103/PhysRevLett.87.182001`.

[14] A. Airapetian et al. "Beam-charge azimuthal asymmetry and deeply virtual Compton scattering." In: *Phys. Rev. D* 75 (1 2007), p. 011103. DOI: `10.1103/PhysRevD.75.011103`. URL: `https://link.aps.org/doi/10.1103/PhysRevD.75.011103`.

[15] A. Airapetian et al. "Measurement of double-spin asymmetries associated with deeply virtual Compton scattering on a transversely polarized hydrogen target." In: *Physics Letters B* 704.1–2 (2011), 15–23. ISSN: 0370-2693. DOI: `10.1016/j.physletb.2011.08.067`. URL: `http://dx.doi.org/10.1016/j.physletb.2011.08.067`.

[16] R. Akhunzyanov et al. "Transverse extension of partons in the proton probed in the sea-quark range by measuring the DVCS cross section." In: *Physics Letters B* 793 (2019), pp. 188–194. ISSN: 0370-2693. DOI: `https://doi.org/10.1016/j.physletb.2019.04.038`. URL: `https://www.sciencedirect.com/science/article/pii/S0370269319302710`.

[17] M.G. Alexeev et al. "Measurement of the cross section for hard exclusive 0 muoproduction on the proton." In: *Physics Letters B* 805 (2020), p. 135454. ISSN: 0370-2693. DOI: `https://doi.org/10.1016/j.physletb.2020.135454`. URL: `https://www.sciencedirect.com/science/article/pii/S0370269320302586`.

[18] G. Altarelli and G. Parisi. "Asymptotic freedom in parton language." In: *Nuclear Physics B* 126.2 (1977), pp. 298–318. ISSN: 0550-3213. DOI: `https://doi.org/10.1016/0550-3213(77)90384-4`. URL: `https://www.sciencedirect.com/science/article/pii/0550321377903844`.

[19]   Guido Altarelli. "Partons in quantum chromodynamics." In: *Physics Reports* 81.1 (1982), pp. 1–129. ISSN: 0370-1573. DOI: https://doi.org/10.1016/0370-1573(82)90127-2. URL: https://www.sciencedirect.com/science/article/pii/0370157382901272.

[20]   B. Andersson, G. Gustafson, G. Ingelman, and T. Sjöstrand. "Parton fragmentation and string dynamics." In: *Physics Reports* 97.2 (1983), pp. 31–145. ISSN: 0370-1573. DOI: 10.1016/0370-1573(83)90080-7. URL: https://www.sciencedirect.com/science/article/pii/0370157383900807.

[21]   M. Arneodo et al. "Measurement of the proton and deuteron structure functions, F2p and F2d, and of the ratio." In: *Nuclear Physics B* 483.1-2 (1997), 3–43. ISSN: 0550-3213. DOI: 10.1016/s0550-3213(96)00538-x. URL: http://dx.doi.org/10.1016/S0550-3213(96)00538-X.

[22]   J. Ashman et al. "A measurement of the spin asymmetry and determination of the structure function g1 in deep inelastic muon-proton scattering." In: *Physics Letters B* 206.2 (1988), pp. 364–370. ISSN: 0370-2693. DOI: https://doi.org/10.1016/0370-2693(88)91523-7. URL: https://www.sciencedirect.com/science/article/pii/0370269388915237.

[23]   B. Badelek, D. Bardin, K. Kurek, and C. Scholz. "Radiative correction schemes in Deep Inelastic muon scattering." In: (1994). DOI: 10.1007/BF01579633. arXiv: hep-ph/9403238 [hep-ph].

[24]   Roger Barlow and Christine Beeston. "Fitting using finite Monte Carlo samples." In: *Computer Physics Communications* 77.2 (1993), pp. 219–228. ISSN: 0010-4655. DOI: https://doi.org/10.1016/0010-4655(93)90005-W. URL: https://www.sciencedirect.com/science/article/pii/001046559390005W.

[25]   V. Barone and P. G. Ratcliffe. *Transverse Spin Physics*. Singapore: World Scientific, 2003.

[26]   G. Baum et al. "New Measurement of Deep-Inelastic e-p Asymmetries." In: *Phys. Rev. Lett.* 51 (13 1983), pp. 1135–1138. DOI: 10.1103/PhysRevLett.51.1135. URL: https://link.aps.org/doi/10.1103/PhysRevLett.51.1135.

[27]   A.V. Belitsky, D. Müller, and A. Kirchner. "Theory of deeply virtual Compton scattering on the nucleon." In: *Nuclear Physics B* 629.1 (2002), pp. 323–392. ISSN: 0550-3213. DOI: https://doi.org/10.1016/S0550-3213(02)00144-X. URL: https://www.sciencedirect.com/science/article/pii/S055032130200144X.

[28]   M. Benali et al. "Deeply virtual Compton scattering off the neutron." In: *Nature Physics* 16 (Feb. 2020). DOI: 10.1038/s41567-019-0774-3.

[29]   M. Benali et al. "Deeply virtual Compton scattering off the neutron." In: *Nature Physics* 16.2 (2020), 191–198. ISSN: 1745-2481. DOI: 10.1038/s41567-019-0774-3. URL: http://dx.doi.org/10.1038/s41567-019-0774-3.

[30]   A. C. Benvenuti. "A High Statistics Measurement of the Proton Structure Functions F(2)(x, Q²) and R from Deep Inelastic Muon Scattering at High Q²." In: *Phys. Lett. B* 223 (1989), pp. 485–489. DOI: 10.1016/0370-2693(89)91637-7.

[31]   J. C. Bernauer et al. "Electric and magnetic form factors of the proton." In: *Physical Review C* 90.1 (2014). ISSN: 1089-490X. DOI: 10.1103/physrevc.90.015206. URL: http://dx.doi.org/10.1103/PhysRevC.90.015206.

[32]   C. Bernet et al. "The COMPASS trigger system for muon scattering." In: *Nuclear Instruments and Methods in Physics Research Section A: Accelerators, Spectrometers, Detectors and Associated Equipment* 550.1 (2005), pp. 217–240. ISSN: 0168-9002. DOI: `https://doi.org/10.1016/j.nima.2005.05.043`. URL: `https://www.sciencedirect.com/science/article/pii/S0168900205012568`.

[33]   E. Bielert, J. Bremer, and N. Doshita et al. "A 2.5 m long liquid hydogen target for COMPASS." In: *Nuclear Instruments and Methods in Physics Research A* 746 (2014), pp. 20–25.

[34]   J. D. Bjorken. "Asymptotic Sum Rules at Infinite Momentum." In: *Phys. Rev.* 179 (5 1969), pp. 1547–1553. DOI: `10.1103/PhysRev.179.1547`. URL: `https://link.aps.org/doi/10.1103/PhysRev.179.1547`.

[35]   J. D. Bjorken and E. A. Paschos. "Inelastic Electron-Proton and γ-Proton Scattering and the Structure of the Nucleon." In: *Phys. Rev.* 185 (5 1969), pp. 1975–1982. DOI: `10.1103/PhysRev.185.1975`. URL: `https://link.aps.org/doi/10.1103/PhysRev.185.1975`.

[36]   E. D. Bloom et al. "High-Energy Inelastic e-p Scattering at 6°and 10°." In: *Phys. Rev. Lett.* 23 (16 1969), pp. 930–934. DOI: `10.1103/PhysRevLett.23.930`. URL: `https://link.aps.org/doi/10.1103/PhysRevLett.23.930`.

[37]   "FORMULAE AND METHODS IN EXPERIMENTAL DATA EVALUATION WITH EMPHASIS ON HIGH-ENERGY PHYSICS. VOL. 3: ARTICLES ON STATISTICAL AND NUMERICAL METHODS." In: (1984). Ed. by R. K. Bock, K. Bos, S. Brandt, J. Myrheim, and M. Regler.

[38]   M. Breidenbach, J. I. Friedman, H. W. Kendall, E. D. Bloom, D. H. Coward, H. DeStaebler, J. Drees, L. W. Mo, and R. E. Taylor. "Observed Behavior of Highly Inelastic Electron-Proton Scattering." In: *Phys. Rev. Lett.* 23 (16 1969), pp. 935–939. DOI: `10.1103/PhysRevLett.23.935`. URL: `https://link.aps.org/doi/10.1103/PhysRevLett.23.935`.

[39]   Carsten Burgard and David Galbraith. *Diagram of the standart model of physics*. 2016. URL: `https://texample.net/media/tikz/examples/PDF/model-physics.pdf`.

[40]   M Burkardt, C A Miller, and W-D Nowak. "Spin-polarized high-energy scattering of charged leptons on nucleons." In: *Reports on Progress in Physics* 73.1 (2009), p. 016201. DOI: `10.1088/0034-4885/73/1/016201`. URL: `https://doi.org/10.1088/0034-4885/73/1/016201`.

[41]   Matthias Burkardt. "IMPACT PARAMETER SPACE INTERPRETATION FOR GENERALIZED PARTON DISTRIBUTIONS." In: *International Journal of Modern Physics A* 18.02 (2003), 173–207. ISSN: 1793-656X. DOI: `10.1142/s0217751x03012370`. URL: `http://dx.doi.org/10.1142/S0217751X03012370`.

[42]   C. G. Callan and David J. Gross. "High-Energy Electroproduction and the Constitution of the Electric Current." In: *Phys. Rev. Lett.* 22 (4 1969), pp. 156–159. DOI: `10.1103/PhysRevLett.22.156`. URL: `https://link.aps.org/doi/10.1103/PhysRevLett.22.156`.

[43]   J. Chadwick. "Possible Existence of a Neutron." In: *Nature* 129 (1932), p. 312. DOI: `10.1038/129312a0`.

[44]   S. Chatrchyan et al. "Observation of a new boson at a mass of 125 GeV with the CMS experiment at the LHC." In: *Physics Letters B* 716.1 (2012), pp. 30–61. DOI: 10.1016/j.physletb.2012.08.021. URL: https://doi.org/10.1016%2Fj.physletb.2012.08.021.

[45]   S Chekanov et al. "Measurement of deeply virtual Compton scattering at HERA." In: *Physics Letters B* 573 (2003), 46–62. ISSN: 0370-2693. DOI: 10.1016/j.physletb.2003.08.048. URL: http://dx.doi.org/10.1016/j.physletb.2003.08.048.

[46]   110 Collaboration et al. *Measurement of R=σ_L / σ_T and the Separated Longitudinal and Transverse Structure Functions in the Nucleon Resonance Region*. 2013. arXiv: nucl-ex/0410027 [nucl-ex].

[47]   J. C. Collins, T. C. Rogers, and A. M. Staśto. "Fully unintegrated parton correlation functions and factorization in lowest-order hard scattering." In: *Physical Review D* 77.8 (2008). ISSN: 1550-2368. DOI: 10.1103/physrevd.77.085009. URL: http://dx.doi.org/10.1103/PhysRevD.77.085009.

[48]   John C. Collins and Andreas Freund. "Proof of factorization for deeply virtual Compton scattering in QCD." In: *Physical Review D* 59.7 (1999). ISSN: 1089-4918. DOI: 10.1103/physrevd.59.074009. URL: http://dx.doi.org/10.1103/PhysRevD.59.074009.

[49]   John Dalton. *A New System of Chemical Philosophy*. Vol. 1. Cambridge Library Collection - Physical Sciences. Cambridge University Press, 2010. DOI: 10.1017/CBO9780511736391.

[50]   M. Defurne et al. "E00-110 experiment at Jefferson Lab Hall A: Deeply virtual Compton scattering off the proton at 6 GeV." In: *Physical Review C* 92.5 (2015). ISSN: 1089-490X. DOI: 10.1103/physrevc.92.055202. URL: http://dx.doi.org/10.1103/PhysRevC.92.055202.

[51]   M. Defurne et al. "E00-110 experiment at Jefferson Lab Hall A: Deeply virtual Compton scattering off the proton at 6 GeV." In: *Physical Review C* 92.5 (2015). ISSN: 1089-490X. DOI: 10.1103/physrevc.92.055202. URL: http://dx.doi.org/10.1103/PhysRevC.92.055202.

[52]   L. Demortier and L. Lyons. "Everything you always wanted to know about pulls." In: (2002). URL: https://lucdemortier.github.io/assets/papers/cdf5776_pulls.pdf.

[53]   M. Derrick et al. "A measurement of tot(p) at S = 210 GeV." In: *Physics Letters B* 293.3 (1992), pp. 465–477. ISSN: 0370-2693. DOI: https://doi.org/10.1016/0370-2693(92)90914-P. URL: https://www.sciencedirect.com/science/article/pii/037026939290914P.

[54]   Alexandre Deur, Stanley J. Brodsky, and Guy F. de Téramond. "The QCD running coupling." In: *Progress in Particle and Nuclear Physics* 90 (2016), 1–74. ISSN: 0146-6410. DOI: 10.1016/j.ppnp.2016.04.003. URL: http://dx.doi.org/10.1016/j.ppnp.2016.04.003.

[55]   R. C. E. Devenish and A. Cooper-Sarkar. *Deep Inelastic Scattering*. New York, USA: Oxford University Press, 2004.

[56]   M. Diehl. "Generalized parton distributions." In: *Physics Reports* 388.2-4 (2003), 41–277. ISSN: 0370-1573. DOI: 10.1016/j.physrep.2003.08.002. URL: http://dx.doi.org/10.1016/j.physrep.2003.08.002.

[57] Yuri L. Dokshitzer. "Calculation of the Structure Functions for Deep Inelastic Scattering and e+ e- Annihilation by Perturbation Theory in Quantum Chromodynamics." In: *Sov. Phys. JETP* 46 (1977), pp. 641–653.

[58] S.D Drell and J.D Walecka. "Electrodynamic processes with nuclear targets." In: *Annals of Physics* 28.1 (1964), pp. 18–33. ISSN: 0003-4916. DOI: `https://doi.org/10.1016/0003-4916(64)90141-1`. URL: `https://www.sciencedirect.com/science/article/pii/0003491664901411`.

[59] R. Dupré, M. Guidal, and M. Vanderhaeghen. "Tomographic image of the proton." In: *Physical Review D* 95.1 (2017). ISSN: 2470-0029. DOI: `10.1103/physrevd.95.011501`. URL: `http://dx.doi.org/10.1103/PhysRevD.95.011501`.

[60] A.V. Efremov and A.V. Radyushkin. "Factorization and asymptotic behaviour of pion form factor in QCD." In: *Physics Letters B* 94.2 (1980), pp. 245–250. ISSN: 0370-2693. DOI: `https://doi.org/10.1016/0370-2693(80)90869-2`. URL: `https://www.sciencedirect.com/science/article/pii/0370269380908692`.

[61] F. J. Ernst, R. G. Sachs, and K. C. Wali. "Electromagnetic Form Factors of the Nucleon." In: *Phys. Rev.* 119 (3 1960), pp. 1105–1114. DOI: `10.1103/PhysRev.119.1105`. URL: `https://link.aps.org/doi/10.1103/PhysRev.119.1105`.

[62] J. J. Thomson M.A. F.R.S. "XL. Cathode Rays." In: *The London, Edinburgh, and Dublin Philosophical Magazine and Journal of Science* 44.269 (1897), pp. 293–316. DOI: `10.1080/14786449708621070`. eprint: `https://doi.org/10.1080/14786449708621070`. URL: `https://doi.org/10.1080/14786449708621070`.

[63] J.J. Thomson F.R.S. "XXIV. On the structure of the atom: an investigation of the stability and periods of oscillation of a number of corpuscles arranged at equal intervals around the circumference of a circle; with application of the results to the theory of atomic structure." In: *The London, Edinburgh, and Dublin Philosophical Magazine and Journal of Science* 7.39 (1904), pp. 237–265. DOI: `10.1080/14786440409463107`. eprint: `https://doi.org/10.1080/14786440409463107`. URL: `https://doi.org/10.1080/14786440409463107`.

[64] L. L. Foldy. "The Electromagnetic Properties of Dirac Particles." In: *Phys. Rev.* 87 (5 1952), pp. 688–693. DOI: `10.1103/PhysRev.87.688`. URL: `https://link.aps.org/doi/10.1103/PhysRev.87.688`.

[65] L. L. Frankfurt, A. Freund, and M. Strikman. "Diffractive exclusive photon production in DIS at DESY HERA." In: *Phys. Rev. D* 58 (11 1998), p. 114001. DOI: `10.1103/PhysRevD.58.114001`. URL: `https://link.aps.org/doi/10.1103/PhysRevD.58.114001`.

[66] L. L. Frankfurt, A. Freund, and M. Strikman. "Deeply virtual compton scattering at HERA - A probe of asymptotia." In: *Physics Letters B* 460 (1999), pp. 417–424. DOI: `10.1016/S0370-2693(99)00803-5`. URL: `https://www.sciencedirect.com/science/article/pii/S0370269399008035`.

[67] N. du Fresne. "Measurement of Hadron Multiplicities in Deep Inelastic Muon-Nucleon Scattering." PhD thesis. Johannes Gutenberg-University, Mainz, 2015.

[68] J Friedrich, O Denisov, and A Vorobyev. *Addendum to the COMPASS-II Proposal*. Tech. rep. COM-PASS has 2 spokespersons, Oleg.Denisov@cern.ch and Jan.Friedrich@cern.ch. Geneva: CERN, 2018. URL: `https://cds.cern.ch/record/2286954`.

[69] R. Frisch and O. Stern. "Über die magnetische Ablenkung von Wasserstoffmolekülen und das magnetische Moment des Protons. I." In: *Zeitschrift fur Physik* 85.1-2 (Jan. 1933), pp. 4–16. DOI: `10.1007/BF01330773`.

[70] H. Fritzsch, Murray Gell-Mann, and H. Leutwyler. "Advantages of the Color Octet Gluon Picture." In: *Phys. Lett. B* 47 (1973), pp. 365–368. DOI: `10.1016/0370-2693(73)90625-4`.

[71] R. Frühwirth. "Application of Kalman filtering to track and vertex fitting." In: *Nuclear Instruments and Methods in Physics Research Section A: Accelerators, Spectrometers, Detectors and Associated Equipment* 262.2 (1987), pp. 444–450. ISSN: 0168-9002. DOI: `https://doi.org/10.1016/0168-9002(87)90887-4`. URL: `https://www.sciencedirect.com/science/article/pii/0168900287908874`.

[72] F Gautheron et al. *COMPASS-II Proposal*. Tech. rep. Geneva: CERN, 2010. URL: `https://cds.cern.ch/record/1265628`.

[73] M Gell-Mann. "THE EIGHTFOLD WAY: A THEORY OF STRONG INTERACTION SYMME-TRY." In: (Mar. 1961). DOI: `10.2172/4008239`. URL: `https://www.osti.gov/biblio/4008239`.

[74] M. Gell-Mann. "A schematic model of baryons and mesons." In: *Physics Letters* 8.3 (1964), pp. 214–215. ISSN: 0031-9163. DOI: `https://doi.org/10.1016/S0031-9163(64)92001-3`. URL: `https://www.sciencedirect.com/science/article/pii/S0031916364920013`.

[75] S. Gerassimov. *PHysics Analysis Software Tools*.

[76] Sergei Gerassimov. private communications. 2020.

[77] M. Gerstner. "Vergleich von Daten- und Monte-Carlo-Ereignissen bei COMPASS." Johannes Gutenberg-University, Mainz, 2020. URL: `https://wwwcompass.cern.ch/compass/publications/theses/2020_bac_gerstner.pdf`.

[78] J. Giarra. "Analysis of the spill profile and the muon flux in 2016." COMPASS note 2021-2. 2021. URL: `https://wwwcompass.cern.ch/compass/notes/2021-2/2021-2.pdf`.

[79] J. Giarra. "Determination of hodoscope positions from data in 2016." COMPASS note. 2021.

[80] J. Giarra. "Determination of the Hodoscope and Trigger Efficiencies in 2016." COMPASS note 2021-1. 2021. URL: `https://wwwcompass.cern.ch/compass/notes/2021-1/2021-1.pdf`.

[81] F. X. Girod et al. "Measurement of Deeply Virtual Compton Scattering Beam-Spin Asymmetries." In: *Physical Review Letters* 100.16 (2008). ISSN: 1079-7114. DOI: `10.1103/physrevlett.100.162002`. URL: `http://dx.doi.org/10.1103/PhysRevLett.100.162002`.

[82] K. Goeke, M.V. Polyakov, and M. Vanderhaeghen. "Hard exclusive reactions and the structure of hadrons." In: *Progress in Particle and Nuclear Physics* 47.2 (2001), 401–515. ISSN: 0146-6410. DOI: `10.1016/s0146-6410(01)00158-2`. URL: `http://dx.doi.org/10.1016/S0146-6410(01)00158-2`.

[83]   T. Goepfert. *KinFitter A Kinematic Fit with Constrains*. URL: `https://github.com/goepfert/KinFitter/wiki/KinFitter---A-Kinematic-Fit-with-Constraints`.

[84]   S. V. Goloskokov and P. Kroll. "Vector-meson electroproduction at small Bjorken-x and generalized parton distributions." In: *The European Physical Journal C* 42.3 (2005), 281–301. ISSN: 1434-6052. DOI: `10.1140/epjc/s2005-02298-5`. URL: `http://dx.doi.org/10.1140/epjc/s2005-02298-5`.

[85]   S. V. Goloskokov and P. Kroll. "An attempt to understand exclusive + electroproduction." In: *The European Physical Journal C* 65.1-2 (2009). ISSN: 1434-6052. DOI: `10.1140/epjc/s10052-009-1178-9`. URL: `http://dx.doi.org/10.1140/epjc/s10052-009-1178-9`.

[86]   S. V. Goloskokov and Kroll P. "Transversity in hard exclusive electroproduction of pseudoscalar mesons." In: (2011). URL: `https://arxiv.org/abs/1106.4897`.

[87]   S.V. Goloskokov and P. Kroll. "The role of the quark and gluon GPDs in hard vector-meson electroproduction." In: *The European Physical Journal C* 53.3 (2007), 367–384. ISSN: 1434-6052. DOI: `10.1140/epjc/s10052-007-0466-5`. URL: `http://dx.doi.org/10.1140/epjc/s10052-007-0466-5`.

[88]   M. Gorzellik. "Cross-section measurement of exclusive π^0 muonproduction and firmware design for an FPGA-based detector readout." PhD thesis. Albert-Ludwigs-University, Freiburg, 2018. URL: `https://wwwcompass.cern.ch/compass/publications/theses/2018_phd_gorzellik.pdf`.

[89]   O. W. Greenberg. "Spin and Unitary-Spin Independence in a Paraquark Model of Baryons and Mesons." In: *Phys. Rev. Lett.* 13 (20 1964), pp. 598–602. DOI: `10.1103/PhysRevLett.13.598`. URL: `https://link.aps.org/doi/10.1103/PhysRevLett.13.598`.

[90]   V. N. Gribov and L. N. Lipatov. "Deep inelastic e p scattering in perturbation theory." In: *Sov. J. Nucl. Phys.* 15 (1972), pp. 438–450.

[91]   G. Grindhammer and S. Peters. *The Parameterized Simulation of Electromagnetic Showers in Homogeneous and Sampling Calorimeters*. 2000. arXiv: `hep-ex/0001020` [`hep-ex`].

[92]   David J. Gross and Frank Wilczek. "Ultraviolet Behavior of Non-Abelian Gauge Theories." In: *Phys. Rev. Lett.* 30 (26 1973), pp. 1343–1346. DOI: `10.1103/PhysRevLett.30.1343`. URL: `https://link.aps.org/doi/10.1103/PhysRevLett.30.1343`.

[93]   P. A. M. Guichon, N. d'Hose, and A. Vidon. *Calculation of the pure Bethe-Heitler cross section*. private communications. 2015.

[94]   M. Guidal. "A fitter code for Deep Virtual Compton Scattering and Generalized Parton Distributions." In: *The European Physical Journal A* 37.3 (2008), 319–332. ISSN: 1434-601X. DOI: `10.1140/epja/i2008-10630-6`. URL: `http://dx.doi.org/10.1140/epja/i2008-10630-6`.

[95]   M. Guidal. "Constraints on the $\tilde{H}$ Generalized Parton Distribution from Deep Virtual Compton Scattering Measured at HERMES." In: *Physics Letters B* 693.1 (2010), 17–23. ISSN: 0370-2693. DOI: `10.1016/j.physletb.2010.07.059`. URL: `http://dx.doi.org/10.1016/j.physletb.2010.07.059`.

[96]   M. Guidal. "Generalized parton distributions from deep virtual compton scattering at CLAS."
       In: *Physics Letters B* 689.4–5 (2010), 156–162. ISSN: 0370-2693. DOI: 10.1016/j.physletb.2010.
       04.053. URL: http://dx.doi.org/10.1016/j.physletb.2010.04.053.

[97]   M. Guidal and H. Moutarde. "Generalized Parton Distributions from Deeply Virtual Compton
       Scattering at HERMES." In: *The European Physical Journal A* 42.1 (2009). ISSN: 1434-601X. DOI:
       10.1140/epja/i2009-10840-4. URL: http://dx.doi.org/10.1140/epja/i2009-10840-4.

[98]   M. Guidal, M. V. Polyakov, A. V. Radyushkin, and M. Vanderhaeghen. "Nucleon form factors
       from generalized parton distributions." In: *Phys. Rev. D* 72 (5 2005), p. 054013. DOI: 10.1103/
       PhysRevD.72.054013. URL: https://link.aps.org/doi/10.1103/PhysRevD.72.054013.

[99]   Michel Guidal. *Extraction of Compton Form Factors from DVCS data*. 2010. arXiv: 1011.4195 [hep-ph].

[100] Michel Guidal, Hervé Moutarde, and Marc Vanderhaeghen. "Generalized parton distributions
       in the valence region from deeply virtual compton scattering." In: *Reports on Progress in Physics*
       76.6 (2013), p. 066202. ISSN: 1361-6633. DOI: 10.1088/0034-4885/76/6/066202. URL: http:
       //dx.doi.org/10.1088/0034-4885/76/6/066202.

[101] H1 and ZEUS Collaborations. *Combination of Measurements of Inclusive Deep Inelastic e-p Scattering
       Cross Sections and QCD Analysis of HERA Data*. 2015. arXiv: 1506.06042 [hep-ex].

[102] Francis Halzen and Alan Martin. *Quarks & Leptons: An introductory course in modern particle physics*.
       New York, USA: John Wiley & Sons, 1984.

[103] L. N. Hand, D. G. Miller, and Richard Wilson. "Electric and Magnetic Form Factors of the Nu-
       cleon." In: *Rev. Mod. Phys.* 35 (2 1963), pp. 335–349. DOI: 10.1103/RevModPhys.35.335. URL:
       https://link.aps.org/doi/10.1103/RevModPhys.35.335.

[104] F. Herrmann. "Development and Verification of a High Performance Electronic Readout Frame-
       work for High Energy Physics." PhD thesis. Albert-Ludwigs-University, Freiburg, 2011.

[105] A. J. G. Hey and J. E. Mandula. "Light-Cone Analysis of Spin-Dependent Deep-Inelastic Electron
       Scattering." In: *Phys. Rev. D* 5 (10 1972), pp. 2610–2614. DOI: 10.1103/PhysRevD.5.2610. URL:
       https://link.aps.org/doi/10.1103/PhysRevD.5.2610.

[106] Robert Hofstadter. "Electron Scattering and Nuclear Structure." In: *Rev. Mod. Phys.* 28 (3 1956),
       pp. 214–254. DOI: 10.1103/RevModPhys.28.214. URL: https://link.aps.org/doi/10.1103/
       RevModPhys.28.214.

[107] G. Ingelman, A. Edin, and Rathsman J. "LEPTO 6.5 - A Monte Carlo Generator for Deep Inelastic
       Lepton-Nucleon Scattering." In: (1996). DOI: 10.1016/S0010-4655(96)00157-9. URL: https:
       //arxiv.org/abs/hep-ph/9605286.

[108] R.L. Jaffe and Aneesh Manohar. "The g1 problem: Deep inelastic electron scattering and the
       spin of the proton." In: *Nuclear Physics B* 337.3 (1990), pp. 509–546. ISSN: 0550-3213. DOI: https:
       //doi.org/10.1016/0550-3213(90)90506-9. URL: https://www.sciencedirect.com/
       science/article/pii/0550321390905069.

[109] Robert L. Jaffe. *Spin, Twist and Hadron Structure in Deep Inelastic Processes*. 1996. arXiv: `hep-ph/9602236 [hep-ph]`.

[110] Xiangdong Ji. "Gauge-Invariant Decomposition of Nucleon Spin." In: *Physical Review Letters* 78.4 (1997), 610–613. ISSN: 1079-7114. DOI: `10.1103/physrevlett.78.610`. URL: `http://dx.doi.org/10.1103/PhysRevLett.78.610`.

[111] Xiangdong Ji. "Off-forward parton distributions." In: *Journal of Physics G: Nuclear and Particle Physics* 24.7 (1998), 1181–1205. ISSN: 1361-6471. DOI: `10.1088/0954-3899/24/7/002`. URL: `http://dx.doi.org/10.1088/0954-3899/24/7/002`.

[112] Xiangdong Ji. "GENERALIZED PARTON DISTRIBUTIONS." In: *Annual Review of Nuclear and Particle Science* 54.1 (2004), pp. 413–450. DOI: `10.1146/annurev.nucl.54.070103.181302`. eprint: `https://doi.org/10.1146/annurev.nucl.54.070103.181302`. URL: `https://doi.org/10.1146/annurev.nucl.54.070103.181302`.

[113] H.S. Jo et al. "Cross Sections for the Exclusive Photon Electroproduction on the Proton and Generalized Parton Distributions." In: *Physical Review Letters* 115.21 (2015). ISSN: 1079-7114. DOI: `10.1103/physrevlett.115.212003`. URL: `http://dx.doi.org/10.1103/PhysRevLett.115.212003`.

[114] P. Jörg. "Scattering at CERN - What is the Size of the Proton?" PhD thesis. Albert-Ludwigs-University, Freiburg, 2017. URL: `https://wwwcompass.cern.ch/compass/publications/theses/2017_phd_joerg.pdf`.

[115] R. Abdul Khalek et al. *Snowmass 2021 White Paper: Electron Ion Collider for High Energy Physics*. 2022. DOI: `10.48550/ARXIV.2203.13199`. URL: `https://arxiv.org/abs/2203.13199`.

[116] Kumeric, Kresimir and Müller, Dieter. "Description and interpretation of DVCS measurements*." In: *EPJ Web of Conferences* 112 (2016), p. 01012. DOI: `10.1051/epjconf/201611201012`. URL: `https://doi.org/10.1051/epjconf/201611201012`.

[117] Kresimir Kumericki, Dieter Mueller, and Kornelija Passek-Kumericki. *Fitting DVCS amplitude in moment-space approach to GPDs*. 2009. arXiv: `0807.0159 [hep-ph]`.

[118] Krešimir Kumerički and Dieter Müller. "Deeply virtual Compton scattering at small xB and the access to the GPD H." In: *Nuclear Physics B* 841.1 (2010), pp. 1–58. ISSN: 0550-3213. DOI: `https://doi.org/10.1016/j.nuclphysb.2010.07.015`. URL: `https://www.sciencedirect.com/science/article/pii/S0550321310003858`.

[119] Christoph Langenbruch. *Parameter uncertainties in weighted unbinned maximum likelihood fits*. 2021. arXiv: `1911.01303 [physics.data-an]`.

[120] Po-Ju Lin. private communications. 2019.

[121] Po-Ju Lin. "The Extraction of Relative Contribution from LEPTO and HEPGEN in the Exclusive-like pi0 Events." COMPASS note 2021-3. 2021. URL: `https://wwwcompass.cern.ch/compass/notes/2021-3/2021-3.pdf`.

[122] L. N. Lipatov. "The parton model and perturbation theory." In: *Yad. Fiz.* 20 (1974), pp. 181–198.

[123]   Aneesh V. Manohar. *An Introduction to Spin Dependent Deep Inelastic Scattering*. 1992. arXiv: hep-ph/9204208 [hep-ph].

[124]   C. Marquet, R. Peschanski, and G. Soyez. "Exclusive vector meson production at HERA from QCD with saturation." In: *Physical Review D* 76.3 (2007). ISSN: 1550-2368. DOI: 10.1103/physrevd.76.034011. URL: http://dx.doi.org/10.1103/PhysRevD.76.034011.

[125]   M. Mazouz et al. "Deeply Virtual Compton Scattering off the Neutron." In: *Phys. Rev. Lett.* 99 (24 2007), p. 242501. DOI: 10.1103/PhysRevLett.99.242501. URL: https://link.aps.org/doi/10.1103/PhysRevLett.99.242501.

[126]   R. W. McAllister and R. Hofstadter. "Elastic Scattering of 188-Mev Electrons from the Proton and the Alpha Particle." In: *Phys. Rev.* 102 (3 1956), pp. 851–856. DOI: 10.1103/PhysRev.102.851. URL: https://link.aps.org/doi/10.1103/PhysRev.102.851.

[127]   B. A. Mecking et al. "The CEBAF Large Acceptance Spectrometer (CLAS)." In: *Nucl. Instrum. Meth. A* 503 (2003), pp. 513–553. DOI: 10.1016/S0168-9002(03)01001-5.

[128]   P. Mergell, Ulf-G. Meißner, and D. Drechsel. "Dispersion-theoretical analysis of the nucleon electromagnetic form factors." In: *Nuclear Physics A* 596.3–4 (1996), 367–396. ISSN: 0375-9474. DOI: 10.1016/0375-9474(95)00339-8. URL: http://dx.doi.org/10.1016/0375-9474(95)00339-8.

[129]   R.P. Mount. "The measurement of intense particle beams." In: *Nuclear Instruments and Methods in Physics Research* 187.2 (1981), pp. 401–405. ISSN: 0167-5087. DOI: https://doi.org/10.1016/0029-554X(81)90367-0. URL: https://www.sciencedirect.com/science/article/pii/0029554X81903670.

[130]   H. Moutarde, P. Sznajder, and J. Wagner. "Border and skewness functions from a leading order fit to DVCS data." In: *The European Physical Journal C* 78.11 (2018). ISSN: 1434-6052. DOI: 10.1140/epjc/s10052-018-6359-y. URL: http://dx.doi.org/10.1140/epjc/s10052-018-6359-y.

[131]   H. Moutarde, P. Sznajder, and J. Wagner. "Unbiased determination of DVCS Compton form factors." In: *The European Physical Journal C* 79.7 (2019). ISSN: 1434-6052. DOI: 10.1140/epjc/s10052-019-7117-5. URL: http://dx.doi.org/10.1140/epjc/s10052-019-7117-5.

[132]   D. Müller, D. Robaschik, B. Geyer, F.-M. Dittes, and J. Hořejši. "Wave Functions, Evolution Equations and Evolution Kernels from Light-Ray Operators of QCD." In: *Fortschritte der Physik/Progress of Physics* 42.2 (1994), 101–141. ISSN: 1521-3979. DOI: 10.1002/prop.2190420202. URL: http://dx.doi.org/10.1002/prop.2190420202.

[133]   New Muon Collaboration (NMC). "Measurement of the proton and the deuteron structure functions, F2p and F2d." In: *Physics Letters B* 364.2 (1995), pp. 107–115. ISSN: 0370-2693. DOI: 10.1016/0370-2693(95)01318-9. URL: https://www.sciencedirect.com/science/article/pii/0370269395013189.

[134]   Y. Nambu. *Preludes in theoretical physics*. Netherlands, Amsterdam 1966.

[135]   Y. Ne'eman. "Derivation of strong interactions from a gauge invariance." In: *Nuclear Physics* 26.2 (1961), pp. 222–229. ISSN: 0029-5582. DOI: https://doi.org/10.1016/0029-5582(61)90134-1. URL: https://www.sciencedirect.com/science/article/pii/0029558261901341.

[136]   B. Parsamyan and F. Tessarotto. *COMPASS Status Report 2021*. Tech. rep. Geneva: CERN, 2021.
        URL: https://cds.cern.ch/record/2770989.

[137]   C.F. Perdrisat, V. Punjabi, and M. Vanderhaeghen. "Nucleon electromagnetic form factors." In:
        Progress in Particle and Nuclear Physics 59.2 (2007), pp. 694–764. ISSN: 0146-6410. DOI: https :
        //doi.org/10.1016/j.ppnp.2007.05.001. URL: https://www.sciencedirect.com/science/
        article/pii/S0146641007000610.

[138]   C.F. Perdrisat, V. Punjabi, and M. Vanderhaeghen. "Nucleon electromagnetic form factors." In:
        Progress in Particle and Nuclear Physics 59.2 (2007), 694–764. ISSN: 0146-6410. DOI: 10.1016/j.
        ppnp.2007.05.001. URL: http://dx.doi.org/10.1016/j.ppnp.2007.05.001.

[139]   G. Peter Lepage and Stanley J. Brodsky. "Exclusive processes in quantum chromodynamics: Evo-
        lution equations for hadronic wavefunctions and the form factors of mesons." In: *Physics Letters
        B* 87.4 (1979), pp. 359–365. ISSN: 0370-2693. DOI: https://doi.org/10.1016/0370-2693(79)
        90554-9. URL: https://www.sciencedirect.com/science/article/pii/0370269379905549.

[140]   N. Pierre. "Multiplicities of hadrons in Deep-Inelastic Scattering of muons on nucleons at COM-
        PASS." PhD thesis. University Paris-Saclay, 2019.

[141]   S. Pisano et al. "Single and double spin asymmetries for deeply virtual Compton scattering mea-
        sured with CLAS and a longitudinally polarized proton target." In: *Physical Review D* 91.5 (2015).
        ISSN: 1550-2368. DOI: 10.1103/physrevd.91.052014. URL: http://dx.doi.org/10.1103/
        PhysRevD.91.052014.

[142]   H. David Politzer. "Reliable Perturbative Results for Strong Interactions?" In: *Phys. Rev. Lett.* 30
        (26 1973), pp. 1346–1349. DOI: 10.1103/PhysRevLett.30.1346. URL: https://link.aps.org/
        doi/10.1103/PhysRevLett.30.1346.

[143]   M. V. Polyakov and C. Weiss. "Skewed and double distributions in the pion and the nucleon."
        In: *Physical Review D* 60.11 (1999). ISSN: 1089-4918. DOI: 10.1103/physrevd.60.114017. URL:
        http://dx.doi.org/10.1103/PhysRevD.60.114017.

[144]   B. Povh, K. Rith, Ch. Scholz, F. Zetsche, and W. Rodejohann. *Particles and Nuclei: An introduction
        to the Physical Concepts*. 9th ed. Heidelberg, Germany: Springer Spektrum, 2013.

[145]   J. Pretz. "The Veto System." COMPASS note. 2002.

[146]   *ROOT Data Analysis Framework*. URL: https://root.cern.

[147]   A. V. Radyushkin. "Nonforward parton distributions." In: *Phys. Rev. D* 56 (9 1997), pp. 5524–5557.
        DOI: 10.1103/PhysRevD.56.5524. URL: https://link.aps.org/doi/10.1103/PhysRevD.56.
        5524.

[148]   A. V. Radyushkin. "Double distributions and evolution equations." In: *Phys. Rev. D* 59 (1 1998),
        p. 014030. DOI: 10.1103/PhysRevD.59.014030. URL: https://link.aps.org/doi/10.1103/
        PhysRevD.59.014030.

[149] A.V. Radyushkin. "Symmetries and structure of skewed and double distributions." In: *Physics Letters B* 449.1-2 (1999), 81–88. ISSN: 0370-2693. DOI: 10.1016/s0370-2693(98)01584-6. URL: http://dx.doi.org/10.1016/S0370-2693(98)01584-6.

[150] P.G. Ratcliffe. "Orbital angular momentum and the parton model." In: *Physics Letters B* 192.1 (1987), pp. 180–184. ISSN: 0370-2693. DOI: https://doi.org/10.1016/0370-2693(87)91163-4. URL: https://www.sciencedirect.com/science/article/pii/0370269387911634.

[151] C. R. Regali. "Exclusive event generation for the COMPASS-II experiment at CERN and improvements for the Monte-Carlo chain." PhD thesis. Albert-Ludwigs-University, Freiburg, 2016.

[152] W. Renz, B. Ketzer, M. Wagner, and Pekeler H. "ECAL Shower parameters for TGEANT." COMPASS note 2019-5. 2019.

[153] Julie Roche. "The DVCS program in Hall A at JLab." In: *PoS* QNP2012 (2012). Ed. by Bernard Pire, p. 036. DOI: 10.22323/1.157.0036.

[154] E. Rutherford. "LXXIX. The scattering of and particles by matter and the structure of the atom." In: *The London, Edinburgh, and Dublin Philosophical Magazine and Journal of Science* 21.125 (1911), pp. 669–688. DOI: 10.1080/14786440508637080. eprint: https://doi.org/10.1080/14786440508637080. URL: https://doi.org/10.1080/14786440508637080.

[155] A. Sandacz. *Modifications to FFS model and predictions*. 2009. URL: https://wwwcompass.cern.ch/compass/gpd/meetings/200904_april22/AS_gpd-Apr2009.ppt.

[156] A. Sandacz and Sznajder P. "HEPGEN generator for hard exclusive leptoproduction." In: (2012). URL: https://arxiv.org/abs/1207.0333v1.

[157] R. Schäfer. "Charakterisierung eines Detektors zum Nachweis von Rückstoßprotonen am COMPASS Experiment." Fakultät für Mathematik und Physik der Albert-Ludwigs-Universität, Freiburg, 2013. URL: https://cds.cern.ch/record/2005748/files/schaefer_diplom_2013.pdf.

[158] S. Scherrers. "Extraction of the exclusive J/Ψ photoproduction cross section at COMPASS, CERN." MA thesis. Fakultät für Mathematik und Physik der Albert-Ludwigs-Universität, Freiburg, 2019.

[159] L. M. Sehgal. "Angular momentum composition of the proton in the quark-parton model." In: *Phys. Rev. D* 10 (5 1974), pp. 1663–1665. DOI: 10.1103/PhysRevD.10.1663. URL: https://link.aps.org/doi/10.1103/PhysRevD.10.1663.

[160] S. Stepanyan et al. "Observation of Exclusive Deeply Virtual Compton Scattering in Polarized Electron Beam Asymmetry Measurements." In: *Physical Review Letters* 87.18 (2001). ISSN: 1079-7114. DOI: 10.1103/physrevlett.87.182002. URL: http://dx.doi.org/10.1103/PhysRevLett.87.182002.

[161] T. Szameitat. "New Geant4-based Monte Carlo Software for the COMPASS-II Experiment at CERN." PhD thesis. Albert-Ludwigs-University, Freiburg, 2016.

[162] *TFractionFitter*. URL: https://root.cern/doc/master/classTFractionFitter.html.

[163]   M. Vanderhaeghen, P. A. M. Guichon, and M. Guidal. "Hard Electroproduction of Photons and Mesons on the Nucleon." In: *Phys. Rev. Lett.* 80 (23 1998), pp. 5064–5067. DOI: 10.1103/PhysRevLett.80.5064. URL: https://link.aps.org/doi/10.1103/PhysRevLett.80.5064.

[164]   M. Vanderhaeghen, P. A. M. Guichon, and M. Guidal. "Deeply virtual electroproduction of photons and mesons on the nucleon: Leading order amplitudes and power corrections." In: *Phys. Rev. D* 60 (9 1999), p. 094017. DOI: 10.1103/PhysRevD.60.094017. URL: https://link.aps.org/doi/10.1103/PhysRevD.60.094017.

[165]   B. Ventura. "Study of Deeply Virtual Compton Scattering at COMPASS at CERN." PhD thesis. University Paris-Saclay, 2021.

[166]   A. Vidon. "Probing the proton structure through Deep Virtual Compton Scattering at COMPASS, CERN." PhD thesis. University Paris-Saclay, 2019. URL: https://wwwcompass.cern.ch/compass/publications/theses/2019_phd_vidon.pdf.

[167]   L. W. Whitlow, E. M. Riordan, S. Dasu, Stephen Rock, and A. Bodek. "Precise measurements of the proton and deuteron structure functions from a global analysis of the SLAC deep inelastic electron scattering cross-sections." In: *Phys. Lett. B* 282 (1992), pp. 475–482. DOI: 10.1016/0370-2693(92)90672-Q.

[168]   M. Wilfert. "Investigation of the spin structure of the nucleon at the COMPASS experiment." PhD thesis. Johannes Gutenberg-University, Mainz, 2017.

[169]   E. J. Wolin and L. L. Ho. "Covariance matrices for track fitting with the Kalman filter." In: *Nucl. Instrum. Meth. A* 329 (1993), pp. 493–500. DOI: 10.1016/0168-9002(93)91285-U.

[170]   G. Zweig. "An SU(3) model for strong interaction symmetry and its breaking. Version 2." In: *DEVELOPMENTS IN THE QUARK THEORY OF HADRONS. VOL. 1. 1964 - 1978*. Ed. by D. B. Lichtenberg and Simon Peter Rosen. Feb. 1964, pp. 22–101.

[171]   P.A. Zyla et al. "Review of Particle Physics." In: *PTEP* 2020.8 (2020), p. 083C01. DOI: 10.1093/ptep/ptaa104.

[172]   COMPASS collaboration. "The fast Readout of HCAL1 and HCAL2 for the COMPASS Muon Trigger." COMPASS note. 2002.

[173]   HERMES collaboration et al. "Measurement of azimuthal asymmetries with respect to both beam charge and transverse target polarization in exclusive electroproduction of real photons." In: *Journal of High Energy Physics* 2008.06 (2008), 066–066. ISSN: 1029-8479. DOI: 10.1088/1126-6708/2008/06/066. URL: http://dx.doi.org/10.1088/1126-6708/2008/06/066.

[174]   The HERMES collaboration. "Separation of contributions from deeply virtual Compton scattering and its interference with the Bethe-Heitler process in measurements on a hydrogen target." In: *Journal of High Energy Physics* 2009.11 (2009), 083–083. ISSN: 1029-8479. DOI: 10.1088/1126-6708/2009/11/083. URL: http://dx.doi.org/10.1088/1126-6708/2009/11/083.

[175]   ZEUS collaboration. "A measurement of the Q2, W and t dependences of deeply virtual Compton scattering at HERA." In: *Journal of High Energy Physics* 2009.05 (2009), 108–108. ISSN: 1029-8479.

DOI: 10.1088/1126-6708/2009/05/108. URL: http://dx.doi.org/10.1088/1126-6708/2009/05/108.

[176] N. d'Hose, E. Burtin, P. A. M. Guichon, J. Marroncle, M. Moinester, J. Pochodzalla, and A. Sandacz. *Possible measurements of GPDs at COMPASS*. 2002. arXiv: hep-ex/0212047 [hep-ex].

[177] N. Bohr Dr. phil. "I. On the constitution of atoms and molecules." In: *The London, Edinburgh, and Dublin Philosophical Magazine and Journal of Science* 26.151 (1913), pp. 1–25. DOI: 10.1080/14786441308634955. eprint: https://doi.org/10.1080/14786441308634955. URL: https://doi.org/10.1080/14786441308634955.

List of Figures

List of Tables

Acronyms

ADC Analog-Digital-Converter.

BH *Bethe-Heitler*.

BMS beam momentum station.

CATCH COMPASS Accumulate, Transfer and Control Hardware.

CEBAF Continues Electron Beam Accelerator Facility.

CERN Conseil européen pour la recherche nucléaire.

CFD Constant-Fraction discriminator.

CFF *Compton Form Factor*.

CLAS CEBAF large acceptance spectrometer.

CMOS Complementary Metal-Oxide-Semiconductor.

CMS center of mass system.

COMPASS Common Muon Proton Apparatus for Structure and Spectroscopy.

CORAL COMPASS Reconstruction Algorithm.

CTA CERN Tape Archive.

DAQ Data Acquisition.

DC Drift Chamber.

DD *double distribution*.

DESY Deutsches Elektron-Synchrotron.

DIS *deep inelastic scattering*.

DRF detector reference frame.

DVCS *Deeply Virtual Compton Scattering*.

DVMP *Deeply Virtual Meson Production*.

DY *Drell-Yann*.

ECAL electromagnetic calorimeter.

EMC European Muon collaboration.

FE Front-End.

FPGA Field-Programmable Gate Array.

FWHM full width half maximum.

GANDALF Generic Advanced Numerical Device for Analog and Logic Functions.

GEANT Geometry and Tracking.

GEM Gas Electron Multiplier detector.

GeSiCA GEM and Silicon Control and Acquisition.

GPD *Generalized Parton Distribution function*.

HCAL hadron calorimeter.

HEMP *Hard Exclusive Meson Production*.

HEPGEN Hard Exclusive Production Generator.

HERA Hadron-Electron Ring Accelerator.

HERMES HERA measurement of spin.

LAN Local Area Network.

LAS Large Angle Spectrometer.

LAST Large Angle Spectrometer Trigger.

LAT large area tracker.

LED Light-Emitting-Diode.

LO leading order.

LT Ladder Trigger.

MAMI Mainz Microtron.

MC Monte-Carlo.

MM Micro-Mesh Gaseous Structure detector.

MRS main spectrometer reference system.

MT Middle Trigger.

MUX-Tiger Trigger Implementation for GANDALF Electronic Readout.

MW muon wall.

MWPC Multi Wire Proportional Chamber.

NLO next to leading order.

NMC New Muon collaboration.

OPE *operator product expansion*.

OT Outer Trigger.

PDF *Parton Distribution Function*.

PHAST Physics Analysis Software Tools.

PMT photomultiplier tube.

pQCD *perturbative quantum chromodynamics*.

QCD *quantum chromodynamics*.

QED *quantum electrodynamics*.

QFD *quantum flavourdynamics*.

QPM *quark-parton model*.

RMS root mean square.

SADC Sampling Analog-Digital-Converter.

SAS Small Angle Spectrometer.

SAT small area tracker.

SCIFI scintillating fibre detector.

SI silicon strip detector.

SLAC Stanford Linear Accelerator Center.

SM *Standart Model*.

SM spectrometer magnet.

SMUX S-Link Multiplexer.

SNR signal to noise ratio.

SPS Super Proton Synchrotron.

TCS Trigger Control System.

TDC Time-Digital-Converter.

TGEANT Total Geometry and Tracking.

TiS time in spill.

TOF time-of-flight.

VME Versacard Multibus Eurocard.

VSAT very small area tracker.

Appendix A

A.1 Hodoscope positions

Figures to illustrate the results of the determination of the hodoscope positions. The hodoscope elements are drawn in black. If the algorithm was only able to determine the element position in one of the projections (X or Y), the elements are drawn in orange. If the position in both projections could not be determined they are drawn in red. In those cases the information from the *detectors.dat* is used. The 2-dimensional distribution show the ratio of extrapolated tracks and tracks with hits in the corresponding hodoscope plane.

(a) HL04

(b) HL05
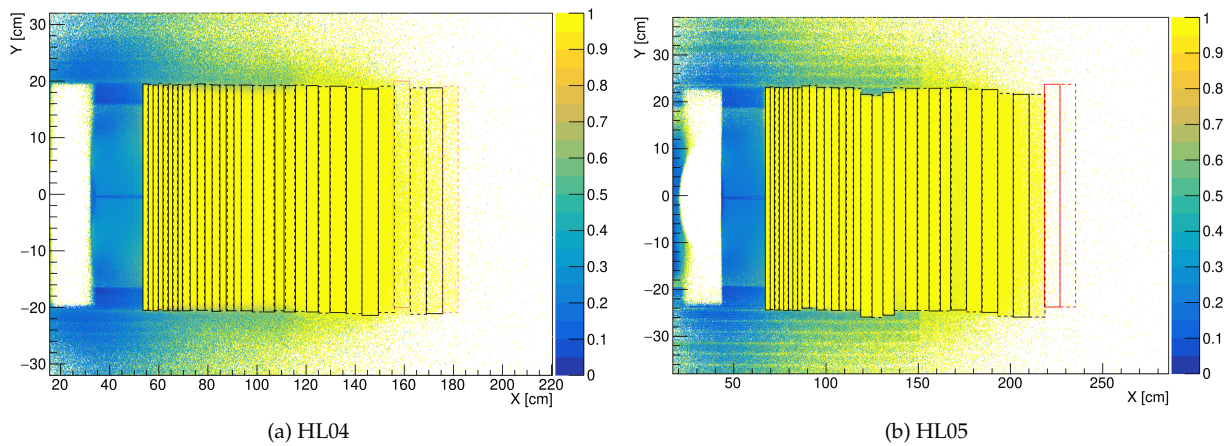
Figure 1: Illustration of the hodoscope positions of HL04 and HL05.

(a) HM04Y1 up

(b) HM05Y1 up

(c) HM04Y1 down

(d) HM05Y1 down
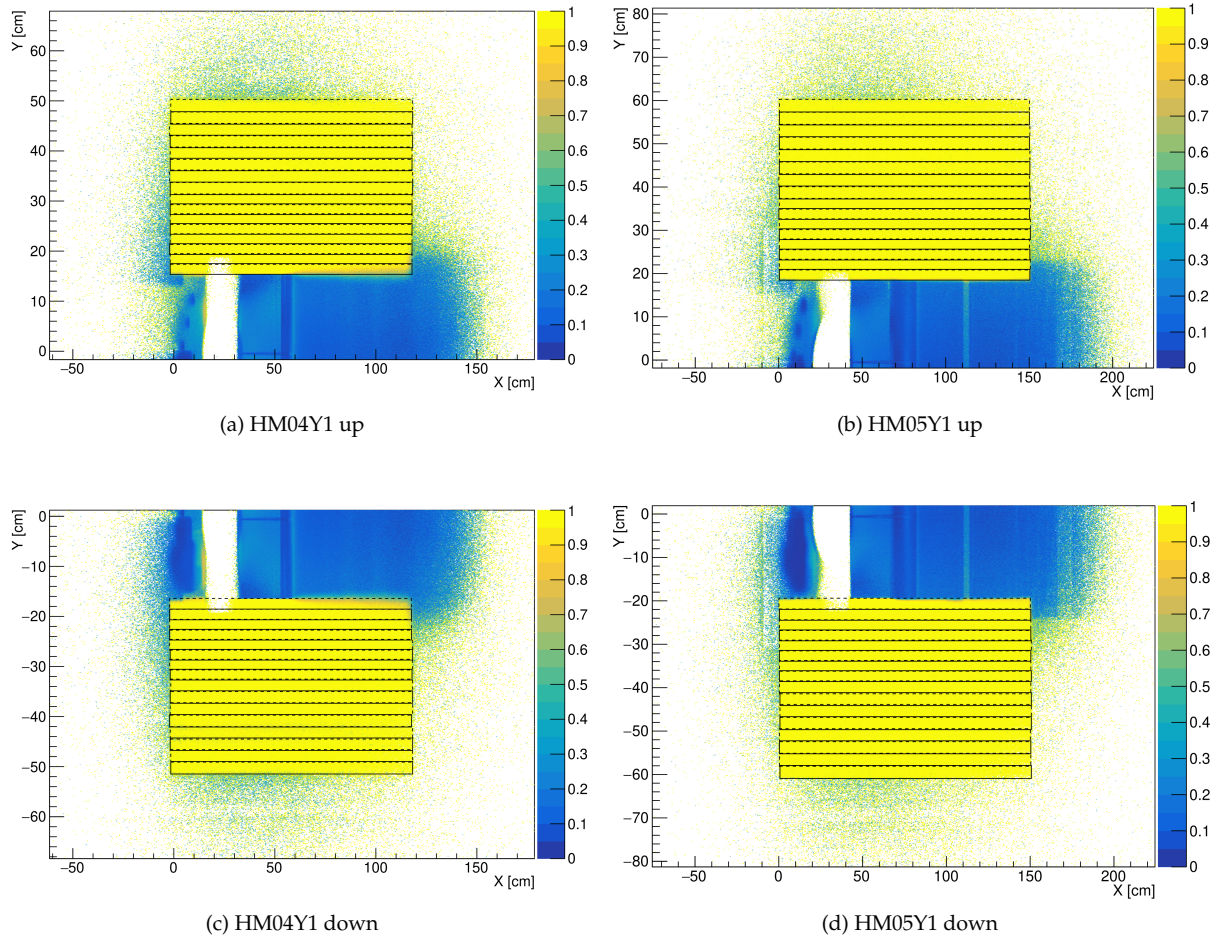
Figure 2: Illustration of the hodoscope positions of HM04 and HM05 (up and down).
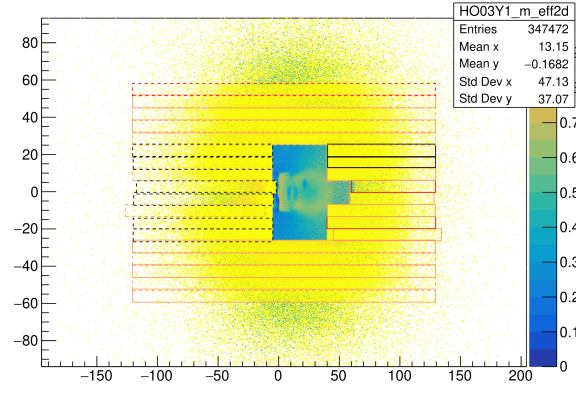
(a) HO03
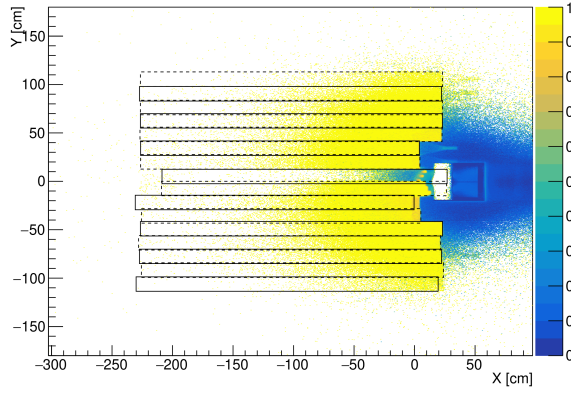
(b) HO04Y2
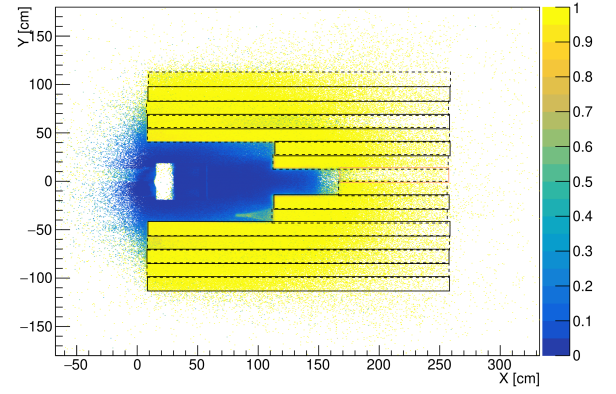
(c) HO04Y1

Figure 3: Illustration of the hodoscope positions of HO03 and HO04.

A.2 Kinematic distributions of the exclusive photon events in data

The plots in this Section present the results of data distributions after the exclusive photon event selection is applied. This also includes the results of the kinematic fit and the removal of the visible π^0-background. To illustrate the impact of the ν-region on the kinematic distribution the contributions are indicated by choosing different colors for each domain. The *reference region* is shown as the white histogram, while the *interference* and *extraction region* correspond to a lighter and darker blue.
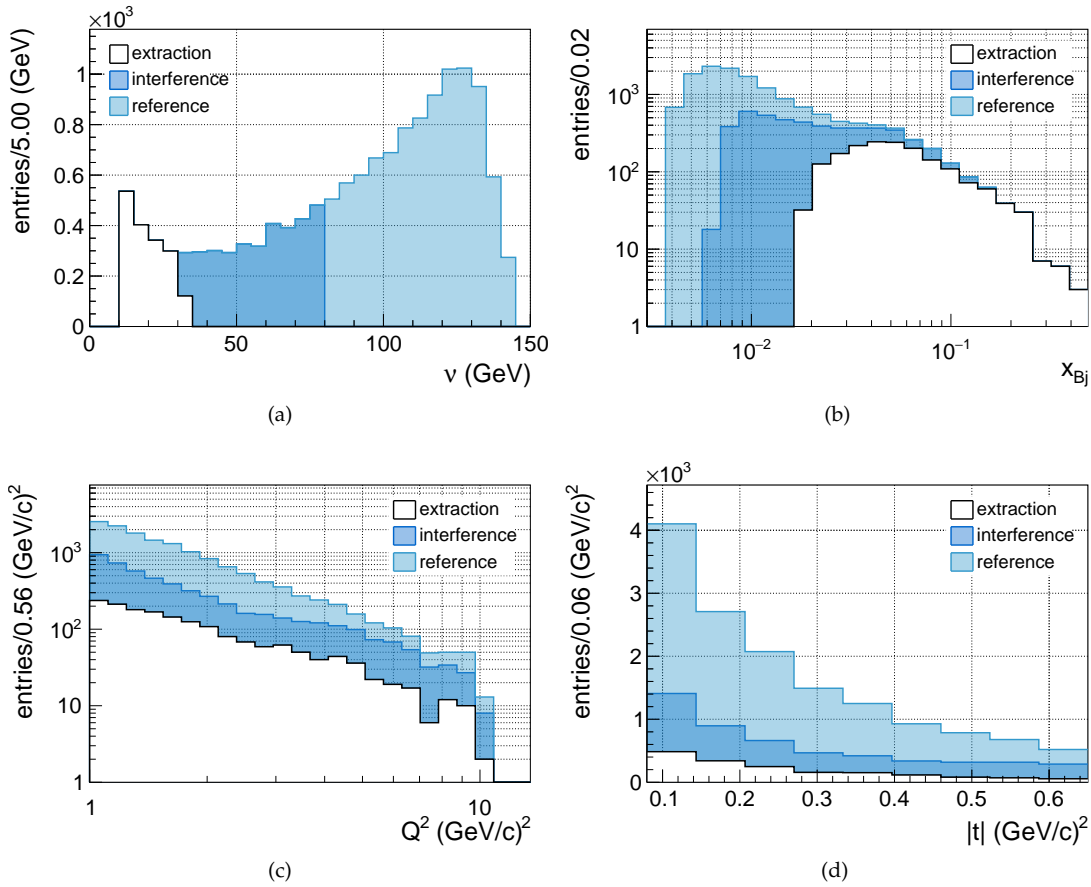
Figure 4: ν, x_{Bj}, Q^2 and $|t|$ distribution for real data in the reference, interference and extraction region.

(a)

(b)

(c)

(d)
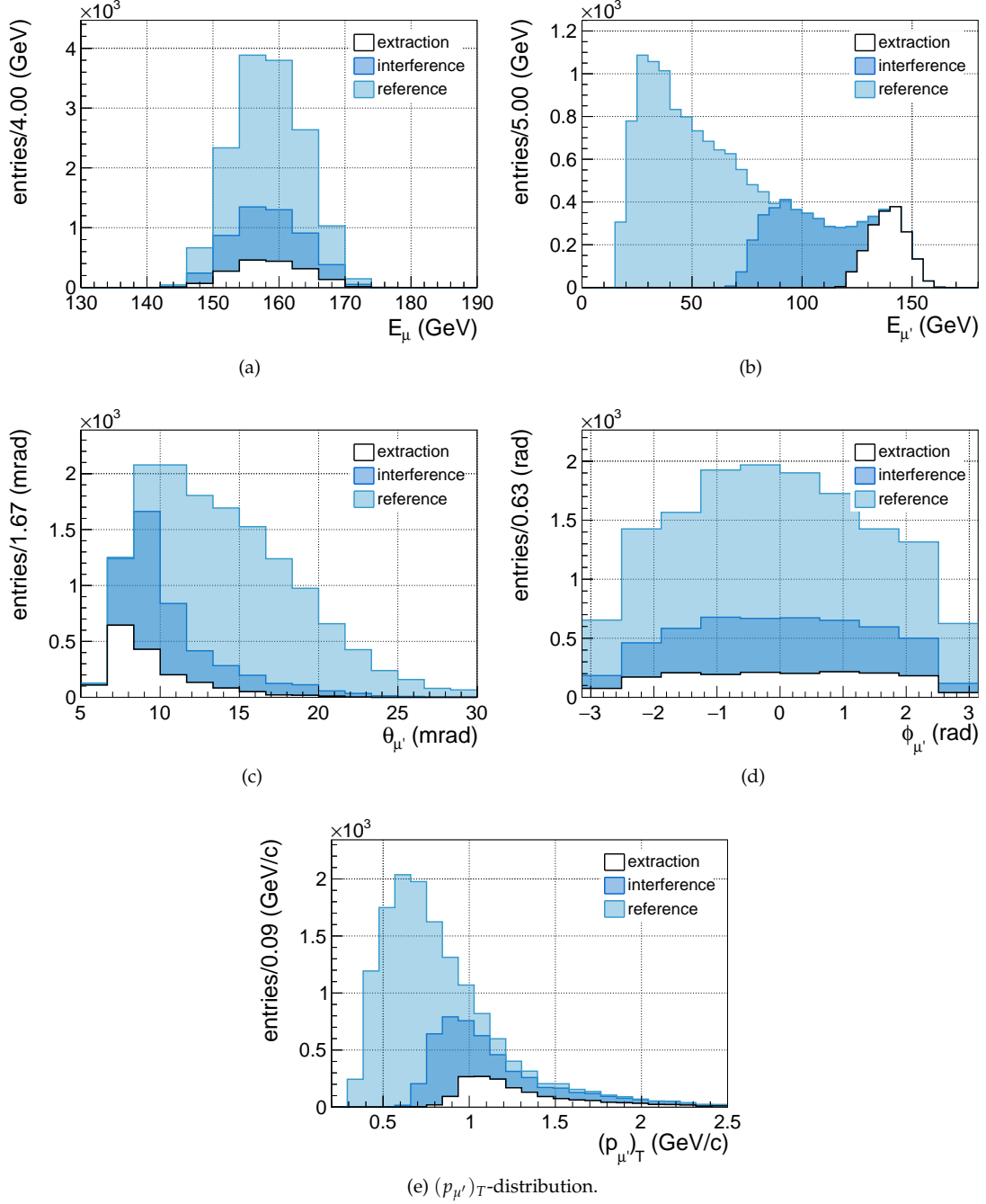
(e) $(p_{\mu'})_T$-distribution.

Figure 5: Distributions of the energy (E) distribution of the beam (μ) and the energy, the polar angle, the azimuthal angle and the transverse momentum (E, θ, ϕ and $(p)_T$) distributions of the scattered (μ') muon in each region.
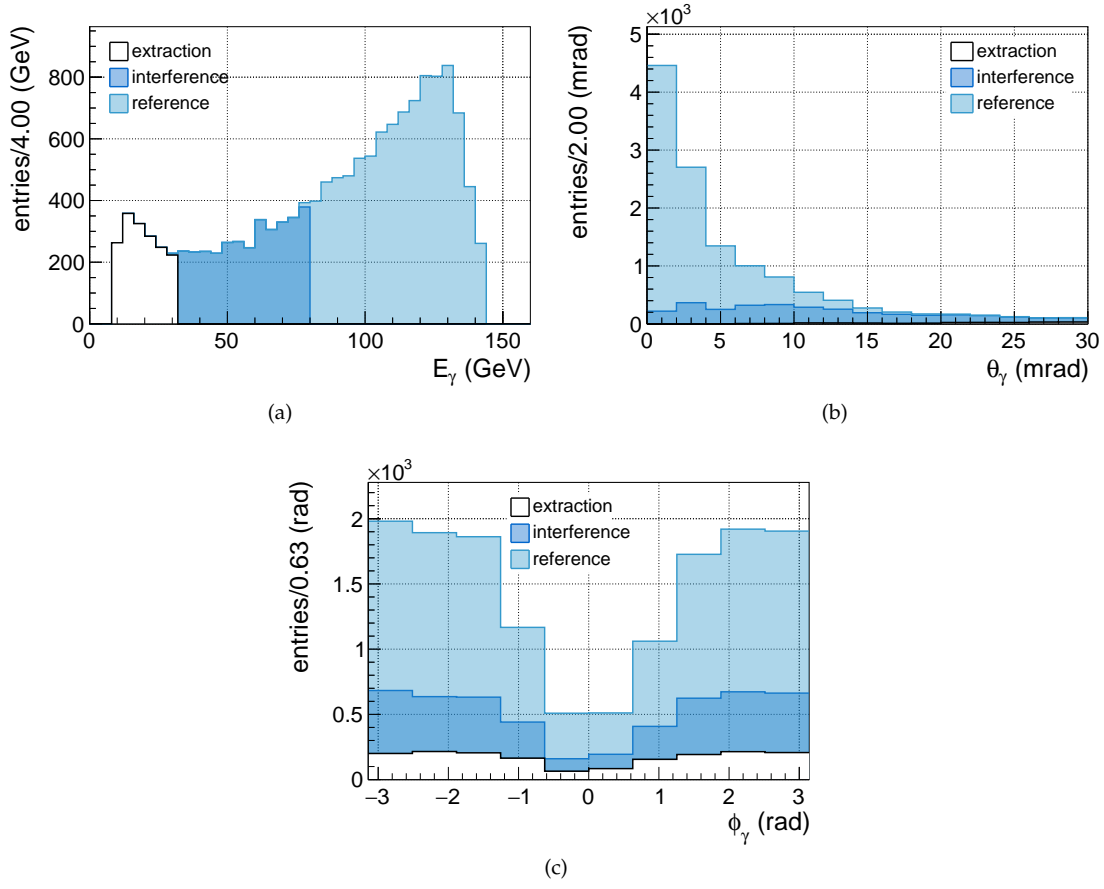
Figure 6: Distributions of the energy, the polar and the azimuthal angle (E, θ, ϕ) for the exclusive photon (γ) in each region.

(a)

(b)

(c)
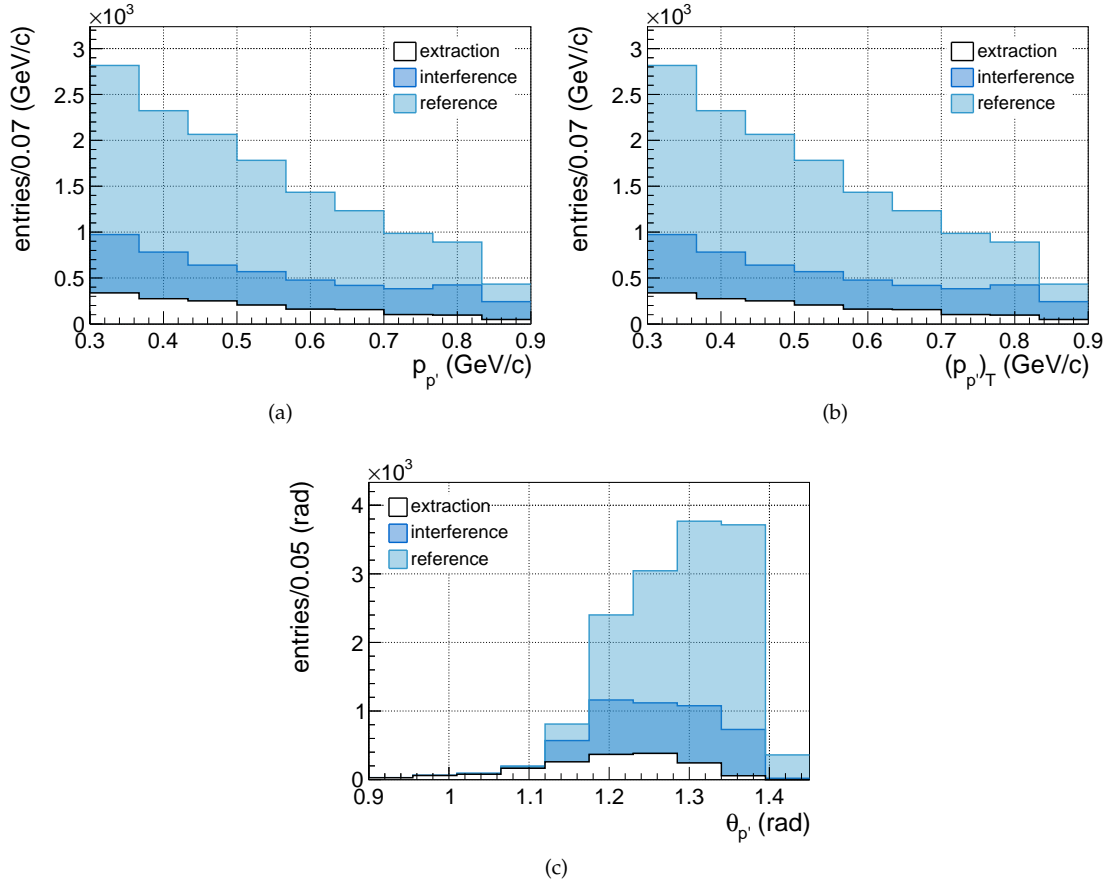
Figure 7: Distributions of the momentum, the transverse momentum, the polar angle (p, $(p)_T$, θ) of the recoil proton (p') in each region.

A.3 Pull distributions

Summary of all pull distributions extracted from the kinematic fit for the real photon, the incoming and outgoing muons and the measured variables of the recoil proton detector.

(a)

(b)

(c)
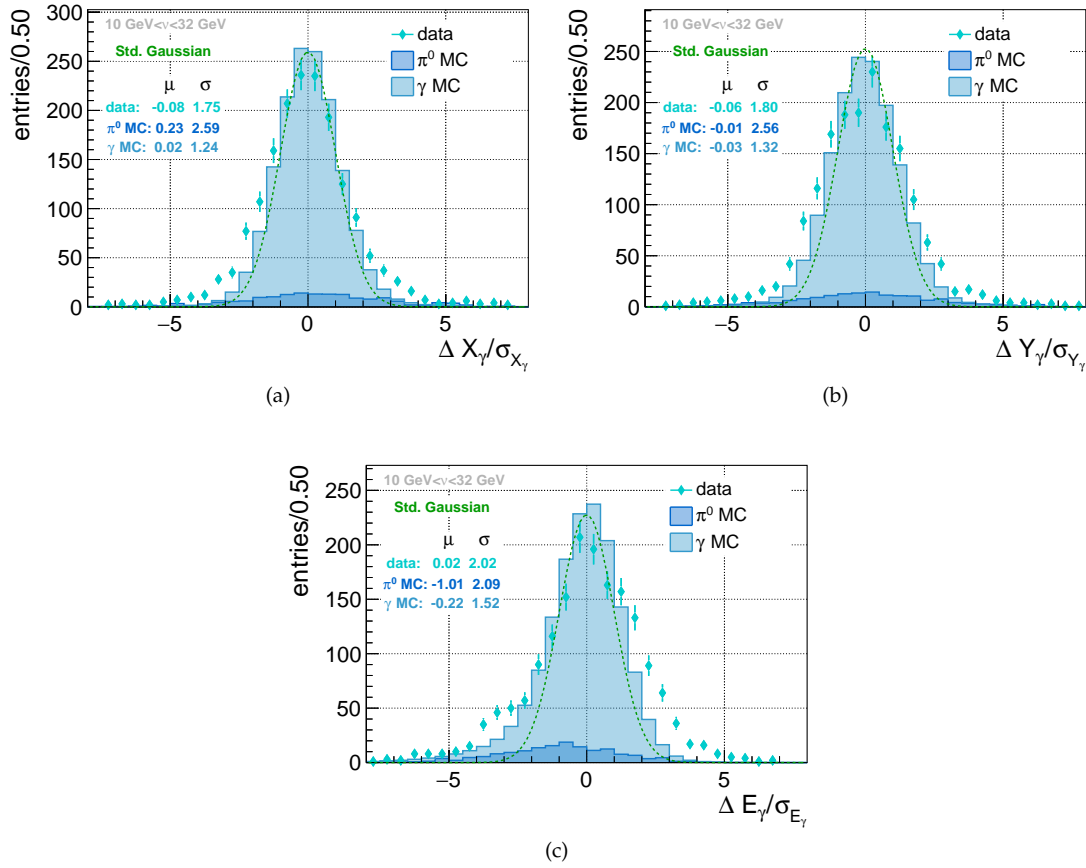
Figure 8: Pull distributions for the X (a) and Y-coordinate (b) of the cluster at the location of the ECAL and its energy (c).
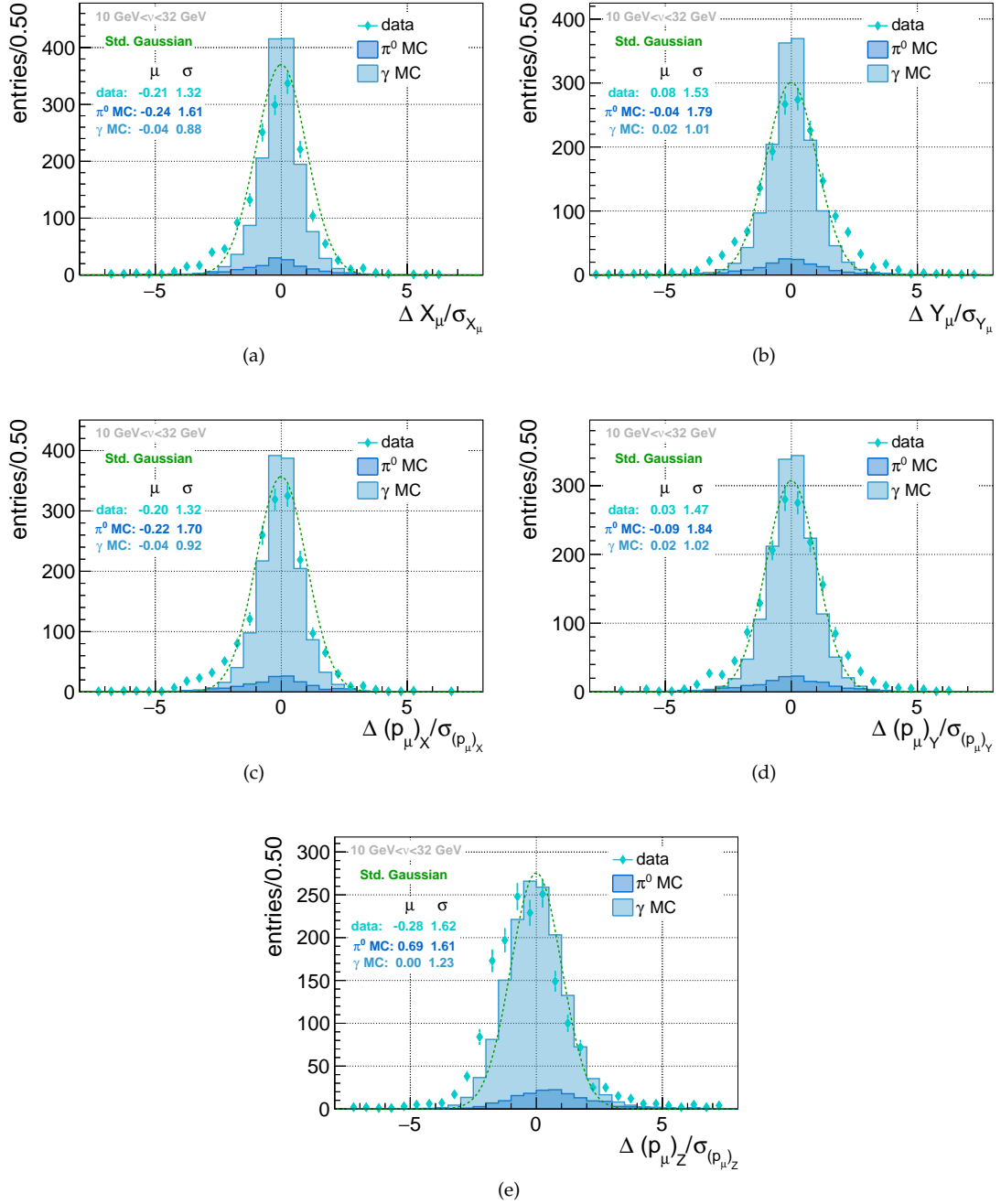
Figure 9: Pull distributions for the X- (a) and Y-coordinate (b) and the X- (c),Y- (d) and Z-component (e) of the momentum of the incoming muon.
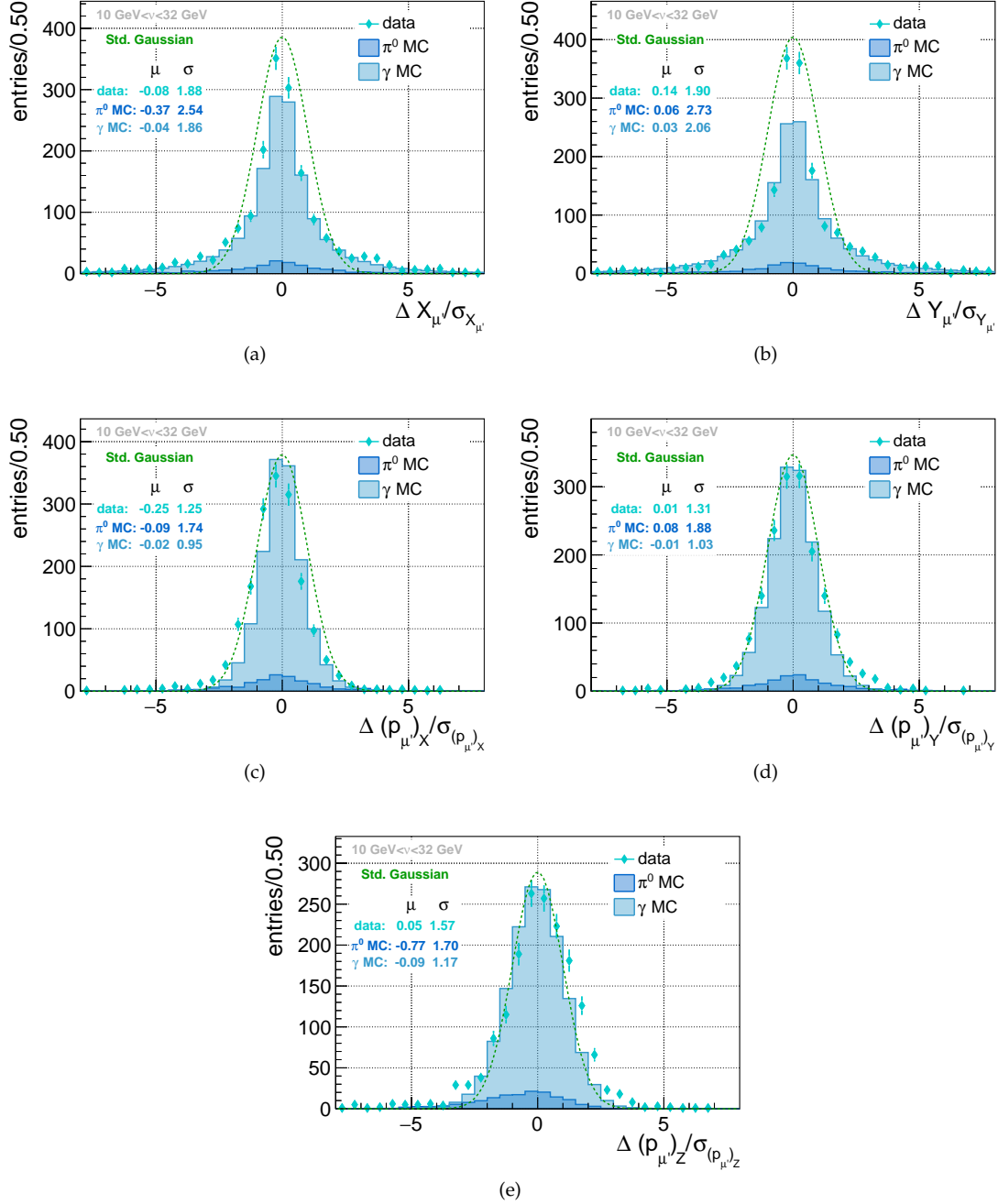
Figure 10: Pull distributions for the X- (a) and Y-coordinate (b) and the X- (c),Y- (d) and Z-component (e) of the momentum of the scattered muon.

(a)

(b)

(c)
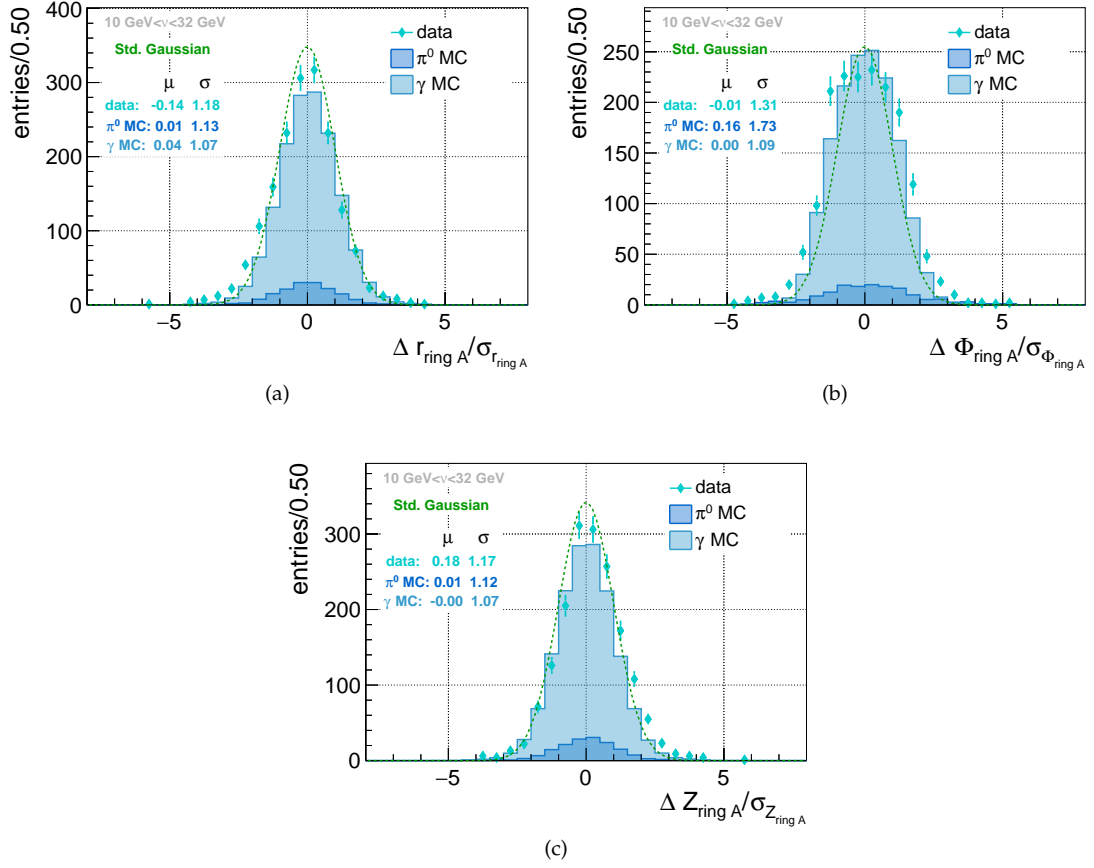
Figure 11: Pull distributions for the radius (a), the azimuthal angle (b) and the Z-position (c) of the hits in ring A.

(a)

(b)

(c)
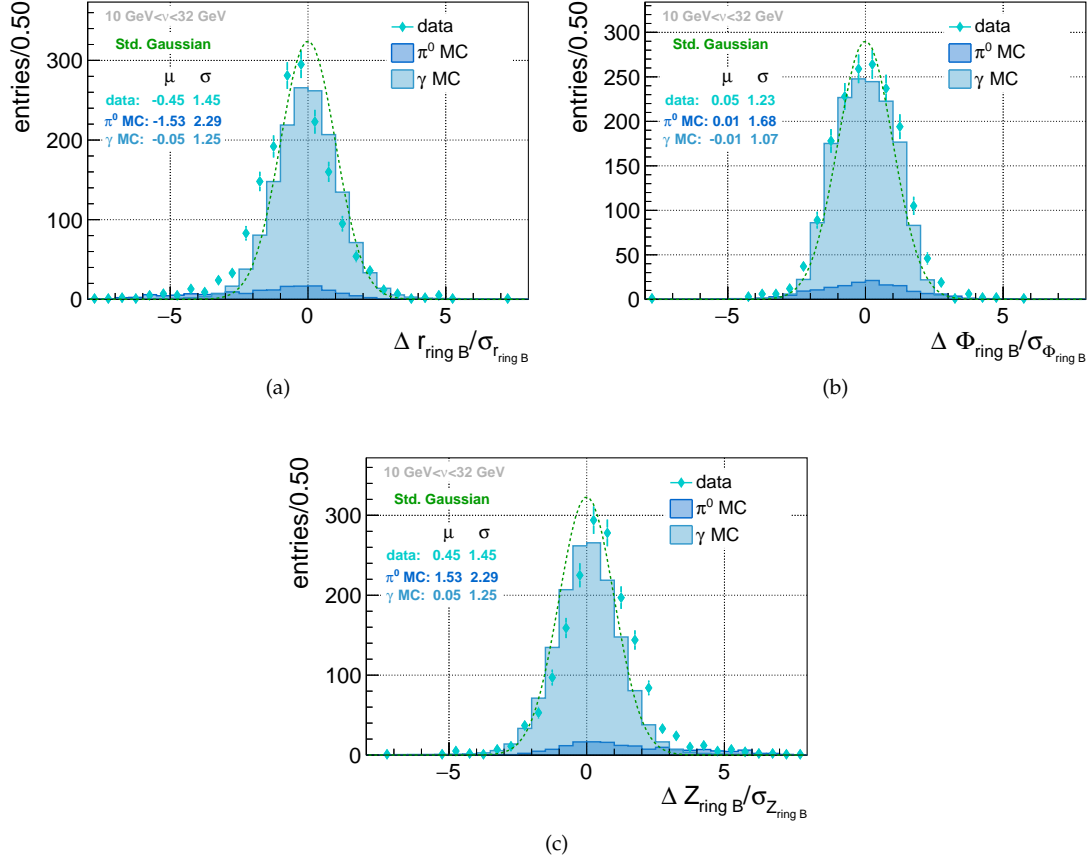
Figure 12: Pull distributions for the radius (a), the azimuthal angle (b) and the Z-position (c) of the hits in ring B.
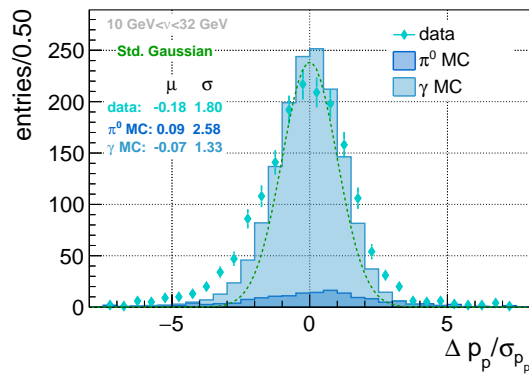
Figure 13: Pull distributions for the momentum of the recoil proton.

A.4 Comparison of excl. photon Monte-Carlo sample to data

Comparison related to the kinematics of the incoming and scattered muon, the real photon and the recoil proton between the data and the exclusive photon Monte-Carlo sample.

(a)   (b)
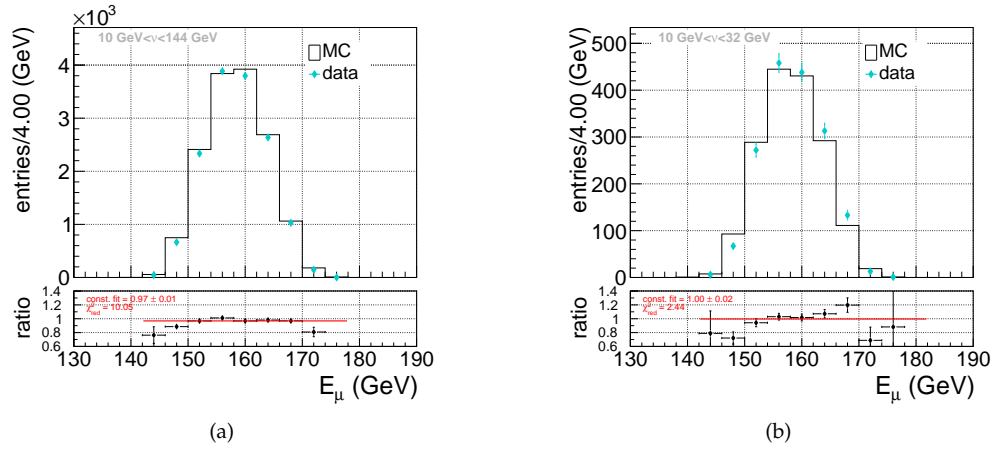
Figure 14: Energy distribution of the incoming muons in the full ν-region (left) and the extraction region (right).
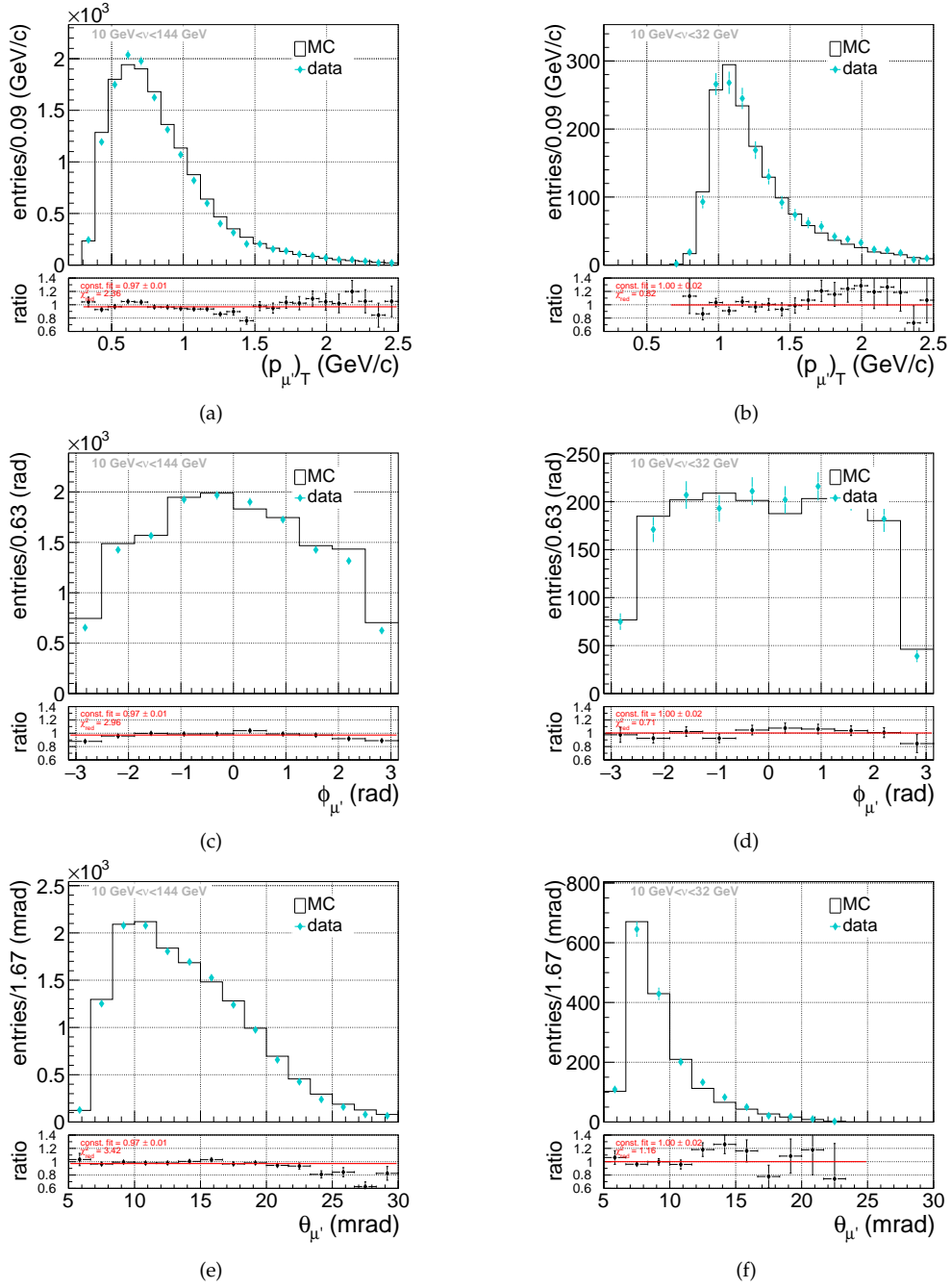
Figure 15: Transverse momentum and azimuthal and polar angle distribution of the scattered muons in the full ν-region (left) and the extraction region (right).

(a)

(b)

(c)

(d)

(e)

(f)
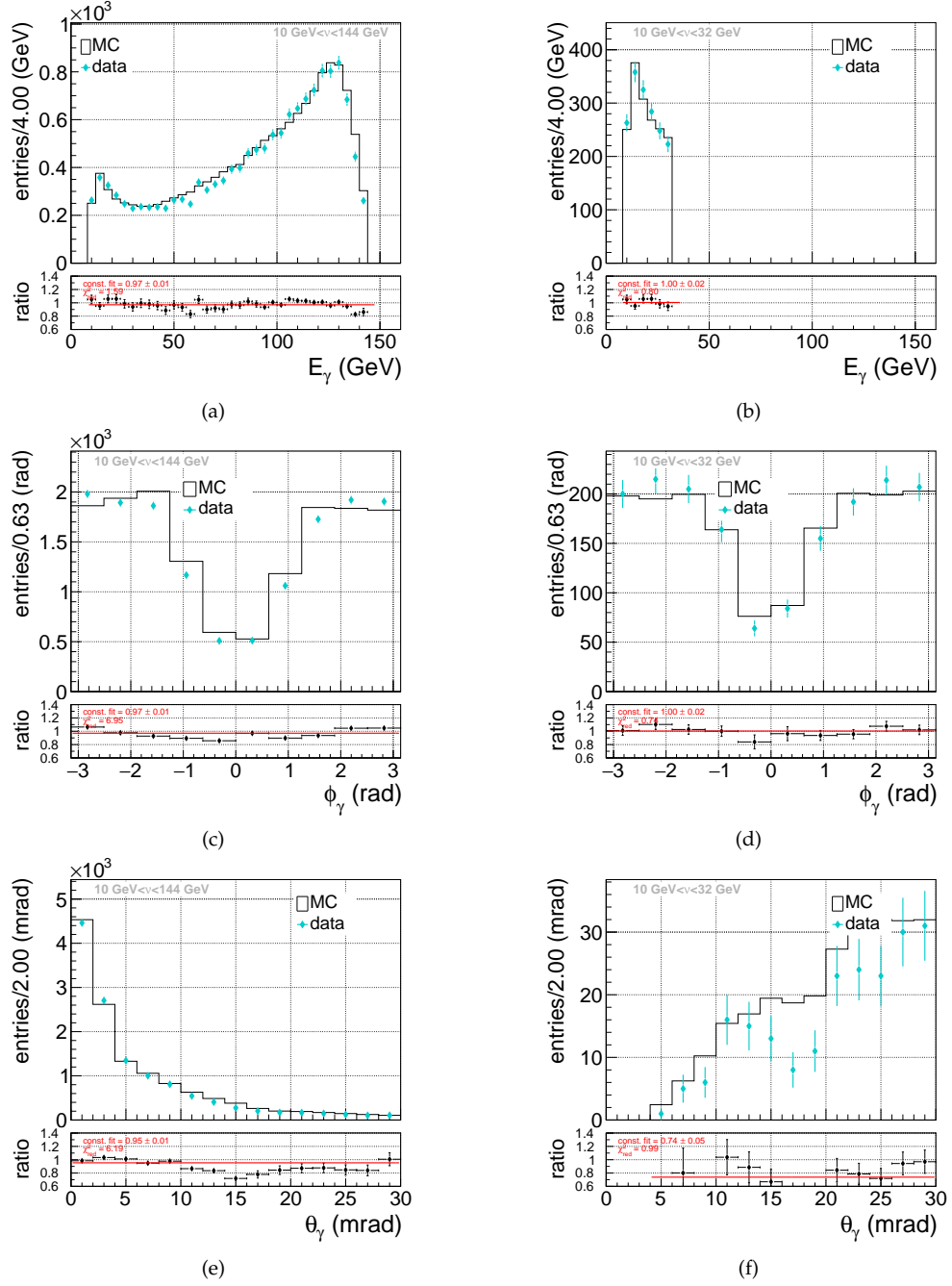
Figure 16: Energy and azimuthal and polar angle distribution of the real photon in the full ν-region (left) and the extraction region (right).
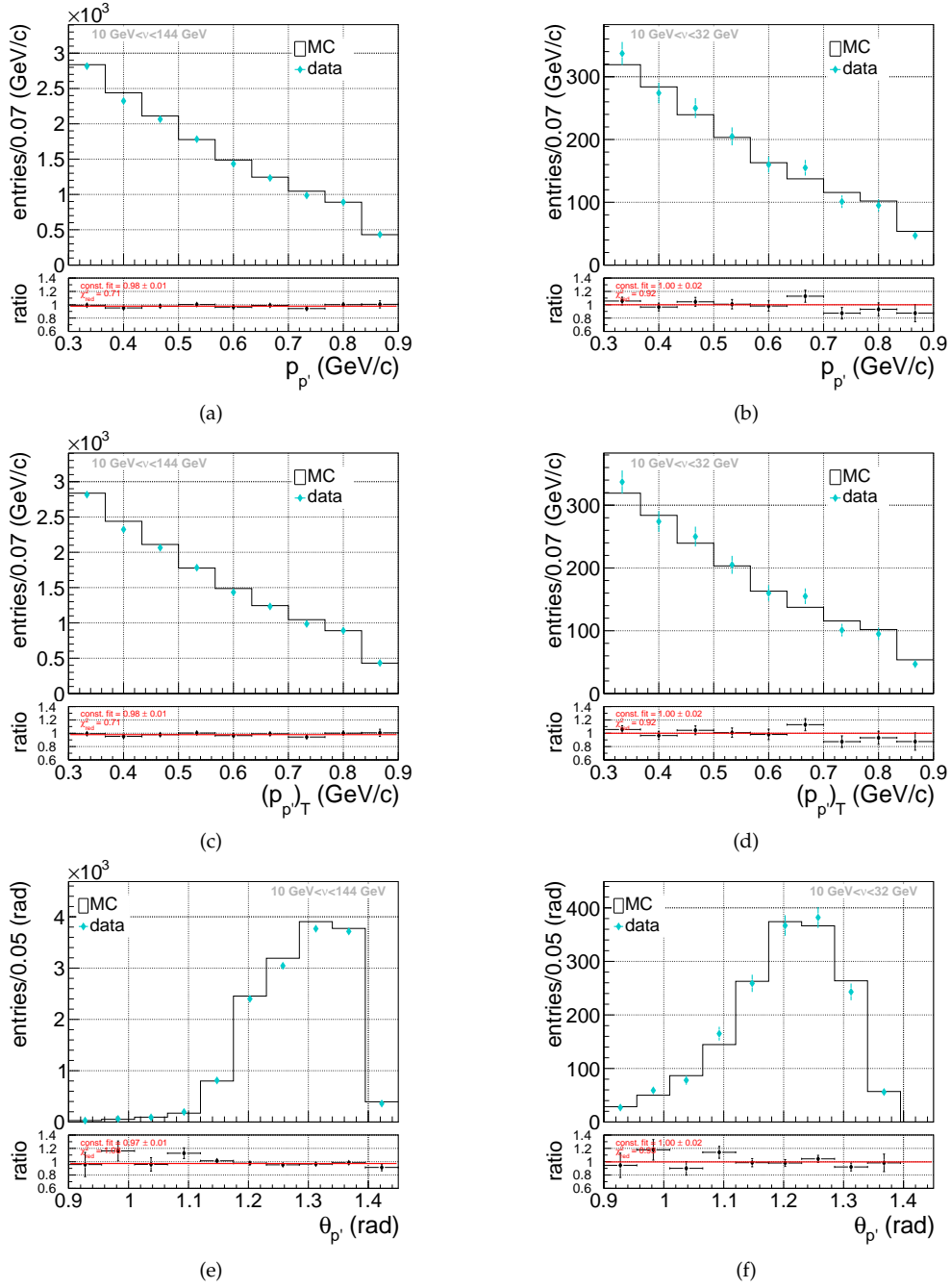
Figure 17: Momentum, transverse momentum and polar angle distribution of the recoil proton in the full ν-region (left) and the extraction region (right).

A.5 Extracted slope parameter for different binning in ν and $|t|$

DVCS cross section and slope parameter for different combination of $|t|$ and ν binning.

(a)

(b)

(c)
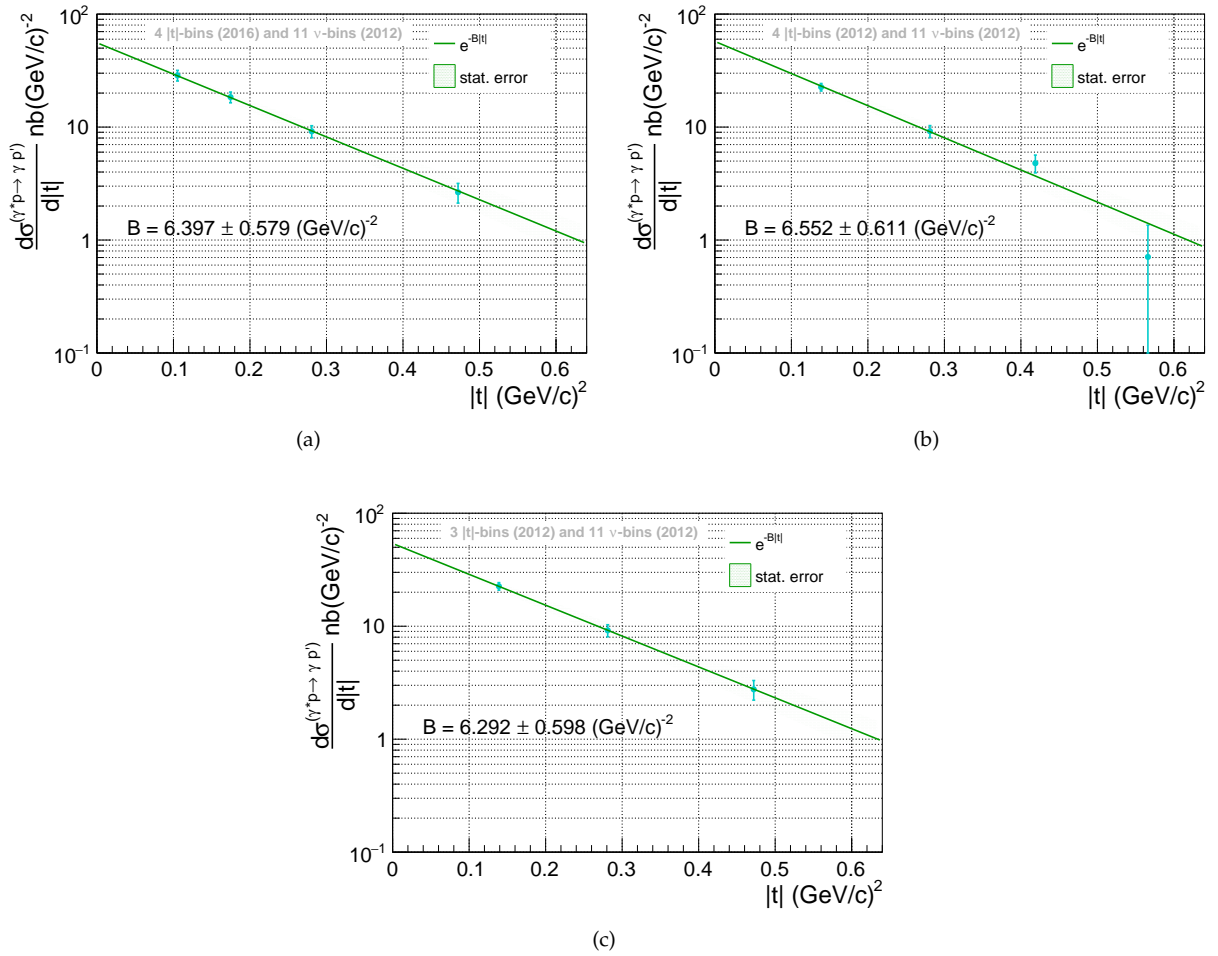
Figure 18: DVCS cross section and slope parameter for 4 equistatistic bins in $|t|$ and 11 equidistant bins in ν (a), 4 equidistant bins in $|t|$ and 11 equidistant bins in ν (b) and with the last two bins in $|t|$ merged for equidistant bins and 11 equidistant bins in ν (c).

A.6 Extracted slope parameter in two x_{Bj}-regions

DVCS cross section and slope parameter determined for two different x_{Bj} regions.
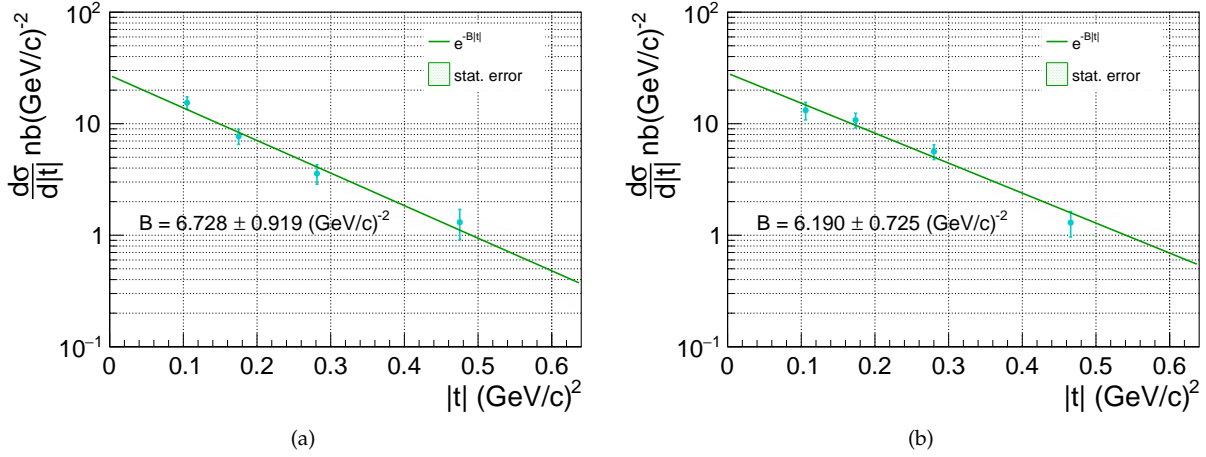
Figure 19: DVCS cross section and slope parameter determined at $\langle x_{Bj} \rangle = 0.04$ (a) and $\langle x_{Bj} \rangle = 0.09$ (b).

Appendix B

B.1 Transformation of the virtual photon flux

Starting from:

$$\Gamma = \frac{K\alpha}{\pi Q^2 x_{Bj} y} \frac{1}{2M\nu E} \left[x y^2 M + \nu \left(1 - y - \frac{\gamma^2 y^2}{4} \right) \left(\frac{Q^2}{Q^2 + \nu^2} \right) \right],$$ (1)

and using $K = \nu(1 - x_{Bj})$ and $Q^2 = x_{Bj} 2M\nu$, the previous Equation can be written as:

$$\Gamma = \frac{\alpha}{2\pi} \frac{(1 - x_{Bj})}{Q^2 y E} \left[y^2 + \frac{2\nu^2}{Q^2 + \nu^2} \left(1 - y - \frac{\gamma^2 y^2}{4} \right) \right].$$ (2)

With $\gamma = 2M x_{Bj}/Q = Q^2/\nu^2$ and $y = \nu/E$ one obtains:

$$\Gamma = \frac{\alpha}{2\pi} \frac{(1 - x_{Bj})}{Q^2 y E} \left[y^2 + \frac{2}{1 + \frac{Q^2}{\nu^2}} \left(1 - y - \frac{Q^2}{4E} \right) \right].$$ (3)

Acknowledgement

Johannes Vincenzo Giarra

Curriculum Vitae

✉ jgiarra@cern.ch

Werdegang

01/2017 - jetzt	**Promotionsstudium**, *Johannes Gutenberg-Universität*, Mainz.
	○ Promotionsstudent in AG COMPASS unter Prof. Dr. E.-M. Kabuß
	○ Mehrjährige Lehrtätigkeit
09/2016 - 12/2016	**Hilfswissenschaftler**, *Johannes Gutenberg-Universität*, Mainz.
	○ Stelle als HIWI in der AG COMPASS unter Prof. Dr. E.-M. Kabuß
08/2013 - 07/2016	**Studium: Master of Science Physik**, *Johannes Gutenberg-Universität*, Mainz.
	○ Arbeitsschwerpunkt: Statistische Datenanalyse
	○ Vorlesungsschwerpunkte: Kern- und Teilchenphysik
	○ Masterarbeit: *Bestimmung von Hadronmultiplizitäten in Lepton-Nukleon-Streuung bei COMPASS*, AG COMPASS unter Prof. Dr. E.-M. Kabuß
08/2013	**Hochschulwechsel: Master of Science Physik**, *Johannes Gutenberg-Universität*, Mainz.
	unter Auflagen
	○ Nachholen der Veranstaltung: Theoretische Mechanik, Quantenmechanik, Veranstaltung aus Experimentalphysik V (Kern- und Teilchenphysik)
03/2012 - 08/2013	**Studium: Angewandte Physik**, *Hochschule RheinMain*, Standort Rüsselsheim.
	○ angestrebter Abschluss: Master of Science
03/2009 - 02/2012	**Studium: Physikalische Technik**, *Hochschule RheinMain*, Standort Rüsselsheim.
	○ Abschluss: Bachelor of Science (06.02.2012)
01/2008 - 12/2008	**Praktikum bei Lufthansa Technik A.E.R.O**, Alzey.
	○ geforderter praktischer Anteil zum Erlangen der Fachhochschulreife
01/2007 - 09/2007	**Zivildienst am Universitätsklinikum**, Mainz.
1997 - 2006	**Besuch des Elisabeth-Langgässer Gymnasiums**, Alzey.
	○ Abgang nach der 12. Klasse mit Erreichen des theoretischen Anteils der Fachhochschulreife